

Numerical and Experimental Investigation of Mechanical Strength of Spot Welded Joints

Xiaohang Kong

**A thesis submitted in partial fulfilment of the requirement of
the Liverpool John Moores University for the degree of
Doctor of Philosophy**

School of Engineering, Liverpool John Moores University

October 2008

ACKNOWLEDGEMENTS

I would like to take this opportunity to express my deepest gratitude and sincerest thanks to my supervisors Dr James Ren, Dr Glynn Rothwell and Dr Russell English for their inspiring supervision of my study and guidance during the production of this thesis.

Many other academic, secretarial and technical members of staff have facilitated the realisation of this thesis and I express them all my gratitude. I would like to thank Mr. Clive Eyre and Mr. Steven Gotts for their invaluable technical support with material testing and funny jokes.

I acknowledge the Liverpool John Moores University and the School of Engineering for the facilities and support provided. I would like to express my appreciation to SSAB Swedish Steel, Jaguar's Halewood Plant for their support on the materials and Swantec Software and Engineering ApS (Denmark) for providing an evaluation version of the welding simulation software SORPAS.

Special thanks also to my group mates, Mrs. Lisa Li, Mr. Jarema Krywonos, Mr. Fuzy Elkul, Mr. Yaodong Gu for their friendship and sharing the experience of being a postgraduate student. I am also grateful of the help of my friends, who gave me help in many ways and shared a great time in my studies and life at Liverpool John Moores University.

Finally, I would like thank my family for sustained encouragement that gave me motivation during my studies, continuous and unselfish love and support.

Xiaohang (Peter) Kong

ABSTRACT

In this work, an inverse FE modelling indentation method to predict the plastic properties of materials has been systematically studied and used to characterise detailed properties of spot welded joints in steel. An inverse program based on a dual indenter approach and continuous indentation curves has been established and validated, which provided the framework for an improved method based on static indentation. The method was successfully used to study two typical auto steels and their spot welded joints. These predicted plastic material parameters were then used to simulate the tensile shear deformation of the spot welded joints and to investigate the effect of dimensional parameters on the strength of welded joints.

Systematic studies of inverse FE modelling approaches with different indenter types showed that there are a variety of materials with different stress-strain relationships but identical indentation curves for Vickers, Knoop or spherical indenters and dual sharp indenters. This suggests that these methods can not be used to predict material plastic properties unless the range of material properties is pre-known. Dual spherical indenters showed significant improvement of the prediction accuracy, but showed strong sensitivity to experimental error. The combination of sharp (Vickers or Knoop) and spherical indenters is proven to be the best approach over a wide range of material properties and showed a clear improvement over other methods.

Based on the framework established, a new method using static indentation data rather than continuous indentation data has been developed. Experimental work on two steels show the stress-strain curves inversely predicted are comparable to standard tensile tests and notched specimen. The method was applied to extract the detailed material properties in spot welded joints and the results were applied to simulate the tensile shear deformation. The validated numerical model was further used to investigate the effect of nugget size and the thickness of the metal sheets on the strength of welded joints.

Contents

Acknowledgements

Abstract

Contents

List of figures

| | |
|--|----|
| Chapter 1 Introduction | 1 |
| 1.1 Introduction..... | 2 |
| 1.2 Aim & objectives..... | 4 |
| 1.3 Outline of the thesis..... | 5 |
| Chapter 2 Literature review | 7 |
| 2.1 Spot welding and its applications..... | 8 |
| 2.1.1 Resistance spot welding process..... | 8 |
| 2.1.2 Applications of resistance spot welding..... | 8 |
| 2.2 Structure of spot welded joints and effect of welding parameters..... | 10 |
| 2.2.1. Microstructure of a spot welded joint..... | 10 |
| 2.2.2 Effects of welding parameters on nugget and heat affected zones..... | 11 |
| 2.3 Mechanical strength of spot welded joints and structures..... | 13 |
| 2.3.1 Main factors affecting the strength of spot welded joint..... | 13 |
| 2.3.2 Elasto-plastic deformation and fracture of metallic materials..... | 14 |
| 2.3.3 Characterisation of the mechanical properties of welding zones..... | 17 |
| 2.4 Indentation techniques and applications..... | 20 |
| 2.5 The mechanics of indentation process..... | 24 |
| 2.6 Material deformation in an indentation process..... | 27 |
| 2.6.1 Elastic recovery | 27 |
| 2.6.2 Piling-up and sinking-in | 28 |
| 2.7 Instrumented indentation test..... | 31 |
| 2.8 Evaluation of material properties by indentation tests..... | 33 |

| | |
|---|-----------|
| 2.8.1 Classification of different approaches..... | 33 |
| 2.8.2 Tabor method based on indentation test..... | 33 |
| 2.8.3 Direct and reverse method..... | 35 |
| 2.8.4 Inverse FE modelling method..... | 38 |
| 2.8.5 Potential use of inverse FE modelling based on indentation for characterising spot welded joints..... | 39 |
| Chapter 3 Research approach and experimental work..... | 60 |
| 3.1 Introduction..... | 61 |
| 3.2 Experimental work..... | 62 |
| 3.2.1 Materials | 62 |
| 3.2.2 Spot welding test and set up | 62 |
| 3.2.3 Tensile and tensile-shear test | 63 |
| 3.2.3.1 Tensile test machine | 63 |
| 3.2.3.2 Tensile test of the base materials (standard and notched specimen)..... | 64 |
| 3.2.3.3 Tensile-shear test of spot welded joints..... | 64 |
| 3.2.4 Micro-hardness test..... | 64 |
| Chapter 4 Inverse FE modelling of continuous indentation test with different indenters..... | 71 |
| 4.1 Introduction..... | 72 |
| 4.2 FE models of indentation tests and effects of testing and material parameters | 73 |
| 4.2.1 FE modelling of the Vickers indentation | 74 |
| 4.2.2 FE modelling of the Knoop indentation..... | 76 |
| 4.2.3 FE modelling of the spherical indentation | 78 |
| 4.3 Inverse FE modelling based on continuous indentation tests | 80 |
| 4.3.1 Inverse analysis based on single indenter method | 81 |
| 4.3.1.1 Inverse FE modelling based on the Vickers indentation..... | 83 |
| 4.3.1.2 Inverse FE modelling based on the Knoop indentation | 84 |
| 4.3.1.3 Inverse FE Modelling based on the spherical indentation..... | 85 |
| 4.3.2 Inverse analysis based on dual indenters method..... | 87 |

| | |
|--|------------|
| 4.3.2.1 Inverse FE modelling based on Vickers and Knoop indentation | 87 |
| 4.3.2.2 Inverse FE modelling based on dual spherical indentations..... | 88 |
| 4.3.2.3 Inverse FE modelling based on Vickers and spherical indentations | 90 |
| 4.3.2.4 Inverse FE modelling based on Knoop and spherical indentations | 91 |
| 4.4 Sensitivity analysis and results | 93 |
| 4.5 Summary | 96 |
| Chapter 5 Inverse finite element modelling based on static indentation test and the strength of spot welded joints..... | 134 |
| 5.1 Introduction..... | 135 |
| 5.2 Inverse FE modelling approach based on force-indentation size ($P-d$) data from static indentation tests..... | 137 |
| 5.2.1. FE models of the Vickers and spherical indentations | 137 |
| 5.2.2 Inverse FE analysis based on static indentation tests.... | 138 |
| 5.2.3 Validation of the inverse analysis program by blind test..... | 140 |
| 5.3 Inverse characterisation of auto steels | 141 |
| 5.3.1 Indentation tests and inverse analysis results | 141 |
| 5.3.2 Verification of inverse FE modelling results with standard tensile tests..... | 142 |
| 5.4 Characterisation of material properties within spot welded joints of steels..... | 145 |
| 5.5 FE modelling of tensile-shear test of spot welded joints..... | 147 |
| 5.5.1. FE models of spot welded joints | 147 |
| 5.5.2 Effects of nugget size and sheet thickness to the mechanical behaviour of spot welded joint under tensile-shear loading..... | 148 |
| 5.6 Summary | 150 |
| Chapter 6 Discussions | 178 |
| 6.1 Use of indentation and inverse FE modelling in characterising material properties | 179 |

| | |
|--|------------|
| 6.2 Factors affecting indentation and inverse FE modelling process based on single and dual indenters method | 182 |
| 6.3 Comparisons of the accuracy with different approaches | 184 |
| 6.4 Sensitivity of the inverse FE modelling to perturbation in the indentation force | 185 |
| 6.5 Approach based on static indentation test and its application to spot welded joints..... | 187 |
| Chapter 7 Conclusion and further work..... | 197 |
| 7.1 Summary and conclusion..... | 198 |
| 7.2 Further works..... | 200 |
| References..... | 201 |
| Publication list..... | 211 |

List of figures

Chapter 2

- Figure 2.1 The setup of a spot welding system and the resistances occurring in welding.....42
- Figure 2.2 Different stages of resistance spot welding operation.....42
- Figure 2.3 Typical optical microstructure of the welded joint of steel.43
- Figure 2.4 Typical spot weld lobe curve.....43
- Figure 2.5 Effect of nugget diameter on tensile-shear strength of spot welded joints of micro alloyed steel.44
- Figure 2.6 Typical elastic and plastic stress-strain curves and the ductile fracture process.....45
- Figure 2.7 Schematic showing different indentation tests.46-47
- Figure 2.8 Schematics of spherical indentation.48
- Figure 2.9 Schematic showing the recovery process for spherical indenter and conical indenter on an elastic-plastic solid.....49
- Figure 2.10 Schematic illustration of sinking-in and piling-up of materials around spherical indents and sharp indents with included apex angle of 68°50
- Figure 2.11 Dependence of the surface deformation parameters on the strain hardening exponent and surface topography around the Vickers indenter.....51-52
- Figure 2.12 Schematic illustration of a typical force (P) indentation depth (h) response of an elasto-plastic material to instrumented sharp indentation.53
- Figure 2.13 Geometry to characterise continuous indentation with conical indenter and the influence of material properties.54
- Figure 2.14 Summary of different methods used to estimate material properties based on indentation tests.55
- Figure 2.15 Flow chart showing typical procedures in forward and reverse method..56
- Figure 2.16 Influence of a perturbation of 3% in normal force on the determination of n57
- Figure 2.17 Flow chart showing typical procedure of an interactive inverse FE modelling method.....58

| | |
|---|----|
| Figure 2.18 Flow chart of Kalman Filter procedure to determine the unknown parameters using instrumented indentation records..... | 59 |
|---|----|

Chapter 3

| | |
|--|----|
| Figure 3.1 Flow chart showing the work plan..... | 65 |
| Figure 3.2 Microstructures of steel A and steel B..... | 66 |
| Figure 3.3 Spot welding machine..... | 67 |
| Figure 3.4 Tensile test machine..... | 68 |
| Figure 3.5 Tensile test of the base steels..... | 69 |
| Figure 3.6 Schematic showing the set-up of the tensile-shear test of spot welded joints..... | 69 |
| Figure 3.7 Leitz micro hardness tester..... | 70 |

Chapter 4

| | |
|---|-----|
| Figure 4.1 FE model of the Vickers indentation test..... | 97 |
| Figure 4.2 Typical force-indentation depth ($P-h$) curve during loading and unloading of the Vickers indentation..... | 97 |
| Figure 4.3 Effect of mesh density and frictional conditions on the modelling results of Vickers indentation..... | 98 |
| Figure 4.4 Comparison of numerical results with some published experimental data of continuous indentation with a Vickers indenter..... | 99 |
| Figure 4.5 Effect of plastic parameters on the $P-h$ curves and curvature coefficients for Vickers indentations..... | 100 |
| Figure 4.6 FE model of the Knoop indentation test..... | 101 |
| Figure 4.7 Typical force-indentation depths ($P-h$) curve during loading and unloading for Knoop indentation..... | 101 |
| Figure 4.8 Effect of mesh density on modelling results of the Knoop indentation... | 102 |
| Figure 4.9 Effect of frictional conditions on modelling results of the Knoop indentation..... | 102 |
| Figure 4.10 Effect of plastic parameters on the $P-h$ curves and curvature coefficients for Knoop indentation..... | 103 |
| Figure 4.11 FE model of the spherical indentation test..... | 104 |

| | |
|---|---------|
| Figure 4.12 Typical force-indentation depths ($P-h$) during loading and unloading for spherical indentation..... | 104 |
| Figure 4.13 Effect of mesh density and frictional conditions on the modelling results of spherical indentation..... | 105 |
| Figure 4.14 Comparison of numerical results with some published experimental data of continuous indentation with a spherical indenter showing the validation of the FE model..... | 106 |
| Figure 4.15 Effects of plastic parameters on the $P-h$ curves of the spherical indentation..... | 107 |
| Figure 4.16 Flow chart showing the inverse FE modelling approach based on single indenter method..... | 108 |
| Figure 4.17 Flow chart showing the process to construct the simulation space using parametric studies in ABAQUS..... | 109 |
| Figure 4.18 Typical data searching process and results based on the Vickers indenter | 110-111 |
| Figure 4.19 Typical predicted properties from single Vickers indenter..... | 112 |
| Figure 4.20 Typical data searching process and results based on the Knoop indenter..... | 113-114 |
| Figure 4.21 Typical predicted properties from single Knoop indenter | 115 |
| Figure 4.22 Typical data searching process and results based on spherical indenter..... | 116-117 |
| Figure 4.23 Typical predicted properties from single spherical indenter | 118 |
| Figure 4.24 Flow chart showing the inverse FE modelling approach based on dual indenters method..... | 119 |
| Figure 4.25 Typical data searching process and results based on the dual indenters method (Vickers+Knoop)..... | 120-121 |
| Figure 4.26 Typical predicted properties with comparable objective functions for a range of materials showing the prediction from dual indenters (Vickers+Knoop) is not unique..... | 122 |
| Figure 4.27 Typical data searching process and results based on dual indenters method (Spherical +Spherical)..... | 123-124 |

| | |
|---|---------|
| Figure 4.28 Typical predicted properties with comparable objective functions for a range of materials from dual indenters (SR05+SR1)..... | 125 |
| Figure 4.29 Typical data searching process and results based on dual indenters method (Vickers+spherical)..... | 126-127 |
| Figure 4.30 Typical predicted properties with comparable objective functions for a range of materials from dual indenters (Vickers+SR05)..... | 128 |
| Figure 4.31 Typical data searching process and results based on dual indenters method (Knoop+spherical)..... | 129-130 |
| Figure 4.32 Typical predicted properties with comparable objective functions for a range of materials from dual indenters (Knoop+SR05)..... | 131 |
| Figure 4.33 Typical sensitivity study results for the three dual indenters methods with an input material property..... | 132 |
| Figure 4.34 Comparison of predicted results by single indenter method and dual indenters method for a typical material set..... | 133 |
| Chapter 5 | |
| Figure 5.1 FE models of the Vickers and spherical indentation test..... | 151 |
| Figure 5.2 Typical loading and unloading curve of Vickers indentation and residual indentation..... | 151 |
| Figure 5.3 Typical loading and unloading curve for the spherical indenter and residual indentation..... | 151 |
| Figure 5.4 Flow chart showing the inverse FE modelling approach based on $P-d$ data..... | 152 |
| Figure 5.5 Flow chart showing the procedure to construct the simulation space for the inverse FE modelling programme..... | 153 |
| Figure 5.6 Force-indentation size data of Vickers indentation tests on base steel A..... | 154 |
| Figure 5.7 Force-indentation size data of spherical indentation tests on base steel A..... | 154 |
| Figure 5.8 Inverse modelling results based on Vickers indentation test results for steel A..... | 155 |
| Figure 5.9 Inverse modelling results based on spherical indentation test results for steel A..... | 156 |

| | |
|--|---------|
| Figure 5.10 Inverse modelling results based on Vickers and spherical indentation tests results for steel A..... | 157 |
| Figure 5.11 Indentation test results of Vickers indentation and spherical indentation tests of steel B..... | 158 |
| Figure5.12 Inverse modelling results based on Vickers indentation test results for steel B..... | 159 |
| Figure5.13 Inverse modelling results based on spherical indentation test results for steel B..... | 160 |
| Figure5.14 Inverse modelling results based on Vickers and spherical indentation tests results for steel B..... | 161 |
| Figure 5.15 Comparison of the stress-strain curves predicted based on the dual indenters method and the tensile test data of steel A and steel B..... | 162 |
| Figure 5.16 Tensile test specimen and FE models of tensile tests..... | 162 |
| Figure 5.17 Comparison of the numerical and experimental force displacement curve of the standard tensile specimen and notched specimen for steel A..... | 163 |
| Figure 5.18 Comparison of the numerical and experimental force displacement curve of the standard tensile specimen and notched specimen for steel B..... | 164 |
| Figure 5.19 Indentation tests of spot welded joint..... | 165 |
| Figure 5.20 Typical Vickers hardness distributions across the spot welded joints of steel A..... | 165 |
| Figure 5.21 Force- indentation size data for three different welding zones in the welded joint of steel A..... | 166 |
| Figure 5.22 Inverse modelling results for the three welding zones of steel A... | 167-168 |
| Figure 5.23 Hardness data and force-indentation size data for three welding zones of in the welded joint of steel B..... | 169 |
| Figure 5.24 Inverse modelling results for the three welding zones of steel B... | 170-171 |
| Figure 5.25 Typical FE model of tensile-shear test of spot welded joint..... | 172 |
| Figure 5.26 FE modelling results of tensile-shear test vs. the experimental data (steel A)..... | 173 |

| | |
|--|-----|
| Figure 5.27 FE modelling results of tensile-shear test vs. the experimental data (steel B)..... | 174 |
| Figure 5.28 Effect of the nugget size and sheet thickness on the tensile shear strength of welded joint of steel A..... | 175 |
| Figure 5.29 Effect of the nugget size and sheet thickness on the tensile shear strength of welded joint of steel B..... | 176 |
| Figure 5.30 Effects of the nugget diameter and sheet thickness on strength of the welded joints under tensile shear loading for steel A and B..... | 177 |

Chapter 6

| | |
|---|-----|
| Figure 6.1 $P-h$ curves of different indenter types..... | 190 |
| Figure 6.2 Comparison of the equivalent plastic strain filed with different type of indenters..... | 191 |
| Figure 6.3 Comparison of the plastic strain field for spherical indenter at different indentation depth..... | 192 |
| Figure 6.4 Comparison of the accuracy of different dual indenters methods with published results..... | 193 |
| Figure 6.5 Comparison of the sensitivity of different dual indenters methods with published results..... | 193 |
| Figure 6.6 Comparison of the predicted yield stress with different methods..... | 194 |
| Figure 6.7 Comparison of the predicted work hardening coefficient with different methods..... | 195 |
| Figure 6.8 The integrated modelling approach to study the effect of welding parameters on the strength of spot-welded joints..... | 196 |

CHAPTER 1
INTRODUCTION

1.1 Introduction

Resistance spot welding (RSW) is widely used in the fabrication of sheet metal assemblies in automotive and aerospace industries. In a spot welding process, two or three overlapped or stacked components are welded together due to the result of the heat, created by the electrical resistance, at the interface between the workpieces held together under pressure between two electrodes. Materials, such as steel, aluminium, titanium and copper alloys, are commercially used in spot welding (Aslanlar, 2006). The main advantages of spot welding are the high speeds and adaptability for automation in high-volume production. Typically, a vehicle body contains several thousands of spot welds joining sheets of different thickness. The design of spot welded joints and their mechanical integrities are critical to the performance of the vehicle in service (Palmonella *et al*, 2005; Aslanlar, 2006). One important design factor is the optimum strength of the spot weld, as it controls the tension, bending and torsion modes and influences the durability, structural integrity and comfort of the vehicle. In addition, manufacturers are increasingly demanding reduced design periods with improved safety requirements, which could potentially be achieved through computational modelling (Zhou *et al*, 2003).

For bonded structures, the extent of the deformation is governed by the interaction between the geometry of the joint, the constitutive material properties, and the performance of the actual bond itself. Several published works (Huh and Kang, 1997; Shriver *et al*, 1999; Feulvarch *et al*, 2004; Santos and Zhang, 2004) were concerned with the formation of spot welded joints in the welding process, while other works focused on the link between the geometric attributes (e.g. nugget size and sheet thickness) and final strength of the welded joints (Aidun and Bennett, 1984; Kimchi, 1984; Han and Indacochea, 1993; Han *et al*, 1993; Lin *et al*, 1993; Aslanlar, 2006). Advances have been made in both directions; however, work directly linking processing parameters selection to the joint strength is still very limited. In general, the FE modelling would require that the correct constitutive material properties to be properly included in the finite element analysis. This is not always straightforward for

spot welding since the material properties can vary widely between the base metal, the heat-affected-zone (HAZ) and the weld nugget itself.

The welding process is a complex thermal mechanical process and the finished assembly consists of regions with significantly different microstructure and properties (e.g. the nugget and the HAZ). For steel, the weld nugget formed by the fusion zone, consists of a martensitic structure due to the high cooling rate while the HAZ is a mixture of tempered structure (Easterling, 1993). These microstructure variations result in gradient material properties within the welding zones, thus making it difficult to predict the final joint strength. Current practice involves using simplified material properties due to difficulties in measuring the localised material properties, which could not accurately represent the material behaviour. A more thorough approach is needed to incorporate the detailed material properties.

Indentation process is a practical tool in characterising welded structures' material properties, as it only requires a small volume of materials, and is well suited for materials with a gradient material property. However, the application of indentation has been limited to hardness measurements. This could not provide direct constitutive material properties of the welding zones, which are very important for design and prediction of the strength of spot welded joints/structures. Therefore, it is essential, for both research and industrial applications, to develop a practical approach to estimate the material parameters based on indentation tests. The detailed constitutive material properties for each welding zone in a spot welded joint could then be used in a finite element (FE) model to accurately predict the performance of spot welded structure, or to assess the effect of geometrical factors such as the nugget size and sheet thickness.

1.2 Aim and objectives

This work aims to develop an inverse finite element (FE) modelling method to characterise the properties of resistance spot welded joints based on indentation tests, and then to develop numerical models using the predicted material properties to investigate the effect of nugget size and sheet thickness on the strength of spot welded joints.

The main objectives are:

- To develop an inverse FE modelling technique based on indentation method to predict the plastic properties (e.g. yielding strength and work hardening coefficient) of elasto-plastic materials;
- To develop an inverse FE modelling approach using static indentation data rather than continuous indentation curves;
- To inversely measure the material properties in the nugget, HAZ and base metal zones of spot welded joints using the inverse FE methods developed;
- To develop numerical models with realistic material properties, from the above objectives, and correlate the modelling results with experimental testing results;
- To predict the effect of key dimensional attributes (e.g. nugget size and sheet thickness) on the strength of spot welded joints.

1.3 Outline of the thesis

In chapter 2, background information and current research on spot welding and the use of indentation method in characterising the material properties have been reviewed. It covers several different types of indentation techniques and recent development of the instrumented indentation methods. A brief review of contact mechanics related to indentation and factors affecting the analysis of indentation data are given. Different approaches to evaluate material properties based on indentation tests are critically reviewed, with discussions on the feasibility of each method to be potentially used in characterising welded joints.

The work plan and main experimental facilities are presented in chapter 3. The experimental work included both indentation test and standard tensile tests of the base metal and tensile-shear tests of spot welded joints of two automotive steels. These are also used to validate the FE models and the inverse FE modelling technique.

Chapter 4 is concentrated on the development of an inverse FE modelling approach of indentation tests based on parametric study technique. Several approaches using different indenter types are compared. A new method based on dual indenters as compared to the single indenter method has been developed. An optimum combination of indenter shapes is presented and validated using blind test with numerical experimental data.

Chapter 5 presents the development of a new approach using static indentation data rather than continuous indentation curves. The application of the latter is greatly limited by the facility requirement and availability of instrumented indentation tester. The new method aims to provide a simpler and more practical approach. The method is validated against standard tensile tests of automotive steels first before being used to characterise the plastic properties of different welding zones of spot welded joint. These plastic material parameters (yield stress and work hardening coefficient) are then used in numerical modelling of tensile-shear deformation of spot welded joints.

The validated numerical models are further used to investigate effects of nugget size and thickness of the metal sheets on the strength of welded joints.

Chapter 6 discusses the structure-strength relationship of spot welded joints. The accuracy and sensitivity of the inverse FE modelling developed in this study are compared to other approaches. The advantage in using dual indenters against single indenter method is discussed and guidelines are provided to use this method in characterising spot welded joints or other material systems.

In Chapter 7, overall conclusions are given and future works are highlighted.

CHAPTER 2
LITERATURE REVIEW

2.1 Spot welding and applications

2.1.1 Resistance spot welding process

Resistance spot welding is used when there are two or more overlapping metallic sheets, joined in one or more spots, by local fusion caused by concentration of a current between cylindrical electrodes. The principle of resistance spot welding operation is schematically shown in Figure 2.1. In this process, heat is generated by resistance through an electric current that flows from the upper electrode, through work pieces held together under pressure exerted by the electrodes. The entire sequence of operations is required to develop sufficient heat, in order to raise a certain volume of metal to its melting point, and then solidify under a constant pressure to hold the parts together. The melt region known as the nugget solidifies very rapidly because it is surrounded by a large amount of cold metal and the water-cooled electrodes which act as a heat sink (Chang and Cho, 1990).

As shown in Figure 2.2, there are three main stages involved in a spot welding cycle: (a) Squeeze time, (b) Welding time and (c) Hold time. Squeeze time is the first period when the electrodes are brought together against the sheets to be joined, for the application of the current. Welding time is the time when the current is flowing from the upper electrode and through the sheets. It is during this time that the metals are fused and the nugget is formed at the interface between the sheets. Once the required volume of the melting metal that forms the nugget is reached, the current flow is ceased and the electrodes are kept in position for some time (i.e. hold time), which allows the nugget to solidify. Finally, the electrodes are released and the upper electrode is withdrawn from its initial position. Several cycles are normally required for one weld (Aravinthan, 2003).

2.1.2 Applications of resistance spot welding

The major advantages of resistance spot welding are that a high volume of work is produced at very high speeds and the welding condition can be controlled automatically. It is also suitable for automation and inclusions in high-production

assembly lines with other fabricating operations (Chang and Cho, 1990). It is widely used in manufacturing industry to produce a broad range of equipment for home appliances (e.g. refrigerators, washing machines, radiators, and storage cupboards) or industrial structures. Spot welding is also widespread in the automobile and aircraft industries for joining elements forming the bodies of cars and aeroplanes. There are over 5000 spot welds in a car body (Dickinson *et al*, 1980). Various types of metals, such as mild steel, high strength steel, stainless steel, nickel, aluminum, titanium alloys, and brass can be welded by resistance spot welding (RSW) (Jou, 2003). Small-scale resistance spot welding (SSRSW) is also one of the main micro-joining processes being employed in the fabrication of electronic components and devices to join thin sheet metals of thickness less than 0.2–0.5 mm (Aslanlar, 2006).

Despite its wide applications, RSW suffers from a major problem of inconsistent quality from weld to weld. This problem is due to both the complexity of the material transformation process and variability of processing parameters (e.g. current, welding time etc.). Any or all of these complicate the automation process, reduce weld quality, demand over-welding (i.e. the production of more welds than are structurally needed, if each were perfect), and drive up production costs (Jou, 2003). For this reason, accurate simulation and prediction of the strength of welded structures has been, and still remains, a major challenge and goal (Jou, 2003). This is particularly important for automotive industries as there is an increased demand on safety of the vehicle and reduced energy consumption. It is essential to develop a methodology to be able to consistently characterise the detailed material properties in a spot welded joint, to establish the relationship between its structure, material properties and welding parameters.

2.2 Structure of spot welded joints and effect of welding parameters

2.2.1 Microstructure of a spot welded joint

Spot welding involves thermal, metallurgical and mechanical processes, which result in a structure with complex microstructure and properties. Figure 2.3 shows a typical cross-section of spot welded joint of a low carbon steel. There are three different regions – the base material, the nugget (fusion zone) and the heat-affected-zone (HAZ). The welding nugget is a block in the centre of the weldment and its microstructure is martensite and bainite, which are both of high hardness and strength (Santella *et al*, 2003). During the welding process of steel, the temperature of the central area is above 1400°C. The materials are melted and then cooled very quickly because the heat is absorbed by the surrounding materials. This process is similar to the quenching process of steel.

The HAZ is the transition zone between the fusion zone (FZ) and the base metal (BM). It is a heterogeneous region with steep gradients in material properties. The HAZ can be divided into several subzones, each with distinct microstructures and mechanical properties. The varying mechanical properties of the HAZ are the result of the non-uniform heat treatment applied during the weld thermal cycle. Regions closest to the FZ experience the highest temperatures and the fastest cooling rates. According to Vogler and Sharped (1992), cooling rates can reach 1000°C/s for a weld produced without hold time (hold time refers to the period of post-weld electrode squeeze, and it is expressed in number of current cycles at 60 Hz). As discussed by Easterling (1993), the number of HAZ subzones depends on the material, but the four main subzones in the HAZ of steel typically are (i) grain coarsened or grain growth, (ii) grain refined or recrystallized, (iii) partially transformed and (iv) tempered zones. The grain growth zone has a temperature about 1100-1400 °C during welding, most of the microstructures within this zone are martensite and the part is similar to nugget but their grain growth direction is mixed. The recrystallized zone has a peak temperature about 900-1100 °C, the microstructure is very complex, including ferrite, bainite, pearlite and martensite and the grain size is small. The partial transformed zone has temperature about 730-900 °C in the welding process, its microstructure is complex and grain size is not uniform because the temperature is not high enough for complete

grain recrystallisation. The tempered zone is next to the base. It has a temperature about 580-600 °C during the welding process, its grain size is larger and the hardness may be slightly lower than before welded (Lancaster, 1986). Most failures occur in HAZ due to its complicated structure and weakened mechanical properties (Zuniga and Sheppard, 1995; Zhou *et al*, 1999).

The welding process is a complex interaction under electrical, thermal, metallurgical and mechanical phenomena, which has been the topic of many research works. One active research field is on the prediction of the dimensional parameters (e.g. the size of the nugget and HAZ) of spot welded joints by simulating the temperature gradient (Huh and Kang, 1997; Feulvarch *et al*, 2004; Santos and Zhang, 2004). Another active research field is on the study of microstructure development. A microstructure model has to consider the thermo-physical properties of the materials in order to describe the phase transformations during heating and cooling stages (Ion *et al*, 1984; Easterling, 1993). A model to describe the simultaneous formation of idiomorphic and allotriomorphic ferrite based on overall transformation kinetics equations has been successfully used to predict the microstructure development when welding both low carbon and high carbon steels (Jones and Bhadeshia, 1997; Santella *et al*, 2003). These modelling works could be used to establish the welding parameter and the dimension of the welding zones.

2.2.2 Effect of welding parameters on nugget and heat affected zones

From the concept of spot welding process, it is clearly shown that there are three main variables that affect weld quality in spot welding, as follow: (1) welding time; (2) welding current; (3) electrode pressure. These variables are not independent of each other and their influence on the welding process may interact with each other. When welding time is reduced, the welding current is increased and vice versa. Increase in electrode force requires an increase in welding current since it results in a decrease in the interface resistance. Another important factor affecting the weld quality is the surface condition because it determines the contact resistance and is greatly influenced by the presence of grease, heavy scale and other contaminant as well as the roughness of the material (Vogler and Sharpped, 1993). The electrode pressure also influences the contact resistance, and the weld quality.

Welding current provides the energy to generate the heat at the interface of materials. At higher current, the heat supplied to the weld is sufficient for the weld to achieve full growth within the selected weld time. This will cause a fully-grown and strong weld. If the current is too low, then undersized and brittle welds are formed because of insufficient heat supply. When the current is too high, expulsion will occur which decreases the strength.

A satisfactory resistance weld is the result of using correct welding settings and techniques and maintaining them for the duration of a particular production run. Factors such as current, time, electrode force must be properly controlled. The weld lobe curve (as schematically shown in Figure 2.4) is a graphical representation of ranges of welding variables over which acceptable spot welds are formed on a specific material welded with a pre-selected electrode force (Dickinson *et al*, 1980). The welding lobe is determined by experimentally making spot welds using different combinations of weld time and welding current. Only welds made with currents and weld times lying within the lobe area are acceptable. Welds made with currents and times exceeding the upper curve experience expulsion and are therefore considered unacceptable. Welds made with currents and times below the lower curve have insufficient nugget size or no weld and therefore are unacceptable.

2.3 Mechanical strength of spot welded joints and structures

2.3.1 Main factors affecting the strength of spot welded joint

Spot welded joints are widely used in many load bearing situations and their mechanical strength has a strong influence on the integrity of the whole structure. A large amount of research work has been conducted to study the deformation of spot welded joints, experimentally or numerically, under different loading conditions, such as tensile-shear, bending, impact, fatigue, etc. (Cavalli *et al*, 2003; Darwish, 2003; Yang *et al*, 2003; Zhou *et al*, 2003). Many published results on the mechanical behaviour of spot welds have been focusing on the correlation between RSW process parameters and the strength of spot-welded joints (e.g. Aidun and Bennett, 1984; Kimchi, 1984; Han and Indacochea, 1993; Han *et al*, 1993; Lin *et al*, 1993). These works have covered a wide range of material systems (e.g. steel, aluminium, copper, etc.) welded under different modes, such as single spot welded joints, multi layer welds with dissimilar thickness, dissimilar materials and multi-spot welded structures. A typical experimental result is shown in Figure 2.5 demonstrating the effect of welding parameters on the nugget size and the strength of the spot welded joint under tensile shear load (Aslanlar, 2006).

Numerical modelling (e.g. Finite element (FE) modelling) has been widely used to study the mechanical strength of spot welded joints under static (e.g. tensile-shear), dynamic loading (e.g. impact) or time dependent behaviour (e.g. creep and fatigue) (Zhou *et al*, 1999; Deng *et al*, 2000; Chang *et al*, 2001; Bae *et al*, 2003; Cavalli *et al*, 2003; Zhou *et al*, 2003; Langrand and Combescure, 2004; Pickett *et al*, 2004; Rodrigues *et al*, 2004a, b; Rusinski *et al*, 2004). Some of these models were pure elastic models, while others considered the elastic-plastic properties and fracture behaviours (Zhou *et al*, 1999; Zhou *et al*, 2003; Langrand and Combescure, 2004; Pickett *et al*, 2004), which are governed by both the structure (nugget size, HAZ size, etc.) and the elasto-plastic behaviour of the materials involved.

2.3.2 Elasto-plastic deformation and fracture of metallic materials

Most of the materials involved in spot welding operations are of typical elasto-plastic behaviour. As schematically shown in Figure 2.6 (a), the plastic behaviour is normally described by the constitutive material equations. In many cases, the three parameter power-hardening rule (Eq. 2.1) is used:

$$\sigma = \sigma_0 + K\varepsilon^n \quad (\text{Eq. 2.1})$$

where the parameter ' σ_0 ' is the yield stress, ' ε ' is the plastic strain, ' K ' is the strength coefficient and ' n ' is the strain hardening exponent. A simpler form can be used for isotropic elasto-plastic behaviour with isotropic work-hardening described by the Ludwig power equation (Lesage *et al*, 2000):

$$\sigma = K(\varepsilon_0 + \varepsilon)^n \quad (\text{Eq. 2.2})$$

This requires three parameters: ' ε_0 ' is the yield strain, ' K ' is the strength coefficient and ' n ' is the strain hardening exponent.

Fracture is separation, or fragmentation of a solid body into two or more parts under the action of stress. The fracture of the spot welding is a complex process; several fracture models have been explored for different loading situation, including Gurson model, cohesive model, the Lemaitre mezzo-scale damage mechanics model, and the Wilkins failure criteria (Cavalli *et al*, 2003, Pickett *et al*, 2004). Fractures of metals can be classified into brittle fracture and ductile fracture. The materials in spot welded joint mainly fail by ductile fracture. As shown in Figure 2.6 (b), the fracture process starts at the necking stage at the ultimate strength (UTS) point where cavities form within the necked region (stage 'i' and 'ii'); The cavities in the necking region coalesce into a crack in the centre of the specimen and propagate toward the surface of the specimen in a direction perpendicular to the applied stress (stage 'iii'); When the crack nears the surface, the direction of the crack changes to 45° to the tensile axis and a cup-and-cone fracture results (stage 'iv' and 'v'). The linking of voids may occur on planes which are perpendicular to the applied stress (normal rupture), or are parallel to it (delamination), or along shear bands at an angle to it (shear fracture). Most attempts at understanding ductile fracture have considered only the first stage. Once a micro-void has been nucleated in a plastically deformed matrix, by either the bending or cracking of a second-phase particles or inclusions, the resulting stress-free

surface of the void causes localized stress and strain concentration of the adjacent plastic field (Wang, 2003).

Gurson model is widely used in ductile fracture mechanics, in which, the fracture of material is considered as the result of void growths in the material volume. The homogenous material surrounding the void is called matrix material. The Gurson model can realistically represent failure, provided the loading state in the sample used to determine the Gurson parameters, is similar to that in the rupture zone of the structure. The most commonly used model based on the Gurson was called Gurson-Tvergaard-Needleman (GTN) model (ABAQUS Theory Manual 6.4), which is briefly described below.

The original model developed by Gurson, assumed plastic yielding of a porous ductile material, where the yield surface was a function of a spherical void as follows:

$$\Phi = \frac{3}{2} \frac{s_{ij}s_{ij}}{\sigma_y^2} + 2f \cosh\left(\frac{3}{2} \frac{\sigma_m}{\sigma_y}\right) - (1 + f^2) = 0 \quad (\text{Eq. 2.3})$$

where σ_y is the yield stress of the material, σ_m is the mean stress, f is the void volume fraction. $f=0$ implies that the material is fully dense, and the Gurson yield condition reduces to that of von Mises; $f=1$ implies that the material is fully voided and has no stress carrying capacity. s_{ij} is the components of stress deviator ($i, j=1, 2, 3$), defined as

$$s_{ij} = \sigma_{ij} - \sigma_m \delta_{ij} \quad (\text{Eq. 2.4})$$

and δ_{ij} is the Kronecher delta

$$\delta_{ij} = \begin{cases} 1 & i = j \\ 0 & i \neq j \end{cases} \quad (\text{Eq. 2.5})$$

Theoretical micromechanical studies for materials containing periodic distribution of cylindrical or spherical voids have been carried out by Tvergaard (1981). By considering the influence of neighbouring voids on each pair of voids, three parameters, q_1 , q_2 and q_3 , have been added to equation (2.3):

$$\Phi = \frac{3}{2} \frac{s_{ij}s_{ij}}{\sigma_y^2} + 2q_1 f \cosh\left(\frac{3}{2} \frac{q_2 \sigma_m}{\sigma_y}\right) - (1 + q_3 f^2) = 0 \quad (\text{Eq. 2.6})$$

q_1 , q_2 , q_3 are material constants and it was found that matching of test results can be achieved for most alloys, by taking the following material values (ABAQUS Theory Manual 6.4):

$$q_1 = 1.5, \quad q_2 = 1 \quad \text{and} \quad q_3 = q_1^2 = 2.25. \quad (\text{Eq. 2.7})$$

Tvergaard and Needleman have further modified the Gurson model by replacing f with an effective void volume fraction, $f^*(f)$:

$$f^* = \begin{cases} f & \text{if } f \leq f_c \\ f_c + \frac{\bar{f}_F - f_c}{f_F - f_c} (f - f_c) & \text{if } f_c < f < f_F \\ \bar{f}_F & \text{if } f \geq f_F \end{cases} \quad (\text{Eq. 2.8})$$

where

$$\bar{f}_F = \frac{q_1 + \sqrt{q_1^2 - q_3}}{q_3} \quad (\text{Eq. 2.9})$$

The parameters f_c and f_F model the material failure due to mechanisms such as micro fracture and void coalescence. f_c is a critical value of the void volume fraction, and f_F is the value of void volume fraction at which there is a complete loss of stress carrying capacity in the material.

The total change in void volume fraction is given as

$$\dot{f} = \dot{f}_{gr} + \dot{f}_{nucl} \quad (\text{Eq. 2.10})$$

where \dot{f}_{gr} is change due to growth of existing voids and \dot{f}_{nucl} is change due to nucleation of new voids. Growth of the existing voids is based on the law of conservation of mass and is expressed in terms of the void volume fraction:

$$\dot{f}_{gr} = (1 - f)\dot{\epsilon}^{pl} : I \quad (\text{Eq. 2.11})$$

$I_{ij} = \delta_{ij}$ the unit second order tensor.

The nucleation of voids is given by a strain-controlled relationship:

$$\dot{f}_{nucl} = A \dot{\bar{\epsilon}}_m^{pl} \quad (\text{Eq. 2.12})$$

where

$$A = \frac{f_N}{s_N \sqrt{2\pi}} \exp \left[-\frac{1}{2} \left(\frac{\bar{\epsilon}_m^{pl} - \epsilon_N}{s_N} \right)^2 \right] \quad (\text{Eq. 2.13})$$

The normal distribution of the nucleation strain has a mean value ϵ_N and standard deviation s_N . f_N is the volume fraction of the nucleated voids. Gurson model has been implemented in several FE modelling software, like ABAQUS, ADINA, SYSTUS, etc, and is widely used by researchers (ABAQUS Theory Manual 6.4).

2.3.3 Characterisation of the mechanical properties of welding zones

The FE modelling relies on accurate presentation of the physical structure and materials properties. Many factors will influence the accuracy of FE models of spot welded joints or structures (Zhou *et al*, 1999; Zhou *et al*, 2003). One important factor is the dimensional attributes, such as nugget size, thickness. The dimensions of weld zones can be directly gained from experimental observations or simulation of spot welding process (Shriver *et al*, 1999; Feulvarch *et al*, 2004; Li *et al*, 2004; Aslanlar, 2006). Another important factor is the material properties of different welding zones (Zhou *et al*, 1999; Zhou *et al*, 2003), since large plastic strains and large local strain rates are likely to develop in the HAZ prior to crack initiation under mechanical loading.

Directly characterising the material properties of welding zones is impossible since standard testing specimen (e.g. tensile tests) is not readily available. Many works on modelling mechanical strengths of spot welded joint/structures have to use elastic model or simplified material properties (Zhou *et al*, 2003; Langrand and Combescure, 2004; Rodrigues, 2004a, b), which could not accurately represent the material behaviours and often cause disagreement with experiment results (Langrand and Combescure, 2004).

Zuniga and Sheppard (1995) have explored a methodology to determine the constitutive response of the HAZ using specially made spot welded specimen. The method involved three main stages. Firstly the fabrication procedure simulating the spot welding process has to be used. A spot welded joint with large size nugget and HAZ was obtained to be able to produce tensile specimen. A notched bar was then made and tested on a tensile testing machine. The data was then processed using a flow curve correlation algorithm to determine the stress-strain curve. However, this method could not be possibly used in a conventional situation or industrial situation due to the complexity of the experimental procedure.

Some researchers have been trying to directly link hardness to the strength of spot welded joints. Zuniga and Sheppard (1995) performed experiments on Zinc-coated

high strength steel by using simulated HAZ material samples, and suggested the following relationship for the zinc-coated steel:

$$\sigma_y = -14.7 + 2.568H_v (MPa) \quad (\text{Eq. 2.14})$$

$$\sigma_{uts} = 65.8 + 2.563H_v (MPa) \quad (\text{Eq. 2.15})$$

where σ_{uts} is the ultimate strength and H_v is Vickers hardness. These two equations also indicate that σ_y and σ_{uts} are almost parallel because the coefficients of H_v in two equations are very close to each other. In another work, Bourges *et al* (1995) proposed a correction between hardness and tensile properties of spot welded joints under tensile shear. A linear relationship is clearly shown in these equations, except in a very small correction of a quadratic term.

$$\sigma_{uts} = 19.13 \times 10^{-4} (H_v)^2 + 1.89H_v + 181.5 (MPa) \quad (\text{Eq. 2.16})$$

$$\sigma_y = \sigma_{uts} + 30.41 \times \log VR - 215.8 (MPa) \quad (\text{Eq. 2.17})$$

$$e = -1.38 + 18.2 \times 10^3 / \sigma_{uts} (\%) \quad (\text{Eq. 2.18})$$

Where VR is cooling rate and e is ductility (elongation).

Zhou *et al* (1999) has developed a material model linking hardness of the HAZ to the strength of the base material. (Equation 2.19 A-D)

$$\sigma_{uts} = \sigma_0 + k_1 H_v \quad (\text{Eq. 2.19A})$$

$$\sigma_y = k_1 H_v \quad (\text{Eq. 2.19B})$$

$$e = k_2 / H_v \quad (\text{Eq. 2.19C})$$

$$H_v = k \cdot H_{Vbase} \quad (\text{Eq. 2.19D})$$

where k_1 , k_2 , and k are constants, σ_{uts} is ultimate tensile strength, σ_y is yield strength, and e is elongation. H_v and H_{Vbase} are hardness values of the concerned part and that of the base metal, respectively. Furthermore, if only steel is considered, the Young's modulus and Poisson's ratio can be fixed as constants ($E = 210$ GPa and $\nu = 0.3$). Therefore, in a design process, only the base metal properties and the hardness ratio (k) between the nugget and base metal are left as material variables.

These works have helped to link the hardness to the mechanical strength of the spot welded joints. However, since hardness is not an intrinsic material property and the

hardness measurement is affected by factors such as the geometry of the indenter, these could not be directly used in design and modelling process. A more thorough and practical approach has to be developed to extract detailed constitutive material parameters from indentation test data.

2.4 Indentation techniques and applications

Indentation test is an important materials testing method in which a sharp or blunt indenter is pressed into the surface of a material. It can be used to test brittle (e.g. ceramics), elasto-plastic (e.g. metals) and soft materials (e.g. foams, rubbers, etc.) (Giannakopoulos and Larsson, 1997; Ren *et al*, 2001). One significant advantage of indentation is that it only requires a small amount of materials; this makes it very attractive for the characterisation of materials with gradient property where standard specimen is not readily available such as *in situ* or *in vivo* tests (Ren *et al*, 2004; Delalleau *et al*, 2006; Ren *et al*, 2006). However, indentation tests can be influenced by many factors (such as indenter shape, materials deformation around the indenter and experimental conditions, etc.). These factors have to be carefully considered when using indentation method.

The hardness of materials is based on the resistance of a solid to local deformation. In the hardness test of elasto-plastic materials (e.g. metals, polymers), a harder indenter is pressed into the specimen surface and the size of the permanent indentation formed can be measured to represent the indentation resistance (i.e. hardness of the material). With rubber-like materials an indenter is pressed into the material and the hardness of the material is assessed by the indentation depth under load.

The indenter shape is one important factor for indentation testing. Commonly used indenters include spherical, cone indenter and pyramidal shape indenters. This has led to different hardness testing systems, typically, Brinell hardness, Vickers hardness, Knoop hardness, Berkovich hardness and Rockwell hardness testing. Details of each indentation method are detailed below.

Brinell hardness test

The Brinell hardness refers to the hardness measured by indentation with a spherical indenter. Typically a $D = 10$ mm sphere is pressed using a 30 kN force for a duration of around 30 seconds. For softer materials the force can be reduced to 15 kN or even 5 kN. The diameter of the impression, d , left in the test material after the indenter is removed is measured with a microscope. The Brinell hardness number is calculated

by dividing the force F applied by the surface area of the spherical cap left after indentation.

$$H_B = \frac{F}{D(D - \sqrt{D^2 - d^2}) \cdot \pi / 2} \quad (\text{Eq. 2.20})$$

where D and d are the diameters of the indenter and the impression (see Figure 2.7 (a)).

Vickers hardness test

The Vickers hardness is measured by indenting the test material with a diamond pyramidal-shape indenter. The indenter has the form of a right pyramid with a square base and an angle of 136° between opposite faces (Figure 2.7 (b)). The indentation is subjected to a force ranging from 10 to 2000 N for duration around 10 to 15 seconds. The two diagonals of the impression area left in the surface of the material after the indenter is removed are measured using a microscope and the average value 'd' is calculated. The Vickers hardness values can be calculated by

$$H_V = \frac{1}{2} \frac{F}{d^2 / \sin(136^\circ / 2)} \approx 1.854 \frac{F}{d^2} \quad (\text{Eq. 2.21})$$

where $d^2/2\sin(136^\circ/2)$ is the area of the sloping surface of the impression (A), and F is the indentation force.

Rockwell hardness test

The Rockwell hardness scale characterises the indentation hardness of materials through the depth of penetration of a cone or spherical indenter, loaded on a material sample and compared to the penetration in some reference material. It involves the use of a minor loading F_m followed by a major loading F_M , and finally the release the major loading as illustrated in Figure 2.7 (c). The hardness value directly according to:

$$H_R = h_R - h \quad (\text{Eq. 2.22})$$

It can be used in almost all metallic materials, plastics and rubbers.

Knoop hardness test

Knoop indentation testing is mainly used to measure hardness at the micro scale. The Knoop indenter is a diamond ground to the pyramidal form, as shown in Figure 2.7

(d), which produces a diamond shaped indentation with a ratio between long and short diagonals of approximately 7:1 and the short diagonal is 4.11 times indentation depth. When Knoop hardness is measured, only the long diagonal 'L' of the indentation is measured. The sort diagonal is calculated as $w = L \tan(130^\circ/2) / \tan(172.5^\circ/2)$, thus the impression area is $A = wL/2 = L^2 \tan(130^\circ/2) / 2 \tan(172.5^\circ/2)$. Finally the Knoop hardness is calculated using

$$H_K = \frac{F}{A} = \frac{F}{CL^2} \quad (\text{Eq. 2.23})$$

where $C = \tan(130^\circ/2) / 2 \tan(172.5^\circ/2) \approx 0.07028$

The Knoop indentation can be used in almost all ceramics, metallic materials and plastics.

Berkovich hardness test

Berkovich indenter is commonly used for nano- and micro-indentation. It has a three sided pyramid shape with the face angle 65.3° (see Figure 2.7 (e)). The hardness is calculated as F/A_c , where F and A_c are the indentation force and projected contact area of the impression, respectively. By geometry, the contact area projection is calculated as:

$$A_c = 3\sqrt{3} \tan^2(65.3^\circ) h_c^2 \approx 24.56 h_c^2 \quad (\text{Eq. 2.24})$$

Table 2.1 lists the correlation between the hardness values based on different indentation tests. Each of these differs from the load range and the suitable material to be tested.

Table 2.1 Typical values showing the correlation between different indentation tests (O'Neil, 1967).

| Brinell (10 mm Ball, 3000 kg load) | Vickers (120 kg) | Rockwell C (120 degree cone 150 kg) | Rockwell B (1/16" ball 100 kg) |
|--|------------------------|---|--------------------------------------|
| 800 | - | 72 | - |
| 712 | 1021 | 66 | - |
| 601 | 746 | 60 | - |
| 502 | 565 | 52 | 119 |
| 401 | 423 | 43 | 114 |
| 301 | 305 | 33 | 107 |
| 200 | 199 | 16 | 93 |
| 105 | 110 | - | 62 |
| 90 | 95 | - | 52 |
| 81 | 85 | - | 41 |
| 76 | 80 | - | 37 |

2.5 The mechanics of indentation process

In 1882, Hertz analysed the stress at the contact of two elastic solid bodies motivated by his study about Newton's optical interference fringes in the gap between two glass lenses (Johnson, 1985). He was concerned about the influence of elastic deformation of the lens surfaces during contact due to the pressure between them. He started to investigate elasticity in order to understand the reversible change in the lens surface change.

In his theory, Hertz made the following assumptions: (i) The surfaces are continuous and non-conforming; (ii) The strains are small; (iii) Each body can be considered as an elastic half-space; (iv) The contact is frictionless.

As shown in Figure 2.8, for spherical contact between isotropic materials, the contact area will be circular and Hertz showed that the radius 'a' of the contact area is given by Johnson (1985)

$$a^3 = \frac{3FR}{4E^*} \quad (\text{Eq. 2.25})$$

where F and R are the applied force and combined radius of curvature.

The reduced modulus E^* is defined as

$$\frac{1}{E^*} = \frac{1-\nu_1^2}{E_1} + \frac{1-\nu_2^2}{E_2} \quad (\text{Eq. 2.26})$$

where E's and ν 's are Young's modulus and Poisson's ratio, and indices '1' and '2' refer to the first and the second body. It is defined in a general case where the indenter is not rigid, and the reduced modulus E^* is defined in the same manner as two springs in series. The combined radius is defined by

$$\frac{1}{R} = \frac{1}{R_1} + \frac{1}{R_2} \quad (\text{Eq. 2.27})$$

In the case of indentation by a rigid spherical indenter (i.e. $E_1 \gg E_2$), the first body being the indenter and the second being the indented material, R reduces to the radius of the indenter and the reduced modulus $E^* = E/(1-\nu^2)$, where $E = E_2$ is the modulus of the material.

In Hertz's solution, the vertical displacement of a point on the surface within the area of contact is given by

$$u_3(r) = \frac{3F}{8aE^*} \left(2 - \frac{r^2}{a^2}\right) \quad (\text{Eq. 2.28})$$

where $r \leq a$, and r is the radial distance from the symmetry axis. The contact pressure distribution:

$$p(r) = p_0 \left(1 - \frac{r^2}{a^2}\right)^{1/2} \quad (\text{Eq. 2.29})$$

where p_0 is the maximum pressure, i.e. pressure at the axis of symmetry. It is related to the applied force through,

$$F = \int_0^a p(r) 2\pi r dr = \frac{2}{3} p_0 \pi a^2 \quad (\text{Eq. 2.30})$$

or

$$p_0 = \frac{3F}{2\pi a^2} \quad (\text{Eq. 2.31})$$

The depth of indentation is,

$$h = u_3(0) = \left(\frac{9F^2}{16RE^{*2}}\right)^{1/3} = \frac{a^2}{R} \quad (\text{Eq. 2.32})$$

It is convenient to express the maximum pressure p_0 independent from the contact radius a , by eliminating it through Eq. (2.33), thus,

$$p_0 = \left(\frac{6FE^{*2}}{\pi^3 R^2}\right)^{1/3} \quad (\text{Eq. 2.33})$$

For a conical indenter, similar equations apply where the radius of circle of contact is related to the indenter load by (Fischer-Cripps, 2004)

$$P = \frac{\pi a}{2} E^* a \cot \alpha \quad (\text{Eq. 2.34})$$

The depth profile of the deformed surface within the area of contact is:

$$h = \left(\frac{\pi}{2} - \frac{r}{a}\right) a \cot \alpha \quad r \leq a \quad (\text{Eq. 2.35})$$

where $r \leq a$ is the cone semi-angle. The quantity 'a' is the depth of penetration h_p measured at the circle of contact. Submitting Eq. 2.34 to 2.35 with $r=0$, we obtain:

$$P = \frac{2E^* \tan \alpha}{\pi} h_s^2 \quad (\text{Eq. 2.36})$$

where h_s is the depth of penetration of the apex of the indenter beneath the original specimen free surface.

For each indenter type, the size of the contact area is proportional to the indentation depth. To simplify this approach, during indentation testing, pyramidal indenters are generally treated as conical indenters with a cone angle that provides the same area to depth relationship as the actual indenter in question. This allows the use of convenient axial-symmetric elastic equations, Eq. 2.34 -2.35, to be applied to contacts involving non-axial-symmetric indenters. Despite the availability of contact solutions for pyramidal punch problem (Barber and Billings, 1990; Bilodeau, 1992; Larsson *et al*, 1996), the conversion to an equivalent axial-symmetric contact has found a wide acceptance. The areas of contact as a function of the depth of the circle of contact for some common indenter geometries are given in Table 2.2.

Table 2.2 The areas of contact as a function of the depth for different indenter types (Fischer-Cripps, 2004).

| Indenter type | Projected area | Semi-angle θ (deg) | Effective cone angle α (deg) |
|---------------|--|--|-------------------------------------|
| Sphere | $A \approx 2\pi R h_s$ | | |
| Berkovich | $A = 3\sqrt{3}h_s^2 \tan^2 \theta$ | 65.27° | 70.3° |
| Vickers | $A = 4h_s^2 \tan^2 \theta$ | 68° | 70.3° |
| Knoop | $A = 2h_s^2 \tan \theta_1 \tan \theta_2$ | $\theta_1 = 86.25^\circ \theta_2 = 65^\circ$ | 77.64° |
| Cube coner | $A = 3\sqrt{3}h_s^2 \tan^2 \theta$ | 35.26° | 42.28° |
| Cone | $A = \pi h_s^2 \tan^2 \alpha$ | α | α |

2.6 Material deformation in an indentation process

For elasto-plastic materials, the indentation involves elastic and plastic deformation until it reaches a full plastic regime at a higher indentation depth (i.e. strain level). The strain level to reach a full plastic condition varies between materials. As pointed out by Tabor (1948), fully plasticity will be reached for mild steel when a/R is greater than 0.1 and, for copper, the strain value to reach full plasticity is much lower. As shown in Figure 2.8, 'a' is the radius of the contact area and R is the radius of the spherical indenter. Based on geometric analysis, when $a/R \geq 0.1$, the mean indentation depth $h \geq 0.005R$. Consequently, for the indenter $R=0.5\text{mm}$, the full plasticity will be reached at the indentation depth 0.0025mm or $a=0.05\text{mm}$; for the indenter $R=0.25\text{mm}$, the full plasticity will be reached at the indentation depth 0.00125 mm or $a=0.025\text{mm}$.

2.6.1 Elastic recovery

When an indenter is pressed into a metal surface and then removed, there is some recovery occurrence under and around the indenter. There is recovery in both the vertical direction and the lateral direction. The recovery in the vertical direction affects the residual indentation depth while the lateral recovery directly affects the size of the impression. In both cases, the curvatures of the indent will be affected. The extent of elastic recovery depends on the indenter size and the material properties (Alcala *et al*, 2000).

Kucharski and Mroz (2001) studied the elastic recovery of indents on an aluminium alloy using spherical indenters. Careful measurements showed that there is little change in the chordal diameter D of the indentation but a marked increase in its curvature. As shown in Figure 2.9 (a), $a = a_t = a_p$, where 'a' is indentation radius, ' a_t ' is total indentation radius and ' a_p ' is plastic indentation radius. The indentation is shallower than if it were of the same curvature as the indenter. To a close approximation the recovered indentation is spherical in shape. According to Hertz's equation for the deformation of contacting spherical surfaces, contact just occurred over the diameter $d_o = 2a$. A similar study has been conducted for conical indenters by Stilwell and Tabor (1961) (Figure 2.9 (b)). It shows that to a first approximation a

conical indentation recovers elastically to give a cone of wider angle than that of the indenter.

2.6.2 Piling-up and sinking-in

For elasto-plastic materials, a distinctive feature of indentation experiments is that the material around the contact area tends to deform upwards or downwards along the z axis, where load is applied. This behaviour results in piling-up or sinking-in of material at the contact boundary as schematically shown in Figure 2.10 (Tabor, 1951; O'Neil, 1967; Fischer-Cripps, 2004). Such surface deformation modes influence hardness measurements as the true contact area between the indenter and the specimen increases in the case where piling-up predominates, and decreases in the event that sinking-in occurs. The development of surface deformation around the indent is also relevant to the analysis of instrumented indentation experiments, where load and depth of penetration are measured continuously during the test.

A quantification of piling-up and sinking-in around spherical indents is given by the parameter, c . Following the Hertz elastic theory, the true depth of penetration, h , of an indenter into a flat surface is given by (Johnson, 1985; Hill *et al*, 1989)

$$h = h_s c^2 = \frac{a^2}{D} \quad (\text{Eq. 2.37})$$

then the scale of pile up or sinking in can be represented by difference between ' h_s ' and ' h ':

$$h - h_s = (c^2 - 1)h_s \quad (\text{Eq. 2.38})$$

where $c^2=0.5$ according to linear elasticity, h_s is the maximum depth of penetration underneath the original surface, and h sets the location of the contact area (see Figure 2.10 (a)). Eq. 2.37-38 is predicated on the basis of infinitesimal deformation where $a \ll D$. The physical significance of ' c ' becomes evident by considering that if plastic deformation takes place at the indented solid, in a manner that the material surrounding the spherical indenter does not undergo any piling-up or sinking-in effects, pure geometrical considerations yield $c^2=1$. Thus, $c^2=1$ sets the transition from piling-up to sinking-in. Eq. 2.37-38 implies that a purely elastic solid ($c^2=0.5$) would experience sinking-in effects by an amount which is exactly half of the maximum

penetration of the indenter into the half-space, h_s . As the vertical displacement, u_z , at the contact boundary is given by the quantity $h_s - a^2/D$ (Figure 2.10 (a)) then, $u_z/h_s = 1 - c^2$. Accordingly, the parameter $c^2 - 1$ provides the amount of piling-up ($c^2 - 1 > 0$) or sinking-in ($c^2 - 1 < 0$) as a fraction of the maximum penetration of the indenter, h_s (e.g., if $c^2 - 1 = 0.5$, the amount of piling-up is half the value of h_s , whereas $c^2 - 1 = -0.5$ indicates that the amount of sinking-in is half the value of h_s).

A systematic study on the development of surface deformation around spherical indenters was conducted by Norbury and Samuel (1928) using early experimental techniques. The amount of piling-up and sinking-in was correlated with the strain hardening exponent of the materials under study. Numerical works by Marx and Balke (1997) and Bolshakov and Pharr (1998), where the amount of piling-up and sinking-in was computed for a wide range of plastic responses, showed that piling-up should predominate for soft materials with a low value of both hardness to Young's modulus ratio (H/E), and strain hardening exponent to Young's modulus ratio (n/E).

Alcala *et al* (2000) studied the influence of plastic hardening on surface deformation modes, around both Vickers and spherical indents, by scanning the indents with a profilometer to record their topographical features. The experimental results were then compared with numerically predicted surface profile. A range of material properties (i.e. work hardening coefficient) have been numerically studied. For Vickers indentation, the true depth of penetration, ' h ' is related to the maximum depth of penetration underneath the original surface ' h_s ' by a surface deformation factor ' α ' following Eq. 2.39

$$h = \sqrt{\alpha} h_s \quad (\text{Eq. 2.39})$$

so the difference between h_s and h is

$$h - h_s = (\sqrt{\alpha} - 1) h_s \quad (\text{Eq. 2.40})$$

Figure 2.11 shows the surface deformation parameters for spherical and Vickers indentation. It clearly showed that the dependency of surface deformation on the work hardening coefficient ' n ' for Vickers indents almost overlaps that for spherical indentation. For both spherical and Vickers tests, the amount of piling-up decrease gradually as n increases. The work also indicated that surface deformation scales with the peak indentation load in such a way that the mean value of $\sqrt{\alpha}$ remains invariant

(this is similar to the case of spherical indentation where c^2 was constant regardless of the applied load). The amount of surface deformation around Vickers and spherical indents is found to correlate well with the strain hardening exponent, whereby the transition from piling-up to sinking-in occurs for $n \approx 0.2$. Surface deformation is affected by unloading from the peak indentation load as load removal leads to a considerable elastic rebound at the imprint. Such elastic rebound favours the development of piling-up.

For spherical and conical indentations, the surface profile is uniform across the perimeter of the indenter but for Vickers indentation, the pattern on the edge and the corner is significantly different due to the geometrical constraints. As predicted in the computational modelling by Giannakopoulos *et al* (1994) and evident from experimental measurement (Alcala *et al*, 2000), the amount of surface deformation vanishes at the corners of the imprint due to the geometrical constraint imposed by the sharp edge of the indenter.

2.7 Instrumented indentation test

Instrumented indentation, also known as depth-sensing indentation, is increasingly being used to probe the mechanical response of materials including metals, ceramics, polymers and biological materials (Fischer-Cripps, 2004; Ren *et al*, 2004). The additional levels of control, sensitivity and data acquisition offered by instrumented indentation systems have resulted in numerous advances in materials science, particularly regarding to fundamental mechanisms of mechanical behaviour.

In an instrumented test, force and displacement are continuously measured during the test. As shown in Figure 2.12, the whole loading curve is used to represent the resistance of the material. In this technique, an evaluation of contact area from measurements of depth of penetration is desirable, as it facilitates the automation of the indentation methodology.

The loading part of an instrumented sharp indentation generally follows Kick's law, which can be expressed as,

$$P = Ch^2, \quad (\text{Eq. 2.41})$$

where P is the indentation load, h is the penetration depth measured from the surface and C is a constant curvature. The projected contact area for indenters with linear relationships between penetration depth and contact radius (conical, Berkovich and Vickers) can be expressed as,

$$A = kh^2 \quad (\text{Eq. 2.42})$$

where k is a constant for a particular material and an indenter geometry.

Dividing Eqs. 2.41 by 2.42 leads to,

$$P_{av} = P/A = C/k = \text{constant} \quad (\text{Eq. 2.43})$$

Such evaluation requires a precise knowledge of the surface deformation modes, as errors of up to 30% can be introduced in the computation of contact area if the development of piling-up and sinking-in is not taken into account. Oliver and Pharr have developed a technique for determining contact area (Oliver and Pharr, 1992; Oliver and Pharr, 2004). The method begins by analysing the indentation force-depth

curve of indentation data, including the unloading branch, as illustrated in Figure 2.13. From the force-depth curve, one can measure the peak force (P_m) at peak depth (h_m) and residual depth (h_r) (*i.e.* the depth after withdrawal of the indenter). The average contact pressure, $P_{ave} = P_m/A_m$ (A_m is the true projected contact area measured at the maximum load P_m), can be correlated to the hardness of the indented material. The maximum indentation depth h_m occurs at P_m , and the initial unloading slope is defined as $dP_u/dh|_{h_m}$, where P_u is the unloading force. The W_t term is the total work done by load P during loading, W_e is the released (elastic) work during unloading, and the stored (plastic) work $W_p = W_t - W_e$. The residual indentation depth after complete unloading is h_r .

The effect of material properties on the $P-h$ data has been studied by Taljat *et al* (1998). The unloading part of the $P-h$ curve is primarily influenced by the Young's modulus 'E', as the unloading process is essentially an elastic process. They also showed that the loading part of the $P-h$ curve correlates with the yielding strength ' σ_y ' and 'n' (Taljat *et al*, 1998). These effects could potentially be used to predict the plastic material behaviour from the indentation force-depth curves. The details will be discussed in the next section.

2.8 Evaluation of material properties by indentation tests

2.8.1 Classification of different approaches

Indentation tests present a simple way to characterize materials: the main advantage is that it only requires a small volume of material. However, hardness value can only be used as a comparative measurement. In many cases, more detailed material parameters are required for design and simulation, etc. For metallic materials, the most important design data required for calculating the load bearing ability of the structure are the plastic parameters, particularly the yielding strength and the work hardening coefficient as shown in Figure 2.6.

Figure 2.14 summarises different methods used to extract material properties based on indentation tests which can be classified into three main approaches. The first one, named Tabor method, is based on representative strain theory (Kucharski and Mroz, 2001; Bucaille *et al*, 2003). The second approach, named forward and reverse method, is recently developed based on indentation load–displacement ($P-h$) curves and reverse analysis (Doerner and Nix, 1986; Oliver and Pharr, 1992; Cheng and Cheng, 1999a; Giannakopoulos and Suresh, 1999; Dao *et al*, 2001; Bucaille *et al*, 2003; Chollacoop *et al*, 2003; Tho *et al*, 2005; Swaddiwudhipong *et al*, 2005a, b). The third one, named inverse method, is based on indentation load-displacement ($P-h$) curves and inverse FE modelling approach (Nakamura *et al*, 2000; Bolzon *et al*, 2004; Ren *et al*, 2006; Nakamura and Gu, 2007).

2.8.2 Tabor method based on indentation tests

Hardness is not an intrinsic property of the material. In particular it depends on the geometry of the indenter and the friction between indenter tip and specimen surface. However, Tabor showed that hardness can be related to the stress of the indented material, σ_r , corresponding to a representative strain, ϵ_r , which represents the mean plastic strain defined by Tabor (1948, 1951). Such a technique allows estimating one point on the true stress–true strain curve.

For Vickers indentations on metals, Tabor (1951) has shown that $\epsilon_r = 0.08$ and that the ratio of the Vickers hardness H_v to the representative stress σ_r is equal to 3

$$\sigma_r \approx H_v / 3 \quad (\text{Eq. 2.44})$$

According to Johnson (1985), the representative strain for a conical indenter can be expressed as:

$$\epsilon_r = 0.2 \tan \beta = 0.2 \cot \theta \quad (\text{Eq. 2.45})$$

where β is the attack angle of the indenter and θ is the included angle for conical indenters. The ratio between hardness and the representative stress, H_v/σ_r decreases as β increases for rigid, perfectly plastic materials (Chitkara and Butt, 1993). For elasto-plastic materials, this ratio also depends on the fraction of elastic deformation with respect to the whole deformation during the indentation process, and for $\theta \sim 70^\circ$ varies between one and three as $E/\sigma_r \cot \theta$ increases from 2.6 to 48 (Johnson, 1970).

For spherical indenters, the representative strain ϵ_r increases as the penetration depth of the indenter increases. The purely elastic behaviour at the onset of loading and during unloading is modelled using theory of elasticity (Johnson, 1985). For intermediate penetration depths, the deformation levels at the indented materials are so small that the strains are elasto-plastic. At high penetration depths, i.e. in the fully plastic regime, the elastic contribution is neglected: in this last stage the hardness of a work-hardened metal is constant according to Tabor (1951). The hardness (H_n) of materials is defined as the ratio between normal force P and projected contact area, A . At higher penetration depths, i.e. in the full plastic flow regime, Tabor suggested the following relationships for evaluating stress and strain from spherical indents.

$$\sigma_r \approx H_n / 2.8, \left(H_n = \frac{P}{A} = \frac{H_v}{0.927} \right) \quad (\text{Eq. 2.46})$$

$$\epsilon_r \approx 0.2a / R \quad (\text{Eq. 2.47})$$

Chaudhri (1998) has shown that Tabor's method of estimating the representative strain could not provide a unique value of the H_n / σ_r ratio for various materials and suggested the use of the maximum value of the flow stress that occurs in indentation. This value has been determined for spherical and Vickers indentations in annealed polycrystalline copper by indenting a cross-sectioned plane of a macro indentation at low loads. The magnitude of the maximum strain increases with an increase in the

penetration depth of the sphere and the value for the Vickers indenter is about 0.36, which is much higher than the value suggested by Tabor. Herbert *et al* (2001) have proposed a comparison between the stress–strain behaviour of an aluminium alloy tested in uniaxial tension and by spherical indentation. The study involved using Tabor’s relation (Eq. 2.46) that relates normal hardness and stress for a given representative strain depending on the penetration depth of the sphere in a fully developed plastic contact. It was shown that Tabor’s equations do not allow reproducing of the correct shape of the uniaxial stress-strain curve. A numerical study presented by Larsson (2001) showed that several materials having different strain characteristics, but the same flow stress at $\epsilon_r = 0.08$, did not have the same Vickers hardness. Furthermore, Bucaille and Felder (2002) have shown that the value of the representative plastic strain depends on the ratio of elastic deformation to the whole deformation. All these studies show that the definition of the representative strain in indentation is still a fundamental question. The values of the representative strain are only valid under certain conditions and must be used with care. As a consequence, determining the true stress-true strain curves by using simple hardness measurements is a complex problem and can only give an approximation of the properties of the material (Bucaille *et al*, 2003).

2.8.3 Forward and reverse method

The forward analysis scheme enables the prediction of the load–displacement response for a material when the elasto-plastic properties (e.g. E , σ_y , n) are provided as inputs. The reverse analysis scheme is then used to estimate the elasto-plastic properties from indentation load–displacement curves.

Many forward methods and reverse methods have been explored to extract material properties from indentation test. Doerner and Nix (1986) and Oliver and Pharr (1992) proposed methods to obtain Young’s modulus of materials from the unloading part of indentation load–displacement curves. Cheng and Cheng (1999b) derived a set of dimensionless functions to associate the characteristics of the indentation load–displacement curve with the elasto-plastic properties of the material. Based on three-dimensional finite-element simulations, Giannakopoulos and Suresh (1999) proposed a set of equations for reverse analysis of indentation experiments.

Dao *et al* (2001) proposed a new set of dimensionless functions and forward and reverse analysis scheme based on extensive finite-element simulations. The frame of the inverse process is shown in Figure 2.15 (a&b). Using dimensional analysis, a new set of dimensionless functions was constructed to characterise instrumented sharp indentation. From these functions and elasto-plastic finite element computations, analytical expressions were derived to relate indentation data to elasto-plastic properties. As shown in Figure 2.15 (a), the forward algorithms allow the calculation of the indentation response for a given set of elasto-plastic properties, whereas the reverse algorithms enable the extraction of elasto-plastic properties from a given set of indentation data (Figure 2.15 (b)). Comprehensive sensitivity analyses were carried out for both forward and reverse algorithms, and the computational results showed good agreement with experimental data for two aluminum alloys 6061-T6511 and 7075-T651 aluminium. A representative plastic strain was identified as a strain level which allows for the construction of a dimensionless description of indentation loading response, independent of strain hardening exponent n . The proposed reverse analysis provides a unique solution of the reduced modulus E^* , a representative stress σ_r , and the hardness H . With this information, values of σ_y and n can be determined for the majority of cases considered in the work, provided that the assumption of power law hardening adequately represents the full uniaxial stress–strain response. A major drawback for the approach lies in the poor sensitivity to variation of testing parameters. The predicted plastic properties are very strongly influenced by even small variations in the parameters extracted from instrumented indentation experiments (Dao *et al*, 2001).

More recently, Tho *et al* (2004) proposed a new method for interpretation of indentation load–displacement curves. In their work, extensive large deformation finite element analyses were carried out to investigate the response of elasto-plastic materials obeying power law strain-hardening during instrumented indentation. The functional form of the relationships between the curvature of the loading curve (C), the gradient at initial unloading from maximum load ($S = (dP/dh)|_{h_m}$) and the ratio of plastic work done to total work done (W_P/W_T) and the material properties of elasto-

plastic materials (E^* , σ_y , n) are examined. The governing equation relating C to the elasto-plastic material properties (E^* , σ_y , n) are formulated:

$$\frac{C}{\sigma_y} = f\left(\frac{E^*}{\sigma_y}, n\right) \quad (\text{Eq. 2.48})$$

and

$$\frac{W_P}{W_T} = f\left(\frac{E^*}{\sigma_y}, n\right). \quad (\text{Eq. 2.49})$$

Based on these dimensionless functions between the indentation P - h curves and material properties from the extensive finite element simulations, Tho *et al* (2004) and Swaddiwudhipong *et al* (2006) have developed an approach to predict the material properties using reverse analysis. The work was validated based on blind test (i.e using numerical results only).

The sensitivity of the predicted material properties due to variations of the input parameters is essentially an intrinsic characteristic of reverse problem (Venkatesh *et al*, 2000, Dao *et al*, 2001, Swaddiwudhipong *et al*, 2005a). The reverse program uses the loading and unloading curve, which can be affected by many factors, therefore requires several precautions when being used to estimate the plastic material properties of metals. Firstly, the geometry of the indenter used for indentation experiments has to correspond to the value used in the numerical analysis. Dao *et al* (2001) have shown that, for a Berkovich tip, a difference of 1° of the angle of the indenter induces a difference of 10% in the calculation of C . Furthermore, as actual indenters do not have a perfectly pointed tips and experiments must be performed for penetration depths large enough for the influence of this tip defect to be neglected. This problem becomes especially important for indenters with small included angles: during indentation experiments the diamond tip can be damaged much more easily. Secondly, function models developed from the direct analysis may not necessarily accurately represent force penetration curve, during loading over a wide range of material properties. The determination of the loading curvature C obtained from experiments is subject to many uncertainties. One of the most common, called indentation size effect, is due to the load dependence of the hardness and the fact that an indentation with a sharp indenter is not self-similar (Begley and Hutchinson, 1998;

Ren *et al*, 2002; Ren *et al*, 2003; Mirshams and Parakala, 2004). In addition, the friction between the indenter and the material may also influence the testing results.

Bucaille *et al* (2003) have systematically investigated the perturbation in force on the predicted results using a reverse method based on Dao's approach. As shown in Figure 2.16, the predicted n value is very sensitive to the perturbation. A 3% increase of the normal force resulted in a difference of 44% on the value of ' n ' for steel. It also showed that the sensitivity increases with the increasing of indenter apex angle. It is shown that smaller indenter apex angle resulted in higher precision. Swaddiwudhipong *et al* (2005a) found that the yield strength exhibits rather strong sensitivity to perturbations in input parameters, especially for regions with large n values. The maximum variation of yielding strength is approximately 70% with a $\pm 1\%$ change of W_P/W_T . At regions with n values less than 0.4, the variation of yield strength due to perturbations in input parameters is capped at 30%. The maximum variation of n in the domain is about 0.1 for a large value of n (0.6). At most other regions in the domain, the variation of n is less than 0.05 (Swaddiwudhipong *et al*, 2005a).

Generally speaking, the forward and reverse method is an effective one to estimate the material properties from the indentation test data, but there are many factors, such as the constants from the extensive finite element simulations, different indenter shape or material properties, leading to different functions between indentation test data and material properties. This would affect the precision and sensitivity of the reverse results.

2.8.4 Inverse FE modelling method

In a complex material and structural system, direct measurements of unknown variables can be difficult and one has to estimate the unknown state variables *via* indirect measurements of other measurable parameters. In a mixed numerical-experimental approach, a measurable data (e.g. P - h curves) of the material is used as input data to a finite element (FE) model to predict immeasurable parameters of materials. This approach has been used on some non-standard specimens or surface loading situations, such as *in vivo* (on living biological systems) tension, indentation,

etc. (Meuwissen *et al*, 1998; Nakamura *et al*, 2000; Shan and Gokhale, 2003; Bolzon *et al*, 2004; Ren *et al*, 2006; Ren *et al*, 2006).

The most commonly used method is the interactive inverse FE method (Figure 2.17). In this process, an optimisation algorithm is coupled with finite element modelling in order to find optimal values for a set of target parameters which produces numerical results matching the experimental results (minimising the objective function). As shown in the flow chart, the FE modelling is repeated with changing material parameters until an optimum combination of material properties is found. This method required re-running of FE models during the optimisation process.

Another approach is a post modelling approach, in which a data space (simulation space) is developed and the optimum property is searched through the data base to match the experimental result. Several methods could be employed. For example, Bolzon *et al* (2004) adopted the ‘‘Trust Region’’ (TR) algorithm for inverse analysis, which is available in the popular Matlab optimisation toolbox. Tho *et al* (2004) constructed an artificial neural network (ANN) model for material characterisation based on simulated load–displacement response for dual sharp indenters. Nakamura *et al* (2000, 2007) have developed a Kalman Filter method for the optimal inverse analysis to estimate effective material properties of functional gradient materials (FGMs). Figure 2.18 shows a flow chart showing the main component of inverse modelling using Kalman Filter method (Nakamura *et al*, 2000). Recently, Ren *et al* (2008) have developed a similar approach to study the non-linear properties of polymer foam. The method is effective in estimating unknown state variables using measurements that may contain substantial error or noise and provides an efficient computational solution based on the least-squares theory. One main advantage of this method lies that it does not require re-running the FE modelling during the optimisation process.

2.8.5 Potential use of inverse FE modelling based on indentation for characterising spot welded joints

In an inverse FE modelling approach, the material properties can be calculated by solving the inverse problem *via* finite element analysis, by incrementally varying

properties in FE modeling, to find a set of material properties which match the measured result. The experimental results can be a load–displacement curve, surface deformation profiles, or full strain field around an indentation (Nakamura *et al*, 2000; Bolzon *et al*, 2004; Bao *et al*, 2005). At present, instruments to measure the local profile of the indented specimen are fairly frequently available in laboratories for different purposes. In particular, e.g., atomic force microscopes (AFM) can provide an accurate mapping of the geometrical consequences of micro and nano-indentation tests (see, e.g., Bhushan *et al*, 1996, Bao *et al*, 2005). However, this method requires high level of experimental means, which is difficult to be used in an engineering situation (such as spot welded joint).

Although many inverse analysis techniques have been introduced in various applications, the techniques are not effective unless they satisfy convergence and consistency conditions. In many cases, direct applications of inverse analysis techniques would not yield accurate solutions since many problems are ill-conditioned (i.e. difficult to converge to unique solution), and some known or presumed conditions must be prescribed to establish a robust procedure for individual case. Many inverse FE modelling results were sensitive to initial guess values and in some case, a wide range of initial data has to be used to produce robust values. As in many inverse analyses, the model is initially “ill-posed” or “ill-conditioned” with single indenter measurement. This problem may be overcome by using an additional indenter. In other words, the accuracy of reverse method can be significantly improved by using dual or more indenters as compared to single indenter method. Recently, Swaddiwudhipong *et al* (2005a) demonstrated the sensitivity of reverse method can be significantly moderated by using more cone indenters. This requires a systematic investigation to find out the best combination of indenters to be able to predict the plastic properties. In addition, the majority of published works (Shan and Gokhale, 2003; Bolzon *et al*, 2004) on inverse modelling requires the use of a continuous depth sensing technique, which has limited the application of this approach in engineering conditions. A simpler and more effective methodology needs to be developed to characterise the material properties using a standard hardness test machine, which could potentially extend the use of the inverse FE modelling based on indentation test. The detailed material properties obtained will then be used to

simulate the deformation of spot welded joints and the effect of dimensional attributes such as nugget size and sheet thickness.

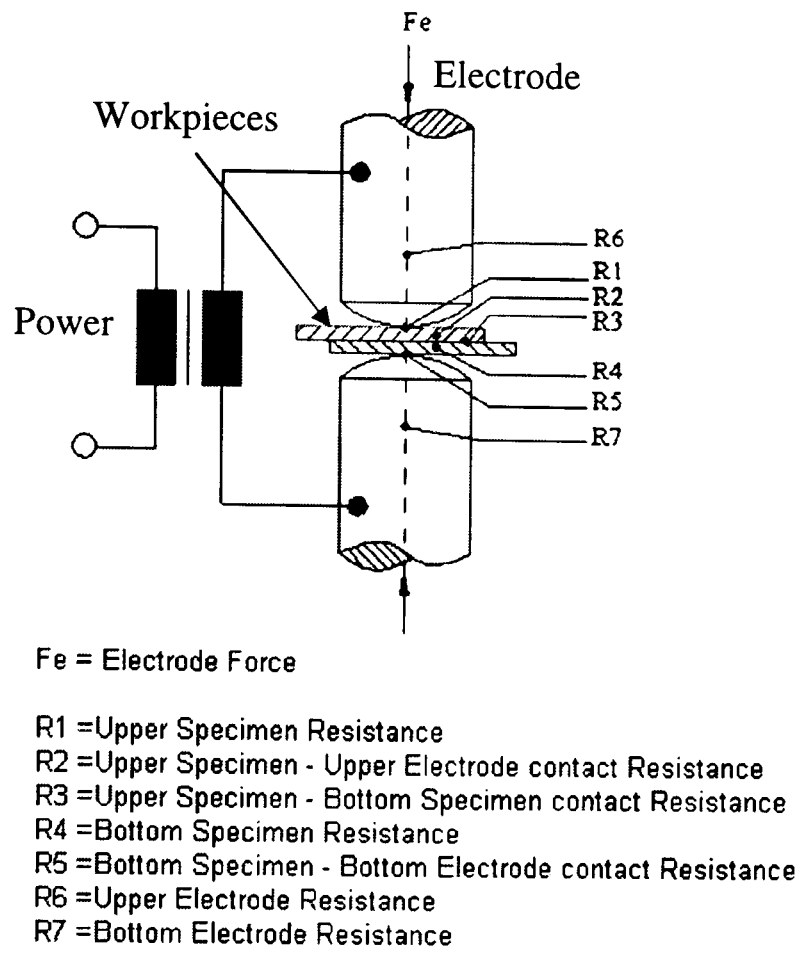


Figure 2.1 The setup of a spot welding system and the resistances occurring in welding (Aslanlar, 2006).

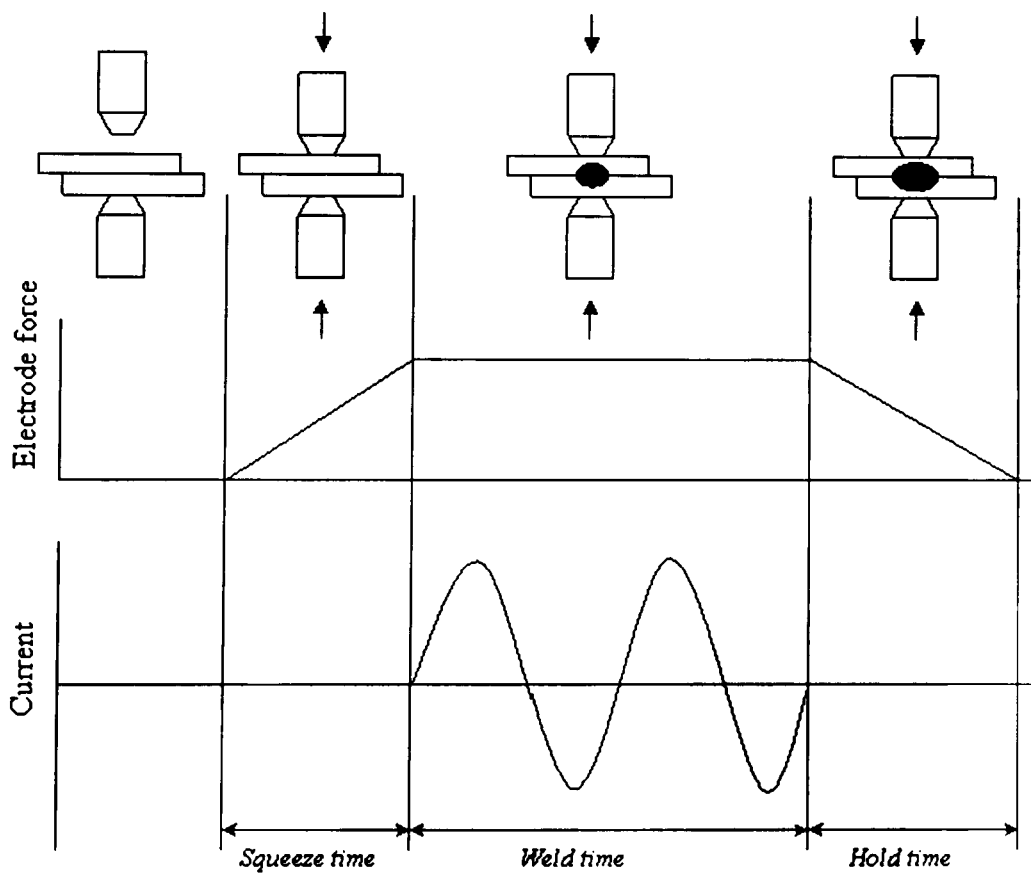


Figure 2.2 Different stages of resistance spot welding operation (Aravinthan, 2003).

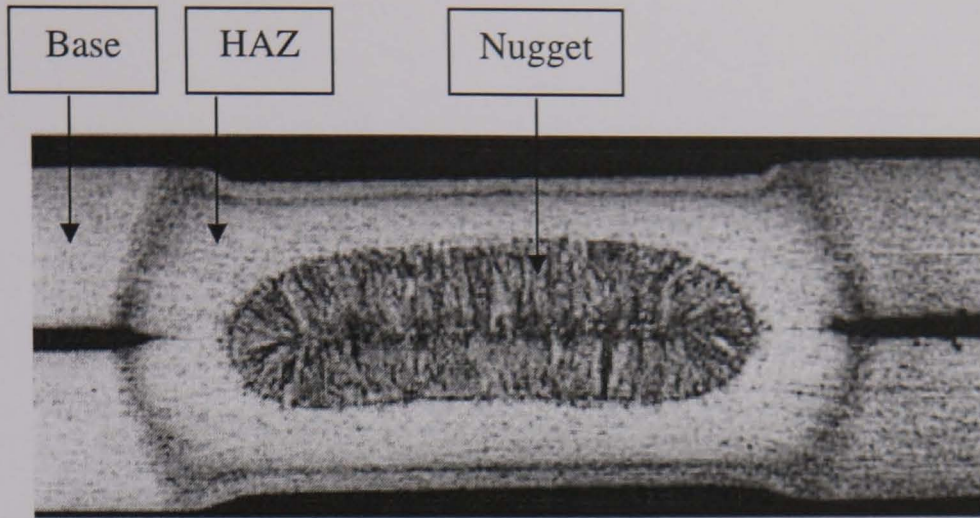


Figure 2.3 Typical optical microstructure of the welded joint of steel (The Welding Institute-TWI).

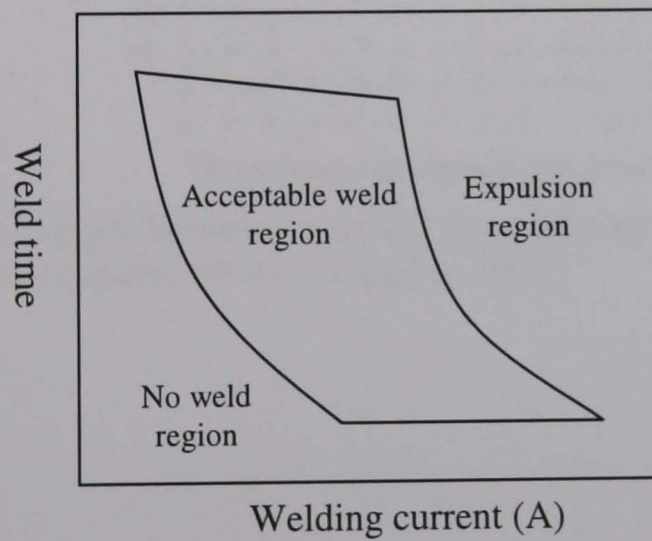


Figure 2.4 Typical spot weld lobe curve (Aravinthan, 2003).

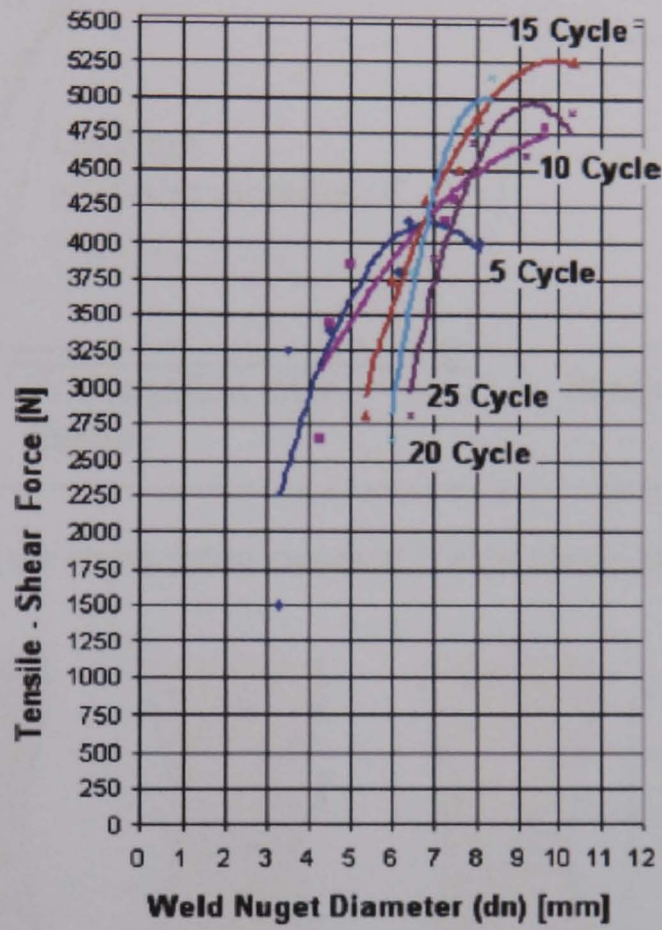
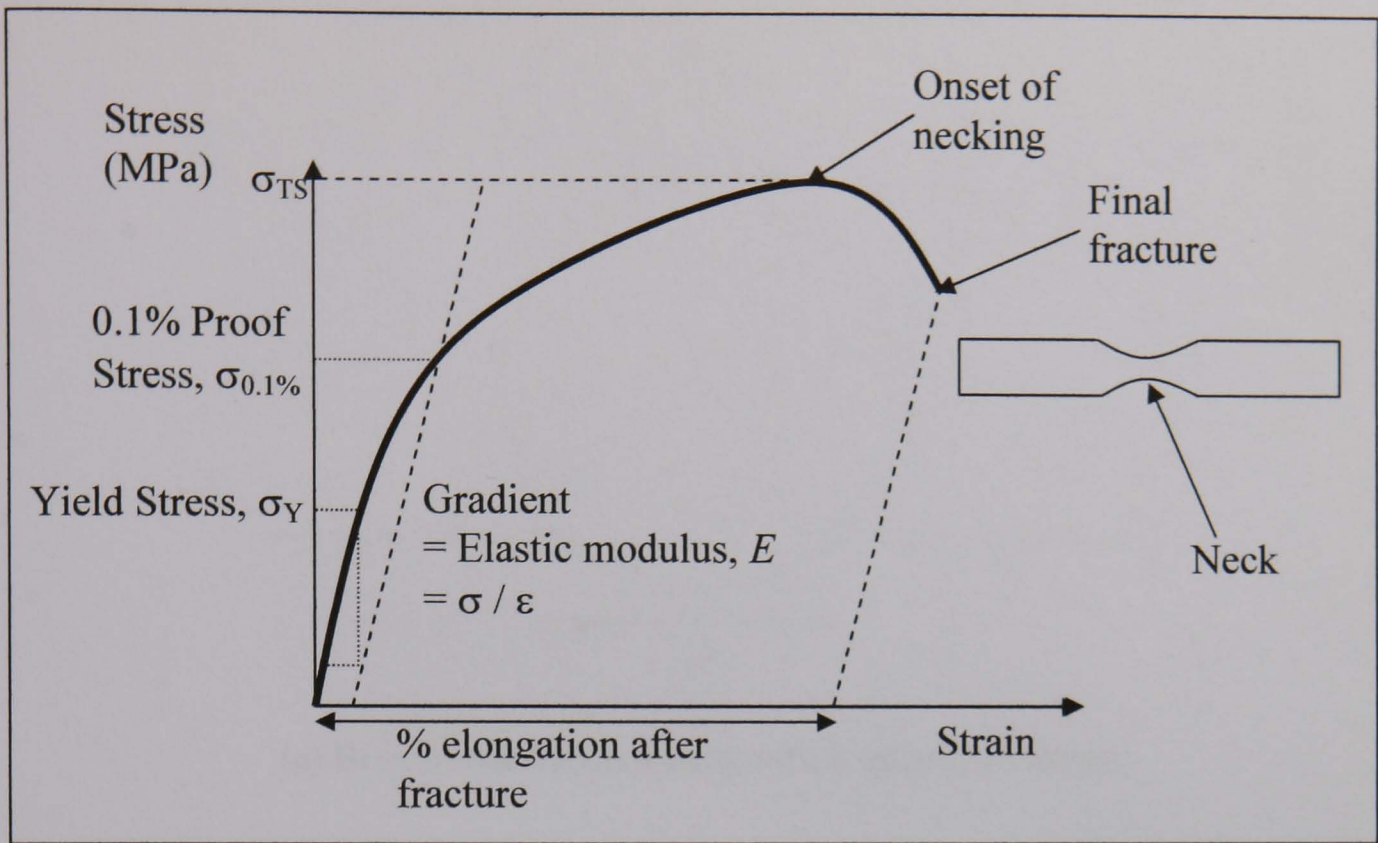
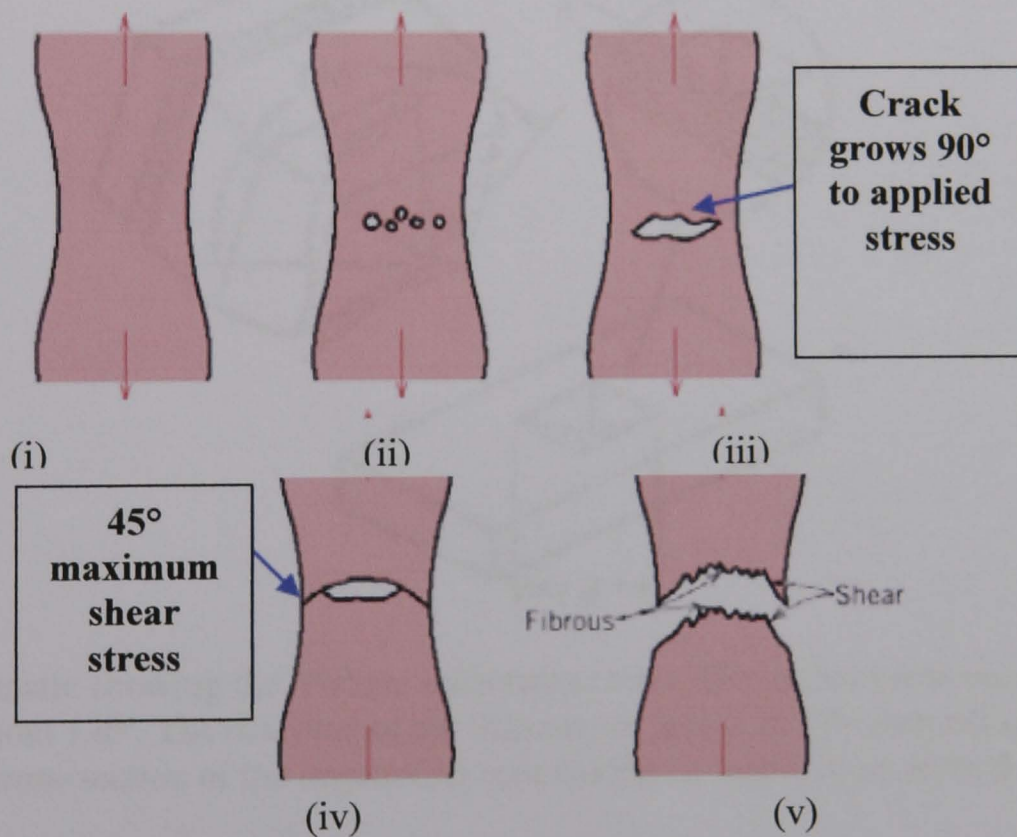


Figure 2.5 Effect of nugget diameter on tensile-shear strength of spot welded joints of micro alloyed steel (frequency: 50 Hz) (Aslanlar, 2006).

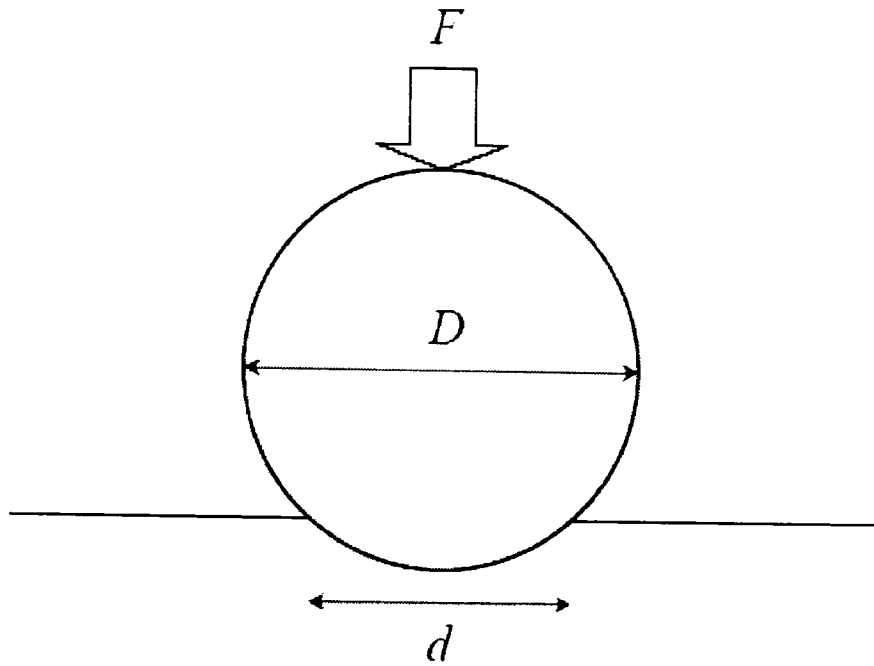


(a) Schematic showing the stress-strain curves of typical elastic and plastic behaviour.

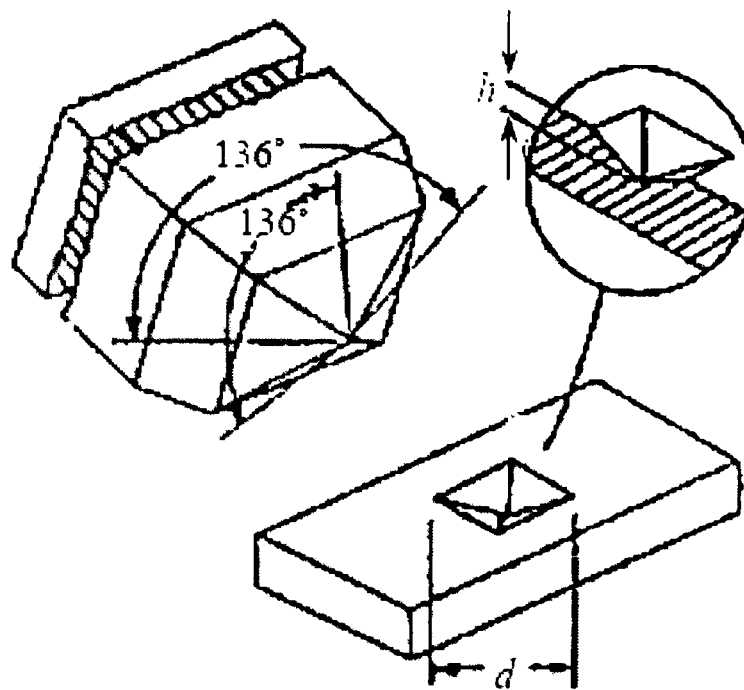


(b) The ductile fracture process: (i) Necking, (ii) Cavity formation, (iii) Cavity coalescence to form crack, (iv) Crack propagation, (v) Fracture

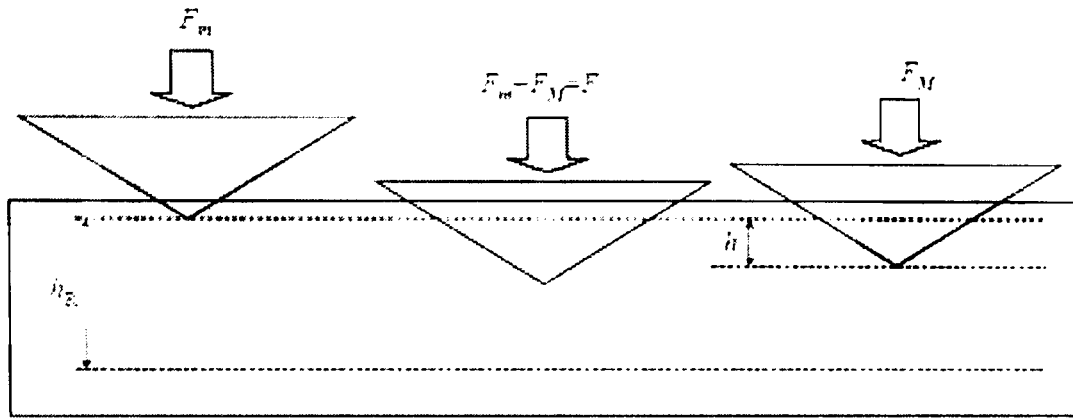
Figure 2.6 Typical elastic and plastic stress-strain curves (a) and the ductile fracture process (b) (Wang, 2003).



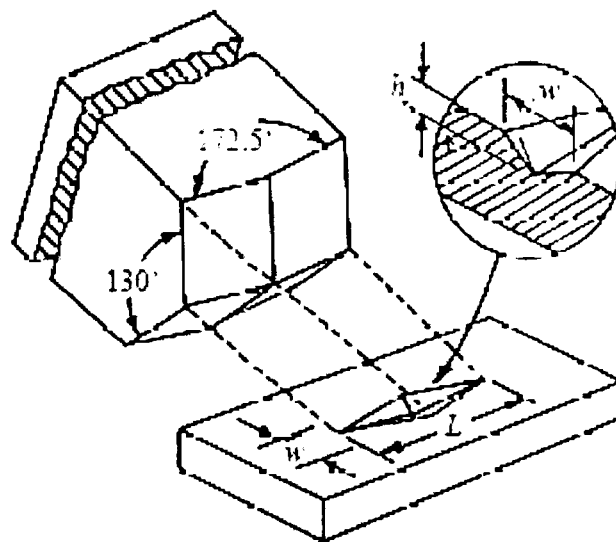
(a) Brinell indentation testing with a spherical indenter.



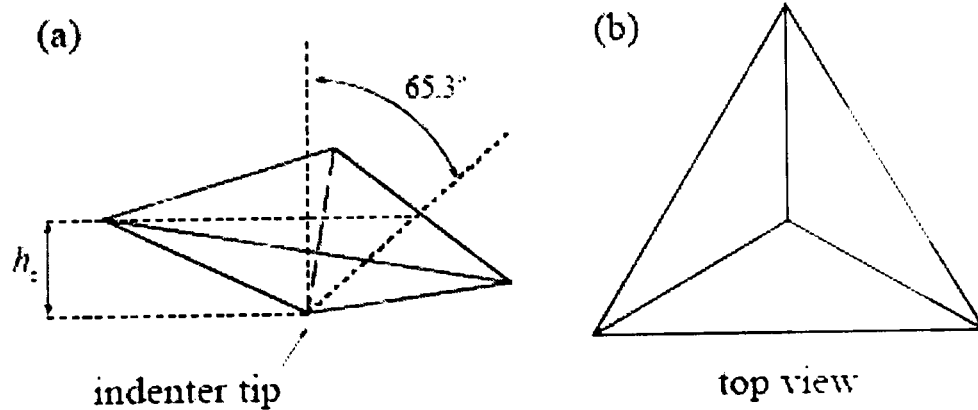
(b) Schematic showing the Vickers indentation tests. The angles between opposite faces are both 136° . The diagonal of the impression area is d . The zoomed inset is the cross-section of the impression area having an indentation depth h .



(c) Schematic showing the Rockwell hardness tests with a cone indenter.



(d) Schematic showing the Knoop indentation test. The angles between opposite faces are 172.5° and 130° . The long and short diagonals of the impression area are L and w , respectively. The zoomed inset is the cross-section of the impression area having an indentation depth h .



(e) Schematic showing the Berkovich indentation test. (a) Indenter impression tip with the face angle is 65.3° . The contact depth is h_c . (b) Top view of the impression area.

Figure 2.7 Schematic showing different indentation tests (Wadjaja, 2007).

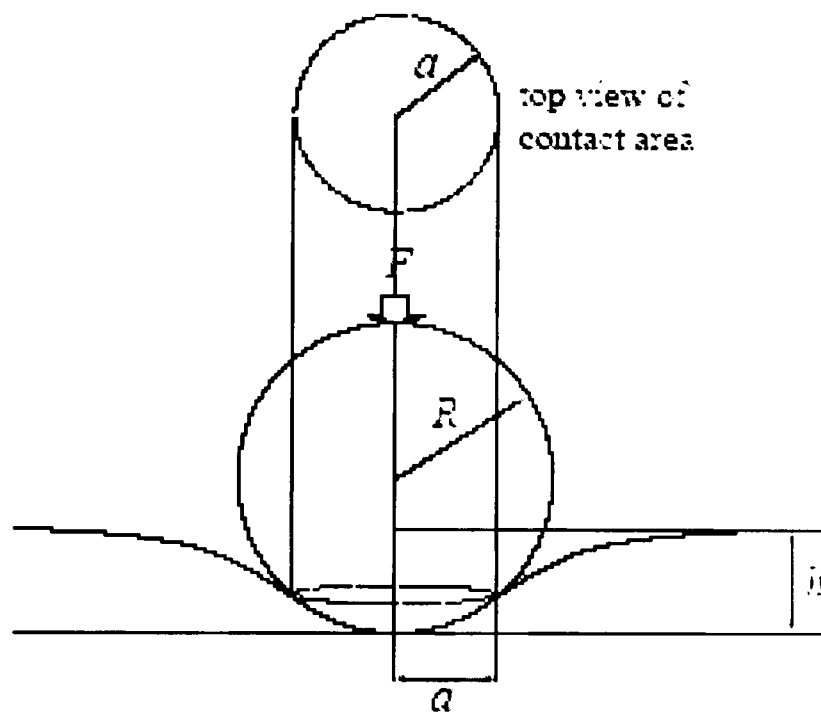
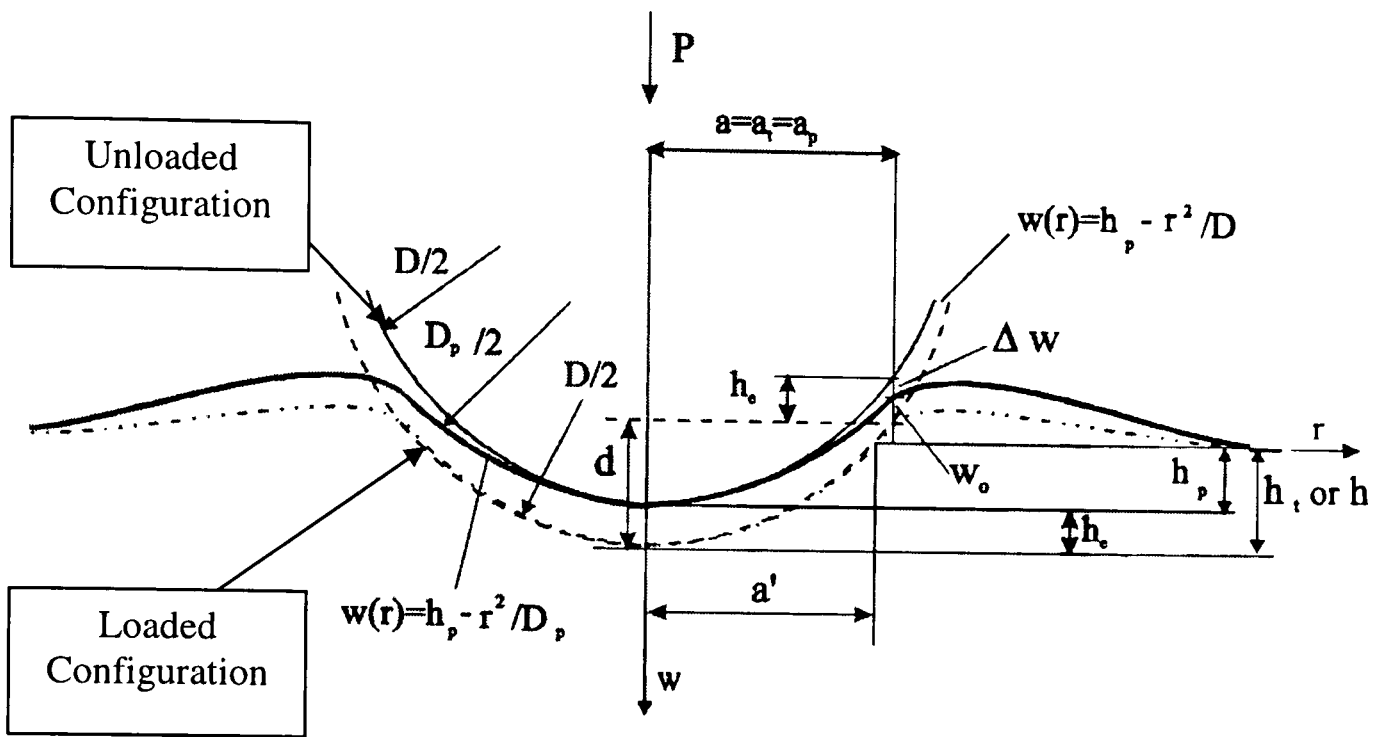
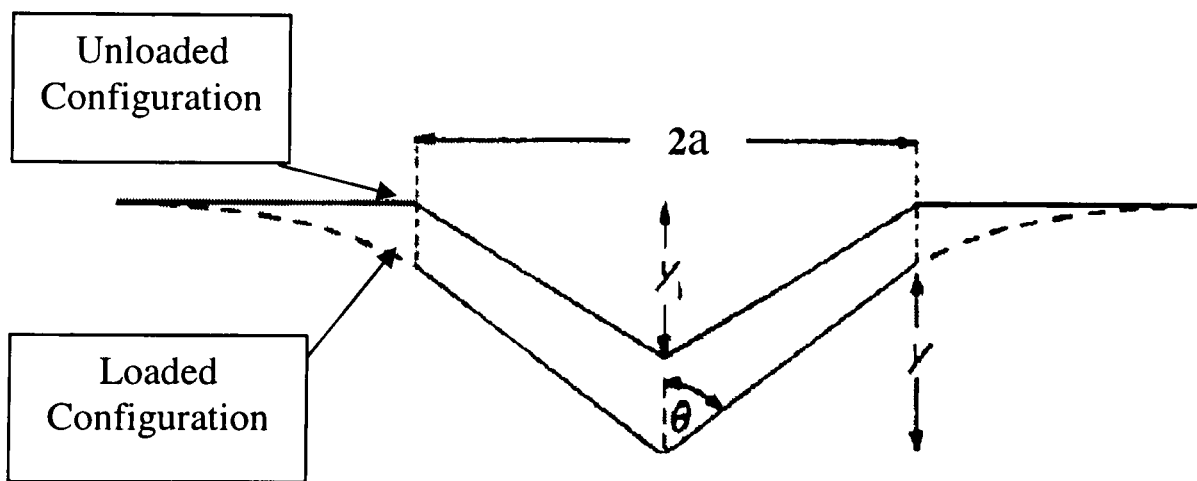


Figure 2.8 Schematics of spherical indentation. R is indenter radius, h is indentation depth, F is indentation force, and a is contact radius and half contact length for spherical indenter (Fischer-Cripps, 2004).



(a) Loaded and unloaded configuration in the spherical indentation test (Kucharski and Mroz, 2001).



(b) Loaded and unloaded configuration in conical indentation test ($y_l < y$) (Stilwell and Tabor, 1961).

Figure 2.9 Schematics showing the recovery process for spherical indenter (a) and conical indenter (b) on an elasto-plastic solid.

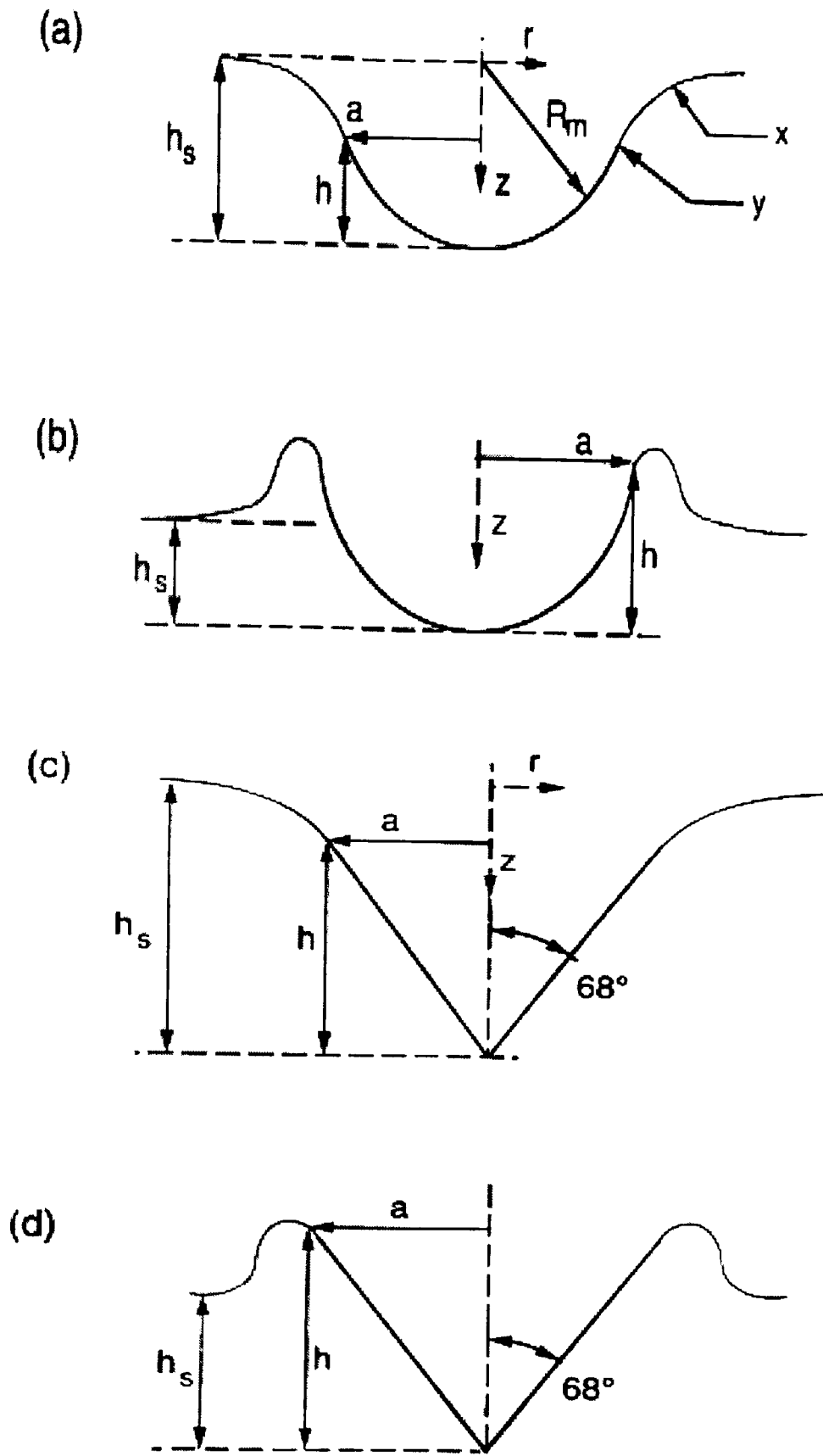
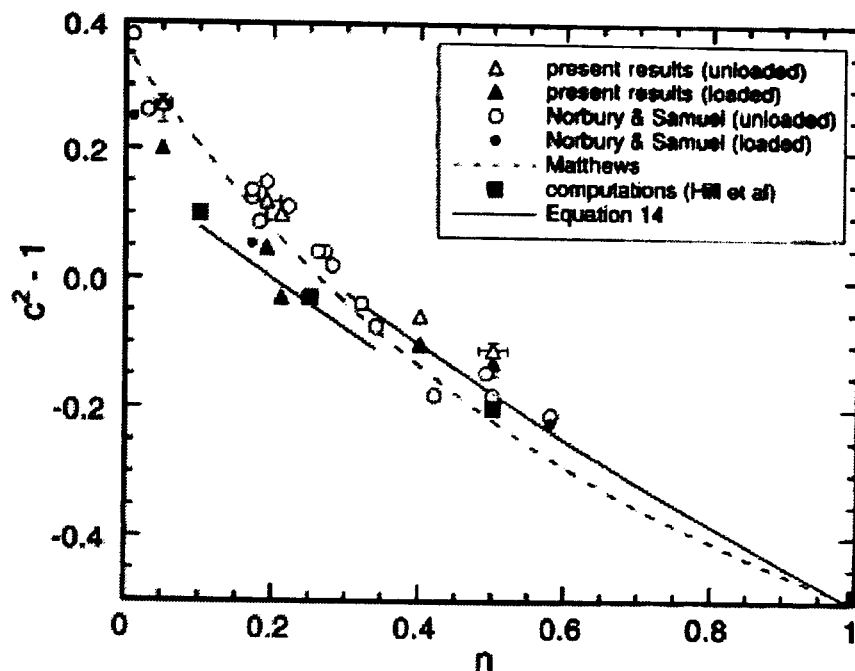
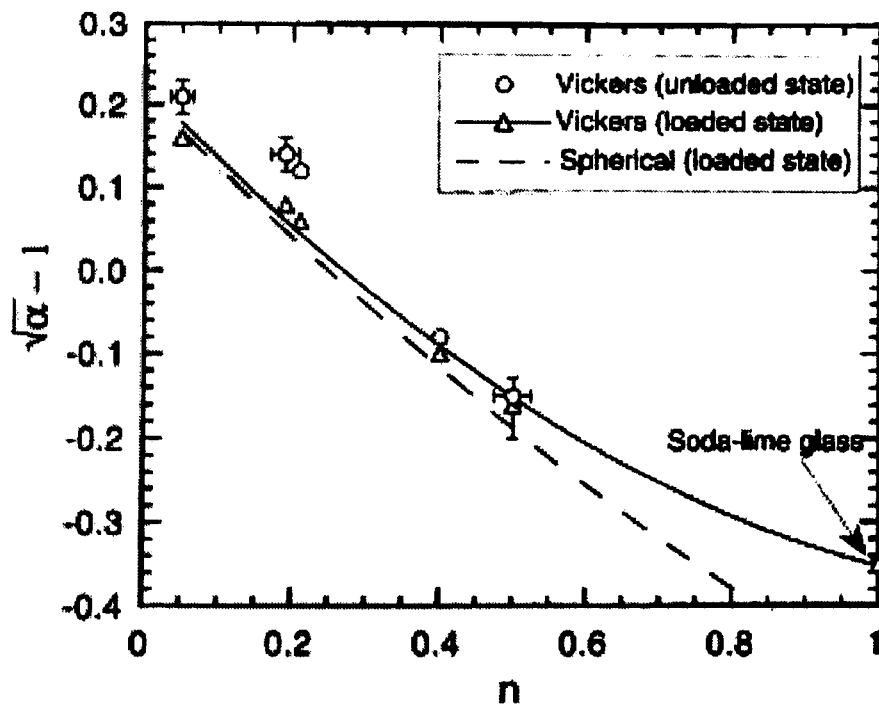


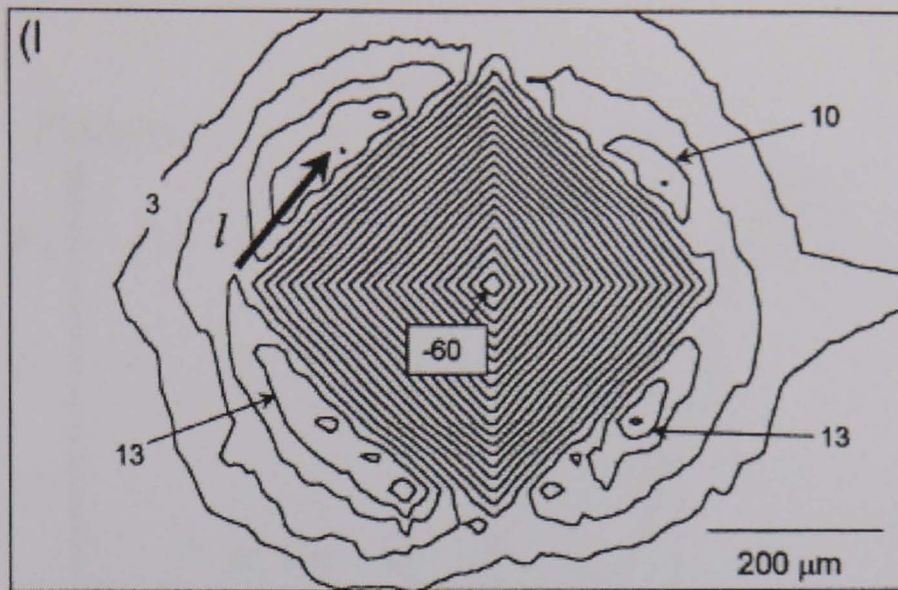
Figure 2.10 Schematic illustration of sinking-in (a, c) and piling-up (b, d) of materials around spherical indents and sharp indents with included apex angle of 68° (Alcala *et al.*, 2000).



(a) Dependence of the surface deformation parameter (c^2-1) for spherical indentation on the strain hardening exponent (n). Bars indicate experimental scatter for the measured surface profiles.



(b) Dependence of surface deformation parameters ($\sqrt{\alpha} - 1$) for Vickers indentation on the strain hardening exponent (n). The best least square fit for the results on spherical indentation is also included for comparison. Bars indicate experimental scatter for the measured surface profiles.



(c) Surface topography around Vickers indenters on work-hardened copper indented at 160 N which exhibits extreme piling-up effect.

Figure 2.11 Dependence of the surface deformation parameters on the strain hardening exponent (n) (a, b) and surface topography around the Vickers indenter (c) (Alcala *et al*, 2000).

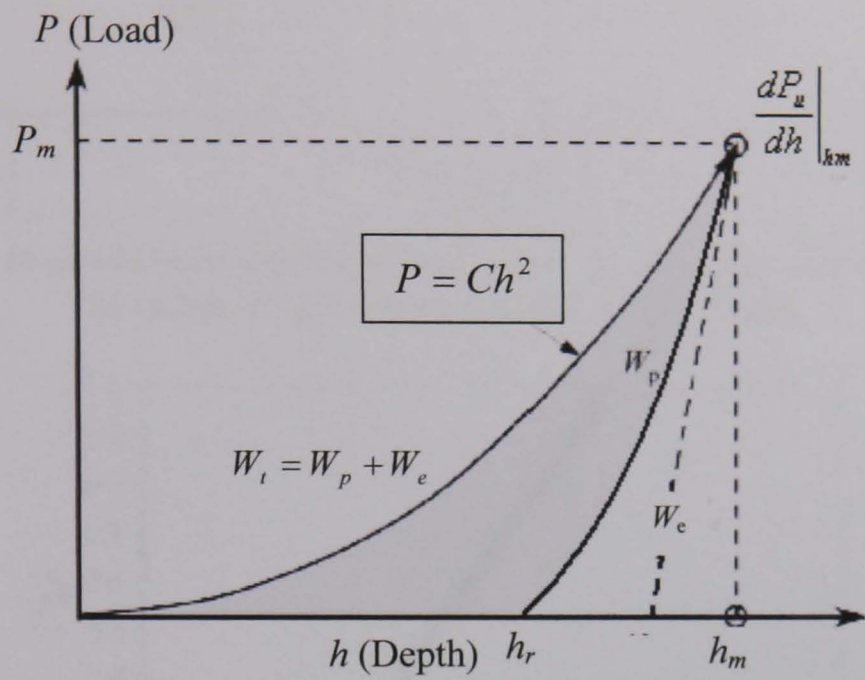
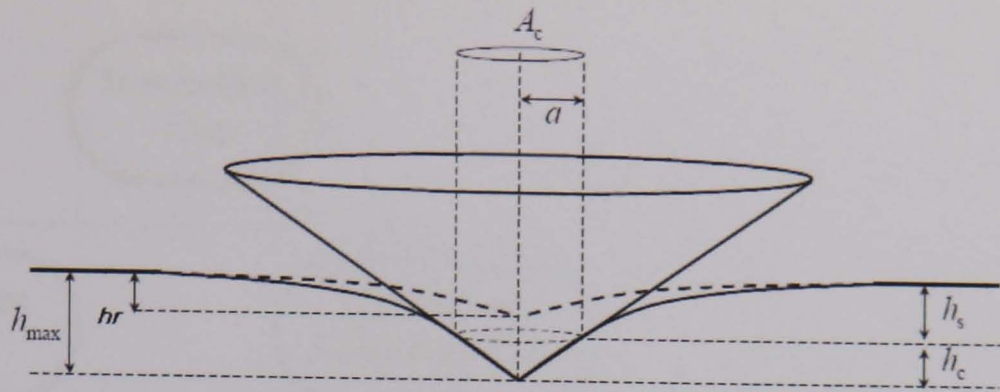
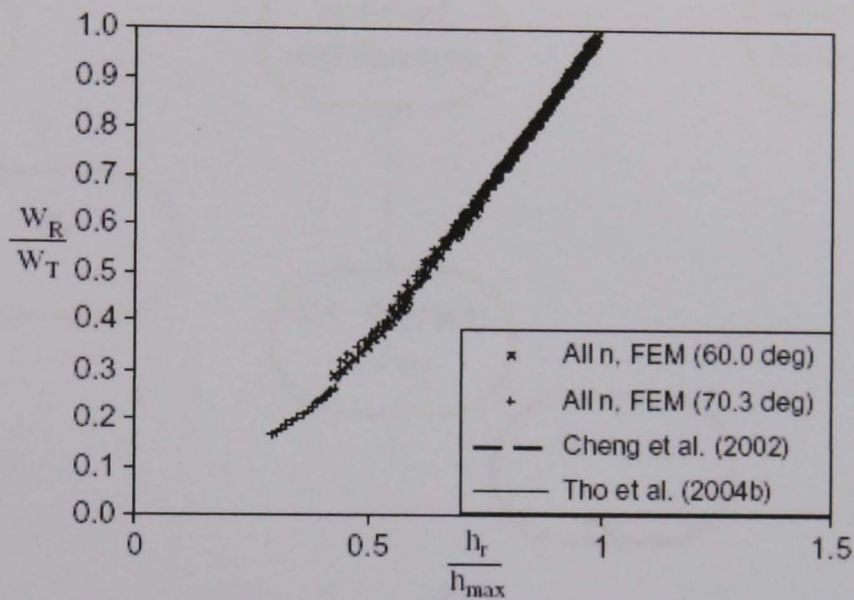


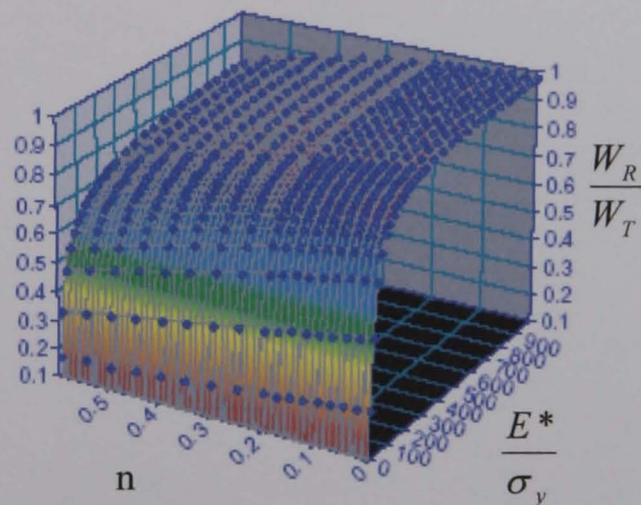
Figure 2.12 Schematic illustration of a typical force (P) indentation depth (h) response of an elasto-plastic material to instrumented sharp indentation (Dao *et al*, 2001).



(a) Geometry to characterise indentation: A_c and a are the projected contact area and its radius, respectively, h_s is the sink-in depth.



(b) Relationship between W_R/W_T and h_r/h_{max} .



(c) Effect of the stiffness-yielding strength ratio and the work hardening coefficient on the W_R/W_T

Figure 2.13 Geometry to characterise continuous indentation with conical indenter and the influence of material properties (Swaddiwudhipong *et al*, 2005).

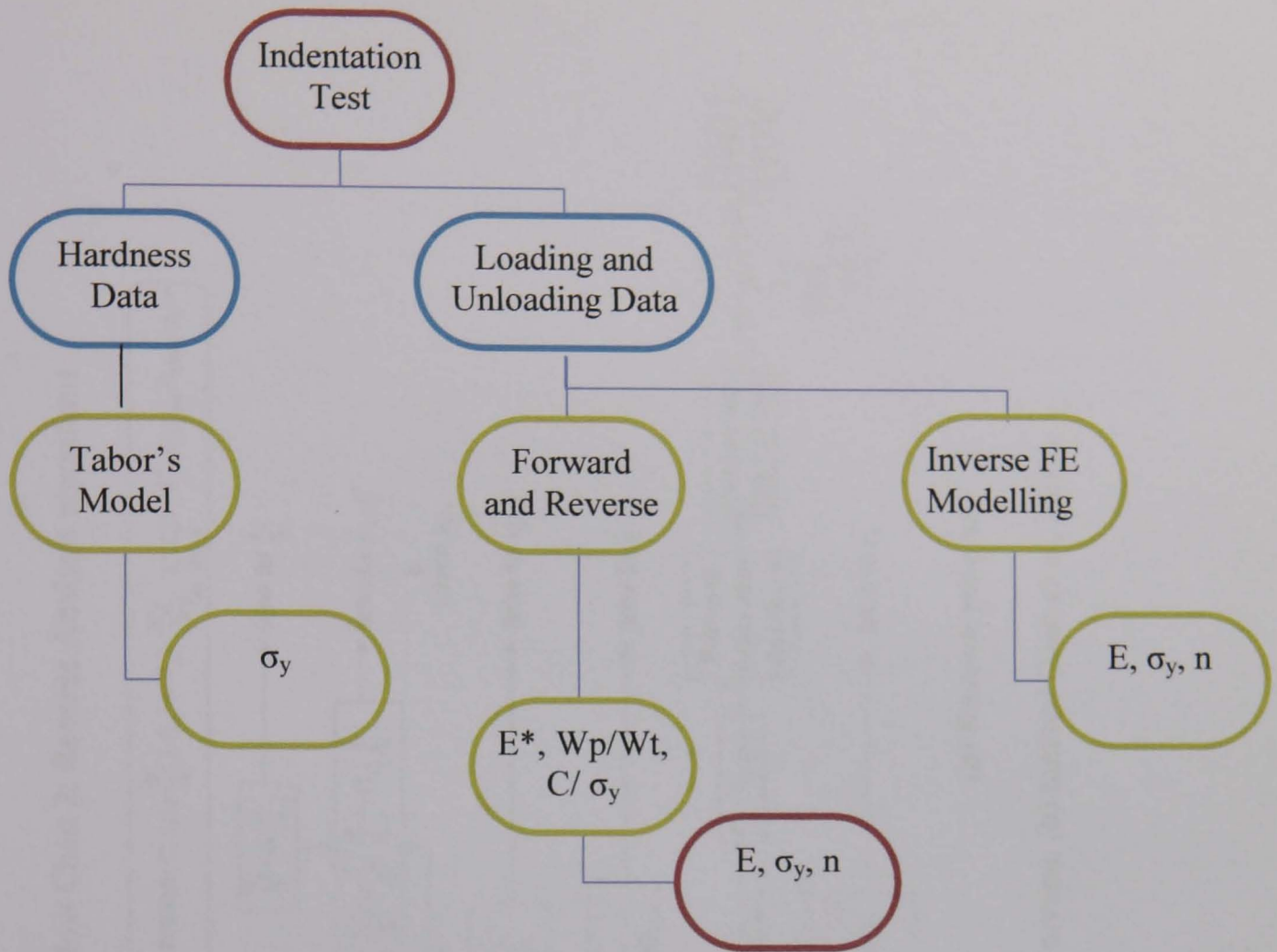
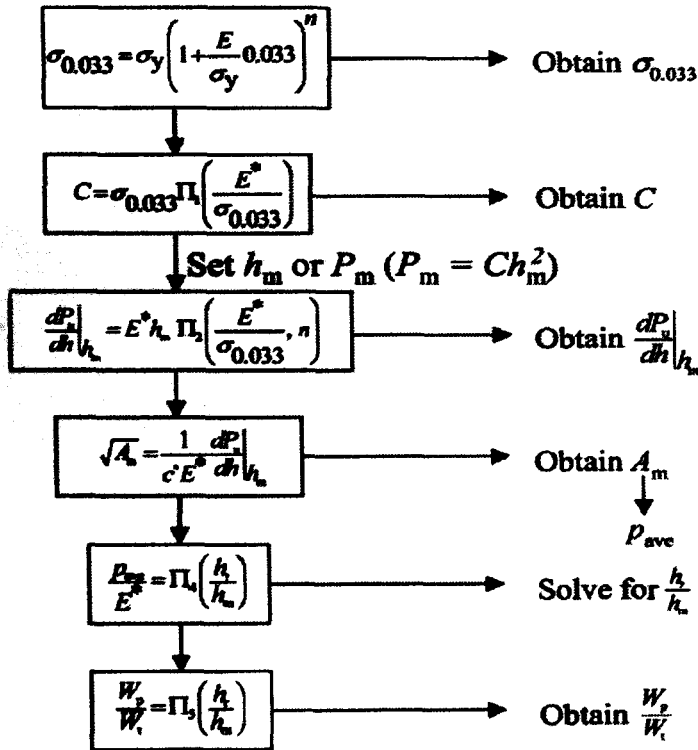


Figure 2.14 Summary of different methods used to estimate material properties based on indentation tests.

Flow Chart 1: Forward Analysis algorithms

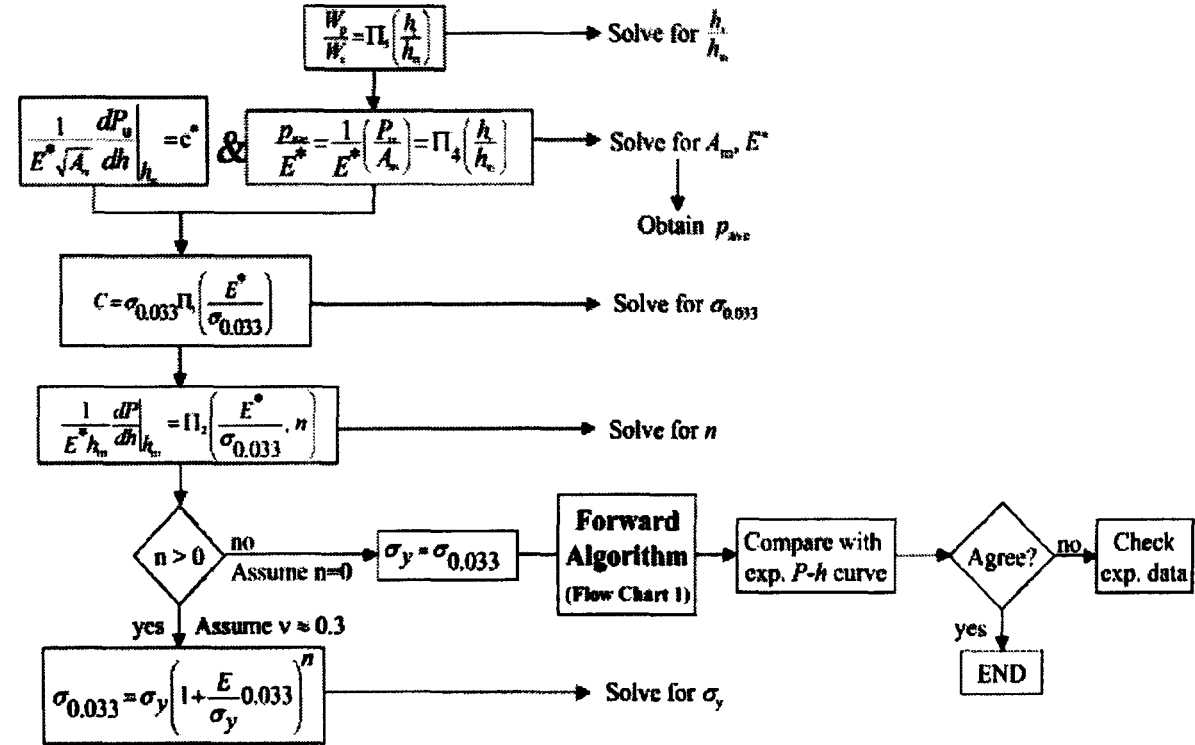
Forward Problem: $E, n, \sigma_y, \nu \implies C, h_r, p_{ave}, \frac{dP_y}{dh} \Big|_{h_m}, \frac{W_p}{W_i}$
 set P_m or h_m



(a) Forward process

Flow Chart 2: Reverse Analysis algorithms

Reverse Problem: C, h_r (or $\frac{W_p}{W_i}$), h_m (or P_m), $\frac{dP_y}{dh} \Big|_{h_m}$ set $\nu \implies E^*, A_m, p_{ave}, \sigma_{0.033}, \sigma_y, n$



(b) Reverse process

Figure 2.15 Flow chart showing typical procedures in forward (a) and reverse (b) method (Dao et al, 2001).

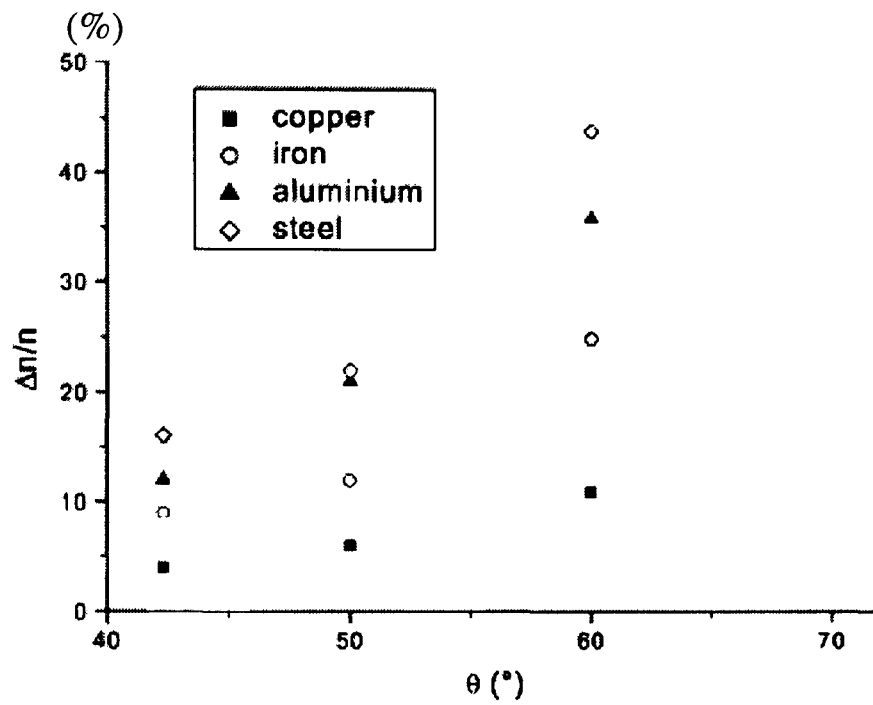


Figure 2.16 Influence of a perturbation of 3% in normal force on the determination of n (Bucaille *et al*, 2005).

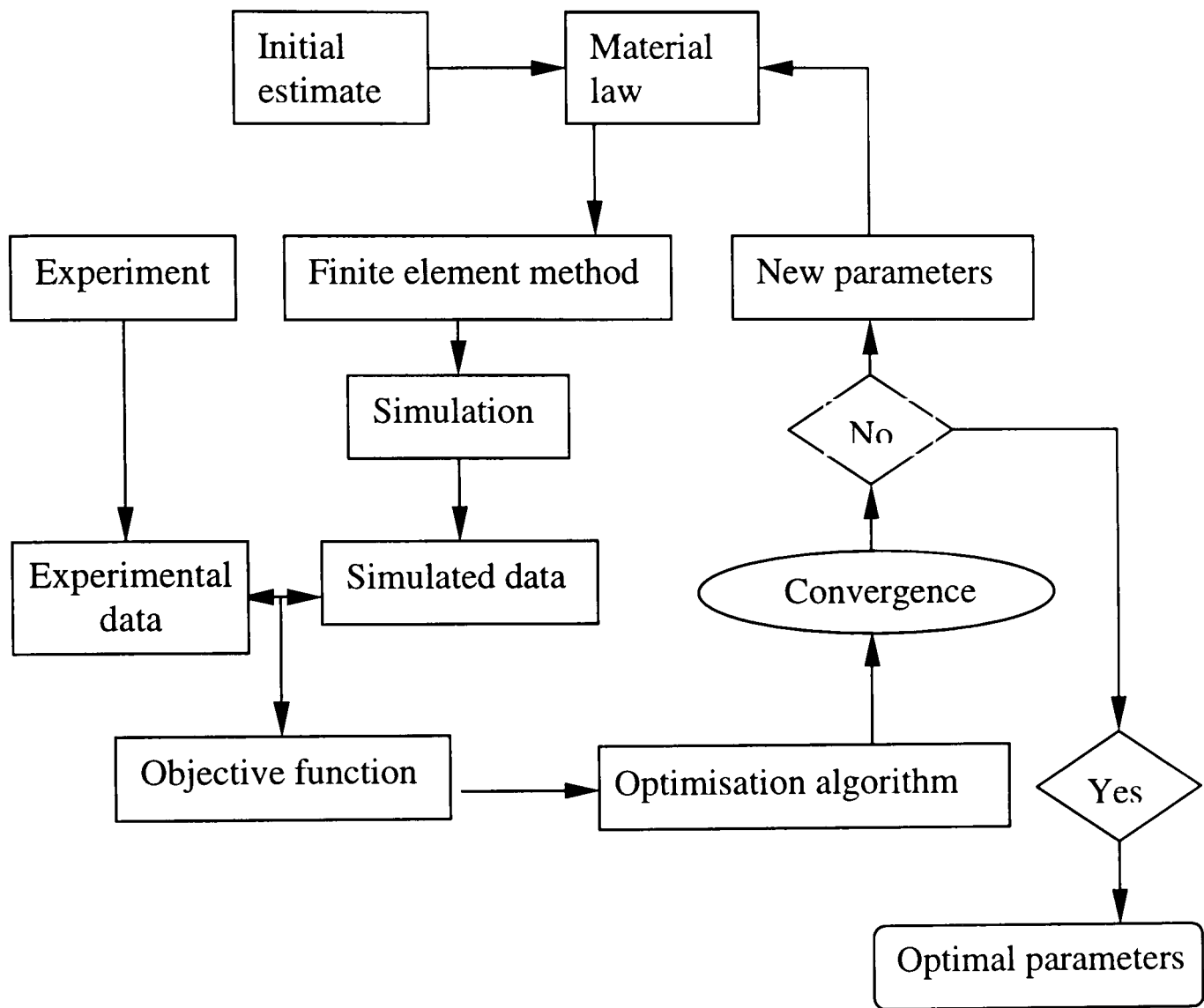


Figure 2.17 Flow chart showing typical procedure of an interactive inverse FE modelling method.

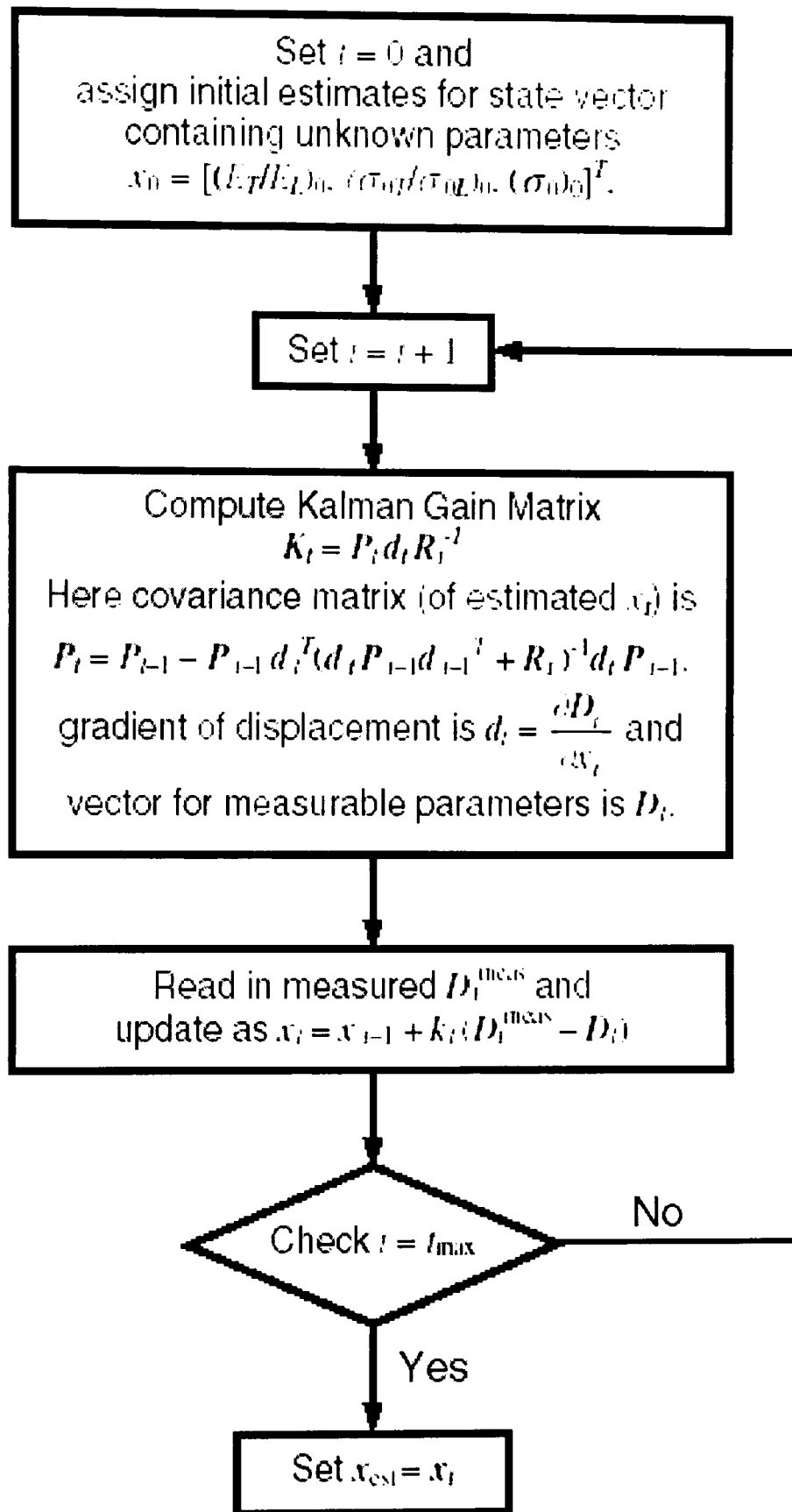


Figure 2.18 Flow chart of Kalman Filter procedure to determine the unknown parameters using instrumented indentation records (Nakamura and Gu, 2007).

CHAPTER 3
RESEARCH APPROACH AND
EXPERIMENTAL WORK

3.1 Introduction

This work is an integrated approach involving development of inverse program, FE modelling and experimental indentation tests, standard tensile tests of base metals and tensile-shear tests to investigate the mechanical strength of spot welded joints.

The overall research plan of the work is shown in Figure 3.1. In the first part, inverse FE modelling approaches based on indentation methods were developed. Different approaches using either single indenter or dual indenters have been comparatively studied and the optimum combination of indenter types to predict accurate and reliable results was established. The sensitivity and validation of the approach was compared to other published data and experimental results.

Based on the established framework using force indentation depth ($P-h$) curves of instrumented indentation, a more convenient method based on force indentation size ($P-d$) data was developed. It was validated and assessed using blind tests, and then applied to characterise two typical auto steels. The results were validated by comparing the predicted material properties from indentation method with standard tensile test results of the same material.

The approach was then used to characterise the plastic properties of the base and welding zones in spot welded joints. The predicted material properties were used in FE model to simulate the deformation of spot welded joints under tensile shear loading. The FE models were then used to study the effects of the weld dimension on the strength of the welded joints, which could potentially guide the welding and design parameters optimisation.

3.2 Experimental work

3.2.1 Materials

The two materials (designated steel A and steel B) used were low carbon steel sheets with different thickness. The chemical compositions of the two base steels are listed in Table 3.1. Steel A is a low carbon steel sheet (width=24mm, and thickness=1.44mm) and supplied in galvanized condition with a coating thickness of 28 μm . The material is widely used in many structure applications in particular in automotive structure. Steel B is a low carbon steel sheet (width=25mm, thickness=0.8mm) from Jaguar and supplied in galvanized condition (thickness=28 μm). The coating is used to improve the corrosion resistance.

Table 3.1 Chemical compositions of steel A and B

| Concentration (%) | C | Mn | Si | Al | Ni | Cr | P | S | Co |
|-------------------|------|-------|--------|-------|-----|-----|-------|-------|-----|
| Steel A | 0.3% | 0.3% | 0.122% | 1.51% | 490 | 260 | 0.05% | 0.05% | 57 |
| | | | | | ppm | ppm | | | ppm |
| Steel B | 0.2% | 0.06% | 0.1% | | | | 0.05% | 0.05% | |

Specimens of two steels were sectioned and mounted in resin, polished and then etched in etchant 4% Nital (Nitric Acid with ethanol) to reveal the microstructures. The microstructure observations were carried out using an Axiovert 200 MAT microscope. As shown in Figure 3.2, the microstructure of steel A is mainly ferrite and pearlite, while the microstructure of steel B is ferrite.

3.2.2 Spot welding tests and set up

The welding tests were performed on a Sciaky S4C25 (model Rapid 25) (Figure 3.3 (a)) resistance welding machine equipped with a coil and a time control Sciaky U.J.S.4.H.C, using a resistive current meter Sciaky WCM/1 measuring the welding current. In the welding process, two metal plates were placed between the electrode

(as shown in Figure 3.3 (b)) and the current was applied. The welding parameters were measured by the Weld Analyzer WA1 (as shown in Figure 3.3 (b)), including welding current, welding time, squeeze time and hold time. The weld analyzer WA1 is an RISC based instrument designed for the comprehensive real-time analysis of resistance welds. It is a compact handheld battery operated unit that is an ideal tool for welding, maintenance and quality control.

According to the sheet thickness of materials, electrode diameter selected is 6 mm for all welding tests. Welding time was fixed at 10 cycles and electrode forces were fixed for the steels, 3.5 kN for steel A, 2kN for steel B. The welding current was varied within 4 different levels ranged between 7000 to 12000A. The welding parameters are listed in Table 3.2. In this range, all the welded joints were acceptable.

Table 3.2 Welding parameters.

| Welding parameter | Electrode force (kN) | Heat (%) | Welding current (A) | Welding time (cycles) |
|-------------------|----------------------|----------|---------------------|-----------------------|
| Steel A | 3.5 | 100 | 7000-12000 | 10 |
| Steel B | 2 | 100 | 7000-12000 | 10 |

3.2.3 Tensile and tensile-shear test

3.2.3.1 Tensile test machine

Tensile tests were performed using a Lloyd LR 30K Universal material testing machine (Figure 3.4 (a)) which can perform both tensile and compression tests. The machine has a maximum loading capacity of 30kN, with the readings being accurate to 0.5% of the force. The Lloyd is interfaced with a microcomputer so graphical printout of the tests can be obtained and test data saved. The control console of the testing machine has a digital display where the machine can be operated either manually or remotely. Tests conducted remotely using the computer have all commands transmitted *via* the RS232 link. The test-piece is loaded into position and the jaws tightened with a pre-load of approximately 50 N. An extensometer (LLOYD, TX 25) with a maximum opening of 50mm was used as shown in Figure 3.4 (b).

3.2.3.2 Tensile test of the base materials (standard and notched specimen)

The tensile strength of the base materials were tested using a typical dog-bone shaped specimen (Figure 3.5(a)) and notched specimen (Figure 3.5 (b)). The uniaxial tensile tests were carried out at room temperature on the specimen to determine the mechanical properties. The experimental results are used to validate the inverse modeling results of material parameters (yield stress, work hardening coefficient and Gurson model parameters). All tensile tests were performed with displacement control with a loading rate of 5mm/ minute.

3.2.3.3 Tensile-shear test of spot welded joints

Figure 3.6 shows the setup of a tensile-shear test of spot welded joint. In the test, the specimen was clamped with two gaskets to avoid the bending during the test. The tensile test was performed at a loading rate of 5mm/minute. The left end was fixed and displacements were applied at the right end. The dimensions of the specimen are shown in Figure 3.6 (b); the total length of the specimen is 175 mm; the width and thickness are different for the two base steel sheets. For steel A, the width is 24mm and thickness is 1.44mm; for steel B, the width is 25mm and the thickness is 0.8 mm. The force-displacement curves were obtained by applying a laser extensometer and the whole force-displace curves of the tensile-shear tests were recorded and compared to the simulated results detailed in chapter 6.

3.2.4 Micro-hardness test

All the hardness tests were carried out using a Leitz Miniload hardness tester (Figure 3.7). Different indenters (Vickers, Knoop, and Sphere) were utilized in characterising the materials and the inverse FE modeling process. The Vickers and Knoop used was newly sharpened standard diamond indenter, while a specially designed spherical indenter ($R=0.5\text{mm}$) was made of tungsten carbides (WC96%) (Precision Ball & Gauge Co.). Indentation tests have been performed to characterise both the base material and spot-welded joints.

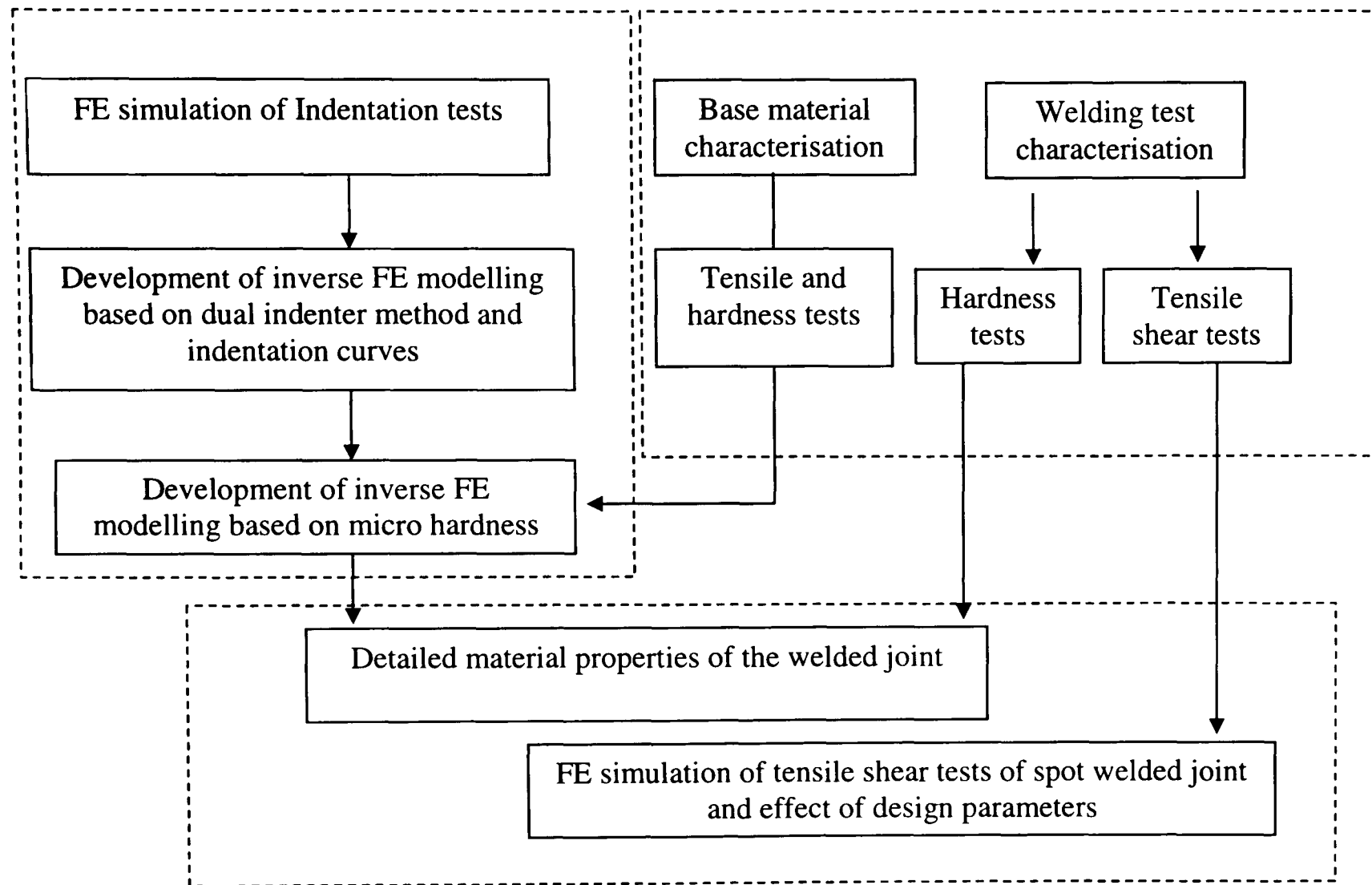
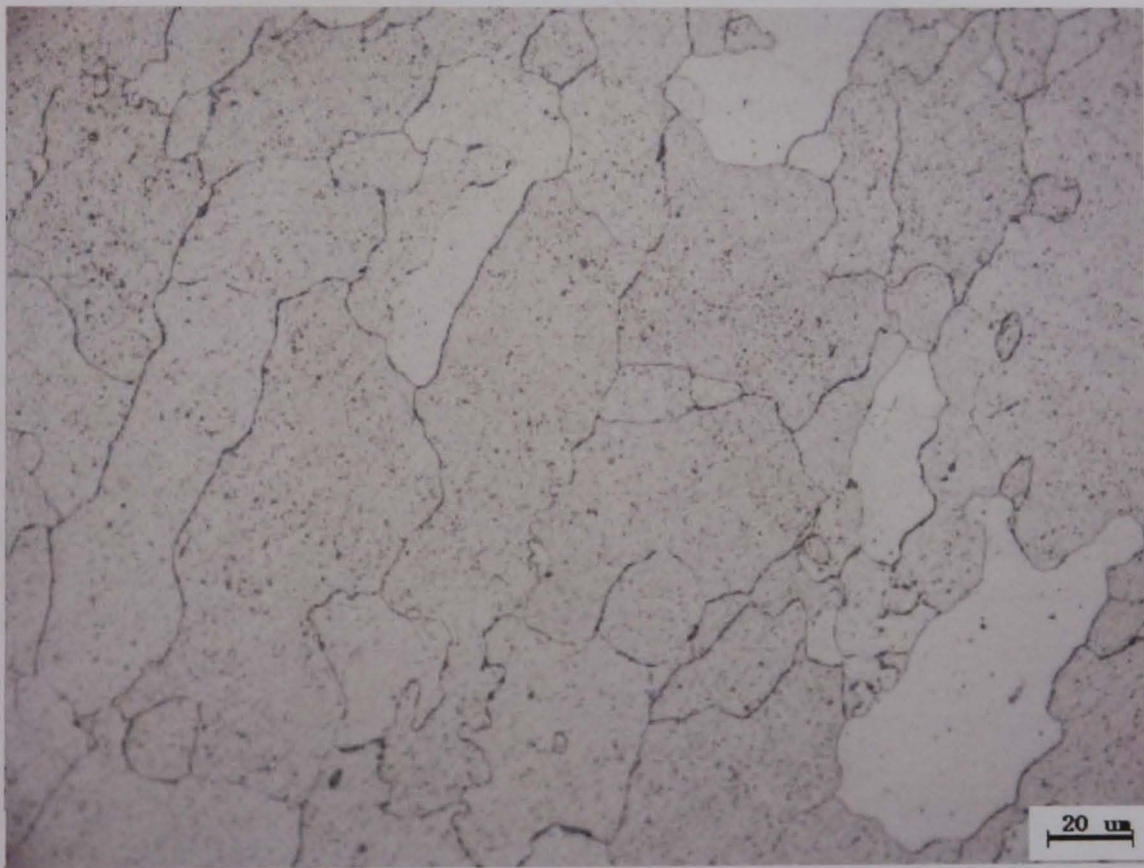


Figure 3.1 Flow chart showing the work plan.

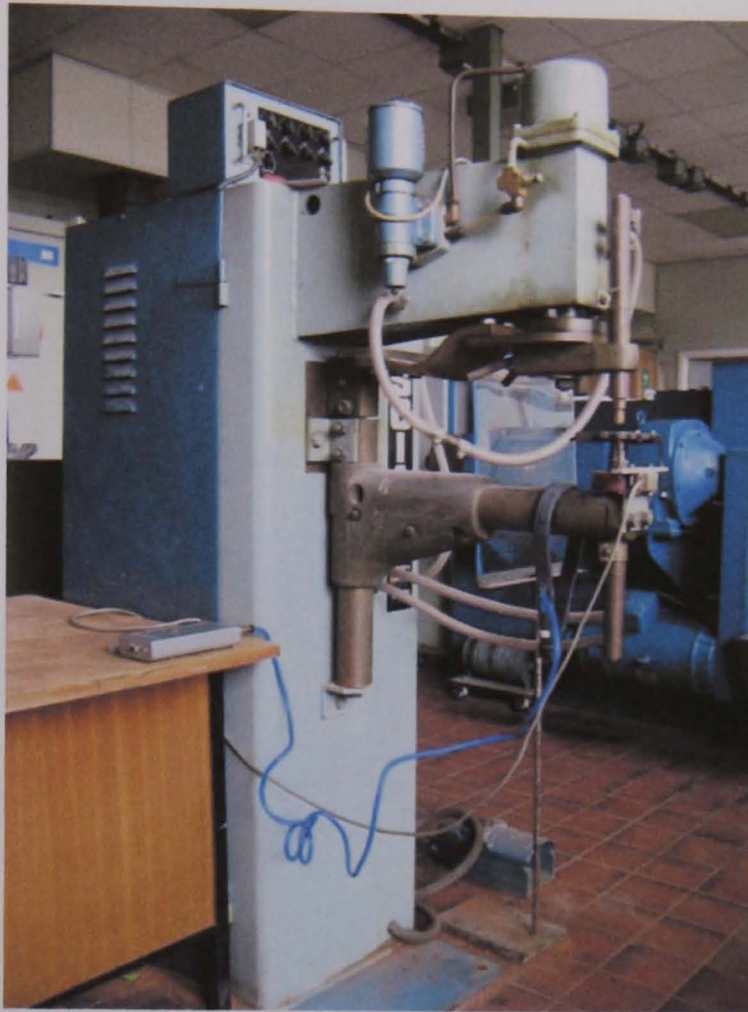


(a) Steel A

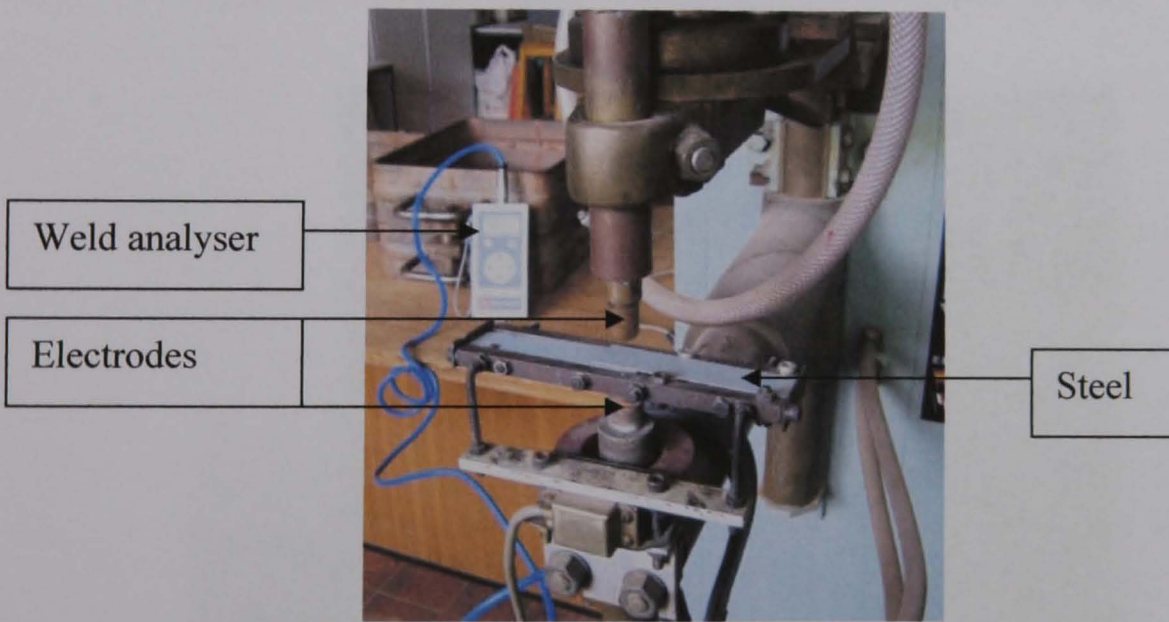


(b) Steel B

Figure 3.2 Microstructures of steel A and steel B.



(a) Spot welding machine.

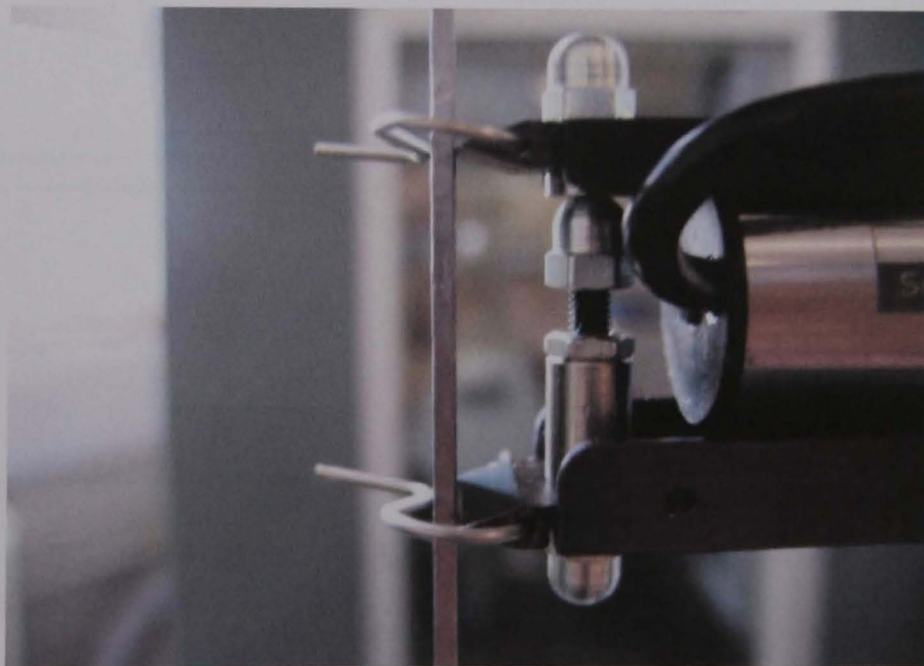


(b) Close-up view of the welding head and weld analyzer.

Figure 3.3 Spot welding machine.

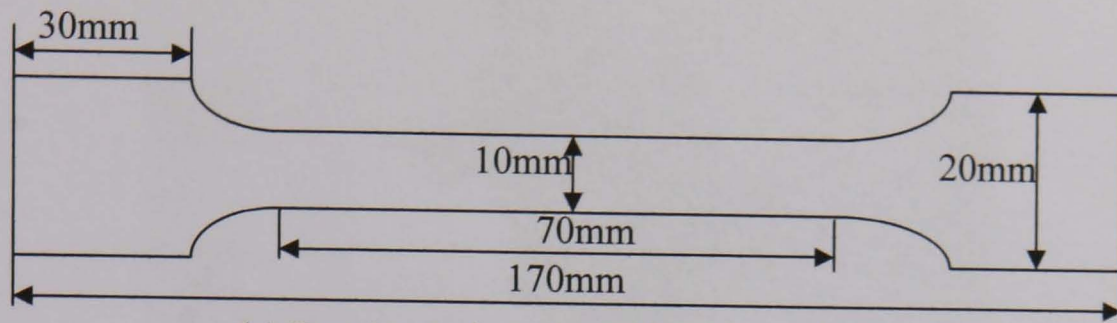


(a) Tensile testing machine.

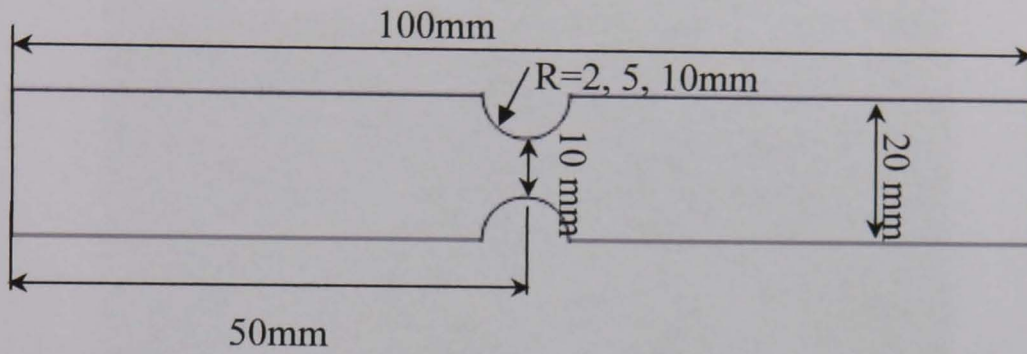


(b) Tensile test of base steel specimen with a clip gauge.

Figure 3.4 Tensile test machine.

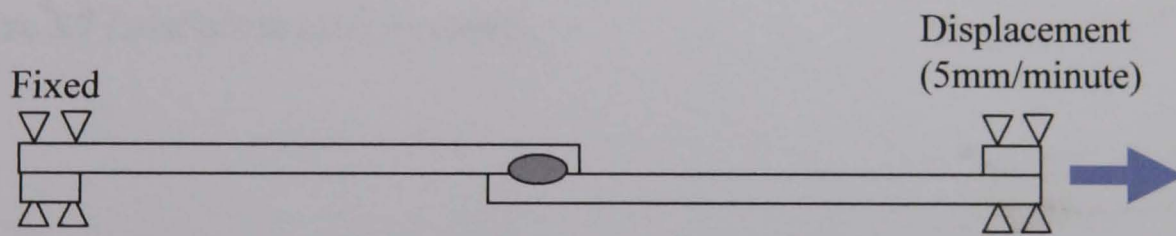


(a) Dog-bone shaped tensile test specimen.

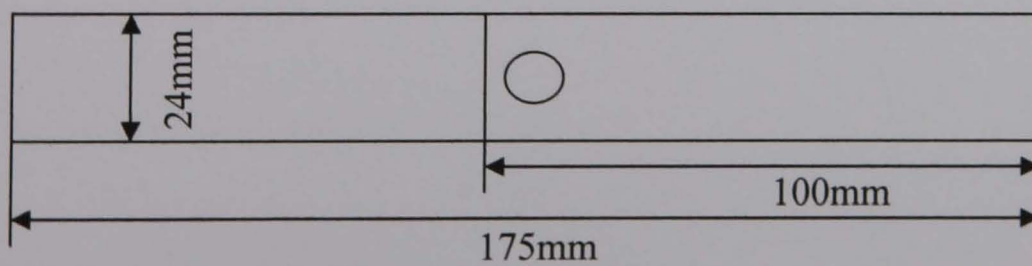


(b) Tensile specimen with different notch radius.

Figure 3.5 Tensile test of the base steels (the thickness for steel A and B is 1.44 mm and 0.8 mm, respectively).



(a)



(b)

Figure 3.6 Schematic showing the set-up of the tensile-shear test of spot welded joints.



Figure 3.7 Leitz micro hardness tester.

CHAPTER 4

**INVERSE FE MODELLING OF
INDENTATION TESTS WITH DIFFERENT
INDENTERS**

4.1 Introduction

In this chapter, the application of indentation with different indenter types to predict plastic material parameters has been investigated to develop a robust and accurate approach for practical applications. An inverse FE modelling program based on indentation test was developed, the use of single indenter and dual indenters have been comparatively studied and new methods with improved robustness and accuracy have been developed. The framework established would help to develop an approach for characterising complex material systems such as spot welded joints, which is detailed in the next chapter.

This chapter consists of three main parts. In the first section, finite element (FE) models of continuous indentation of three commonly used indenters (Vickers, Knoop and Spherical indenter) were developed. For each indenter type, the effect of some key modelling parameters (such as mesh density, frictional conditions, etc.) on the loading curves were investigated using parametric studies and the optimum modelling parameters were established. Some models were validated against published experimental data. The models were then used to map the effects of material properties on the loading curves using parametric studies in ABAQUS. In the second part, an inverse FE modelling program was developed. A simulation space covering a wide potential range of plastic material properties (i.e. yield strength and work hardening coefficients) for metals was constructed. The inverse program was then used to predict material properties which produce an indentation curve(s) matching the input experimental data. In the third part, the inverse program was evaluated using blind tests with numerical experimental data (numerical results with known material properties). The validity and accuracy of each approach with different types of indenters (Vickers, Knoop or spherical indenter) were assessed and a new approach based on dual indenters has been developed. The sensitivity of the estimated mechanical plastic properties to variations of the input parameters (e.g. potential perturbation of the load) was also investigated.

4.2 FE models of indentation tests and effect of testing and material parameters

FE models of different types of indenters (Vickers, Knoop and spherical) have been developed using ABAQUS. In an indentation process, the indenter is continuously pressed into the material of interest. This process was simulated by applying a displacement (h) and recording the reaction force (P), and the force-indentation depth data is designated as P - h curves.

In the models, the material was treated as an elasto-plastic material with a true stress–strain behaviour following the constitutive law (Eq. 4.1).

$$\sigma = \begin{cases} E\varepsilon, & \text{for } \sigma \leq \sigma_y \\ R\varepsilon^n, & \text{for } \sigma \geq \sigma_y \end{cases} \quad (\text{Eq. 4.1})$$

where ‘E’ is the Young’s modulus, ‘R’ is a strength coefficient, ‘n’ is the strain hardening exponent, ‘ σ_y ’ is the initial yield stress and ‘ ε_y ’ is the corresponding yield strain, such that

$$\sigma_y = E\varepsilon_y = R\varepsilon_y^n \quad (\text{Eq. 4.2})$$

Here the yield stress (σ_y) is defined at zero offset strain. So the true stress–true strain behaviour is rewritten to be (Swaddiwudhipong *et al*, 2005 b):

$$\sigma = \begin{cases} E\varepsilon, \\ \sigma_y \left(\frac{E}{\sigma_y} \right)^n \varepsilon^n \end{cases} \quad (\text{Eq. 4.3})$$

In these indentation FE models, the Young’s modulus ‘E’ of the work piece materials was set to 200 GPa and Poisson’s ratio was set to 0.3, which were commonly used values for steels (Chen *et al*, 2007).

4.2.1 FE modelling of the Vickers indentation

Figure 4.1(a) shows the FE model of the Vickers indentation. Only a quarter of the indenter and the material column was simulated as a result of plane symmetric geometry. The sample size is more than 10 times the maximum indentation depth, which is sufficiently large to avoid any sample size effect or boundary effect (Johnson, 1985). The bottom face of the material volume was fixed in all degrees of freedom (DOF) and the two side faces (A and B) were symmetrically fixed in z and x direction. The element type used is C3D8R (a reduced-integration element used in stress/displacement analysis). Contact was defined at the indenter facet, the material of interest was allowed to move and the contact between the indenter surface and the material was maintained at all the times. The mesh in the regions with large deformation such as that directly under the indenter tip was refined with high mesh density in order to obtain more accurate results (Figure 4.1 (b)).

The Vickers indenter has the form of a right pyramid with a square base and an angle of 136° between opposite faces. It is normally made of diamond with a Young's modulus of over 1000GPa, which is significantly stiffer than steel ($E=200\text{GPa}$). The indenter was considered as a rigid body to improve the modelling efficiency. A predefined displacement was applied in a ramp mode and the reaction force is recorded on a reference point, representing the overall load on the indenter. Figure 4.2 (a) shows a typical full numerical force indentation depth curve ($P-h$ curve) for a material with yield strength of 350 MPa and work hardening coefficient of 0.15. The loading curve represents the resistance of the material, while difference between the loading and unloading curve represents the energy loss (Swaddiwudhipong *et al*, 2005a). The unloading part of the $P-h$ curve is primarily influenced by E , as it is essentially an elastic process; while the loading part of the $P-h$ curve correlates with σ_y and n (Taljat, 1998). This work is focused on the studies of plastic parameters, so only the loading curve was utilised to predict the plastic material parameters.

Mesh size sensitivity tests and results

In FE modelling, the accuracy of the results is influenced by many factors such as the mesh density, frictional condition and validation of the boundary conditions. The most relevant factors for the simulation of indentation process are the mesh density and frictional conditions (Taljat, 1998). The meshes in the model were generated with pertinent symmetry consideration to reduce the domain size with different mesh density for different regions. The potential influence of all these factors on the accuracy of the modelling process needs to be investigated. This was assessed by varying the mesh size (i.e. density) in the FE models, and then comparing the $P-h$ curves. Figure 4.3 (a) shows the $P-h$ curves with different mesh densities (i.e. element numbers). It is clearly shown that models with coarser mesh (larger element size) have resulted in higher indentation forces and, eventually the results became insensitive to the mesh density. As shown in Figure 4.3 (b), the P_{max} at indentation depth of 0.015mm is almost the same as models of more than 7200 elements, which was set as the suitable mesh density. Tests on other material properties showed similar results.

Effects of frictional conditions

The friction condition at the indenter sample interface is an important factor. To investigate its effect on the $P-h$ curve of Vickers indentation, a series of FE models with different friction coefficients ($\mu=0-0.3$), which is commonly used for metal contact (Mata and Alcalá, 2004) have been developed. As shown in Figure 4.3 (c), there is a clear difference between $P-h$ curves with frictional and frictionless ($\mu=0$) conditions but the effect of friction coefficients ($\mu=0.1-0.3$) on the $P-h$ curves is not significant over the range of parameters studied. This agrees with some published result (Bucaille *et al*, 2003; Mata and Alcalá, 2004). A friction coefficient of 0.15 between metal and diamond was used in this work.

Validation of the FE model against published experimental data

The FE model of Vickers indentation test was verified by comparing the numerical results from this work with some published modelling and experimental results. Typical result is shown in Figure 4.4. The material properties in the FE model were

adapted from the data used by Dao *et al* (2001), and then the predicted $P-h$ curves were compared to the published numerical and experimental data. As shown in the curves, for both materials, the predicted results agree well with the experimental data. This suggests that the models are accurate and valid.

Effect of material properties and curvature of the $P-h$ curves

Figure 4.5 illustrates the effect of material properties on the $P-h$ curves with E set at 200 GPa for steel. It is clearly shown that both the yield stress and work hardening coefficient influence the indentation curves. According to Kick's law, the loading indentation curve of an elasto-plastic material generally follows a power law formation (Eq. 4.4) (Swaddiwudhipong *et al*, 2005a),

$$P = Ch^2 \quad (\text{Eq. 4.4})$$

where P and h are the load and indentation depth on the loading curve, respectively. C is a curvature coefficient, which is a function of the yield stress and the work hardening coefficient. The effect of material parameters on the curvature was systematically studied using ABAQUS parametric study, in which the yield stress and work hardening coefficients were varied over a wide range. Variations of the curvature (C_V) with respect to σ_y and n for Vickers indenter were illustrated by the surface shown in Figure 4.5 (c). The data for construction of these surfaces were obtained numerically through indentation finite element analysis encompassing a domain of σ_y from 100 to 1000 MPa and n varying from 0.01 to 0.5. It clearly showed that the curvature coefficients increased with σ_y and n but with different gradients for different regions.

4.2.2 FE modelling of the Knoop indentation

The Knoop indentation can be used on almost all ceramics, metallic materials and plastics. The indenter is a diamond ground to the pyramidal form, which produces a diamond shaped indentation with a ratio between long and short diagonals of approximately 7:1. The FE model of Knoop indentation is shown in Figure 4.6.

Similar to the Vickers indentation model, only a quarter of the indenter and the material column needs to be simulated as a result of symmetric considerations of the Knoop indenter. The bottom faces of material volumes were fixed in all degrees of freedom (DOF) and the two side faces (A and B) were symmetrically fixed in z and x directions. The sample size is more than 10 times the maximum indentation depth, which is sufficiently large to avoid any sample size effect. The element type used was C3D8R (a reduced-integration element used in stress/displacement analysis). Contact has been defined at the indenter sample interface with finer meshed regions underneath and around the indenter to increase the accuracy of the model.

The pyramidal form of a Knoop indenter is different from the Vickers indenter, the angle opposite to the long diagonal is 172.5° and the angle opposite to the short diagonal is 130° . When Knoop hardness is measured, only the longest diagonal of the indentation is used. Similar to the Vickers indenter, the Knoop indenter was considered as a rigid body in the model. A predefined displacement was applied to the indenter in a ramp mode and the reaction force is recorded using a reference point representing the overall load on the indenter. Figure 4.7 shows a typical full numerical force indentation depth curves ($P-h$ curve) including both the loading and unloading curves for a material with yield stress of 350 MPa and work hardening coefficient of 0.15. The overall curve is very similar to the Vickers indentation but the force for a given depth is much higher due to a larger contact area.

Mesh size sensitivity tests and results

Sensitivity tests on mesh size have been systemically performed by comparing results from models with different mesh densities. Figure 4.8 (a) and (b) show the $P-h$ curves and the maximum force at an indentation depth of 0.015mm from models with different mesh densities represented by the total element numbers. It is clearly shown that, at lower density level, the curves are significantly different with higher forces, but eventually the results become less sensitive to the mesh density. When the model consists of more than 8000 elements, the $P-h$ curves become identical and P_{max} is almost constant. This mesh density was selected as the suitable one giving an accurate result with an optimum requirement on computational resources. Tests on other material properties showed a similar trend.

Effects of frictional conditions

To investigate the effects of frictional condition on the $P-h$ curve of the indentation test, a series of FE models with different friction coefficients ($\mu=0-0.3$) have been developed. As shown in Figure 4.9, there is obvious difference between $P-h$ curves of frictional and frictionless ($\mu=0$) conditions but the effect of different friction coefficients ($\mu=0.1-0.3$) on the $P-h$ curves is not significant over the range of parameters studied. This agrees with some published result (Bucaille *et al*, 2003; Mata and Alcalá, 2004). A friction coefficient of 0.15 between metal and diamond was used in this work.

Effect of material properties and curvature of the $P-h$ curves

Figure 4.10 (a) and (b) illustrate the effect of plastic material properties on the $P-h$ curves of the Knoop indentation. It clearly shows that both the yield stress and work hardening coefficient influence the results. Similar to the approach used for the Vickers indentation, the $P-h$ curve of the Knoop indentation can be described by the curvature (Eq. 4.4) of the $P-h$ curves (designated C_K). Variation of C_K with respect to σ_y and n over a wide range of materials is illustrated by the surface plot shown Figure 4.10 (c). The data for construction of these surfaces were obtained numerically through indentation finite element analysis encompassing a domain of σ_y from 100 to 1000 MPa and n varying from 0.01 to 0.5. It clearly showed that the curvature coefficients increased with σ_y and n but with different gradients for different regions.

4.2.3 FE modelling of the spherical indentation

Different from the Vickers and Knoop indenters, spherical indenter is fully axisymmetric, a typical FE model is shown in Figure 4.11. A planar specimen ($3 \times 3 \text{ mm}^2$) has been used and this specimen size is large enough to avoid potential sample size effect. The movement of the indenter was simulated by displacing a rigid arc (rigid body) along the Z axis. The bottom line was fixed in all degrees of freedoms (DOF) and the central line was symmetrically constrained. The element types used in

the spherical indentation model are CAX4R and CAX3 (4-node bilinear axisymmetric quadrilateral and 3-node linear axisymmetric triangle element used in stress/displacement analyses without twist). A gradient meshing scheme has been developed for different regions. The mesh size is $5\mu\text{m}$ in the regions underneath and around the indenter, while the mesh sizes of other regions from the nearest region to the outer edge varied from $10\mu\text{m}$, 0.05mm and 0.1mm ; the mesh of the transitional regions is mainly triangle elements following a free meshing scheme. Figure 4.12 shows a typical numerical force indentation depth curve (loading and unloading curves) of a spherical indenter ($R=0.5\text{mm}$). The curve is significantly different from Vickers and Knoop indentations with much higher forces due to the larger contact area in a spherical indentation.

Similar to the Vickers and Knoop indentations, the results were sensitive to the mesh density. Mesh size effect was assessed by varying the mesh density and the results are shown in Figure 4.13 (a) and (b). At lower mesh density level, the curves are significantly different and the forces are considerably lower, but eventually the result becomes less sensitive to the mesh density. When the total element number is over 5037, the $P-h$ curves became identical and P_{max} became constant. This mesh scheme with 5037 elements was selected as the suitable mesh density. Tests on other material properties showed similar trend.

Figure 4.13 (c) shows the $P-h$ curves of the spherical model with the friction coefficient varied from 0-0.3. Similar to the results of Vicker and Knoop indentation, there is a clear difference between frictional and frictionless condition but the effect of different friction coefficients on the $P-h$ curves is not significant over the range of parameters studied. Similar results have been observed for indenter of other sizes. A coefficient of 0.15 was selected for all the models to be consistent with the Vickers and Knoop indentation models.

Verification of spherical indentation model against published experimental data and effect of material properties

The FE models of spherical indentation tests were verified using published experimental data (Kucharski and Mroz, 2001). A FE model of a spherical indenter

with a radius of 1.25mm was developed with the reported material properties. As shown in Figure 4.14, the numerical results showed good agreement with the experimental data, which suggests that the FE model is valid and the results are accurate. Figure 4.15 (a) shows the results with σ_y change from 100 to 500 MPa and a fixed n (0.16), while in figure 4.15 (b), n varied from 0.01 to 0.3 and σ_y is fixed at 600 MPa. It clearly shows that both yield stress and work hardening coefficient significantly affect the results.

4.3 Inverse FE modelling based on continuous indentation tests

In an inverse FE modelling approach based on indentation tests, the load-indentation depth data of the material is used as input data to a finite element (FE) model that mimics the geometry and boundary conditions of the experiment. This approach has been used on some non-standard specimen or surface loading situation, such as *in vivo* tension, indentation (Meuwissen *et al*, 1998; Gu *et al*, 2003; Ren *et al*, 2003; Shan and Gokhale, 2003; Bolzon *et al*, 2004; Ren *et al*, 2004). The local plastic properties can be calculated by solving the inverse problem *via* finite element analysis to find a similar simulated load–displacement curve as compared with experimental data. A range of approaches and indenter types have been explored (Shan and Gokhale, 2003; Gu *et al*, 2003; Bolzon *et al*, 2004), however, the uniqueness and accuracy of each approach is not well established. In many cases, the final results depend on the pre-knowledge of the materials. This made it difficult to apply this technique in practical situations.

This section presents a systematic and comparative study using different indenter types aiming to develop a robust and non-initial value dependent approach. Two main approaches have been studied to predict the plastic material parameters from indentation tests. The first one is to use one type of indentation test only (designated single indenter method). This approach has been used by many researchers but the accuracy and validity was not well established. In many cases, it depends on the pre-knowledge about the material (Cheng and Cheng, 1999a; Giannakopoulos and Suresh, 1999; Dao *et al*, 2001; Bucaille *et al*, 2003). The other new approaches explored the use of two different types of indenters (designated dual indenters method). One hypothesis to be tested is that, by using indenters of different dimensions and sizes, material behavior at different strain-stress conditions could be produced and this would potentially help to predict multiple material parameters.

4.3.1 Inverse analysis based on single indenter method

Figure 4.16 is a flow chart showing the inverse FE modelling process based on the single indenter method. The program consists of three main parts — experimental data, FE modelling data/simulation space and an inverse program based on an objective function comparing the numerical and experimental input data. The simulation space included a group of $P-h$ curves from numerical models covering a wide range of material properties. In the searching process, the program calculates the difference between the input data and simulated $P-h$ data of different sets of material properties within the simulation space. In each case the optimum material parameters, which produces the $P-h$ curves best matching the experimental results, were determined by mapping the the objective function (Eq. 4.5) (Bolzon *et al*, 2004).

$$G = \sum_{i=1}^n \left(\frac{F_{i,e} - F_{i,n}}{F_{i,e}} \right)^2 \quad (\text{Eq. 4.5})$$

where :

- G is the objective function that needs to be minimised.
- $F_{i,e}$ is the experimental force of the indenter at the observation i and $F_{i,n}$ is the numerical model force of the indenter at the observation i .
- The number of observation (*indentation depth*) is n .

The simulation space was developed using parametric studies in ABAQUS. Parametric studies allow the user to generate, execute, and gather the results of multiple analyses that differ only in the values of some of the input parameters, such as material parameters or dimensional parameters. In this case, the two variables are the yield stress and the work hardening coefficient. As shown in Figure 4.17, in the initial stage, multiple FE models with different combinations of the material parameters were automatically generated and solved. In the parametric studies, the yield stress was varied from 100 to 900 with an increment of 10. The strain hardening coefficients used were from 0.01 to 0.3 with an increment of 0.01. The numerical results were then recorded and stored into a database to form a simulation space. The simulation space was structured in an excel program, which allows easy interpretation.

In the searching process, the input data was transformed into a discrete form with evenly spaced points against the indentation depth (termed indentation points). At each indentation point, the objective function values are calculated using a predefined program in Microsoft excel for each set of material properties (σ_y , n). The overall objective function was determined by the sum over the whole curve. The material data which give minimum objective function value was defined as the optimum solution.

The inverse program was evaluated using blind tests with numerical experimental data (numerical results with known material properties). This is a commonly used approach in developing inverse programs (Delalleau *et al*, 2006). It allows the uniqueness, accuracy and sensitivity of these inverse FE methods to be systemically investigated. The results when using Vickers, Knoop and spherical indenters were presented in the section 4.3.1.1-3.

4.3.1.1 Inverse FE modelling based on the Vickers indentation

Figure 4.18 shows a typical process to extract plastic material properties based on the Vickers indentation. Figure 4.18(a) is a typical numerical $P-h$ curve with known material properties ($\sigma_y=350$ and $n=0.155$) used as numerical experimental data in the blind test. The input data was transformed into a discrete form with evenly spaced points against the indentation depth (termed indentation points). In this work the input numerical experiment curve was divided into 100 points. For each indentation depth, there is a corresponding simulation space (force) over a potential range of material properties. Two typical simulation spaces are shown in Figure 4.18 (b) at indentation depths of 0.005mm and 0.009mm, which represent the resistance of the material to indentation at the specific depth.

At each indentation point, the objective function value is calculated using predefined program in Microsoft excel for each set of material properties (σ_y , n), then the sum of the objective function integrated over the whole indentation curve was determined. Figure 4.18 (c) shows the surface plot of objective functions *vs.* the two material parameters. The minimum point ($\sigma_y=320$, $n=0.18$) at the bottom of the valley of the surface is highlighted with an arrow. The surface showed that many sets of material

properties were found to have very close objective function values at the valley. Figure 4.18 (d) plots the material points with objective function values close to the minimum point. The material data with $G \leq 0.01$ gives an error within 1% between the numerical $P-h$ curve and the input data. All the data with lower objective functions lie approximately on a straight line. The true stress-strain curves based on these data are plotted in Figure 4.18 (e) showing significantly different true stress-strain relationships. Multiple FE models have been developed with these material properties and the $P-h$ curves are compared with the input numerical experiment data. As shown in Figure 4.18 (f), these $P-h$ curves agree very well with the numerical experimental data. This suggests that these materials have different stress-strain curves but identical $P-h$ curves, in other words, the plastic material property could not be determined uniquely using Vickers indentation only.

Several input data have been used to represent a wide range of materials and some typical predicted material data are shown in Figure 4.19. In each case, there are multiple sets of material properties of different stress-strain relationships that could produce $P-h$ curves matching the input data. As shown in Figure 4.19, all the data approximately fall on a straight line. This suggests the material can not be uniquely predicted using single indenter method based on Vickers indentation unless a pre-knowledge of the material being studied was known. This agrees with some published results (Cheng and Cheng, 1999a; Bucaille *et al*, 2003; Swaddiwudhipong *et al*, 2005a).

4.3.1.2 Inverse FE modelling based on the Knoop indentation

Figure 4.20 shows a typical process to extract material properties based on the Knoop indentation. Figure 4.20(a) shows a typical numerical $P-h$ curve of known material properties used as numerical experimental data in the blind test. The input data was transformed into a discrete form with evenly spaced points against the indentation depth. In this case, the input numerical experiment data was divided into 100 points. For each indentation depth, there is a corresponding simulation space (force) over a potential range of material properties (i.e. σ_y, n). Two typical simulation spaces are shown in Figure 20 (b) for the indentation depth of 0.005mm and 0.009mm. These

surfaces represent the resistance of the material to indentation at the specific depth under a Knoop indenter.

At each indentation point, the objective function value is calculated using predefined program in Microsoft excel for each set of material properties (σ_y , n), then the sum of the objective functions integrated over the whole indentation curve was determined. The objective function values G (Eq. 4.5) for each material property set (σ_y , n) over the simulation space was calculated and plotted in Figure 4.20 (c). As marked on the surface, the material set with the lowest objective function is $\sigma_y=430$, $n=0.09$. Similar to the Vickers results, there are many sets of material properties at the valley of the surface with similar objective function values. Figure 4.20 (d) plots typical material sets with objective function values close to the minimum point. The material data with $G \leq 0.01$ represents an error within 1% between the predicted and input $P-h$ curves. Curve fitting showed that the data can be approximated as a straight line. The true stress-strain curves and $P-h$ curves of these data are plotted in Figure 4.20 (e) and (f). It clearly shows that these materials have significantly different stress-strain curves, but have a similar $P-h$ curve. This suggests that the plastic material property could not be determined uniquely based on the Knoop indentation.

Several input data have been used representing a wide range of materials. Some typical predicted material data are shown in Figure 4.21. In each case, there are multiple sets of material properties of different stress-strain relationships that could produce $P-h$ curves matching the input data. All the data approximately fall on a straight line. This suggests the plastic material property could not be determined uniquely based on the Knoop indentation.

4.3.1.3 Inverse FE Modelling based on the spherical indentation

Figure 4.22 shows the typical process to extract material properties using a spherical indenter of radius 0.5 mm. The input numerical experimental data (Figure 4.22(a)) was extracted from FE model with a material property of $\sigma_y=350$, $n=0.155$. The $P-h$ curve is significantly different from the Knoop and Vickers indentation, the force is much higher for the same indentation depth. The input data was transformed into a

discrete form with evenly spaced points against the indentation depth (termed indentation points). In this case, the input numerical experiment data was divided into 100 points. For each indentation depth, there is a corresponding simulation space (force) over a potential range of material properties (i.e. σ_y , n). Two typical simulation spaces are shown in Figure 4.22 (b) for indentation depths of 0.005mm and 0.009mm. These surfaces represent the resistance of the material to indentation at these specific depths.

The objective function values G (Eq. 4.5) for each material set (σ_y , n) within the simulation space was calculated, which represents the match between the indentation curve and the input data. Figure 4.22 (c) shows the surface plot of the objective function vs. the power-law material parameters. The material set with the lowest objective function is marked on the surface plot. There are several sets of material properties over a large range having very close objective function values at the valley. Figure 4.22 (d) plots typical material property sets with objective function values close to the minimum value point. Curve fitting showed that all the data with $G \leq 0.01$ are roughly located on a straight line, however, the range is much narrower than that for Vickers and Knoop indentations. The true stress strain curves and $P-h$ curves based on these data are plotted in Figure 4.22 (e) and (f). It is clearly shown that the stress-strain curves are significantly different but all these $P-h$ curves agree very well with the numerical experimental data. This suggests that the plastic material property could not be determined uniquely using spherical indenter only.

Several initial material properties have been used to assess the program over a wide range of material properties. Figure 4.23 (a) plots the predicted material properties for some typical materials. In each case, there are multiple material properties over a wide range which can produce $P-h$ curves matching the initial input data. The inverse analysis based on different spherical indenters size (R0.25mm and R1mm) were systemically studied, following the steps used in previous indentations, and all results show inverse analyses based on single spherical indentation can not produce a unique result. This suggests that the plastic material property could not be determined uniquely using spherical indenter over the indentation depth in this work.

4.3.2 Inverse analysis based on dual indenters method

Figure 4.24 shows the flow chart for the dual indenters method to predict the plastic material properties. In this case, two experimental data with different indenter types (or sizes in the case of spherical indenters) were used. The input curves were compared to the curves in the simulation space for each indenter. The objective function was defined as

$$G_s = \sum_{i=1}^n \left(\frac{F_{i,e} - F_{i,n}}{F_{i,e}} \right)^2_{\text{Indenter1}} + \sum_{i=1}^n \left(\frac{F_{i,e} - F_{i,n}}{F_{i,e}} \right)^2_{\text{Indenter2}} \quad (\text{Eq. 4.6})$$

where :

- G_s is the sum of objective function results with two indentation models, which need to be minimised.
- $F_{i,e}$ is the experimental force of the indenter at the observation i and $F_{i,n}$ is the numerical model force of the indenter at the observation i .
- The number of observation (*indentation depth*) is n .

Four approaches have been investigated including combination of Vickers and Knoop (V+K), spherical and spherical (S+S), Vickers and spherical (V+S) and Knoop and spherical (K+S). The inverse FE program was evaluated using blind tests with numerical experimental data of known material properties. The sensitivity of the estimated plastic properties to variations in the input parameter (e.g. perturbation in the applied forces) was investigated.

4.3.2.1 Inverse FE modelling based on Vickers and Knoop indentations

Figure 4.25 (a) shows typical input numerical experimental data of the Vickers and Knoop indentation with a known material property set ($\sigma_y=350$, $n=0.155$). The input data was transformed into a discrete form with evenly spaced points against the indentation depth. In this case, each input numerical experimental data was divided into 100 points. For each indentation depth, there is a corresponding simulation space (force) over a potential range of material properties (i.e. σ_y , n). Figure 4.25 (b) shows typical simulation spaces for the two indenters at depths of 0.005mm and 0.009mm. The calculated objective function following Eq. 4.6 over a wide range of material

parameters are plotted in Figure 4.25(c). As shown in the Figure 4.25 (c), there are many sets of material properties with objective function values close to the minimum G point at the valley. Figure 4.25 (d) shows typical material sets with lower objective functions. It clearly shows that there are several material sets with objective functions close to the minimum point within 0.02 (error $\leq 1\%$). Curve fitting showed that all the data are approximately on a straight line. Figure 4.25 (e) and (f) plots the true stress strain curves and $P-h$ curves based on these data in comparison to the input curves. Similar to the results for single of the Vickers and Knoop indenters, these stress-strain curves are significantly different but all $P-h$ curves closely match the numerical experimental data.

Several input data have been used representing a wide range of materials. Typical results are shown in Figure 4.26. In each case there are multiple material data sets matching the input data, which fall on a straight line. This suggests that the combination of Vickers and Knoop could not predict unique material properties.

4.3.2.2 Inverse FE modelling based on dual spherical indentations

In this work, spherical indenters with different radius were used. Figure 4.27 shows the input numerical experimental data of two indenters ($R=0.5\text{mm}$ and $R=1.0\text{ mm}$) with a known material property set ($\sigma_y=350$, $n=0.155$). The input data was transformed into a discrete form with evenly spaced points against the indentation depth. In this case, each input numerical experiment data was divided into 100 points. For each indentation point, there is a corresponding simulation space over a potential range of material properties (i.e. σ_y , n). Figure 4.27 (b) shows the typical simulation spaces for the two indenters at depths of 0.005mm and 0.009mm. The objective functions as a function of the yield stress and work hardening coefficients are plotted in Figure 4.27(c). The surface is much smoother than that of the V+K method and there are limited material properties with objective function close to the minimum point ($\sigma_y=360$, $n=0.15$). Figure 4.27 (d) plots typical material sets with lower objective function values at the valley of the surface. There are several material sets that have G values lower than 0.02 (within 1% error) close to the minimum G point. However, the ranges of both parameters are much narrower than the results for the single and V+K

indentation. The true stress-strain curves are plotted in Figure 4.27(e) and $P-h$ curves based on these data were plotted in Figure 4.27(f) together with the input curves. It clearly shows that the true stress-strain curves are different but the $P-h$ curves using the predicted material properties agreed very well with the numerical experimental data.

Several data with different combinations of material properties (σ_y and n) have been used as input data to assess the accuracy of the approach. Typical results are listed in Table 4.1 and shown in Figure 4.28. In each case, there were multiple material data matching the input data and these data approximately fall on a straight line. However, these material set points fell on a narrower range than the single and V+K methods discussed before, and almost symmetrical about the minimum G point. The accuracy achieved is significantly higher than the single and V+K method. This suggests that the dual spherical indenters could be used to predict stress-strain curves.

Table 4.1 Typical predicted results by inverse FE modelling based on dual spherical (SR05 and SR1) indentations.

| Initial value | | Predicted value | | Up limit | | Low limit | |
|---------------|-------|-----------------|------|------------|------|------------|------|
| σ_y | n | σ_y | n | σ_y | n | σ_y | n |
| 180 | 0.13 | 180 | 0.13 | 170 | 0.15 | 190 | 0.11 |
| 200 | 0.05 | 200 | 0.05 | 190 | 0.07 | 210 | 0.03 |
| 200 | 0.1 | 200 | 0.1 | 190 | 0.12 | 210 | 0.08 |
| 200 | 0.15 | 200 | 0.15 | 190 | 0.17 | 210 | 0.13 |
| 200 | 0.2 | 200 | 0.2 | 190 | 0.22 | 210 | 0.18 |
| 200 | 0.25 | 200 | 0.25 | 190 | 0.27 | 210 | 0.23 |
| 350 | 0.055 | 360 | 0.05 | 320 | 0.1 | 380 | 0.01 |
| 350 | 0.155 | 340 | 0.17 | 310 | 0.21 | 390 | 0.1 |
| 350 | 0.255 | 360 | 0.25 | 320 | 0.29 | 320 | 0.22 |
| 400 | 0.05 | 400 | 0.05 | 380 | 0.07 | 420 | 0.02 |
| 400 | 0.1 | 400 | 0.1 | 380 | 0.12 | 420 | 0.07 |
| 400 | 0.15 | 400 | 0.15 | 380 | 0.17 | 420 | 0.12 |
| 400 | 0.2 | 400 | 0.2 | 380 | 0.22 | 420 | 0.17 |
| 400 | 0.25 | 400 | 0.25 | 380 | 0.27 | 420 | 0.22 |
| 500 | 0.1 | 500 | 0.1 | 480 | 0.12 | 520 | 0.08 |
| 500 | 0.2 | 500 | 0.2 | 480 | 0.22 | 520 | 0.18 |
| 600 | 0.05 | 600 | 0.05 | 560 | 0.09 | 640 | 0.01 |
| 600 | 0.1 | 600 | 0.1 | 560 | 0.14 | 640 | 0.06 |
| 600 | 0.15 | 600 | 0.15 | 560 | 0.19 | 640 | 0.11 |
| 600 | 0.2 | 600 | 0.2 | 560 | 0.24 | 640 | 0.16 |
| 600 | 0.25 | 600 | 0.25 | 560 | 0.29 | 640 | 0.21 |
| 800 | 0.15 | 800 | 0.15 | 730 | 0.21 | 860 | 0.1 |

| | | | | | | |
|-----|-------|-----|------|-----|------|--|
| 880 | 0.155 | 860 | 0.17 | 760 | 0.25 | |
|-----|-------|-----|------|-----|------|--|

4.3.2.3 Inverse FE modelling based on the Vickers and spherical indentations

The inverse modelling process when using a Vickers and a spherical curve is shown in Figure 4.29. Due to different geometry, the force of the spherical indenter is significantly higher than that of the Vickers indenter (Figure 4.29 (a)). For the same indentation depth, the input data was transformed into a discrete form to form data with evenly spaced points against the indentation depth. In this case, each input numerical experimental data was divided into 100 points. For each indentation point, there is a corresponding simulation space over a potential range of material properties (σ_y , n). Figure 29 (b) shows typical simulation spaces for the two indenters at depths of 0.005mm and 0.009mm. The objective function values as a function of the yield stress and work hardening coefficients are plotted in Figure 4.29 (c). Figure 4.29 (d) plots typical material sets with lower objective functions at the valley. It clearly shows that there is a narrow region around the minimum objective function point. The true stress-strain curves using the predicted parameters are plotted in Figure 4.29 (e), these stress-strain curves are identical. Figure 4.29 (f) compared the $P-h$ curves of these material property sets with the input data ($\sigma_y=350$, $n=0.155$). The $P-h$ curves using the predicted material properties agree very well with the input numerical experimental data. The result suggests that the V+S approach could predict material properties over a narrow range with comparable stress-strain curves.

Several data with different combination of material properties (σ_y and n) have been used as input data to assess the accuracy of the approach. Typical results are listed in Table 4.2 and shown in Figure 4.30. In each case, there are only a few material data sets that match the input data focused on a small region. The accuracy achieved is significantly better than the other methods. This suggests the combination of Vickers and spherical indentations could produce unique stress-strain curves. The accuracy achieved is significantly better than some of the reported programs in the literature (Giannakopoulos and Suresh 1999; Dao *et al*, 2001; Bucaille *et al*, 2003).

Table 4.2 Typical predicted results by inverse FE modelling based on the Vickers and spherical indentations.

| Initial value | | Predicted value | | Up limit | | Low limit | |
|---------------|-------|-----------------|------|------------|------|------------|------|
| σ_y | n | σ_y | n | σ_y | n | σ_y | n |
| 180 | 0.13 | 180 | 0.13 | 180 | 0.13 | 180 | 0.13 |
| 200 | 0.05 | 200 | 0.05 | 200 | 0.05 | 200 | 0.05 |
| 200 | 0.1 | 200 | 0.1 | 200 | 0.1 | 200 | 0.1 |
| 200 | 0.15 | 200 | 0.15 | 200 | 0.15 | 200 | 0.15 |
| 200 | 0.2 | 200 | 0.2 | 200 | 0.2 | 200 | 0.2 |
| 200 | 0.25 | 200 | 0.25 | 200 | 0.25 | 200 | 0.25 |
| 350 | 0.055 | 350 | 0.05 | 350 | 0.06 | 360 | 0.05 |
| 350 | 0.155 | 360 | 0.15 | 350 | 0.15 | 360 | 0.15 |
| 350 | 0.255 | 360 | 0.25 | 340 | 0.26 | 360 | 0.25 |
| 400 | 0.05 | 400 | 0.05 | 390 | 0.06 | 410 | 0.04 |
| 400 | 0.1 | 400 | 0.1 | 390 | 0.11 | 410 | 0.09 |
| 400 | 0.15 | 400 | 0.15 | 390 | 0.16 | 410 | 0.14 |
| 400 | 0.2 | 400 | 0.2 | 390 | 0.21 | 410 | 0.17 |
| 400 | 0.25 | 400 | 0.25 | 380 | 0.27 | 410 | 0.24 |
| 500 | 0.1 | 500 | 0.1 | 490 | 0.11 | 510 | 0.09 |
| 500 | 0.2 | 500 | 0.2 | 490 | 0.21 | 510 | 0.19 |
| 600 | 0.05 | 600 | 0.05 | 580 | 0.06 | 620 | 0.04 |
| 600 | 0.1 | 600 | 0.1 | 580 | 0.11 | 620 | 0.09 |
| 600 | 0.15 | 600 | 0.15 | 580 | 0.16 | 620 | 0.14 |
| 600 | 0.2 | 600 | 0.2 | 580 | 0.21 | 630 | 0.18 |
| 600 | 0.25 | 600 | 0.25 | 580 | 0.26 | 620 | 0.24 |
| 800 | 0.15 | 800 | 0.15 | 780 | 0.16 | 820 | 0.14 |
| 880 | 0.155 | 890 | 0.15 | 850 | 0.17 | | |
| 880 | 0.255 | 890 | 0.25 | 850 | 0.27 | | |

4.3.2.4 Inverse FE modelling based on the Knoop and spherical indentations

A typical inverse modelling process when using Knoop and spherical (K+S) indentations is shown in Figure 4.31. Due to the different geometry, for the same indentation depth, the force is significantly higher for the spherical indenter (Figure 4.31 (a)). As shown in Figure 4.31 (b), both input numerical experimental data were divided into 100 points and objective functions were calculated. Figure 4.31 (c) plots the surface of objective function over the material domain and Figure 4.31 (d) plots typical material sets with lower objective function values at the valley. It clearly shows that there are limited numbers of material properties over a narrow region with G lower than 0.02 close to the minimum point. The true stress-strain curves using these parameters are plotted in Figure 4.31 (e) and Figure 4.31 (d) compared the $P-h$ curves of these materials to the input numerical experimental data. It shows that the

stress-strain curves of these materials are comparable. RMS analysis showed that the $P-h$ curves agree very well with the input data. This suggests that the K+S approach could predict material properties with comparable stress-strain curves.

Several data with different combinations of material properties (σ_y and n) have been used as input data. Typical results are listed in Table 4.3 and shown in Figure 4.32. In each case, there are a few material data sets over a small region matching the input data. This suggests the combination of Knoop and spherical indenters could produce unique results. The accuracy achieved is significantly better than some of the reported programs in the literature review (Giannakopoulos and Suresh 1999; Dao *et al*, 2001; Bucaille *et al*, 2003).

Table 4.3 Typical predicted results by inverse FE modelling based on the Knoop and spherical indentations.

| Initial value | | Predicted value | | Up limit | | Low limit | |
|---------------|-------|-----------------|------|------------|------|------------|------|
| σ_y | n | σ_y | n | σ_y | n | σ_y | n |
| 180 | 0.13 | 180 | 0.13 | 180 | 0.13 | 180 | 0.13 |
| 200 | 0.05 | 200 | 0.05 | 200 | 0.05 | 200 | 0.05 |
| 200 | 0.1 | 200 | 0.1 | 200 | 0.1 | 200 | 0.1 |
| 200 | 0.15 | 200 | 0.15 | 200 | 0.15 | 200 | 0.15 |
| 200 | 0.2 | 200 | 0.2 | 200 | 0.2 | 200 | 0.2 |
| 200 | 0.25 | 200 | 0.25 | 200 | 0.25 | 200 | 0.25 |
| 350 | 0.055 | 360 | 0.04 | 350 | 0.06 | 360 | 0.04 |
| 350 | 0.155 | 360 | 0.15 | 350 | 0.15 | 370 | 0.14 |
| 350 | 0.255 | 360 | 0.25 | 340 | 0.26 | 360 | 0.25 |
| 400 | 0.05 | 400 | 0.05 | 390 | 0.06 | 410 | 0.04 |
| 400 | 0.1 | 400 | 0.1 | 390 | 0.11 | 410 | 0.09 |
| 400 | 0.15 | 400 | 0.15 | 390 | 0.16 | 410 | 0.14 |
| 400 | 0.2 | 400 | 0.2 | 390 | 0.21 | 410 | 0.17 |
| 400 | 0.25 | 400 | 0.25 | 380 | 0.27 | 410 | 0.24 |
| 500 | 0.1 | 500 | 0.1 | 490 | 0.11 | 510 | 0.09 |
| 500 | 0.2 | 500 | 0.2 | 490 | 0.21 | 510 | 0.19 |
| 600 | 0.05 | 600 | 0.05 | 580 | 0.06 | 620 | 0.04 |
| 600 | 0.1 | 600 | 0.1 | 580 | 0.11 | 620 | 0.09 |
| 600 | 0.15 | 600 | 0.15 | 580 | 0.16 | 630 | 0.13 |
| 600 | 0.2 | 600 | 0.2 | 580 | 0.21 | 620 | 0.17 |
| 600 | 0.25 | 600 | 0.25 | 580 | 0.26 | 620 | 0.24 |
| 800 | 0.15 | 800 | 0.15 | 780 | 0.16 | 820 | 0.14 |
| 880 | 0.155 | 890 | 0.15 | 850 | 0.17 | | |
| 880 | 0.255 | 890 | 0.25 | 850 | 0.27 | | |

4.4 Sensitivity analysis and results

Sensitivity of the predicted material properties due to variations of the input parameters is essentially an intrinsic characteristic of the problem, which has been a major difficulty in using inverse or reverse method (Venkatesh *et al*, 2000; Dao *et al*, 2001). In this work the input data were taken from the numerical models. However, in a real testing situation, there can be potentially both system and random errors. Factors such as error in the indenter angle, roundness of the tip, and accuracy of the recorded indentation force or depth all influence the measurement results (Dao *et al*, 2001).

From the results shown in Section 4.2 and 4.3, three dual indentation combinations can predict accurate stress-strain curves — spherical and spherical (S+S), Vickers and spherical (V+S), Knoop and spherical (K+S). Therefore, the sensitivity of the estimated plastic properties to variations in the input parameters was investigated in these three cases. This is conducted by adding a systematic percentage error to the input data.

Figure 4.33 shows the sensitivity of estimated plastic properties to the perturbation in the indentation force for three dual indentation approaches (V+S, K+S, S+S) with an original plastic property of $\sigma_y = 350$ and $n = 0.055$. The result showed that the yield strength of low strain-hardening coefficient materials can be predicted within 20MPa variation if the $P-h$ response can be measured with 5% error. The work hardening coefficient of these materials can be determined using the existing inverse FE modelling within 0.015 if the $P-h$ response can be measured with 5% error. These results show the combinations of sharp and spherical indentations have better accuracy and sensitivity. The V+S and K+S methods have similar performance in the accuracy and sensitivity investigation. They are better than that of inverse analysis by the spherical and spherical indentations.

Several initial materials have been used to investigate the accuracy and sensitivity with respect to the material parameters (σ_y and n) of inverse FE modelling by Vickers and spherical indentations. The predicted results and sensitivity respecting to 3%

perturbation in the indentation force of indentation are listed in Table 4.4. The smaller scatter in the predicted σ_y and n reflects the higher accuracy and the greater scatter in the sensitivity results reflects the stronger sensitivity with respect to σ_y and n . The scatters of σ_y of all 9 materials are within 10MPa and the scatters of n are within 0.005. The percentage scatters of σ_y ($\Delta\sigma_y/\sigma_y$) of all 9 materials with respect to the 3% perturbation of P (indentation force) are from 2.78% to 6.25%. The percentage scatters of n ($\Delta n/n$) of all 9 materials with respect to the 3% perturbation of P (indentation force) are from 2.0% to 11.0% and the smaller n value in the initial material properties in Table 4.4 has bigger percentage scatters which mean the stronger sensitivity with respect to perturbation of P . This suggests that the yield strength of strain-hardening materials can be extracted using the existing inverse FE modelling within 6.25% error if the $P-h$ response can be measured within accuracy greater than 97%. The work hardening coefficient of these materials can be determined using the existing inverse FE modelling within 11.11% error if the $P-h$ response can be measured with accuracies greater than 97%.

Table 4.4 Accuracy and sensitivity study results of inverse FE modelling (V+S).

| | | | Accuracy study | | | | | | Sensitivity study (with 3% error of P) | | | |
|------------|-------|--------------|------------------|------|------------------------------|------------|------------------------------|--------------|---|------------|------------------------------|--------------|
| Input | | | Predicted values | | Differences with input value | | Accuracy (error%) | | Differences with input value | | Sensitivity (error%) | |
| σ_y | n | E/σ_y | σ_y | n | $\Delta \sigma_y$ | Δn | $\Delta \sigma_y / \sigma_y$ | $\Delta n/n$ | $\Delta \sigma_y$ | Δn | $\Delta \sigma_y / \sigma_y$ | $\Delta n/n$ |
| 160 | 0.16 | 1250 | 160 | 0.16 | 0 | 0 | 0 | 0 | -10 | 0 | -6.25% | 0 |
| 180 | 0.13 | 1111 | 180 | 0.13 | 0 | 0 | 0 | 0 | -10 | 0.005 | -5.56% | 3.85% |
| 350 | 0.055 | 571.4 | 350 | 0.05 | 0 | -0.005 | 0 | -9% | -20 | 0.005 | -5.56% | 10.00% |
| 350 | 0.155 | 571.4 | 360 | 0.15 | 10 | -0.005 | 2.90% | -3.20% | -10 | 0.005 | -2.78% | 3.33% |
| 350 | 0.255 | 571.4 | 360 | 0.25 | 10 | -0.005 | 2.90% | -2% | -20 | 0.005 | -5.56% | 2.00% |
| 350 | 0.09 | 571.4 | 350 | 0.09 | 0 | 0 | 0 | 0 | -20 | 0.01 | -5.71% | 11.11% |
| 500 | 0.1 | 400 | 500 | 0.1 | 0 | 0 | 0 | 0 | -20 | 0.01 | -4.00% | 10.00% |
| 880 | 0.155 | 227.3 | 890 | 0.15 | 10 | -0.005 | 1.10% | -3.20% | -50 | 0.005 | -5.62% | 3.33% |
| 880 | 0.255 | 227.3 | 890 | 0.25 | 10 | -0.005 | 1.10% | -2% | -30 | 0.015 | -3.37% | 6.00% |

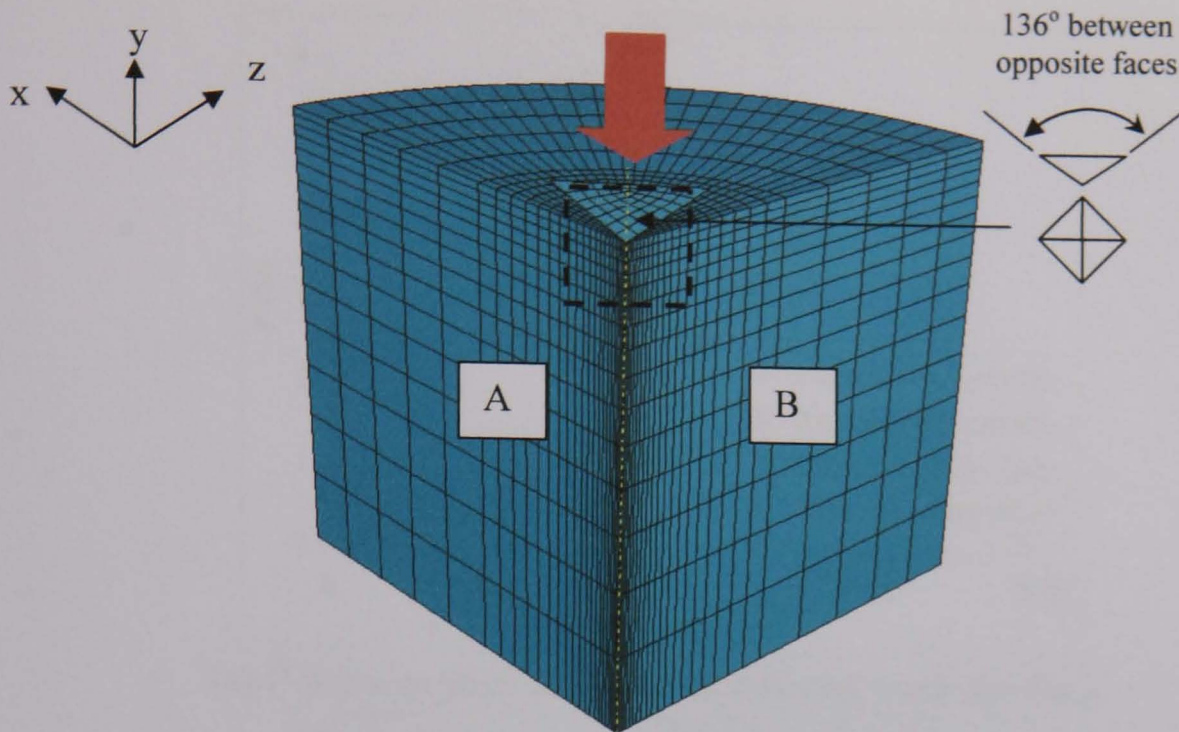
*The sensitivity study is using 3% perturbation of the P in the $P-h$ curves.

4.5 Summary

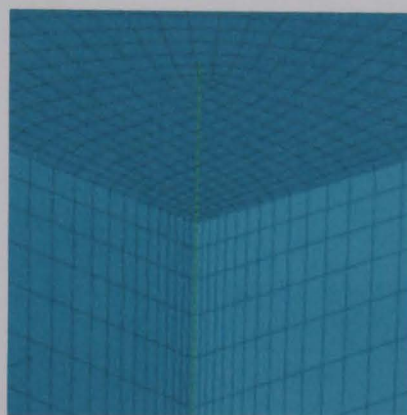
In this chapter, FE models of three typical indenters have been developed, the effect of mesh size and frictional conditions has been systematically assessed. The numerical results showed good agreements with some published data. An inverse FE modelling based on the indentation $P-h$ curves was successfully developed to predict the material properties. Simulation spaces over a wide range of material properties have been developed, which provided the data for the properties prediction. Inverse FE modelling based on both single and dual indenters have been investigated and a new method based on dual indenters of sharp and spherical indenters has been established and its accuracy and sensitivity have been studied.

The results showed that there are multiple materials with different stress-strain relationships matching the indentation curves with Vickers, Knoop or spherical indenters. This suggests that approach based $P-h$ curve from single indenter could not predict the material plastic properties unless the range of material properties was pre-known. The combination of two sharp indenters (e.g. Vickers and Knoop) could not extract the materials properties either. Dual spherical indenters method showed improvement in terms of convergence, but the results is very sensitivity to perturbation in the force or other experimental error. The combination of sharp (Vickers or Knoop) and spherical indenter is proven to be the best approach with accurate and robust results over a wide range of material properties.

The work also demonstrated that material properties with different stress-strain curves but matching the indentation $P-h$ curves from single indenter can be approximated onto a straight line. This suggests that there is an interlink between two plastic parameters (σ_y and n) affecting the $P-h$ curve. Figure 3.34 plots the material properties matching the $P-h$ curves of different indenters with the same input data. It clearly shows that these lines intersect at the same point around the true material property. The lines for Vickers and Knoop are roughly on the same line, while there is a clear difference between the spherical indenters with different sizes. The most significant difference is between the sharp and spherical indenters which probably helped to distinguish the material properties.



(a) FE model of the Vickers indentation test.



(b) Close-up view showing the mesh underneath the indenter.

Figure 4.1 FE model of the Vickers indentation test.

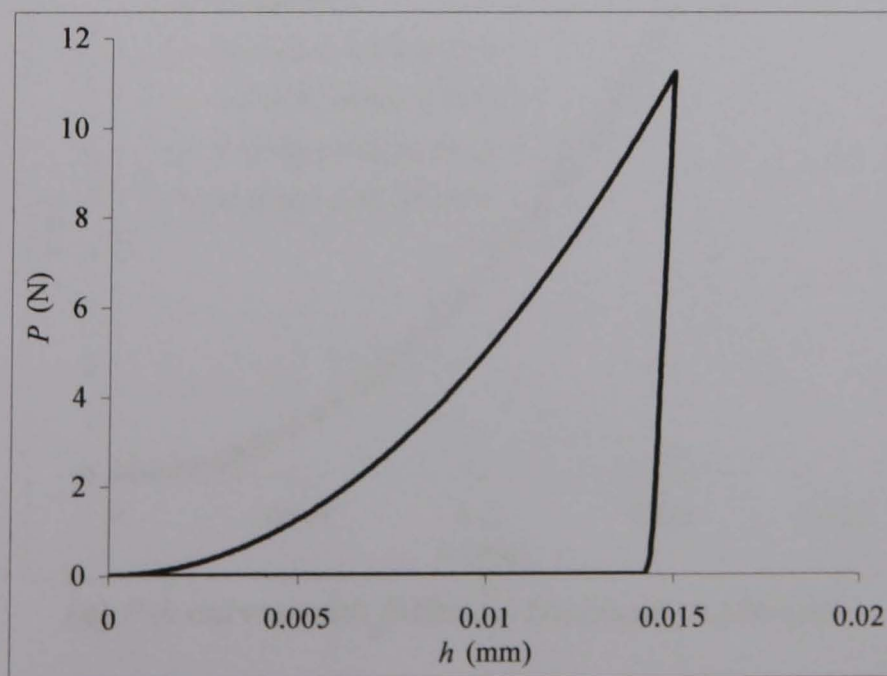
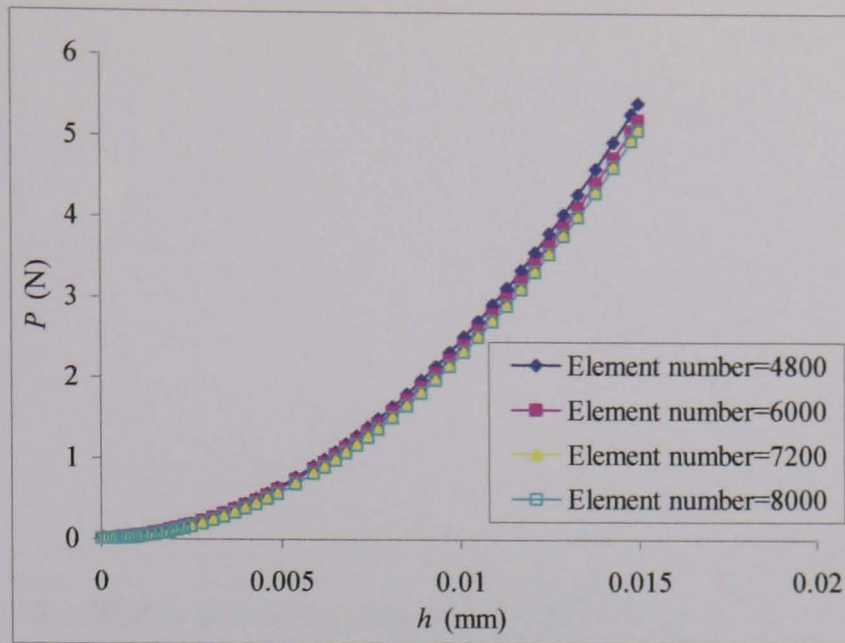
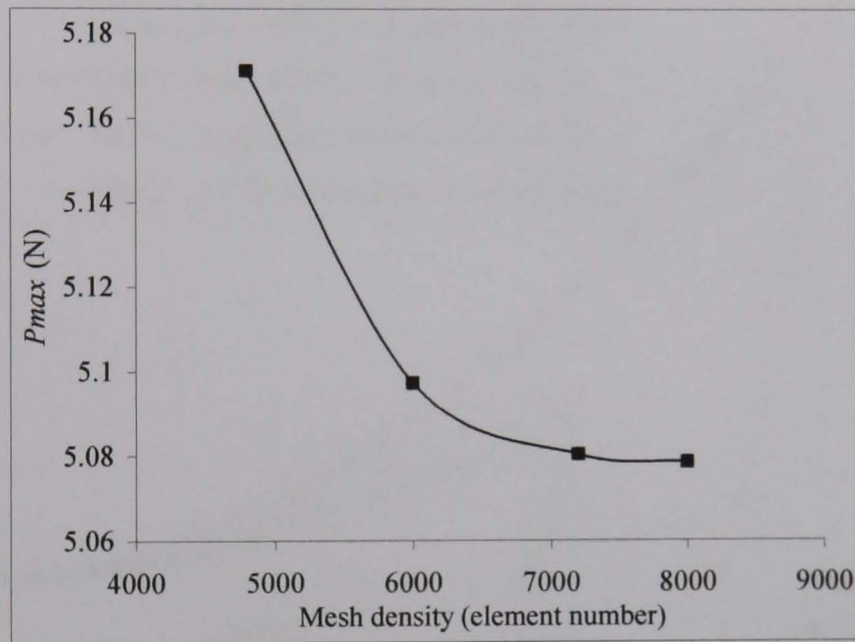


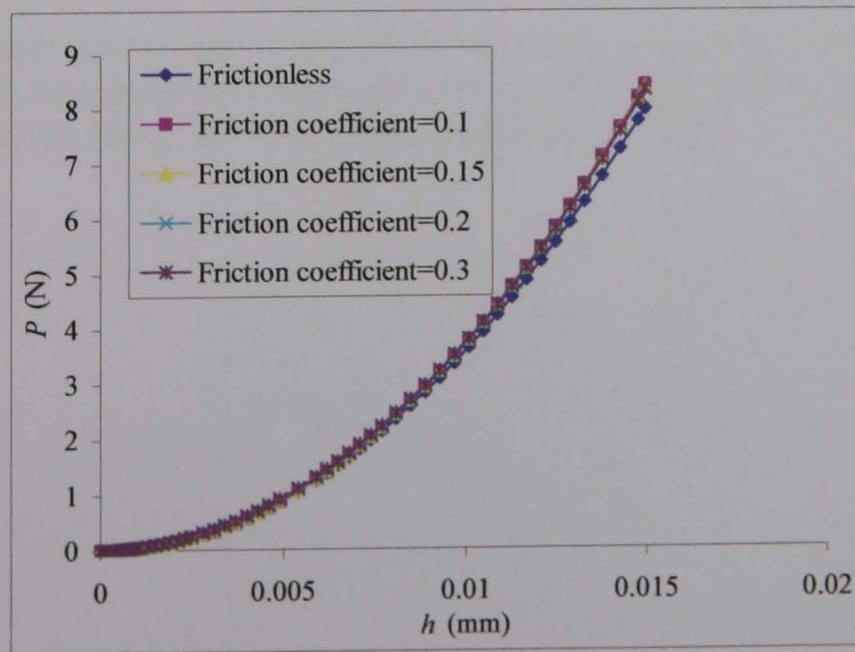
Figure 4.2 Typical force-indentation depth ($P-h$) curve during loading and unloading of the Vickers indentation.



(a) $P-h$ curves from models with different mesh densities.



(b) Effect of mesh densities on the force at indentation depth of 0.015mm.



(c) $P-h$ curves with different frictional conditions.

Figure 4.3 Effect of mesh density (a-b) and frictional conditions (c) on the modelling results of Vickers indentation.

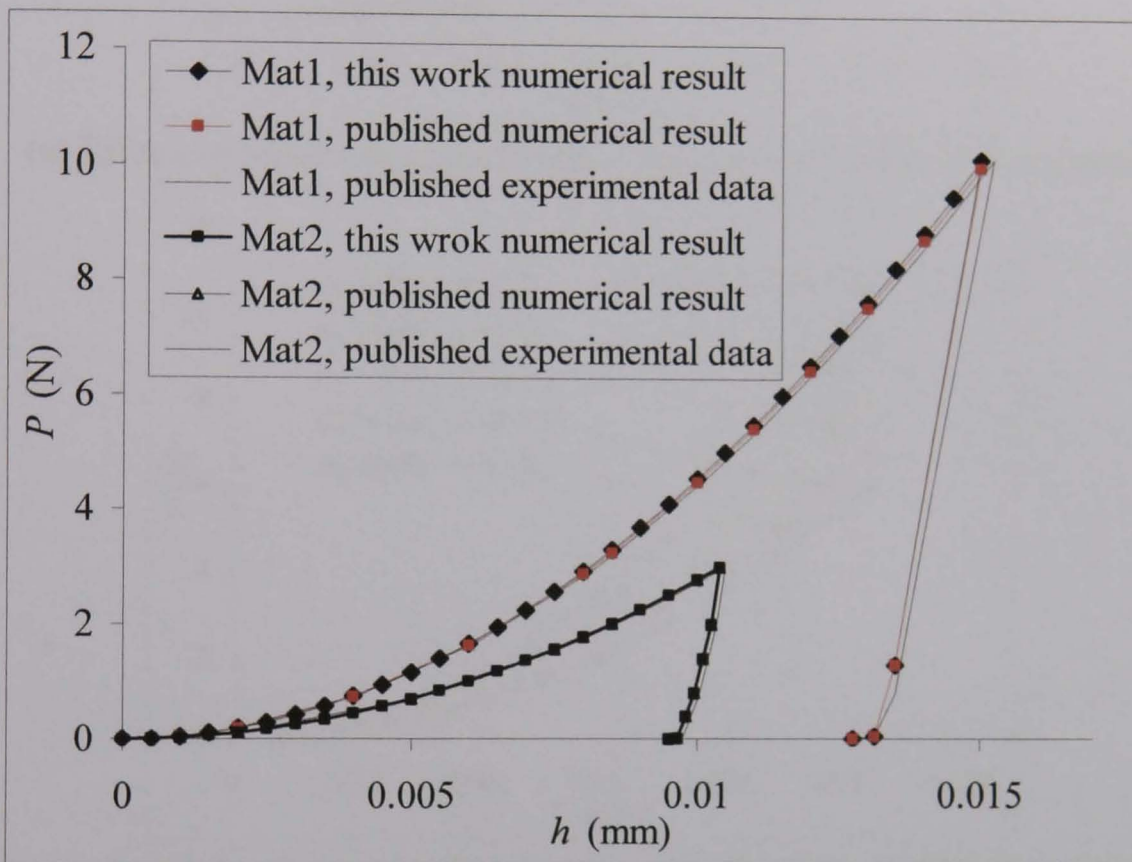
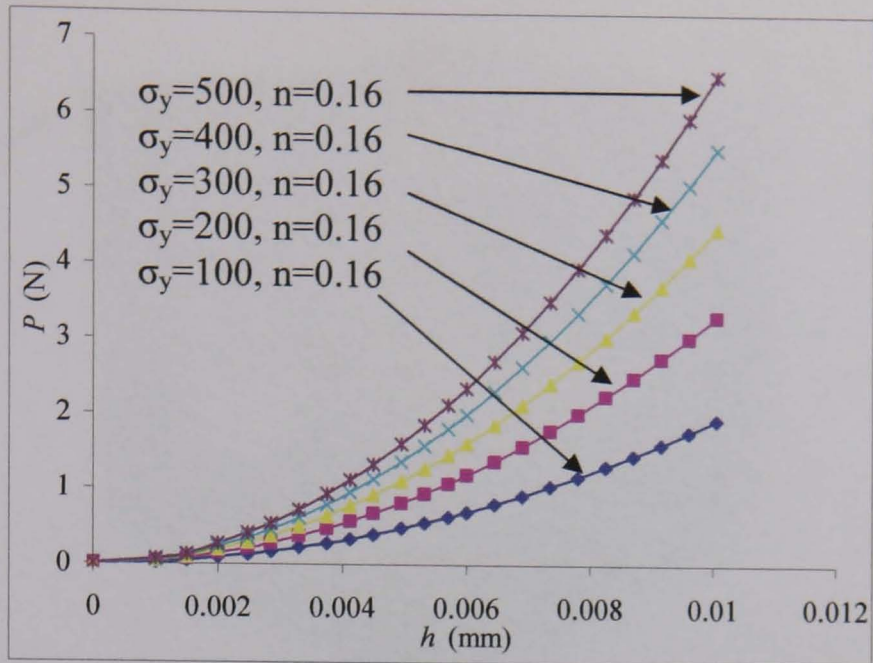
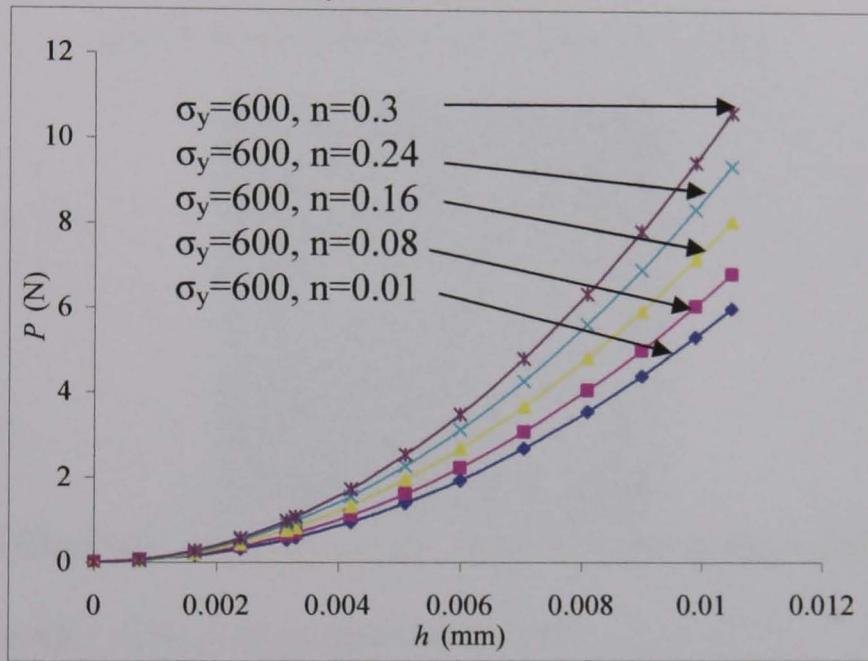


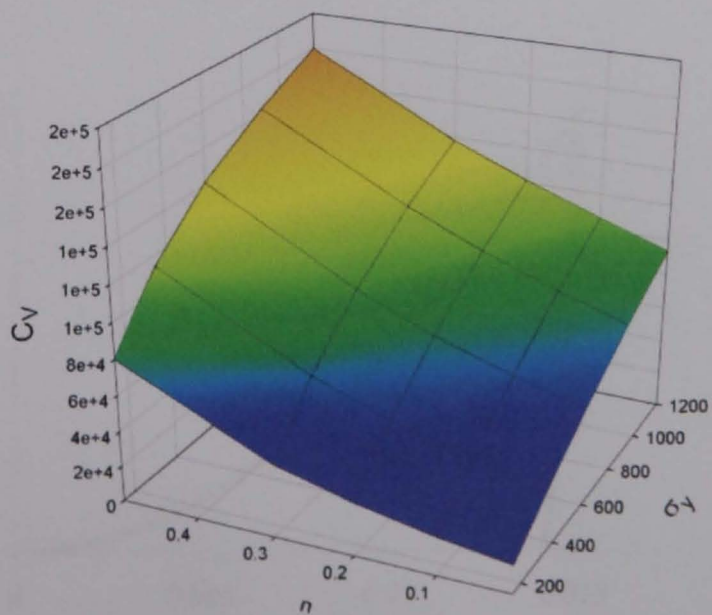
Figure 4.4 Comparison of numerical results with some published experimental data (Dao *et al*, 2001) of continuous indentation with a Vickers indenter. (Mat1: $E=70\text{GPa}$, $\sigma_y=300\text{MPa}$, $n=0.05$; Mat2: $E=70\text{GPa}$, $\sigma_y=500\text{MPa}$, $n=0.122$)



(a) Effects of yield stress (σ_y) on the P - h curves of Vickers indentation.

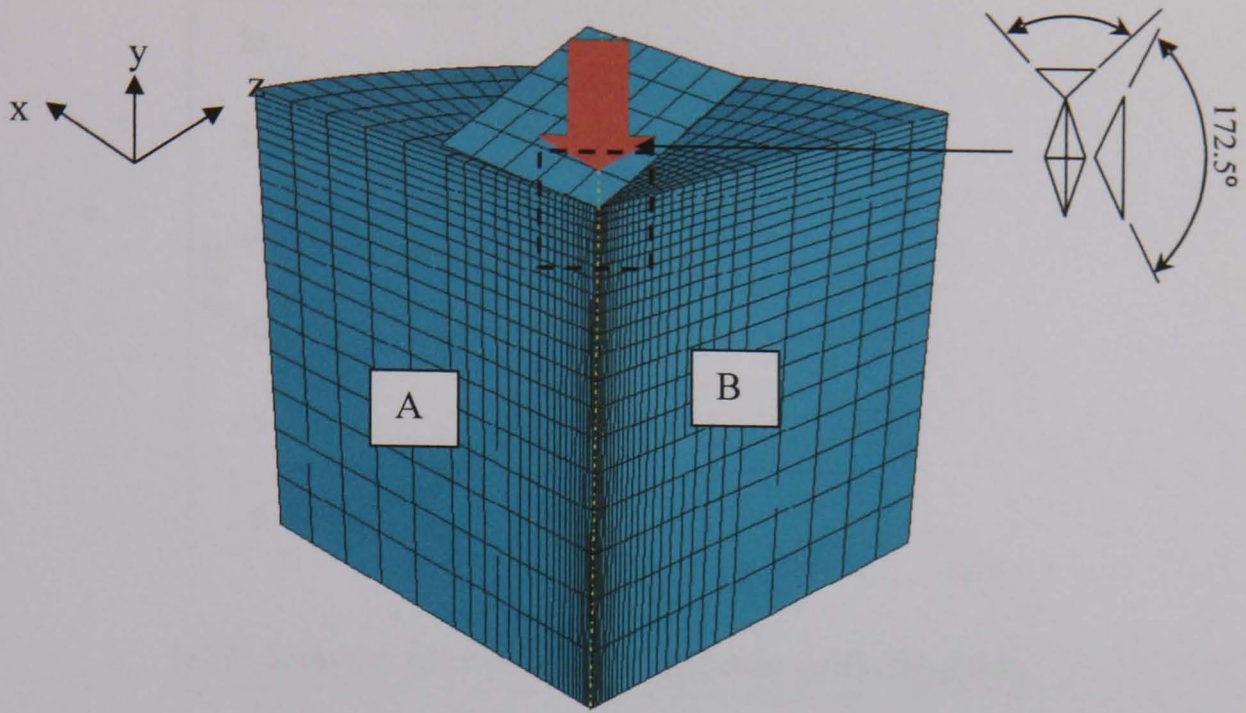


(b) Effects of work hardening coefficient (n) on the P - h curves of Vickers indentation.

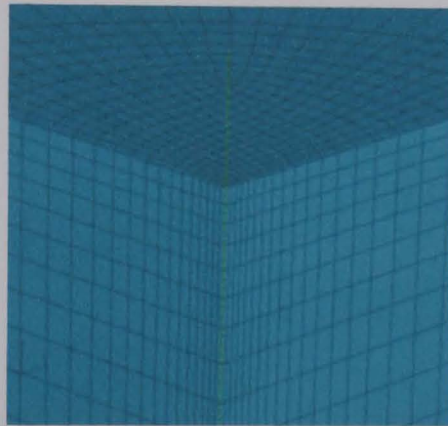


(c) Map of curvature coefficients ($C_{Vickers}$) for the Vickers indentation.

Figure 4.5 Effect of plastic parameters on the P - h curves and curvature coefficients ($C_{Vickers}$) for the Vickers indentation.



(a) FE model of the Knoop indentation test.



(b) Close-up view showing the mesh underneath the indenter.

Figure 4.6 FE model of the Knoop indentation test.

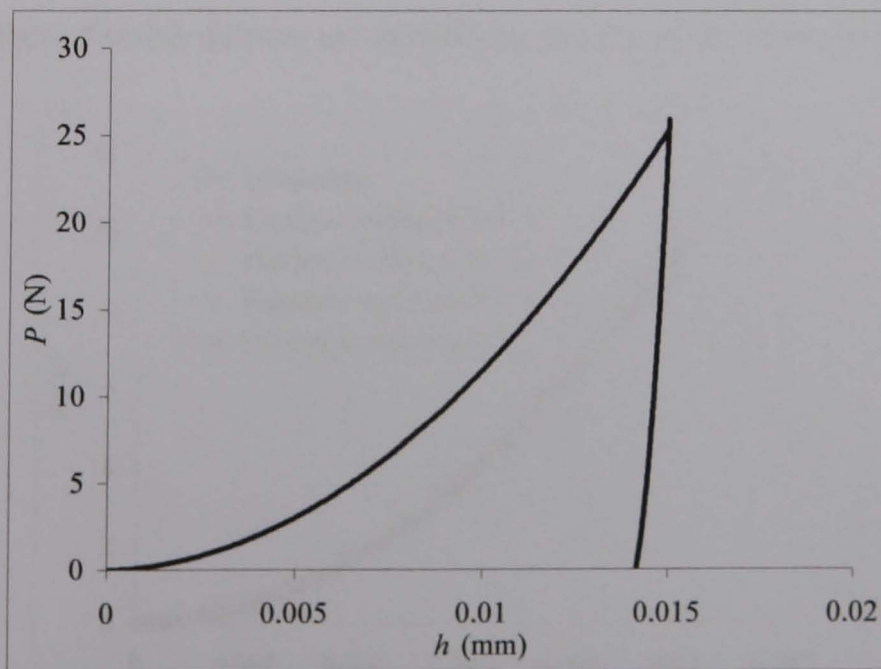
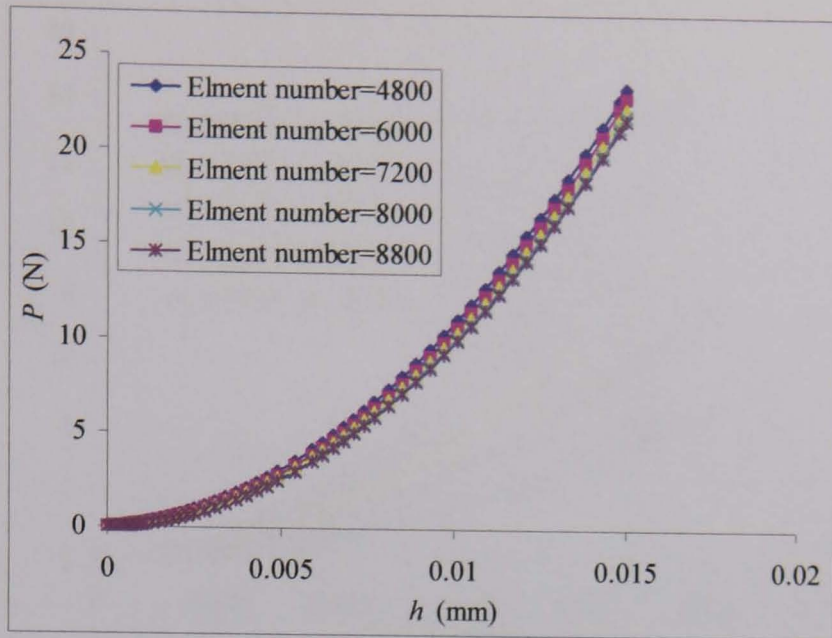
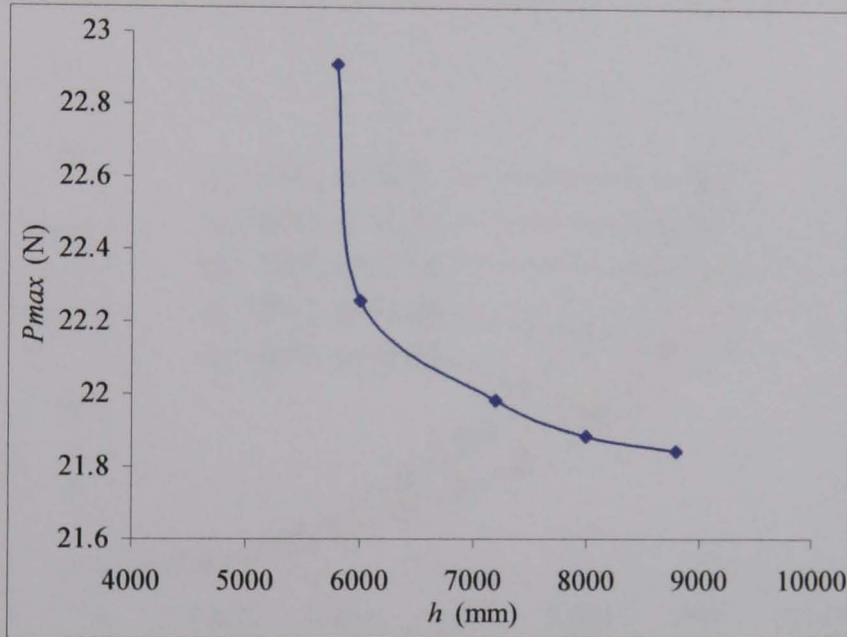


Figure 4.7 Typical force-indentation depth (P - h) curve during loading and unloading for Knoop indentation ($\sigma_y = 350$ MPa, $n=0.16$).



(a) P - h curves from models of different mesh densities.



(b) Effect of mesh densities on peak force at indentation depth of 0.015mm.

Figure 4.8 Effect of mesh density on modelling results of the Knoop indentation.

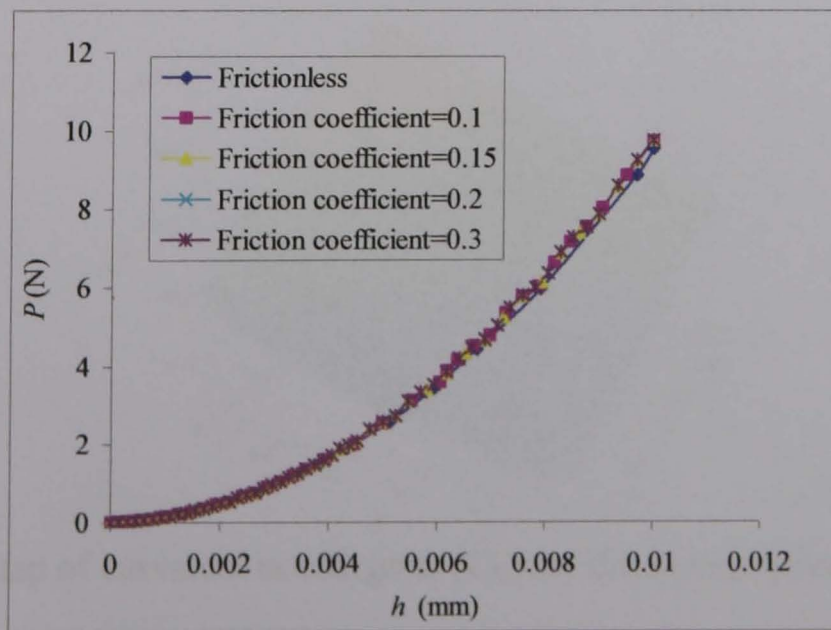
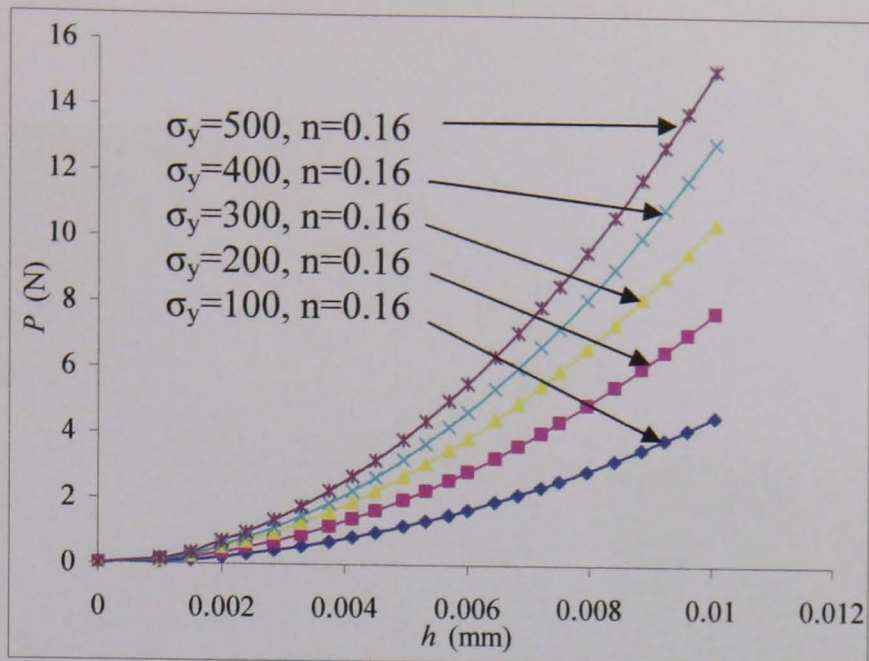
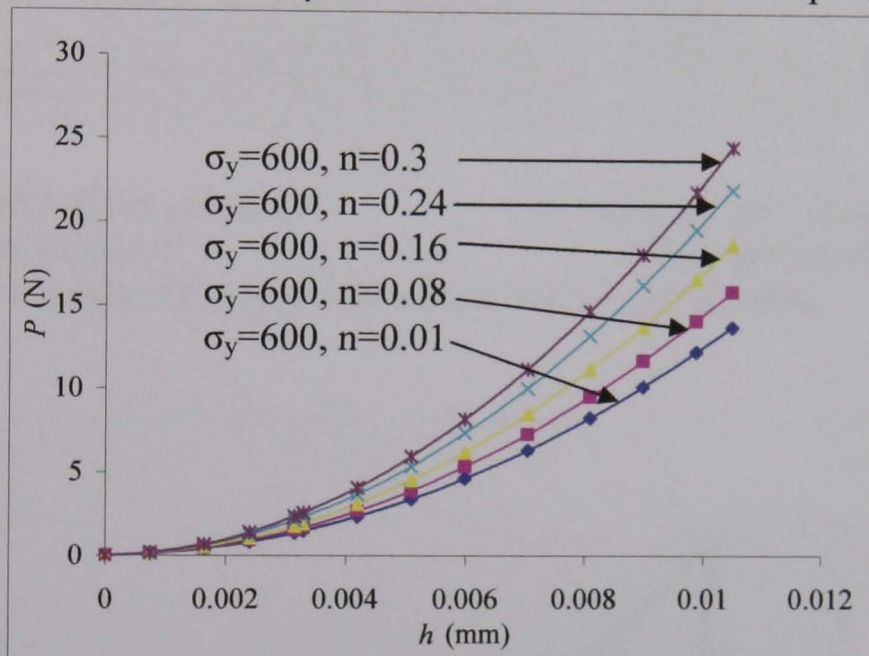


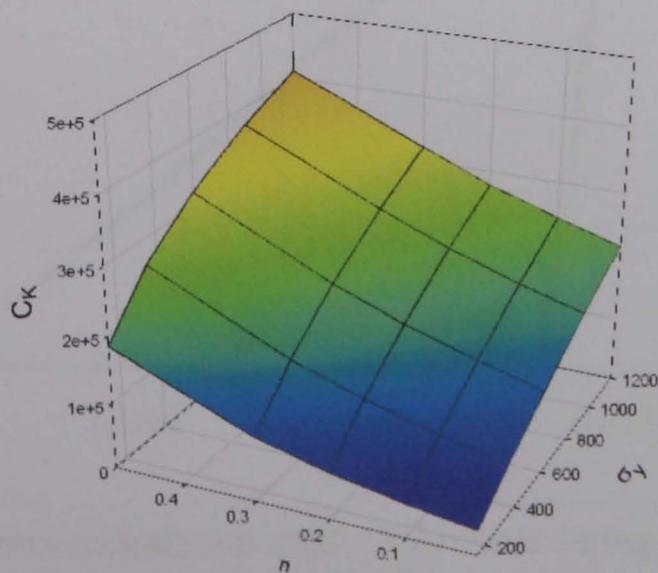
Figure 4.9 Effect of frictional conditions on modelling results of the Knoop indentation.



(a) Effects of yield stress (σ_y) on the $P-h$ curves of the Knoop indentation.

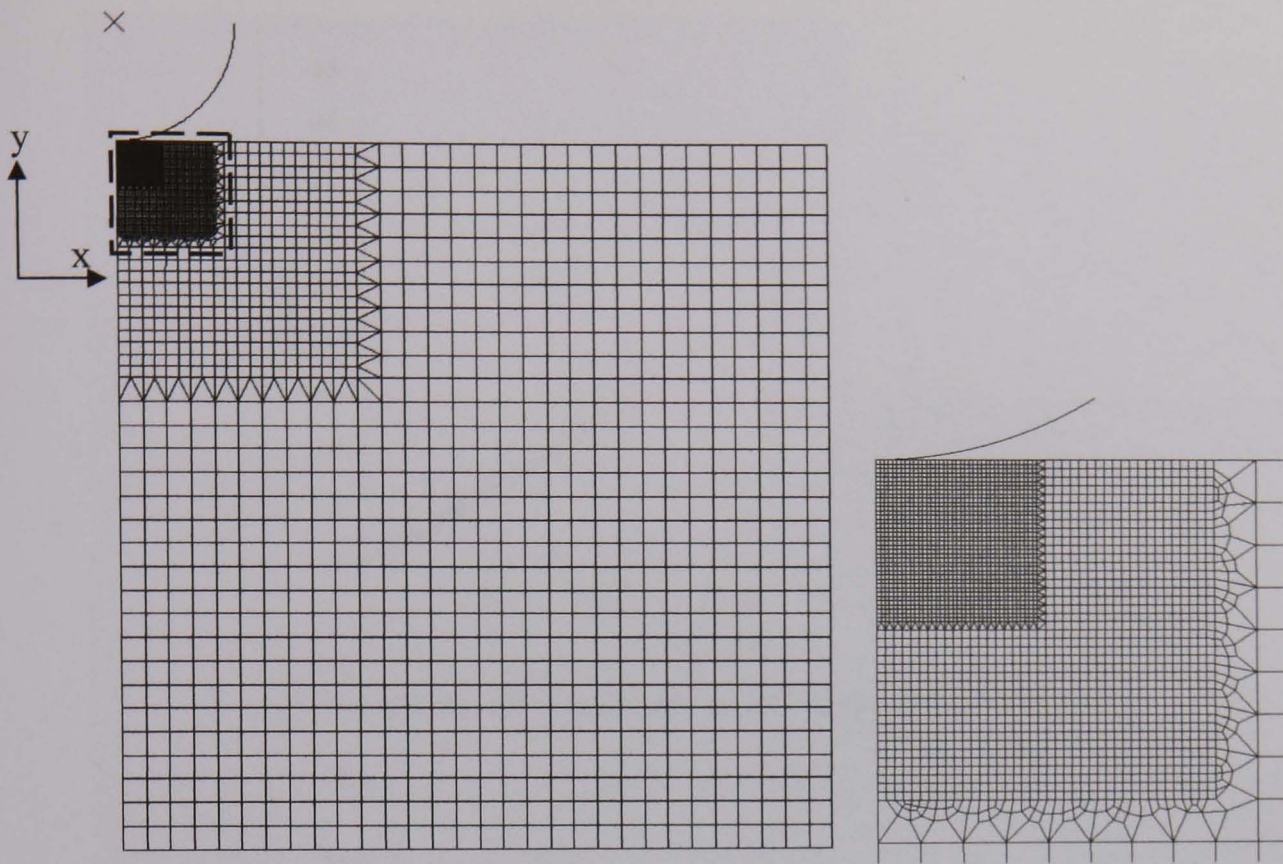


(b) Effects of work hardening coefficient (n) on the $P-h$ curves of the Knoop indentation.



(c) Map of curvature coefficients (C_K) for the Knoop indentation.

Figure 4.10 Effect of plastic parameters on the $P-h$ curves and curvature coefficients (C_K) for the Knoop indentation.



(a) FE model of the spherical indentation test.

(b) Close-up view showing the mesh underneath the indenter.

Figure 4.11 FE models of the spherical indentation test ($R=0.5\text{mm}$).

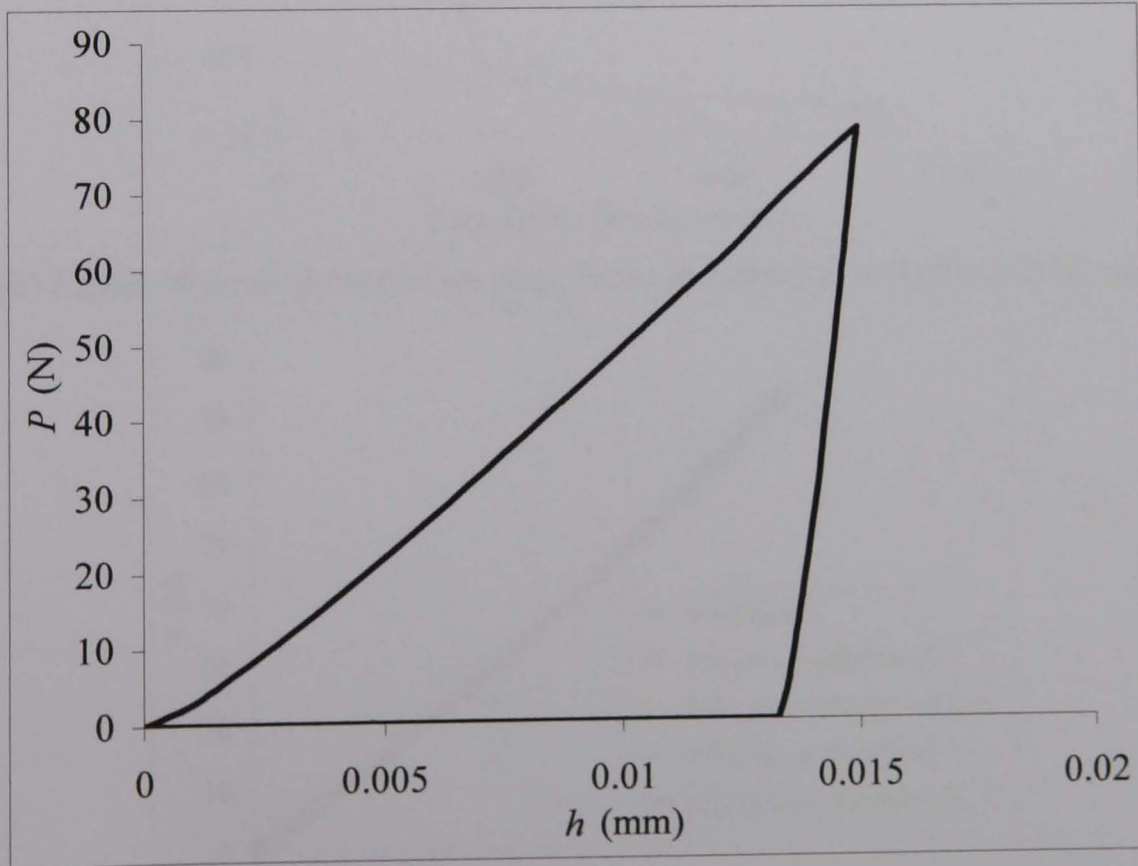
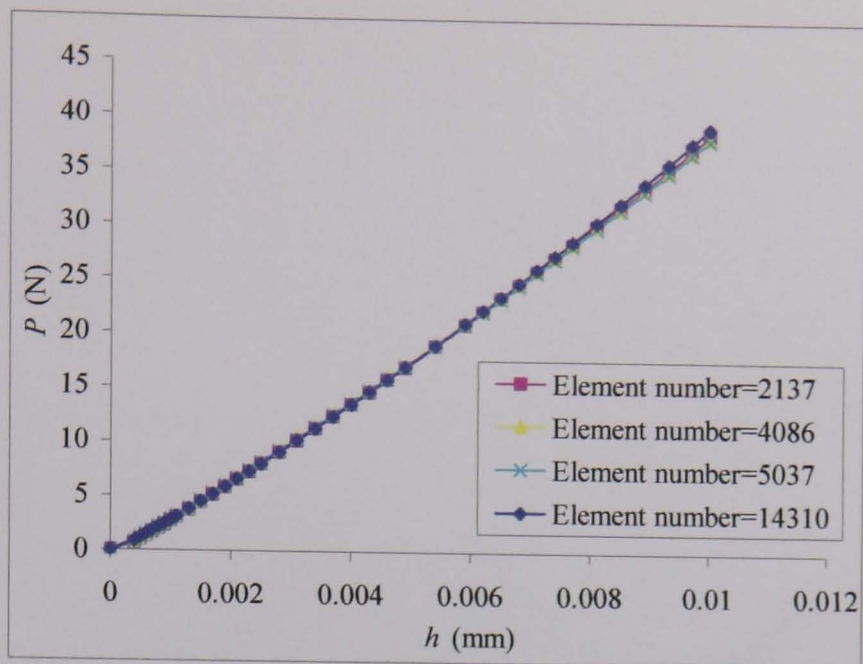
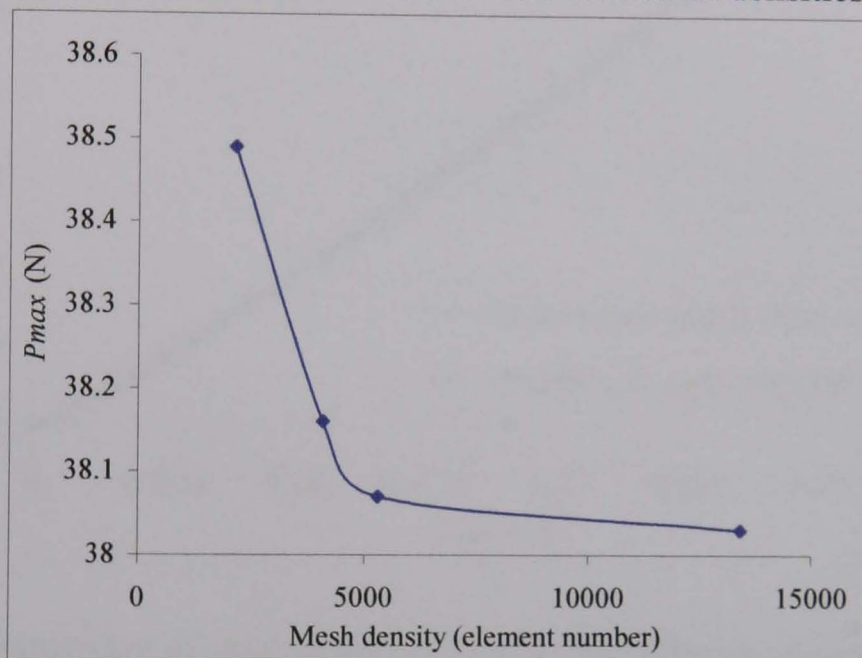


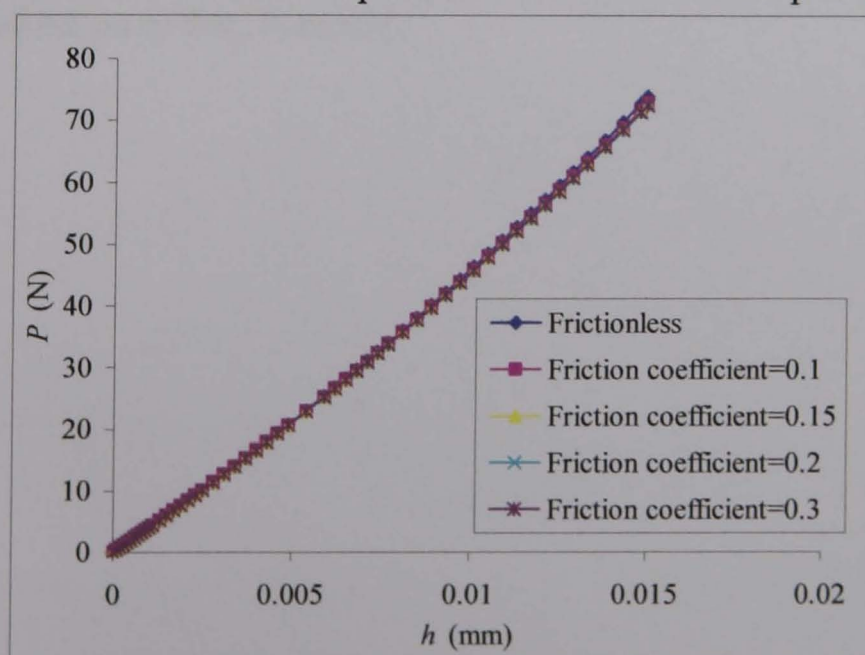
Figure 4.12 Typical force-indentation depth ($P-h$) curve during loading and unloading for spherical indentation ($\sigma_y = 350\text{ MPa}$, $n=0.16$).



(a) P - h curves from models of different mesh densities.



(b) Effect of mesh densities on peak force at indentation depth of 0.01mm.



(c) P - h curves with different frictional conditions.

Figure 4.13 Effect of mesh density (a-b) and frictional conditions (c) on the modelling results of spherical indentation.

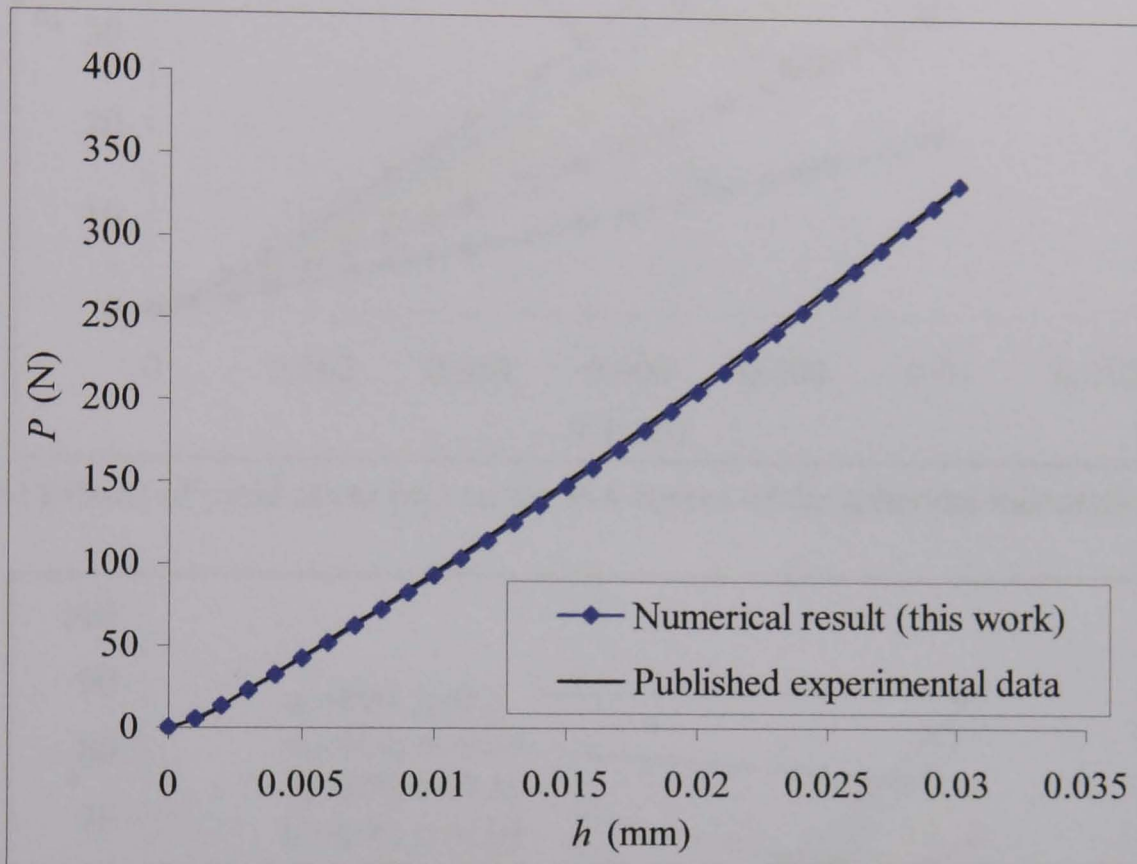
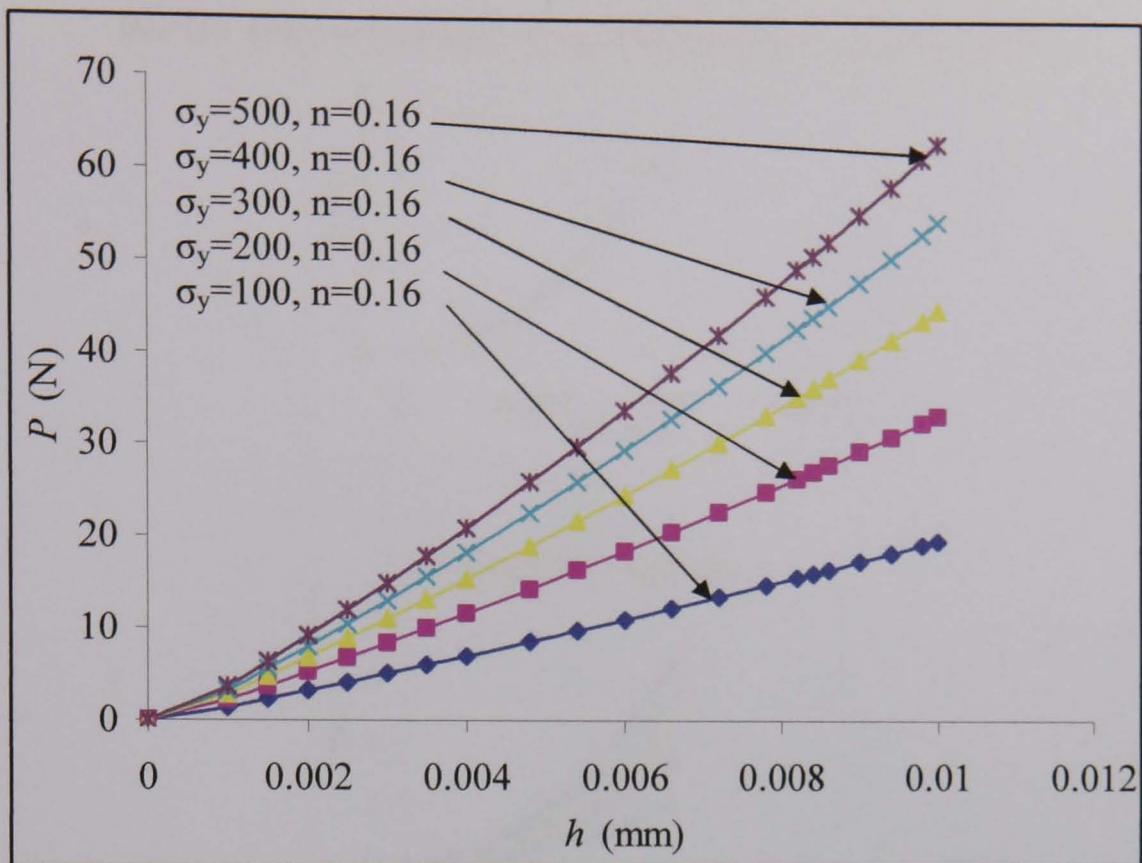
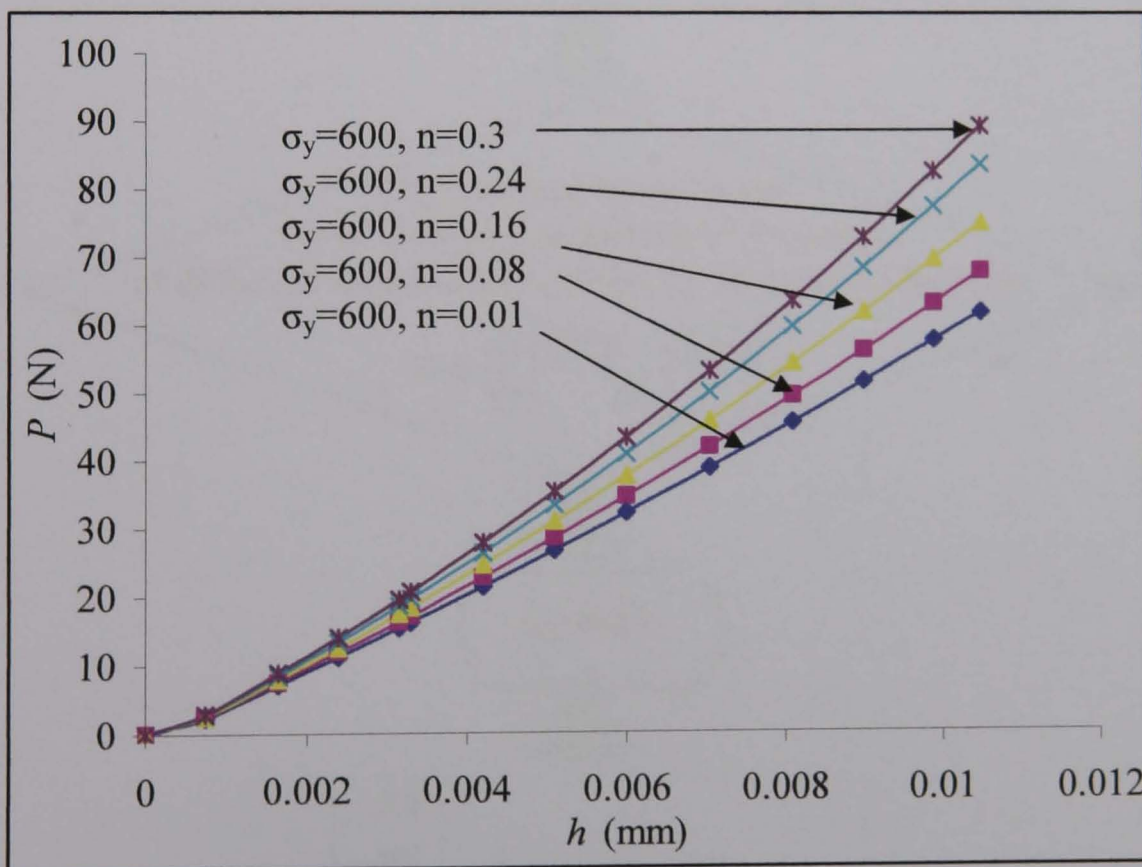


Figure 4.14 Comparison of numerical results with published experimental data (Kucharsk *et al*, 2001) of continuous indentation with a spherical indenter (R1.25mm) showing the validation of the FE model.



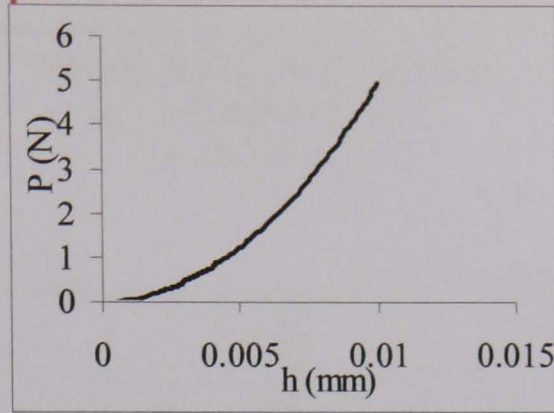
(a) Effects of yield stress (σ_y) on the P - h curves of the spherical indentation.



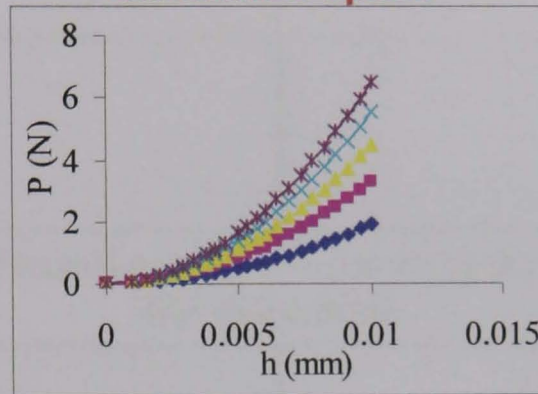
(b) Effects of work hardening coefficient (n) on the P - h curves of the spherical indentation.

Figure 4.15 Effects of plastic parameters on the P - h curves of the spherical indentation.

INPUT (experimental force-indentation depth data)



Simulation space



Comparison between the input data and numerical $P-h$ curves of different material properties by Objective Function

$$G = \sum_{i=1}^n \left(\frac{F_{i,e} - F_{i,n}}{F_{i,e}} \right)^2$$



σ_y and n

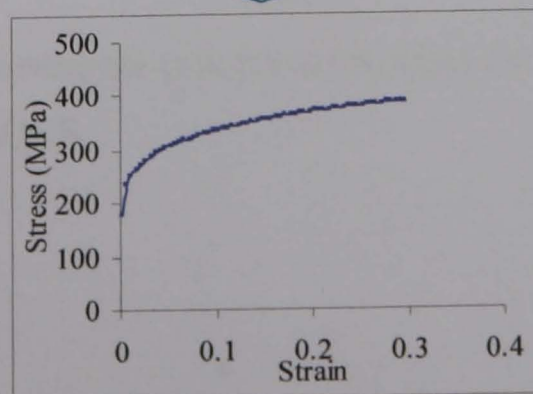


Figure 4.16 Flow chart showing the inverse FE modelling approach based on the single indenter method.

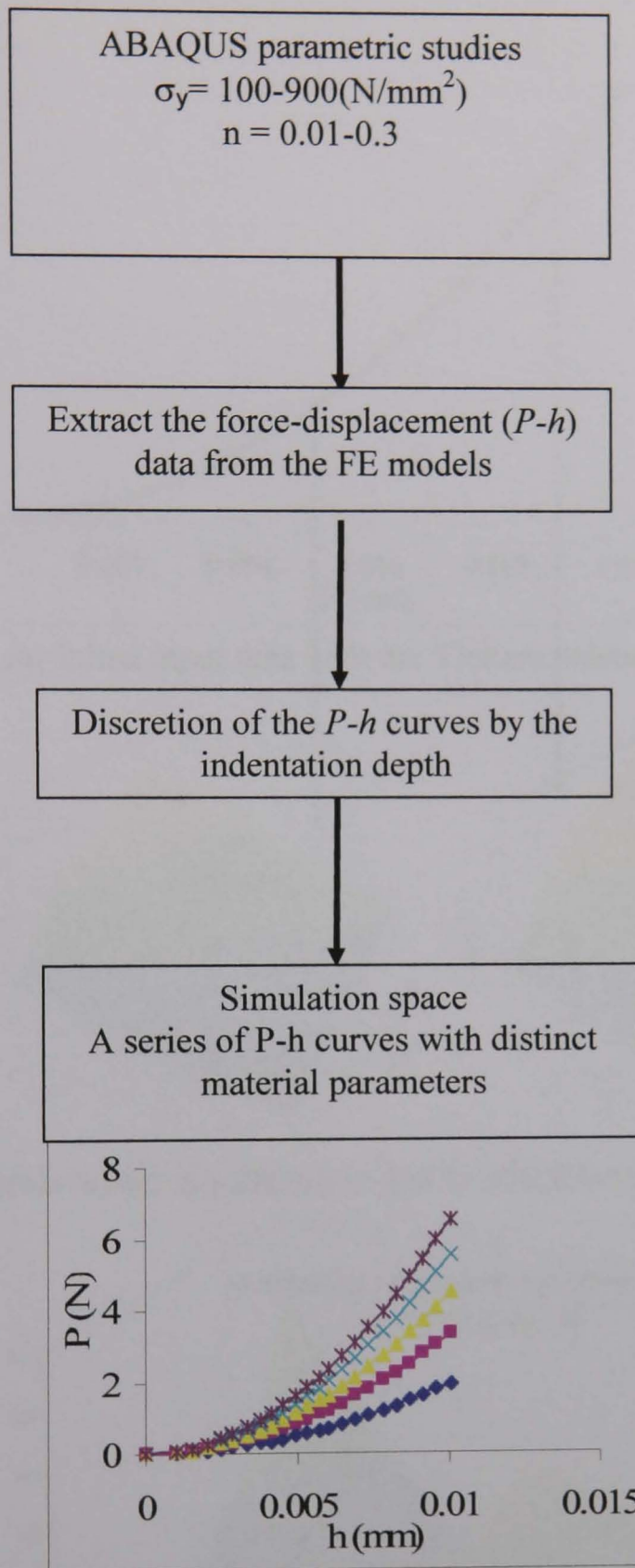
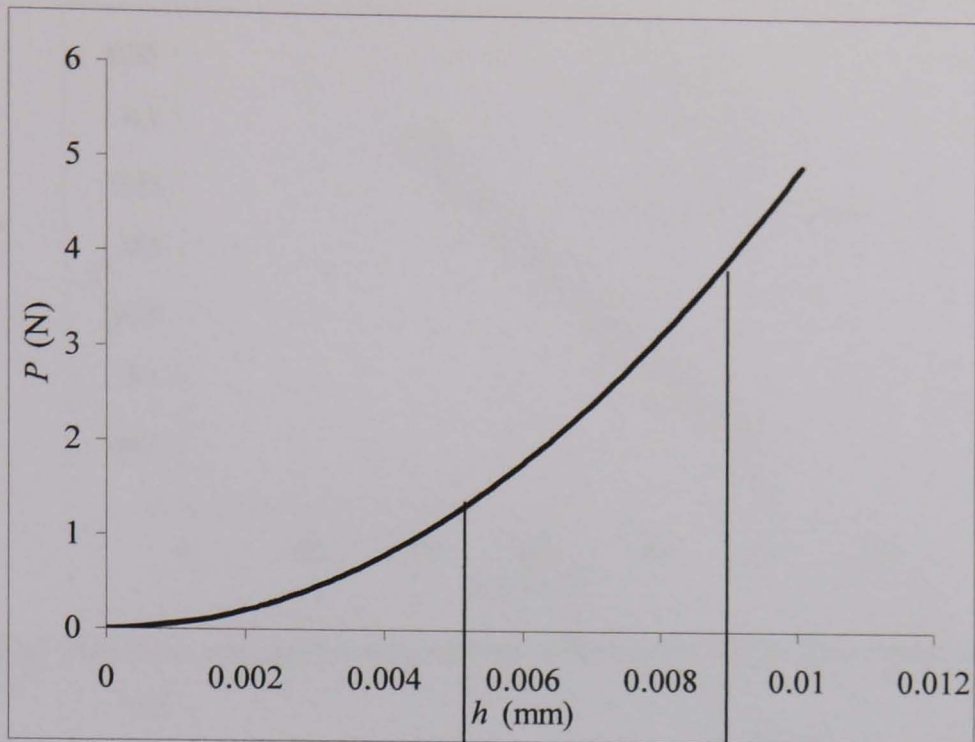
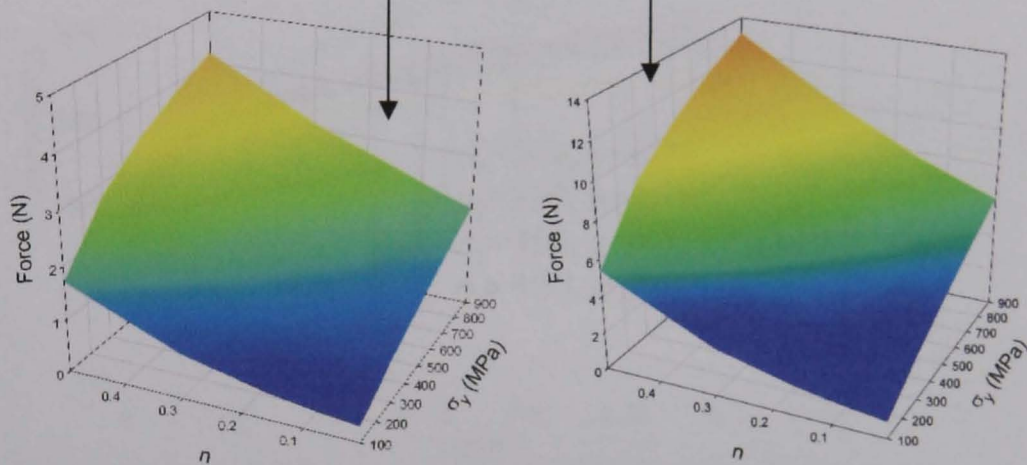


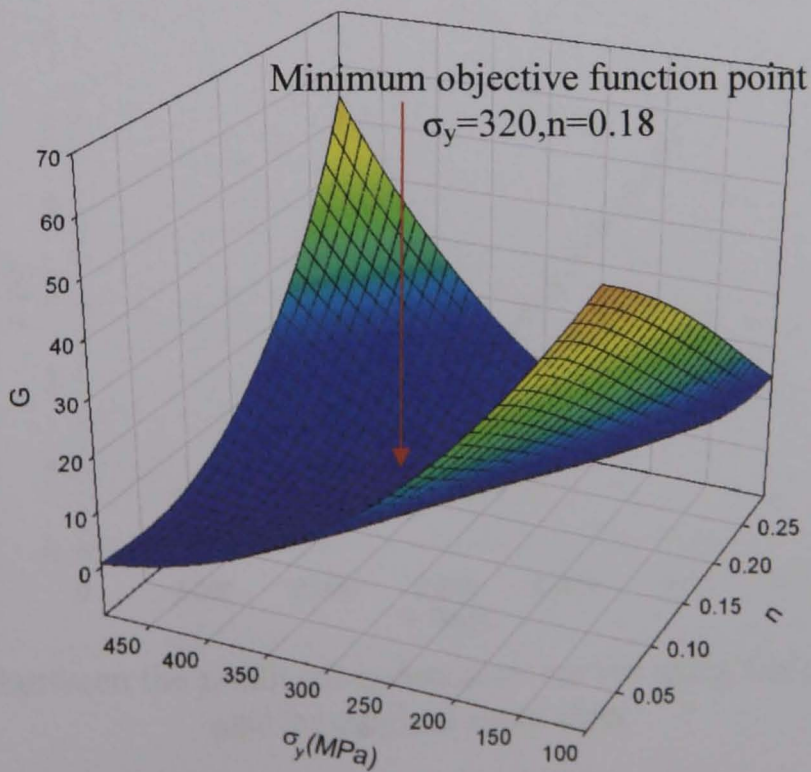
Figure 4.17 Flow chart showing the process to construct the simulation space using parametric studies in ABAQUS.



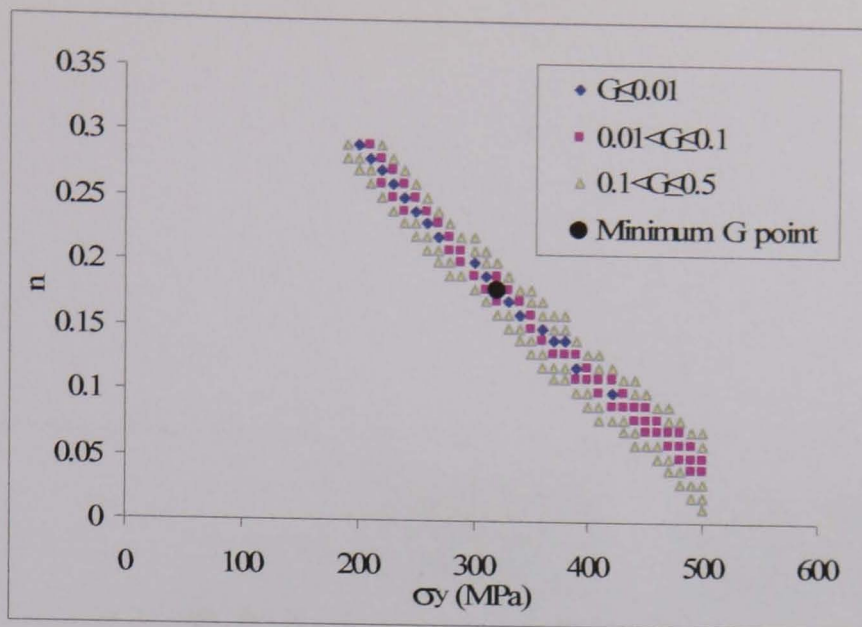
(a) Initial input data with the Vickers indenter.



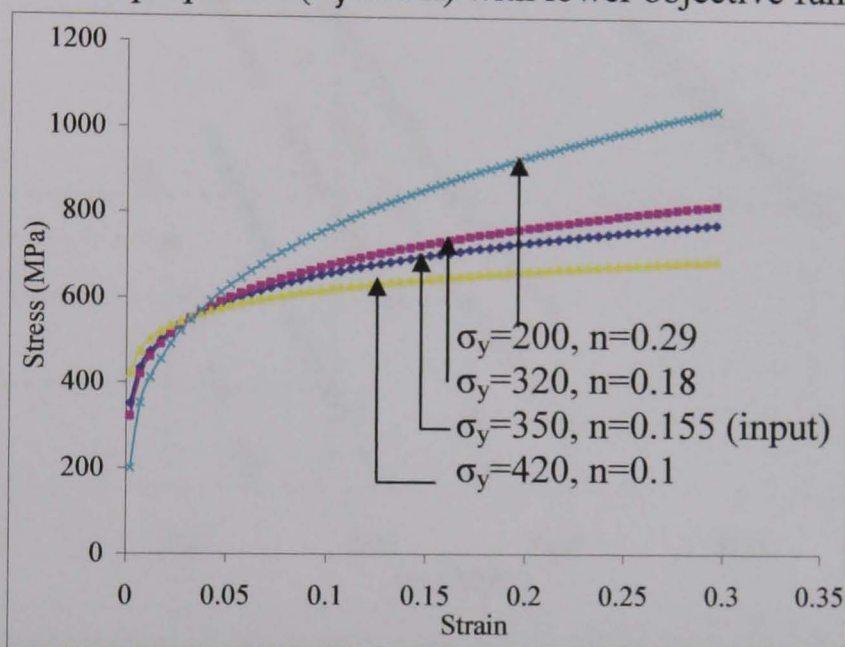
(b) Simulation space at indentation depths of 0.005 and 0.009 mm.



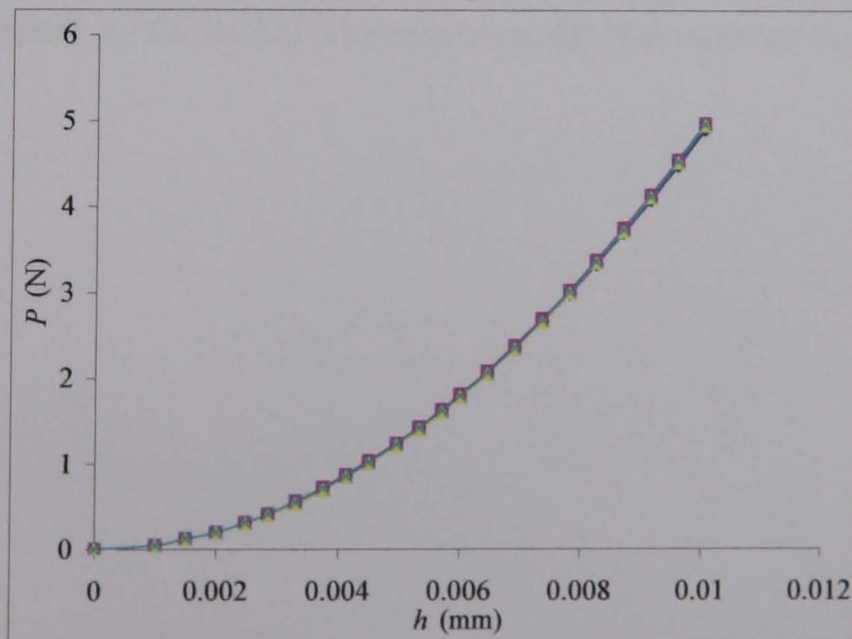
(c) Surface plot of objective functions vs. the material properties (σ_y and n).



(d) Plot of material properties (σ_y and n) with lower objective function values.



(e) True stress-strain curves using the data with $G \leq 0.01$ in (d).



(f) Comparison between the predicted indentation curves using the material sets in (e) and the original input data.

Figure 4.18 Typical data searching process and results based on the Vickers indenter.

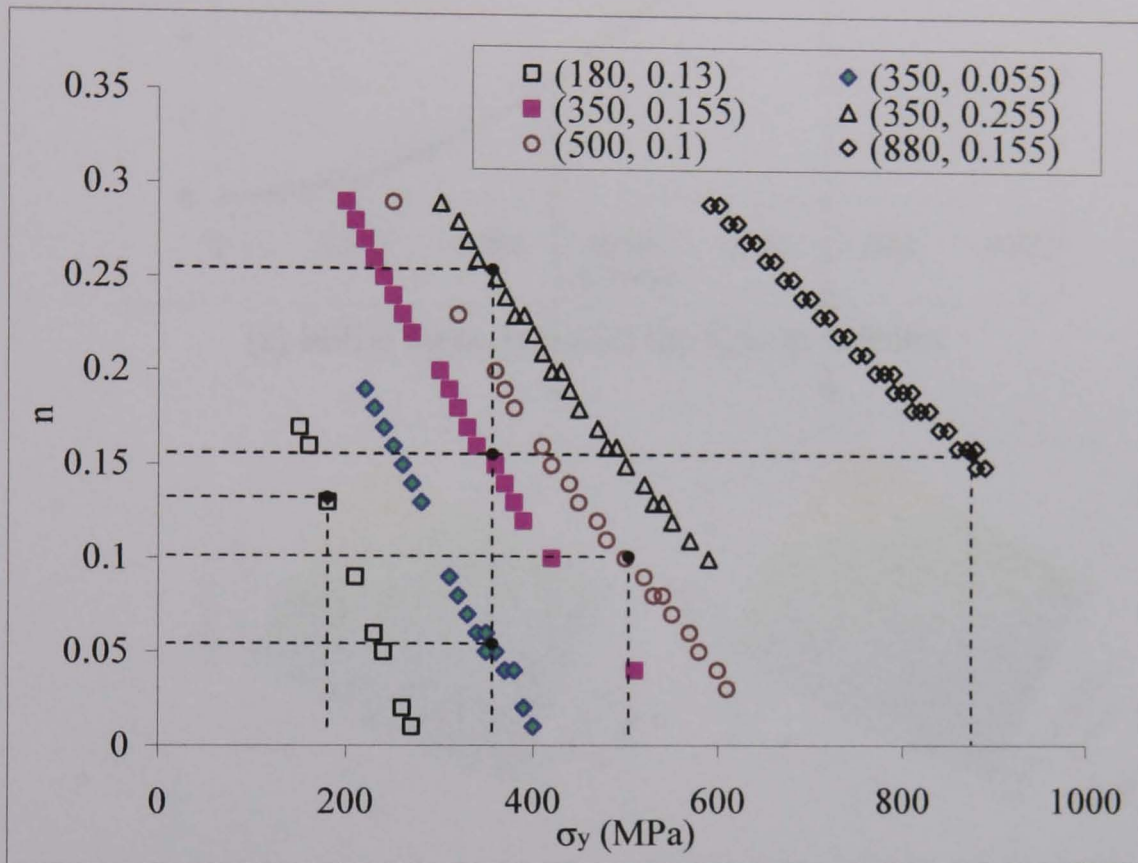
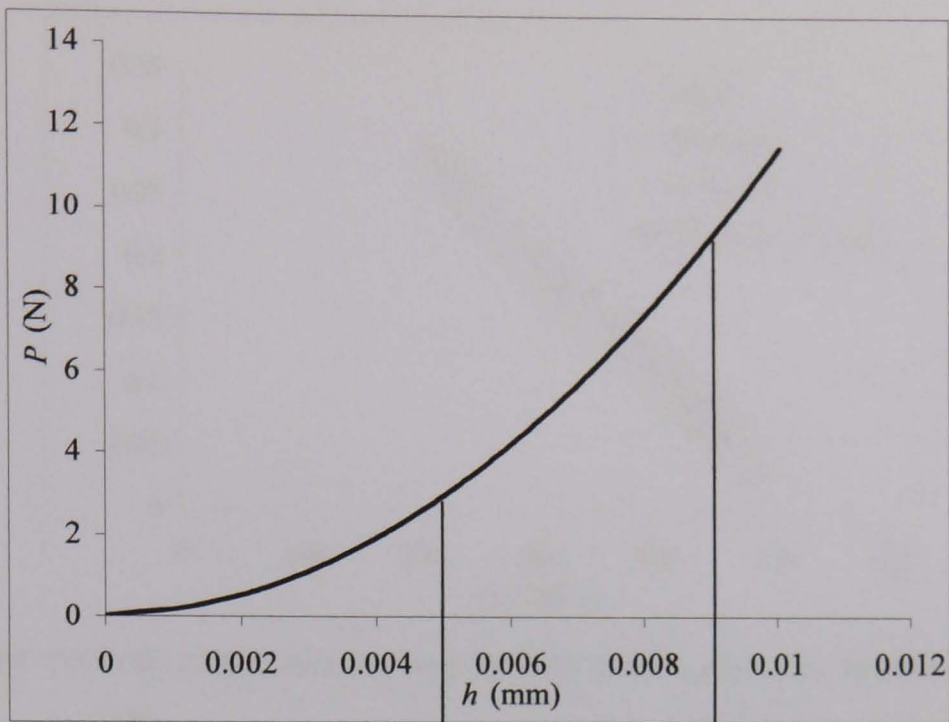
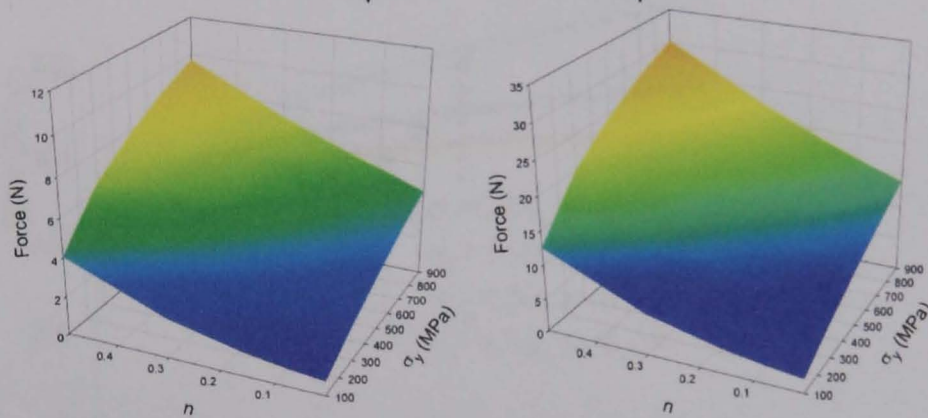


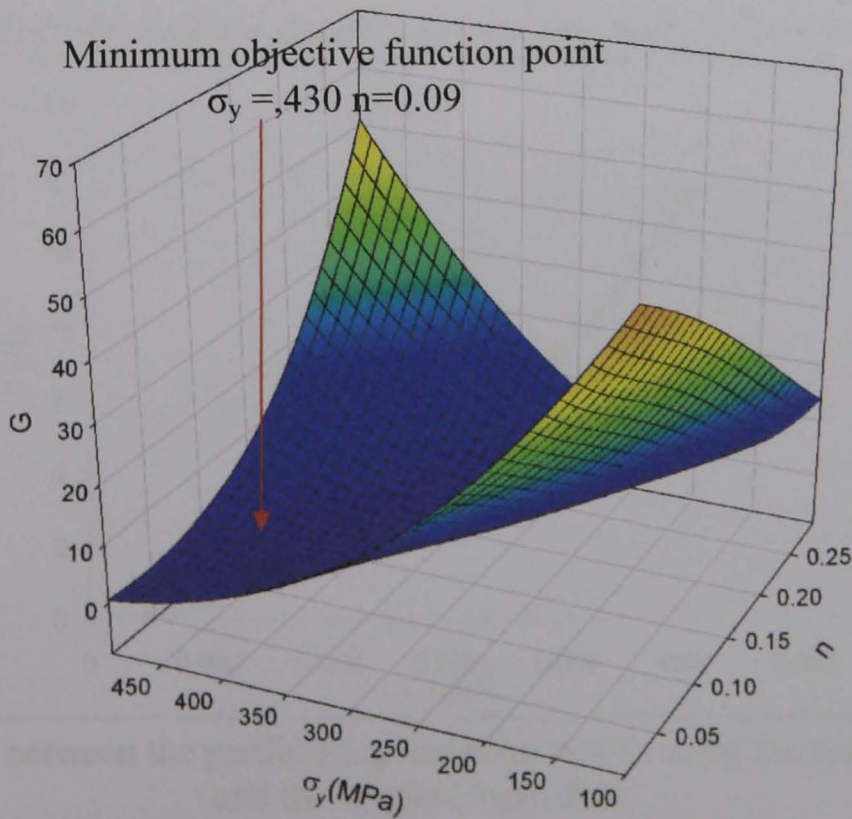
Figure 4.19 Typical predicted properties with comparable objective functions for a range of materials showing the prediction from single Vickers indenter is not unique. The point highlighted by the dotted line represents the true material data.



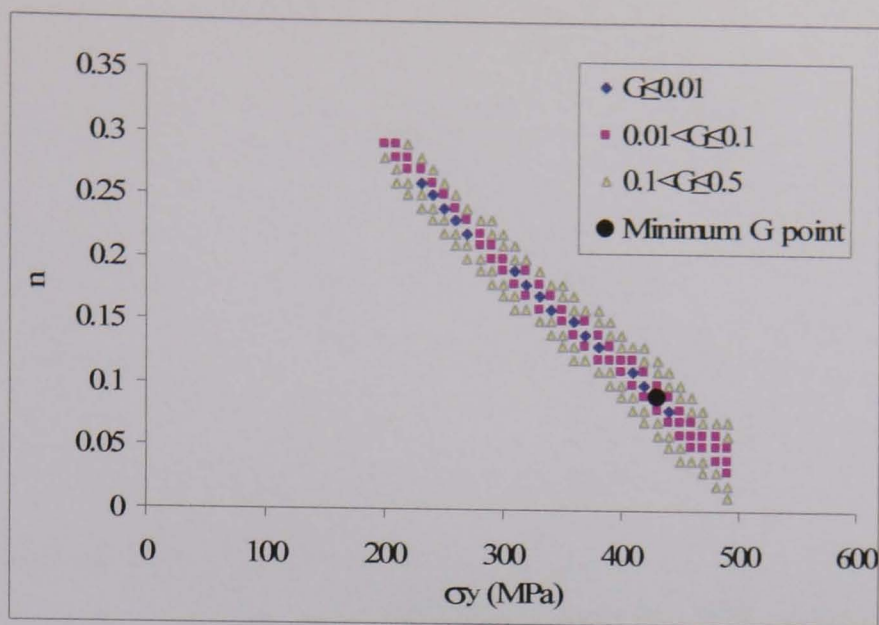
(a) Initial input data with the Knoop indenter



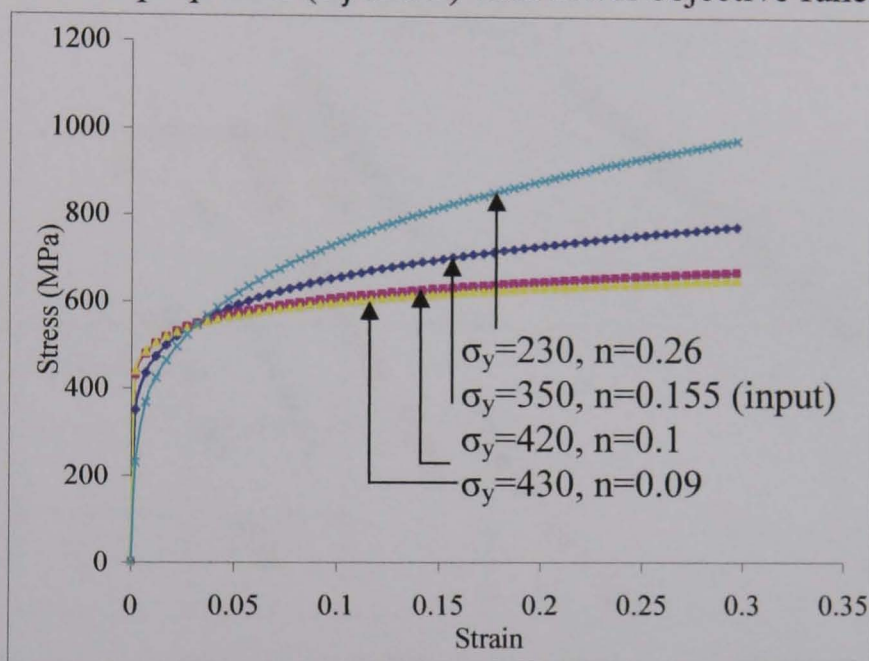
(b) Simulation space at indentation depths of 0.005 and 0.009 mm.



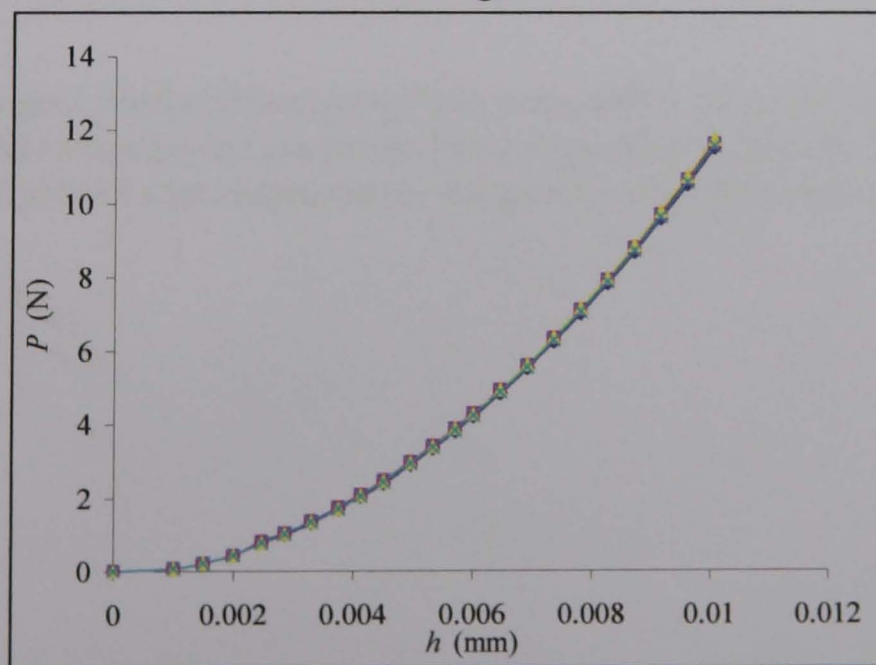
(c) Surface plot of objective functions vs. the material properties (σ_y and n).



(d) Plot of material properties (σ_y and n) with lower objective function values.



(e) True stress-strain curves using the data with $G \leq 0.01$ in (d).



(f) Comparison between the predicted indentation curves using the material sets in (e) and the original input data.

Figure 4.20 Typical data searching process and results based on the Knoop indenter.

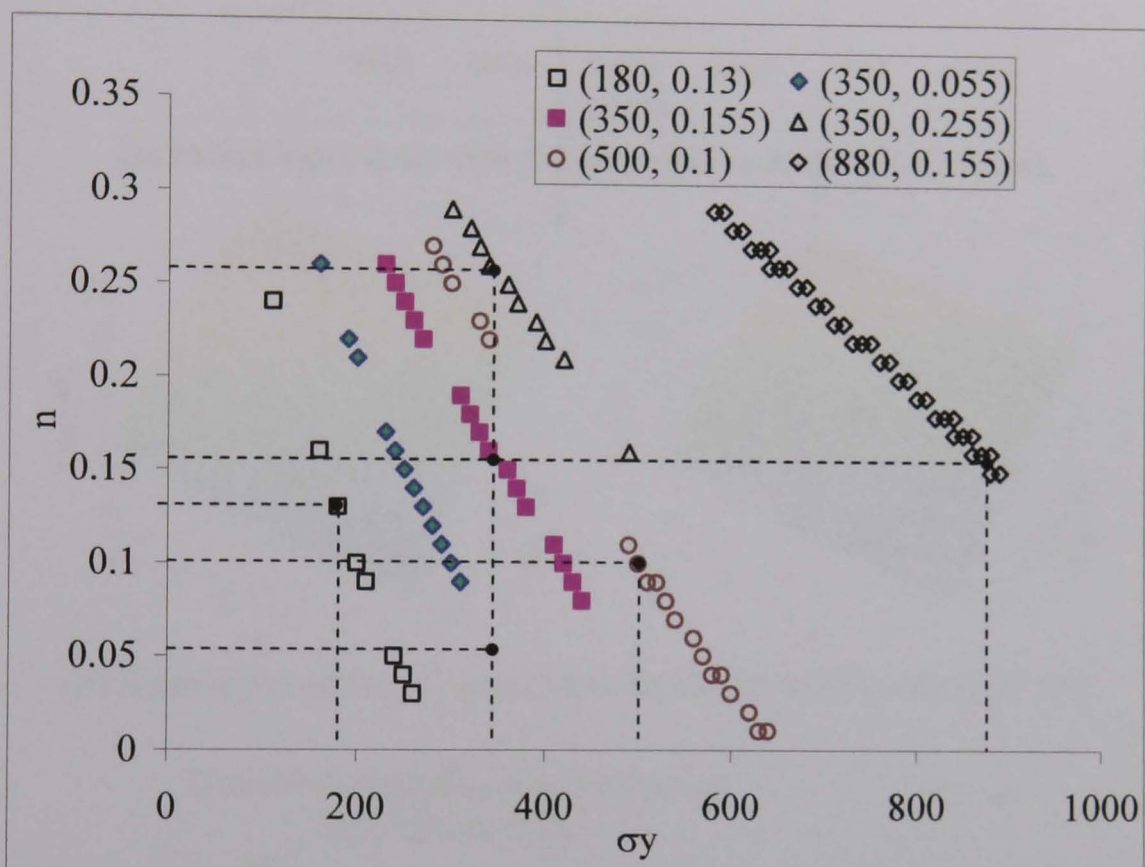
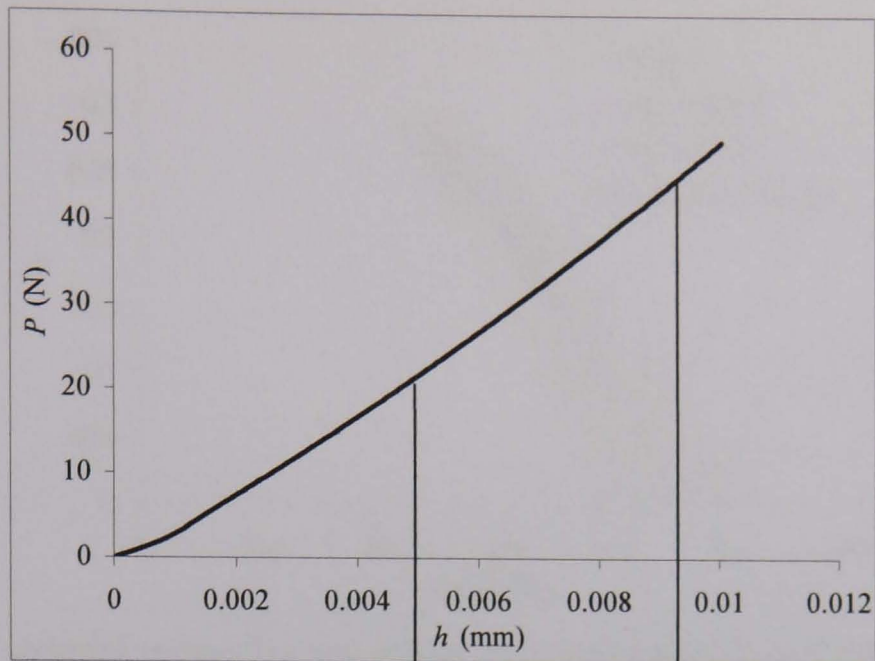
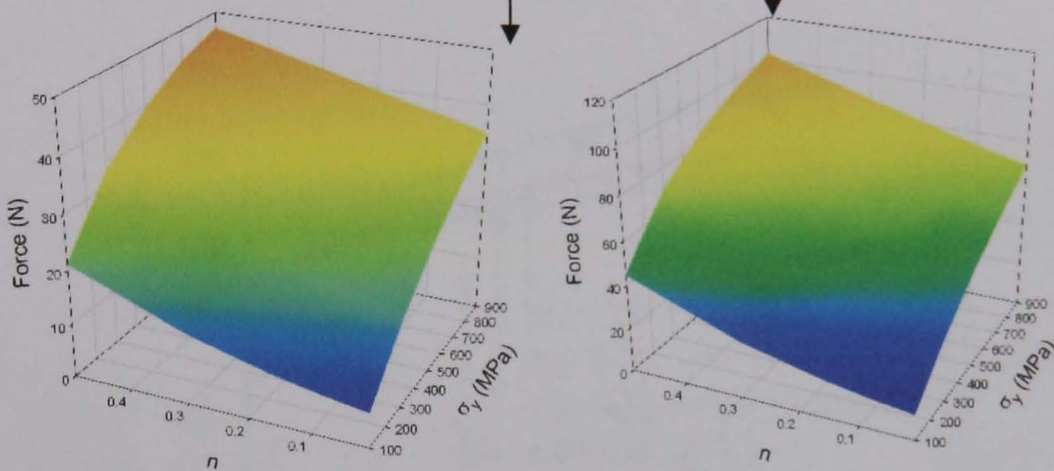


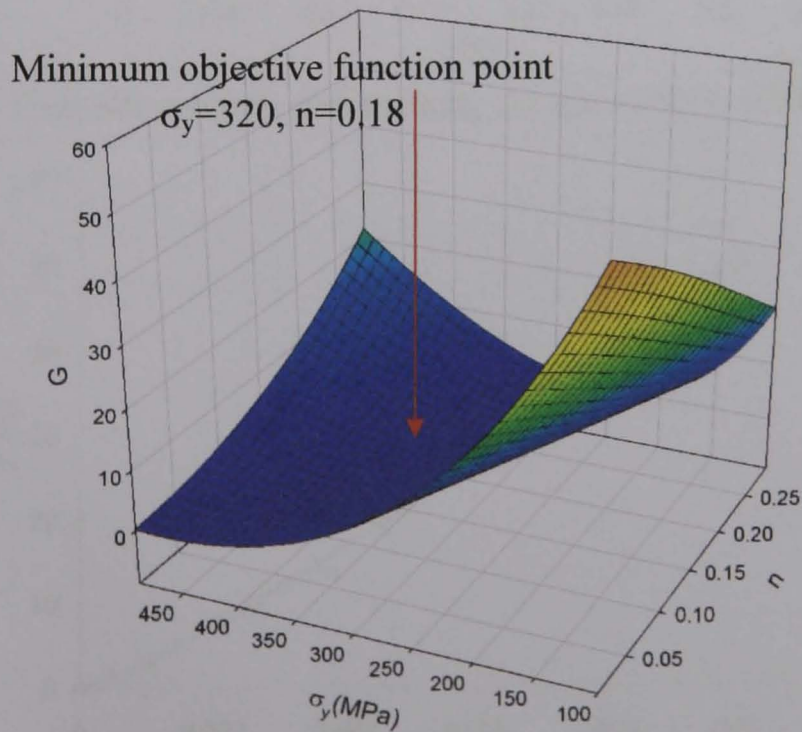
Figure 4.21 Typical predicted properties with comparable objective functions for a range of materials showing the prediction from single Knoop indenter is not unique. The point highlighted by the dotted line represents the true material data.



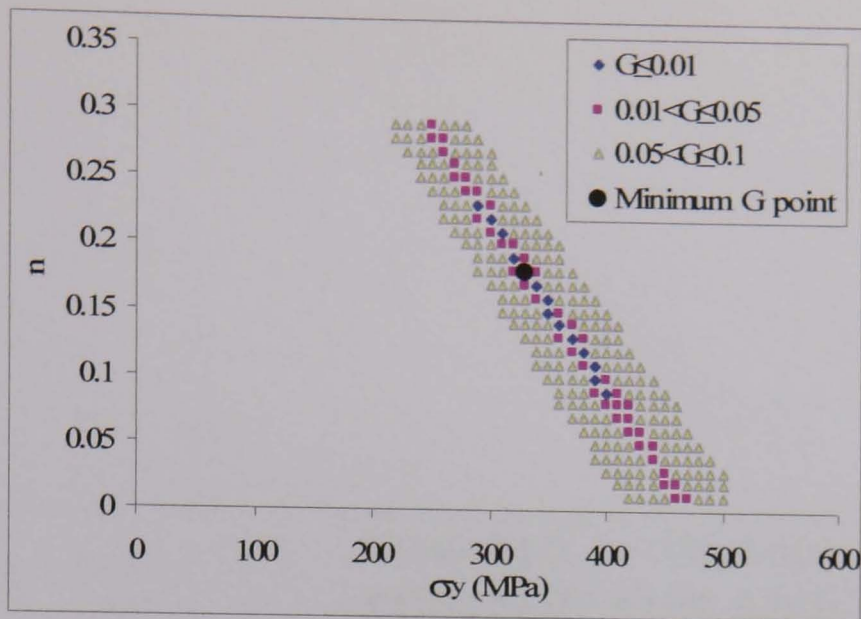
(a) Initial input data with the spherical indenter ($R=0.5\text{mm}$).



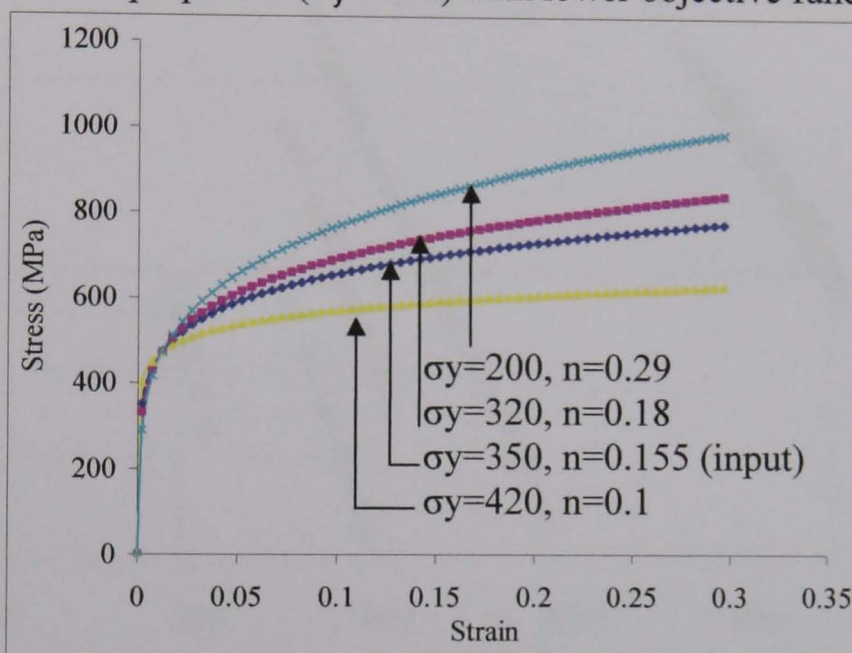
(b) Simulation space at indentation depths of 0.005 and 0.009 mm.



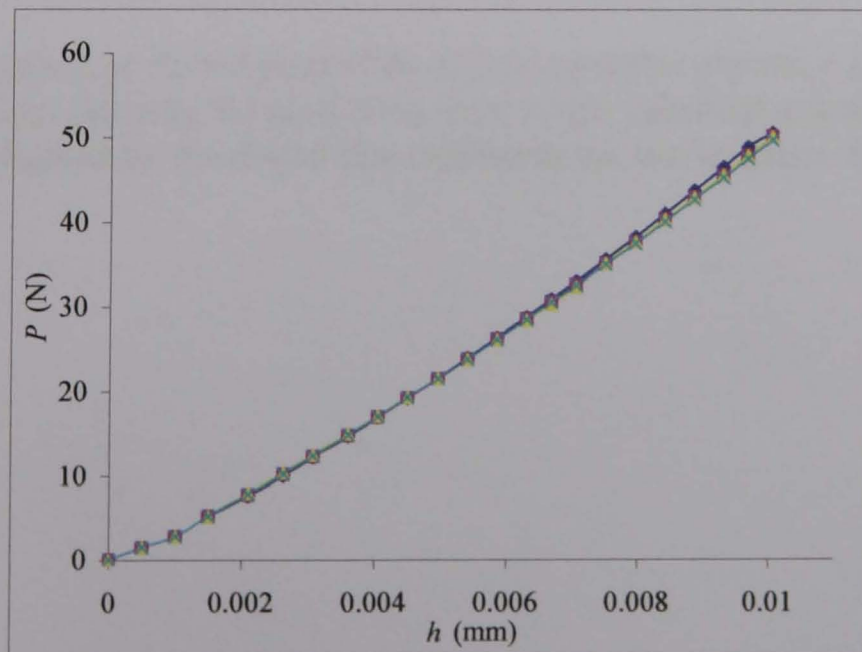
(c) Surface plot of objective functions vs. the material properties (σ_y and n).



(d) Plot of material properties (σ_y and n) with lower objective function values.



(e) True stress-strain curves using the data with $G \leq 0.01$ in (d).



(f) Comparison between the predicted indentation curves using the material sets in (e) and the original input data.

Figure 4.22 Typical data searching process and results based on spherical indenter ($R=0.5\text{mm}$).

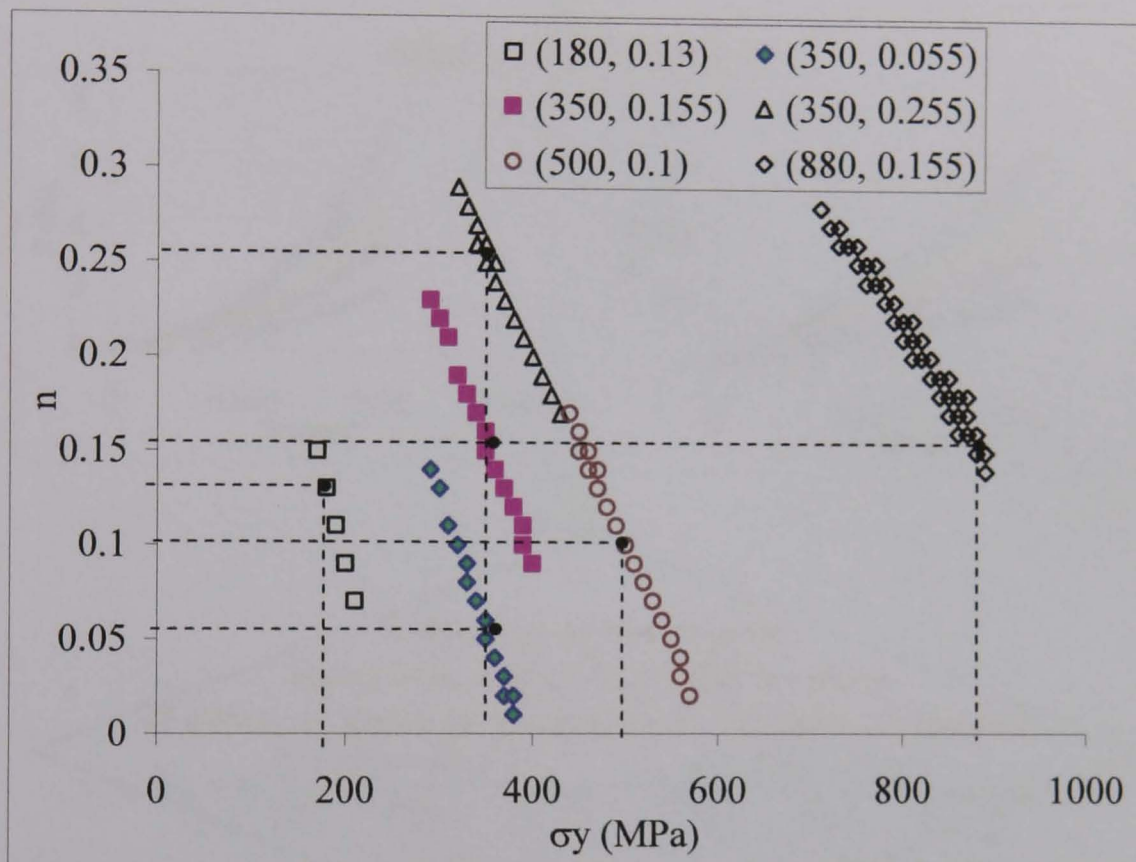
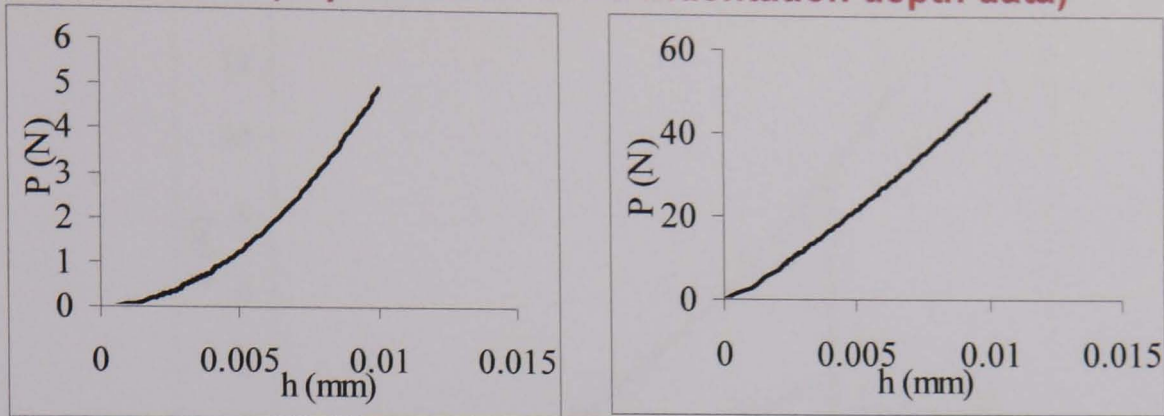
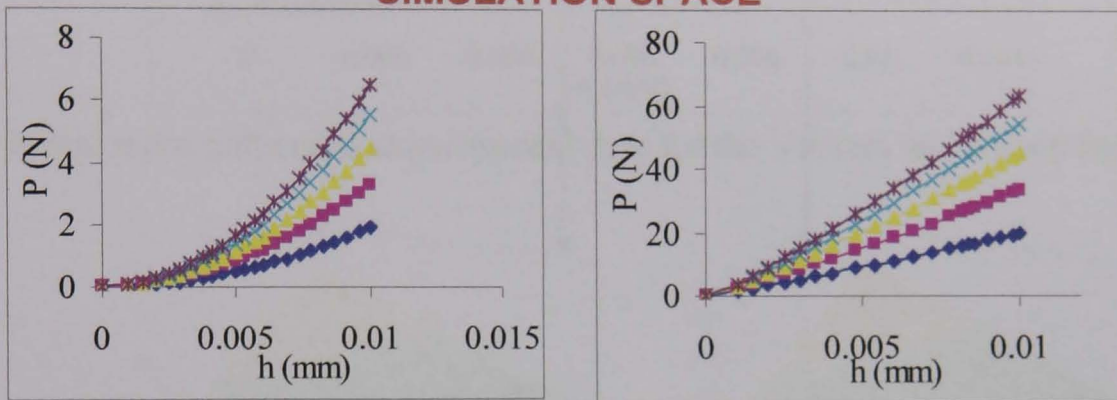


Figure 4.23 Typical predicted properties with comparable objective functions for a range of materials showing the prediction from single spherical indenter is not unique. The point highlighted by the dotted line represents the true material data.

INPUT (experimental force-indentation depth data)



SIMULATION SPACE



Comparison between the input data and numerical $P-h$ curves of different material properties by Objective Function

$$G_S = \ln \sum_{i=1}^n \left(\frac{F_{i,e} - F_{i,n}}{F_{i,e}} \right)^2_{\text{Indenter1}} + \ln \sum_{i=1}^n \left(\frac{F_{i,e} - F_{i,n}}{F_{i,e}} \right)^2_{\text{Indenter2}}$$

σ_y and n

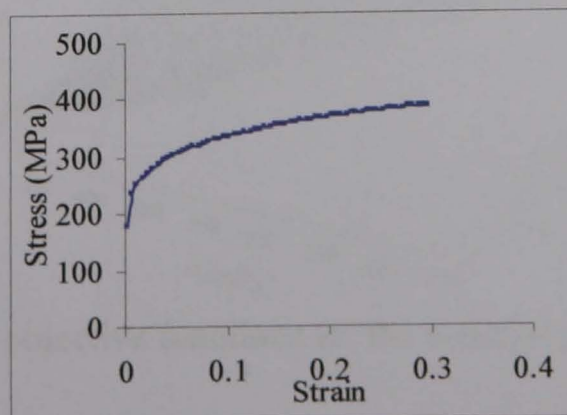
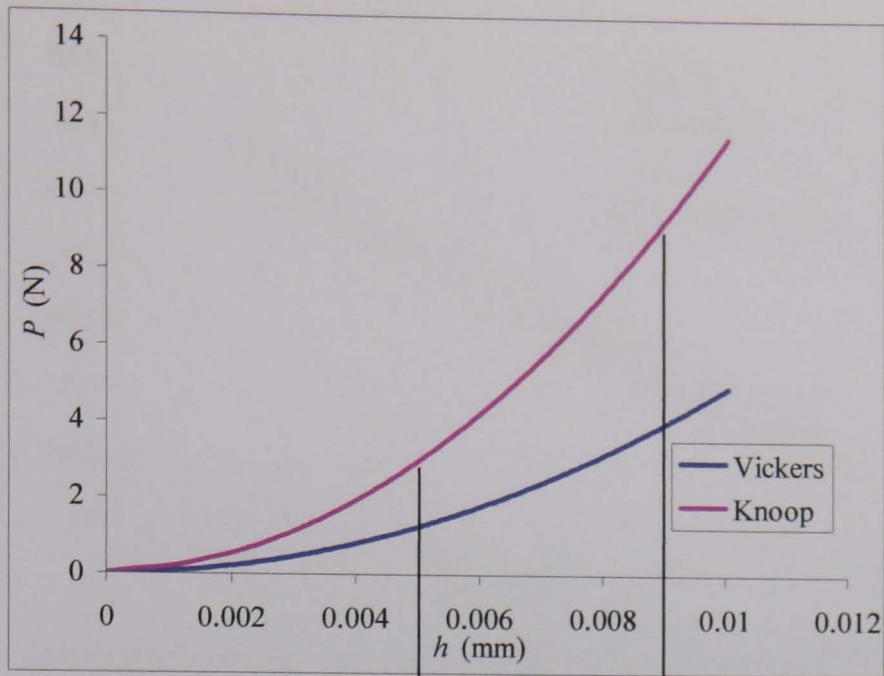
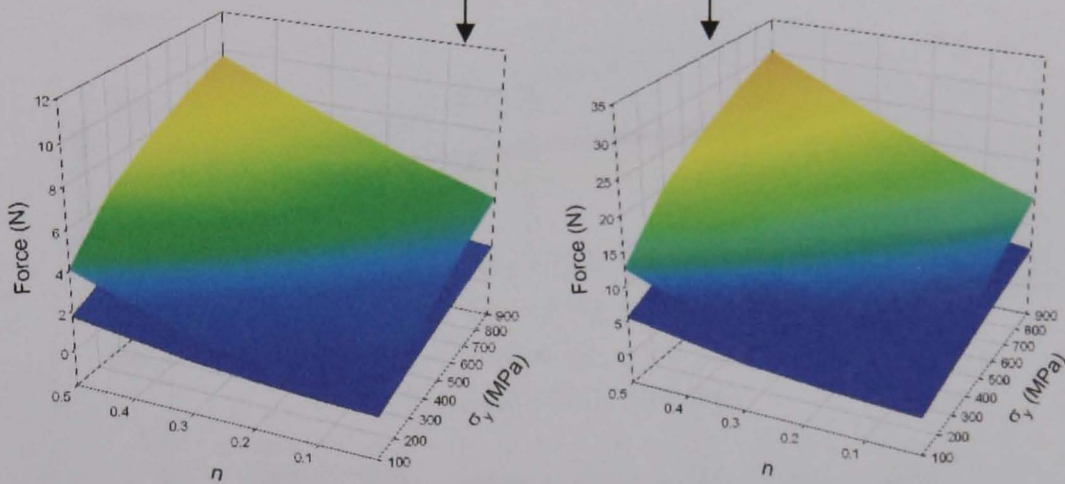


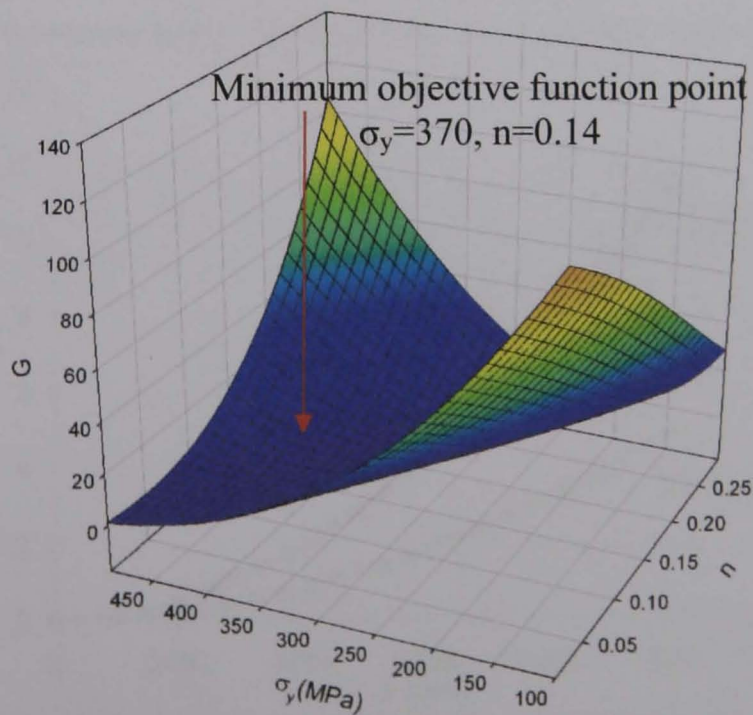
Figure 4.24 Flow chart showing the inverse FE modelling approach based on the dual indenters method.



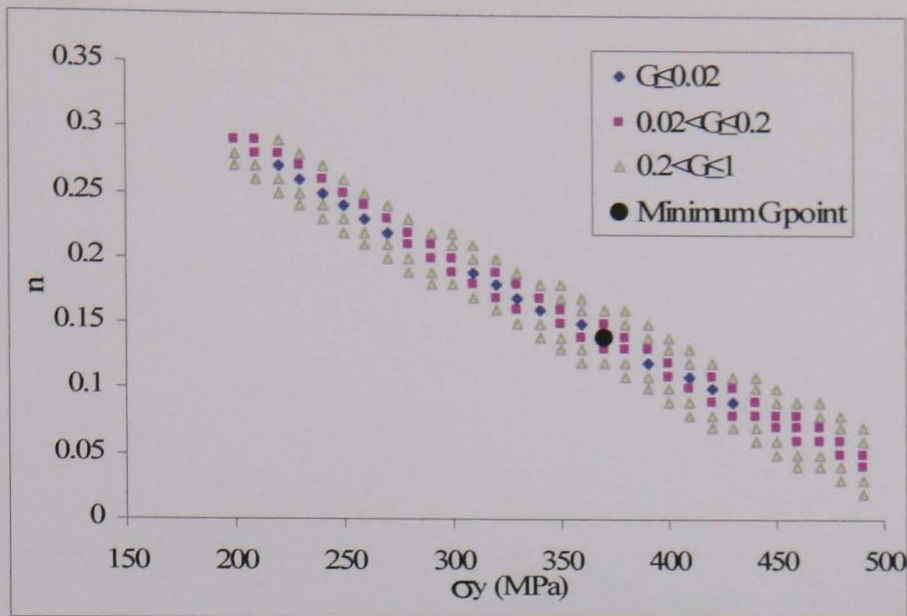
(a) Initial input numerical experimental data for the Vickers and Knoop indenters.



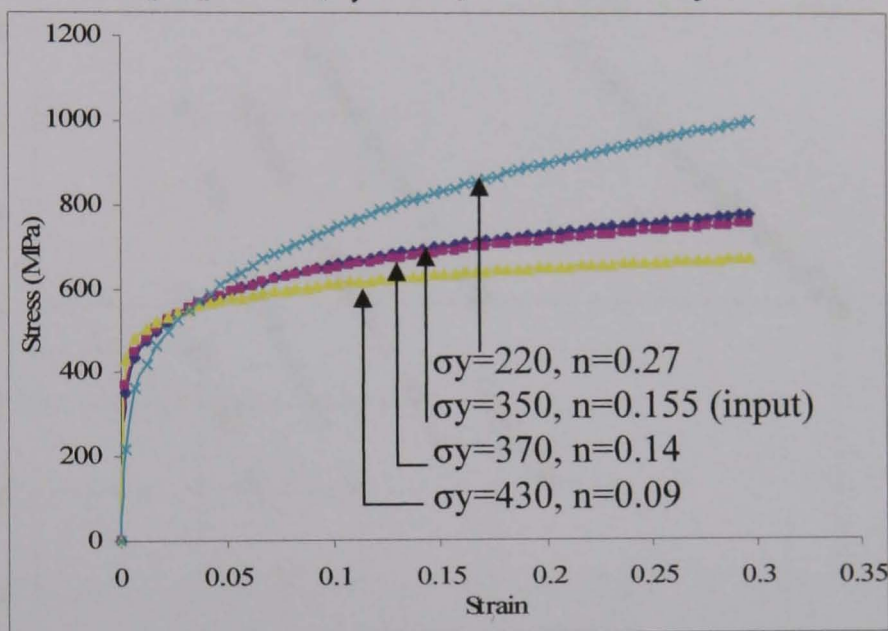
(b) Simulation space at indentation depths of 0.005 and 0.009 mm.



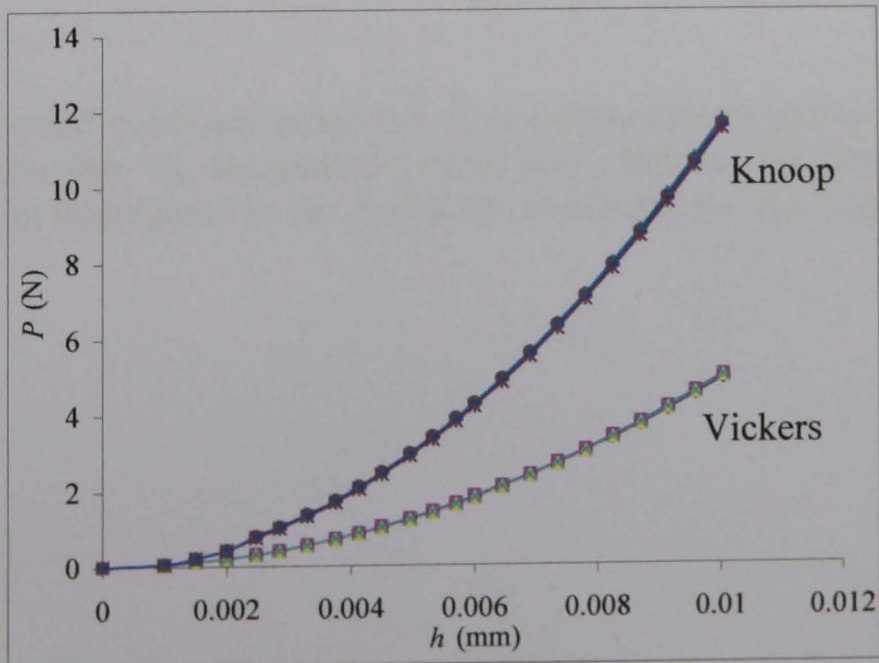
(c) Surface plot of objective functions vs. the material properties (σ_y and n).



(d) Plot of material properties (σ_y and n) with lower objective function values.



(e) True stress-strain curves using the data with $G \leq 0.02$ in (d).



(f) Comparison between the predicted indentation curves using the material sets in (e) and the original input data.

Figure 4.25 Typical data searching process and results based on the dual indenters method (Vickers+Knoop).

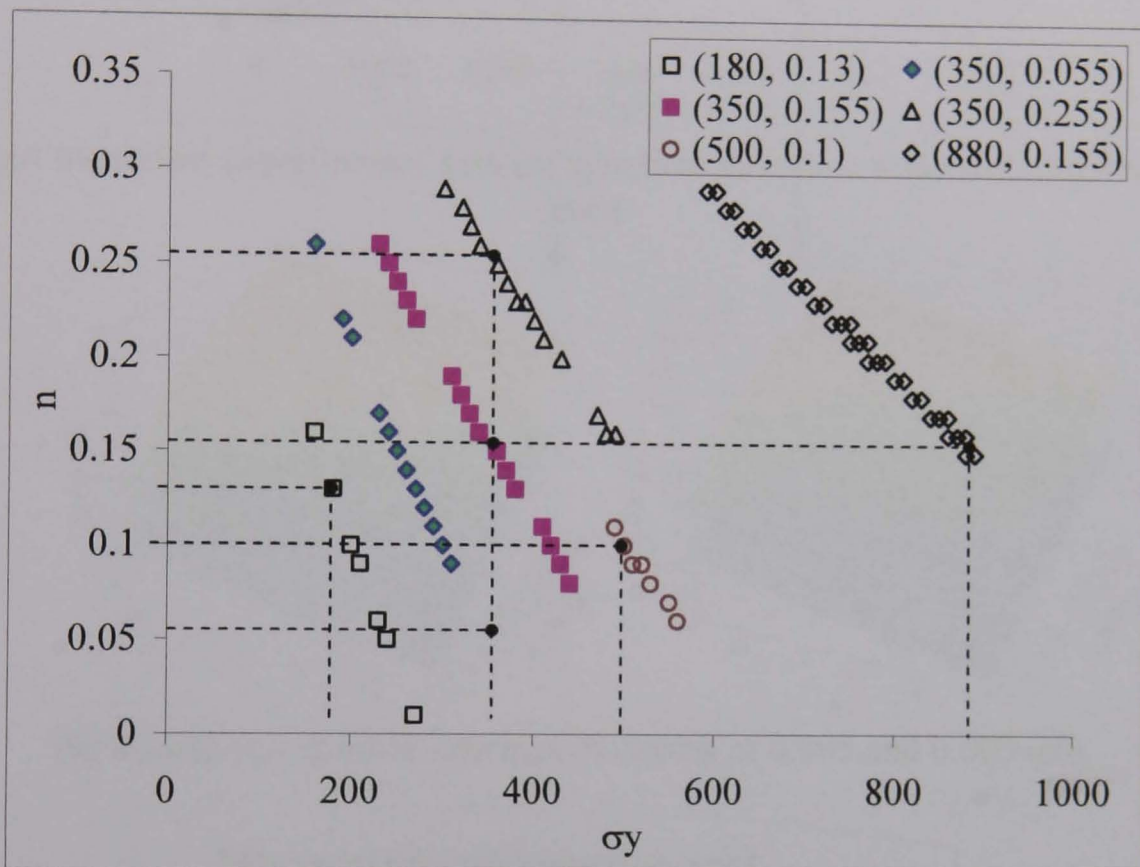
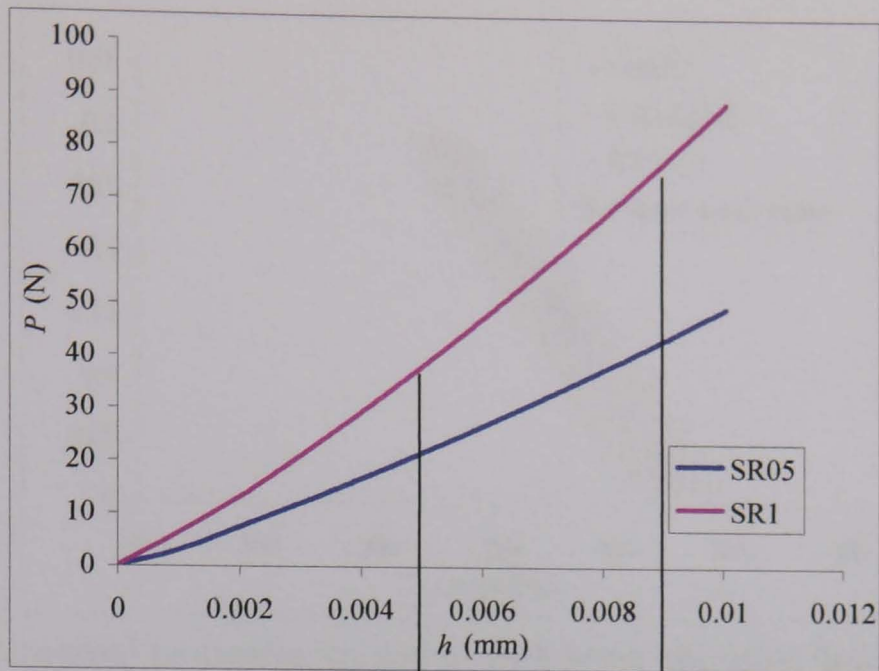
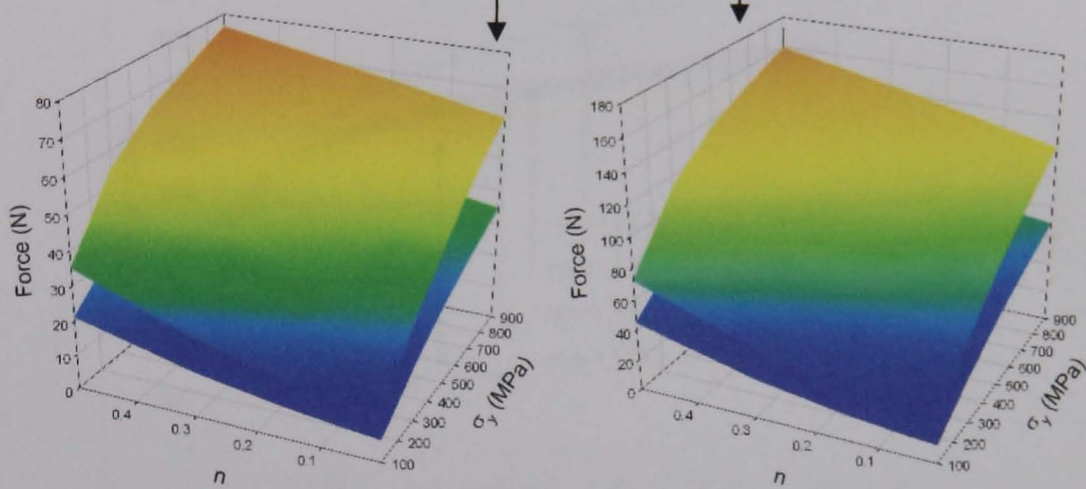


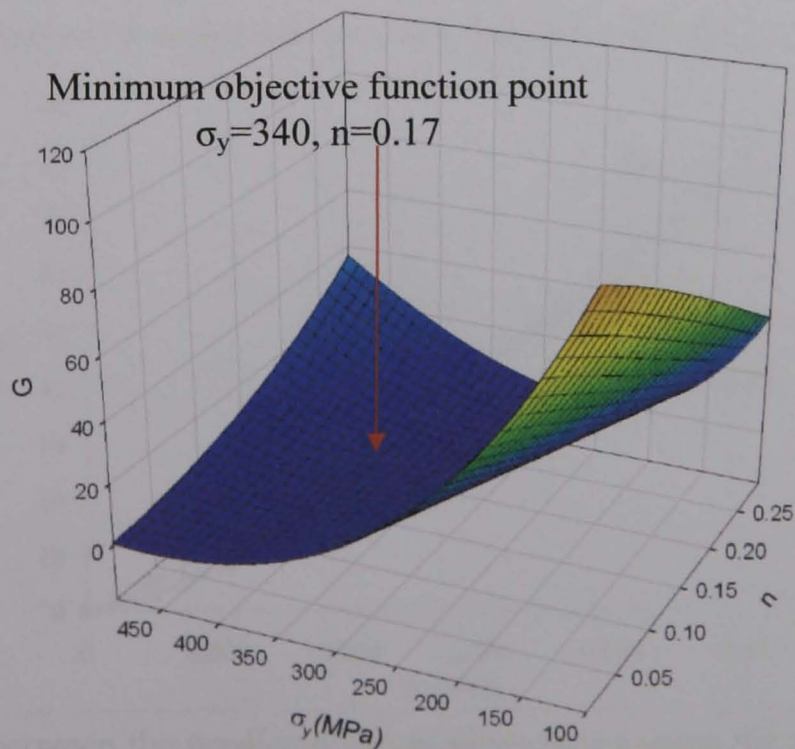
Figure 4.26 Typical predicted properties with comparable objective functions for a range of materials showing the prediction from dual indenters (Vickers+Knoop) is not unique. The point highlighted by the dotted line represents the true material data.



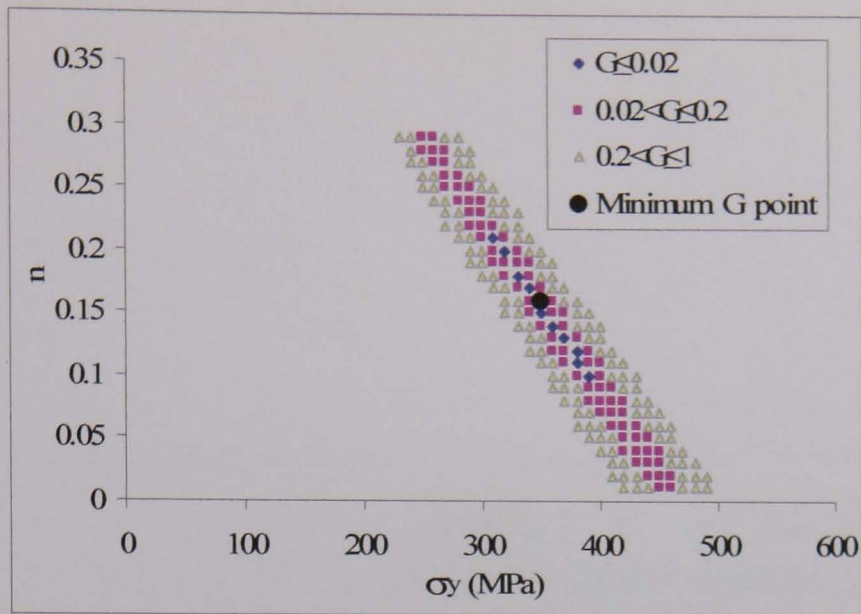
(a) Input numerical experimental data for spherical indenters with radii of 0.5 mm and 1 mm.



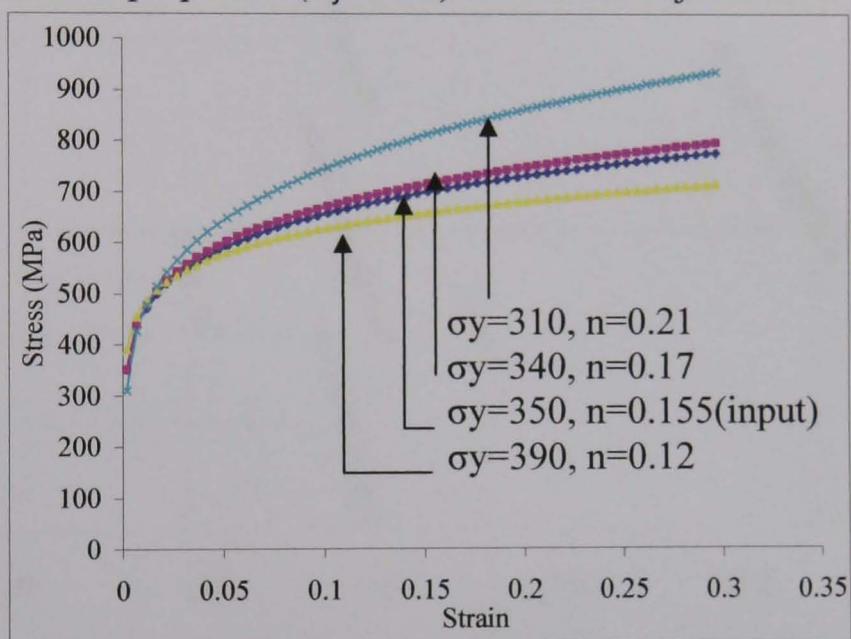
(b) Simulation space at indentation depths of 0.005 and 0.009 mm.



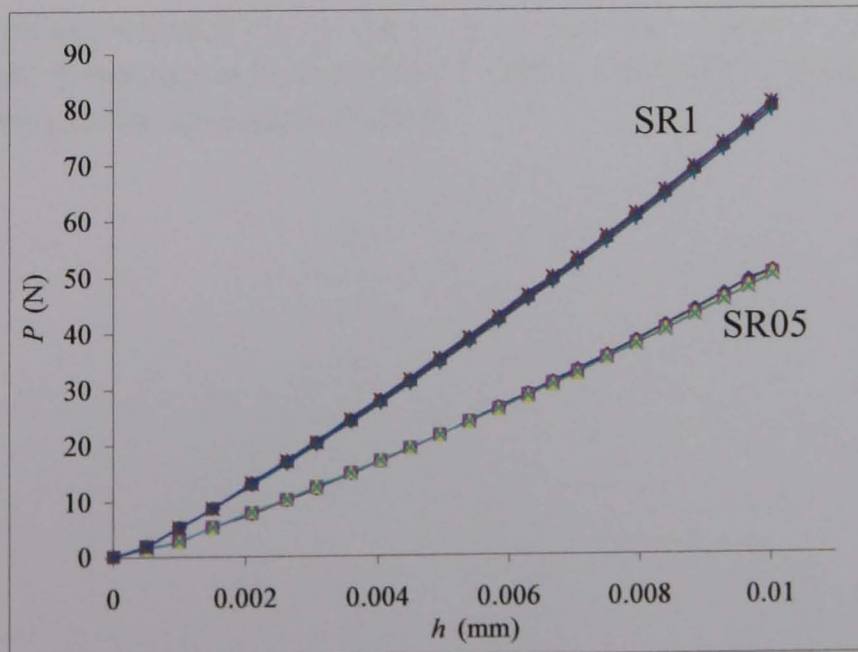
(c) Surface plot of objective functions vs. the material properties (σ_y and n).



(d) Plot of material properties (σ_y and n) with lower objective function values.



(e) True stress-strain curves using the data with $G \leq 0.02$ in (d).



(f) Comparison between the predicted indentation curves using the material sets in (e) and the original input data.

Figure 4.27 Typical data searching process and results based on dual indenters method (Spherical + Spherical).

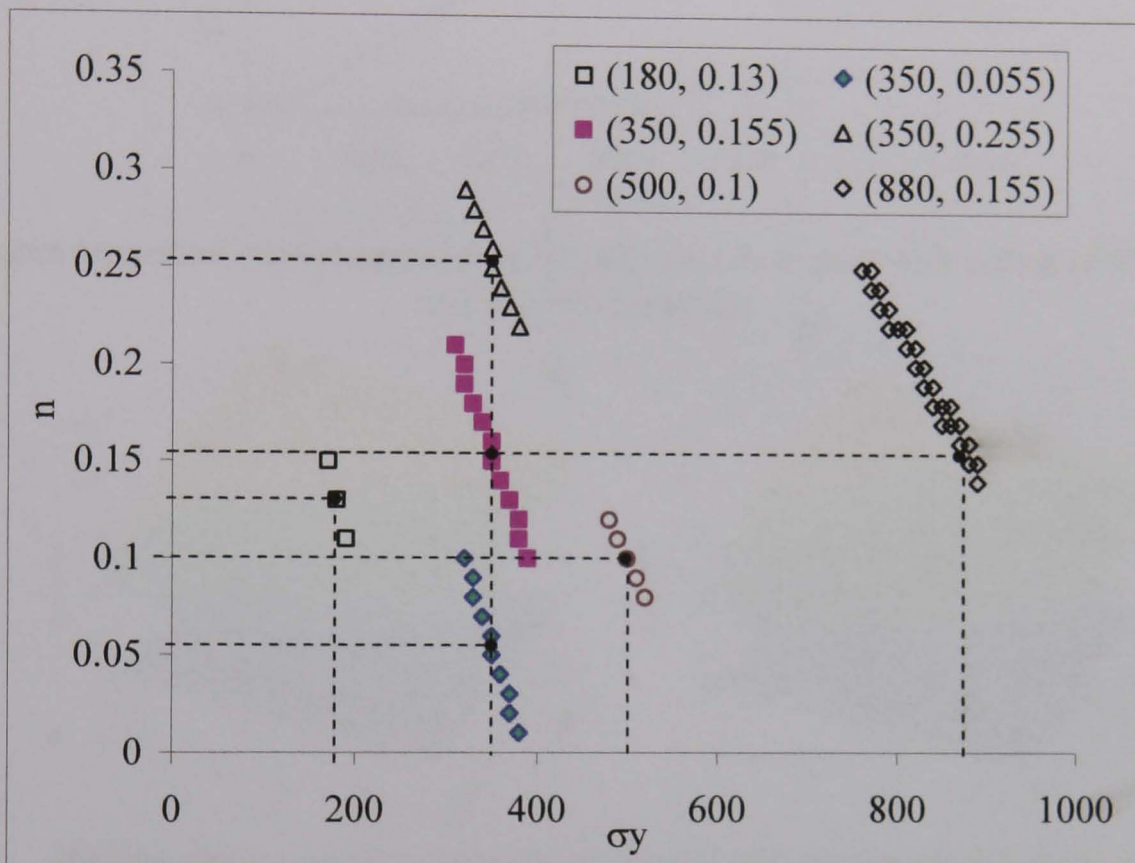
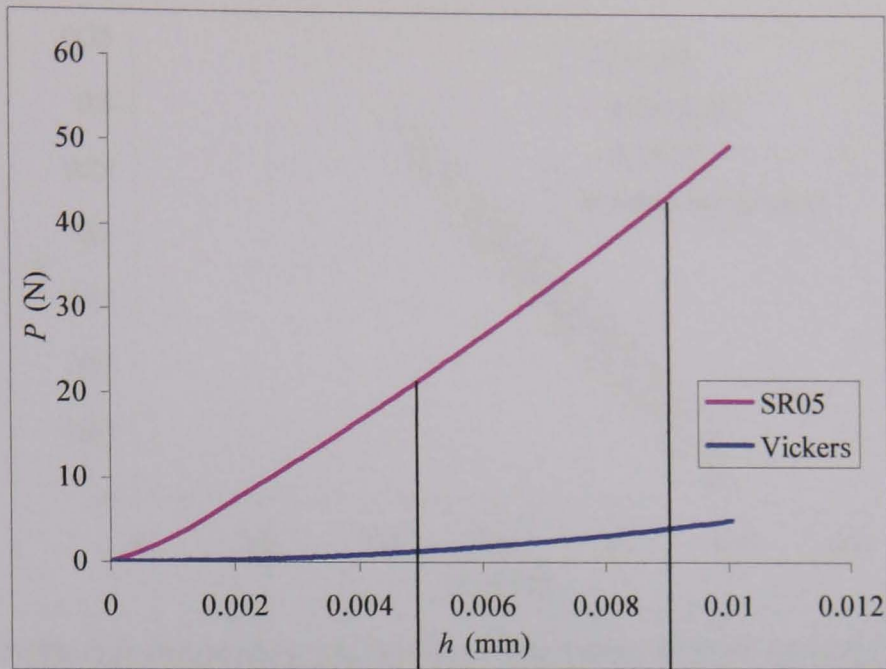
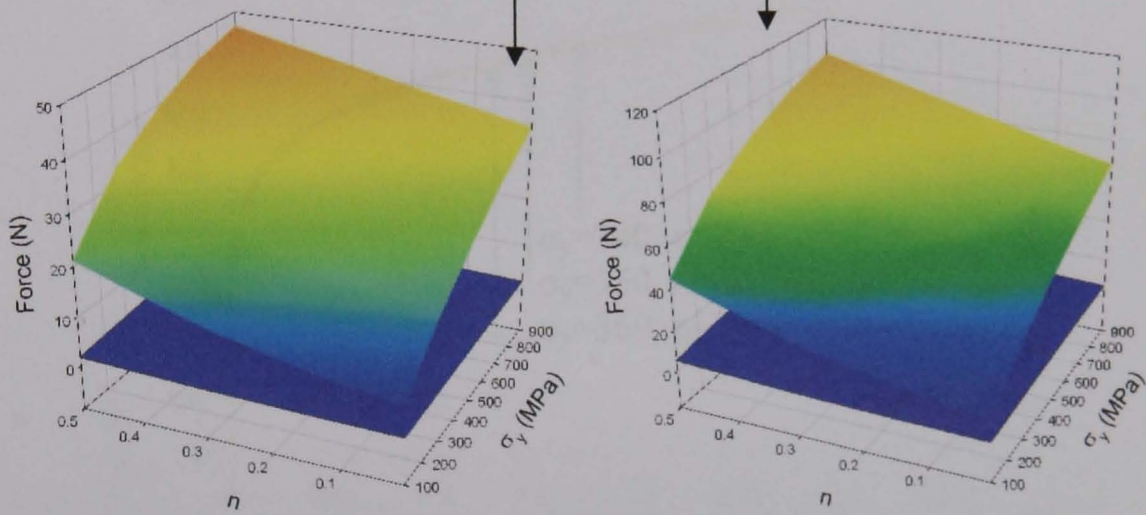


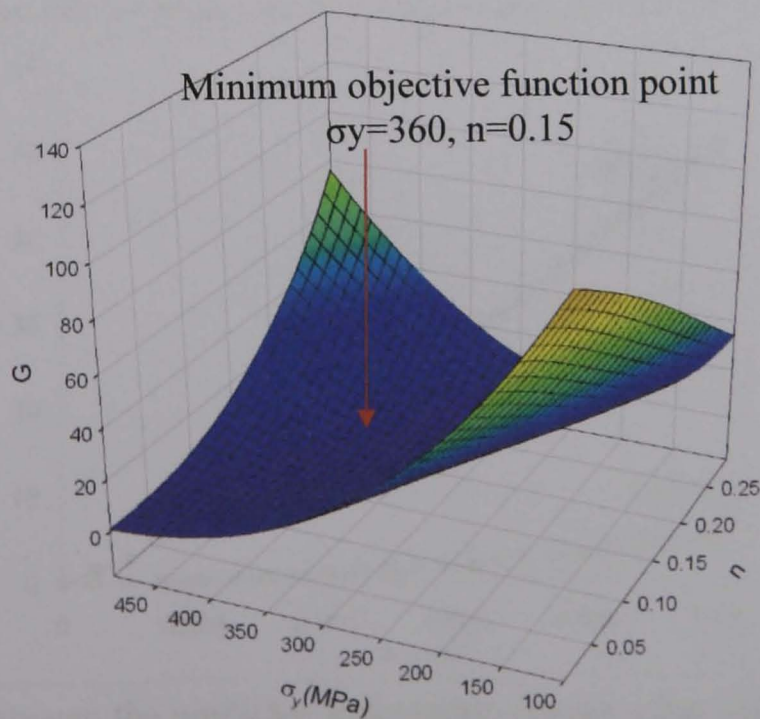
Figure 4.28 Typical predicted properties with comparable objective functions for a range of materials from dual indenters (SR05+SR1). The point highlighted by the dotted line represents the true material data.



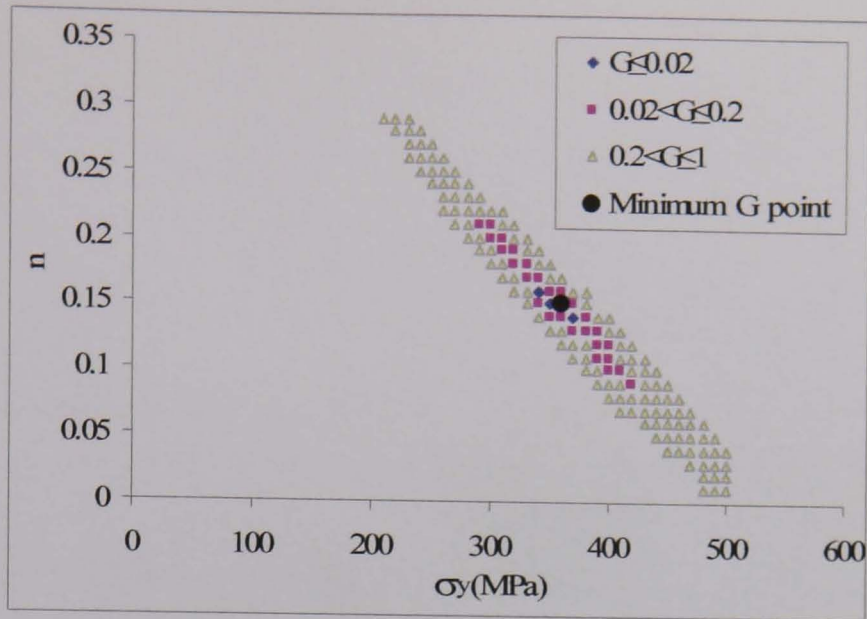
(a) Input numerical experimental data for spherical indenters with radius of 0.5 mm and Vickers indenter.



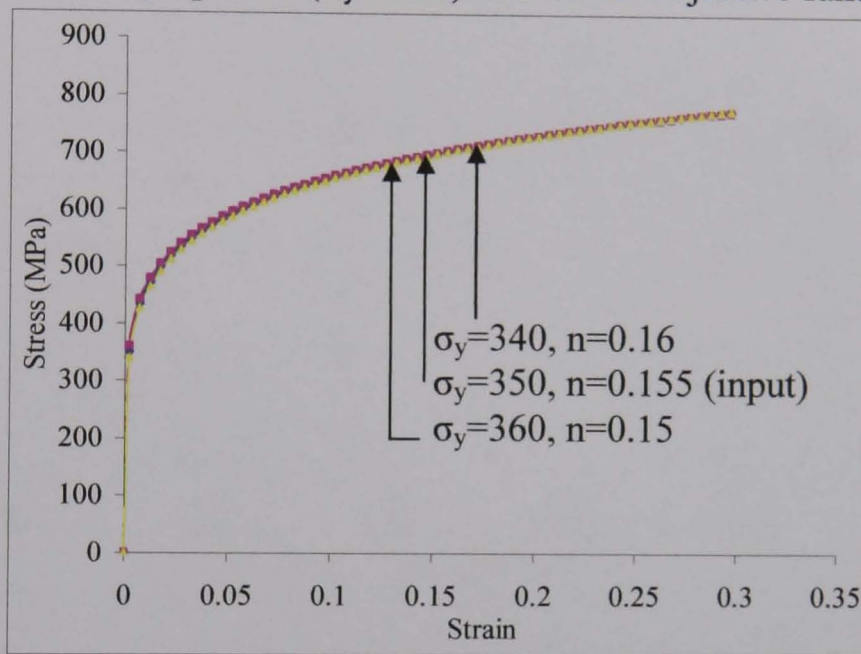
(b) Simulation space at indentation depths of 0.005 and 0.009 mm.



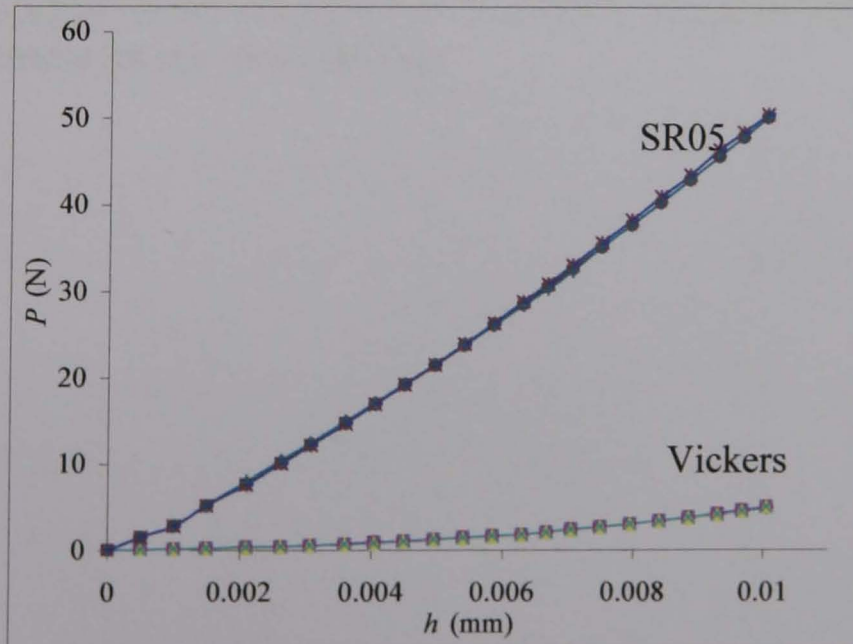
(c) Surface plot of the objective functions over a range of material properties with dual indenters (Vickers indenter and spherical indenter ($R=0.5\text{mm}$)).



(d) Plot of material properties (σ_y and n) with lower objective function values.



(e) True stress-strain curves using the data with $G \leq 0.02$ in (d).



(f) Comparison between the predicted indentation curves using the material sets in (e) and the original input data.

Figure 4.29 Typical data searching process and results based on dual indenters method (Vickers + Spherical).

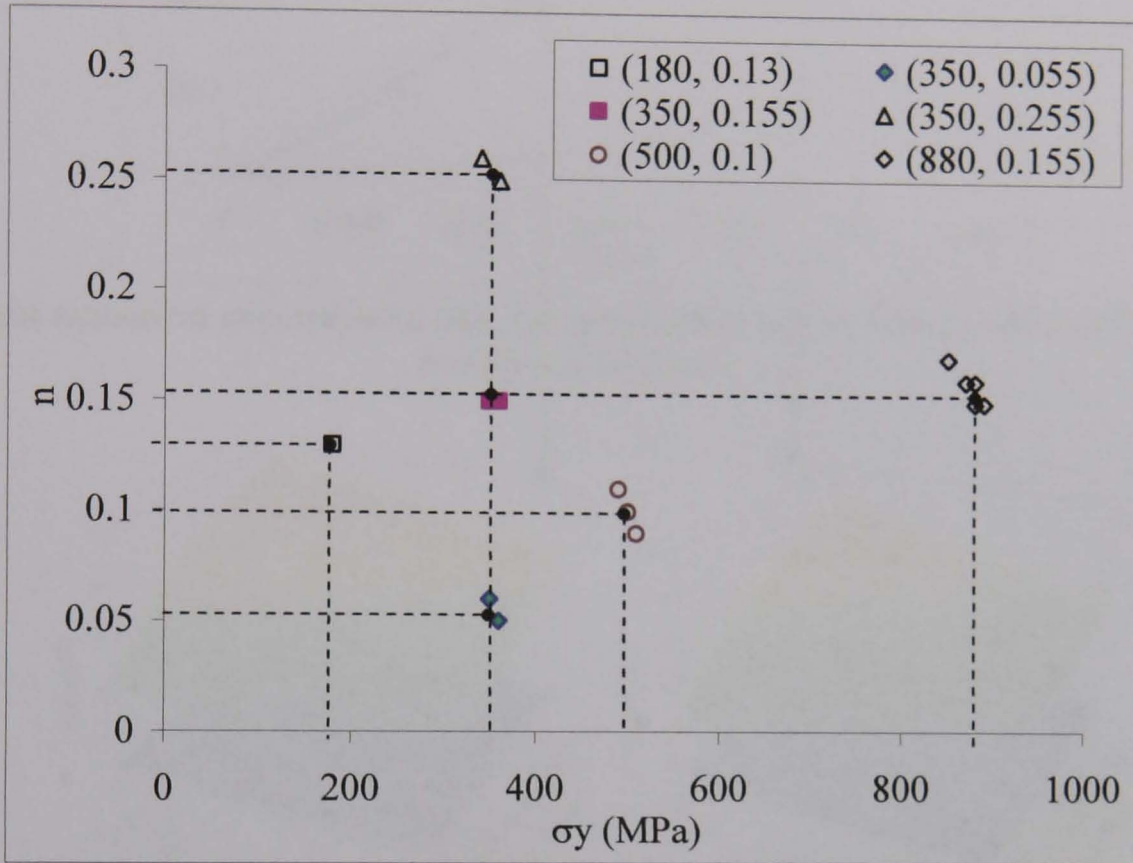
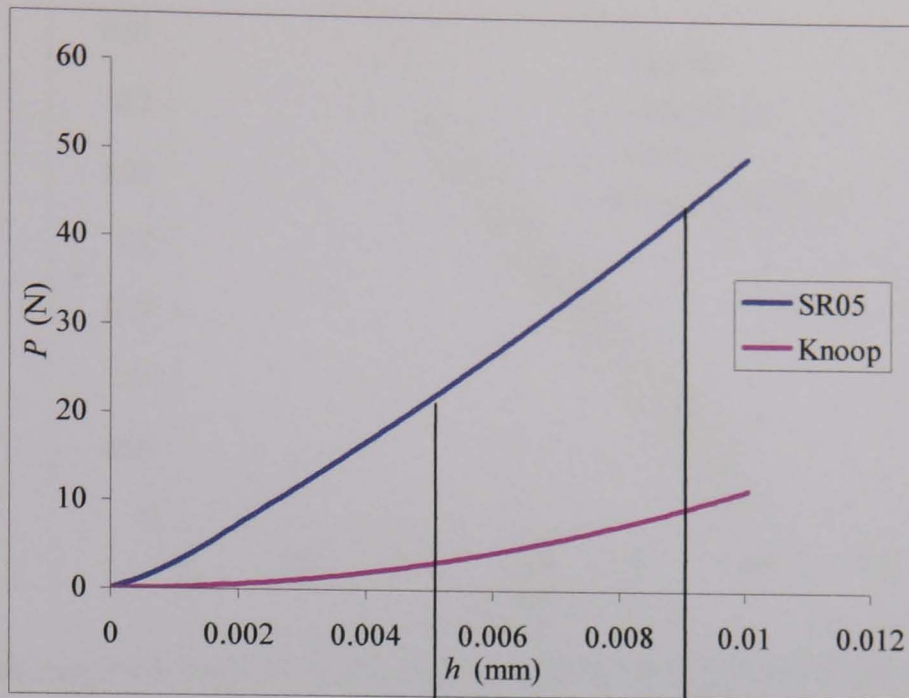
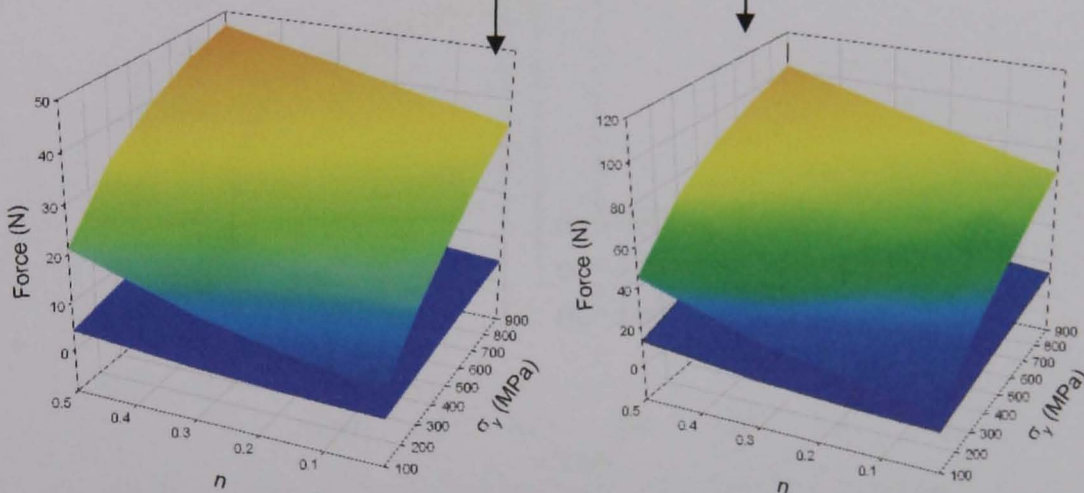


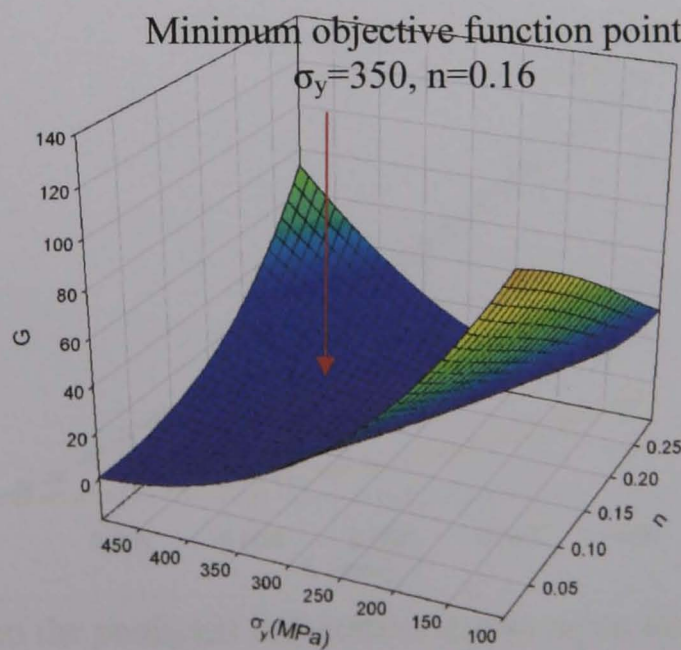
Figure 4.30 Typical predicted properties with comparable objective functions for a range of materials from dual indenters (Vickers+SR05). The point highlighted by the dotted line represents the true material data.



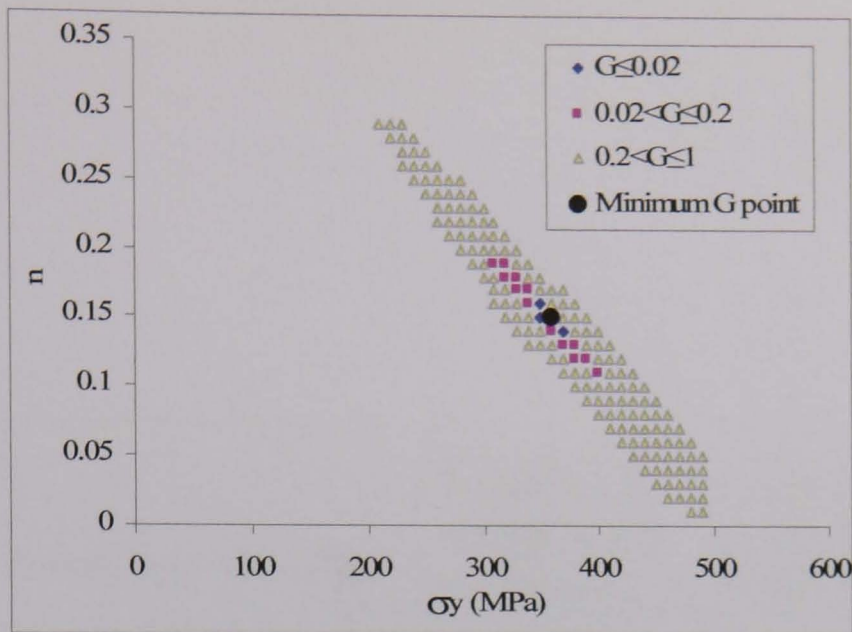
(a) Input numerical experimental data for spherical indenters with a radius of 0.5 mm and Knoop indenter.



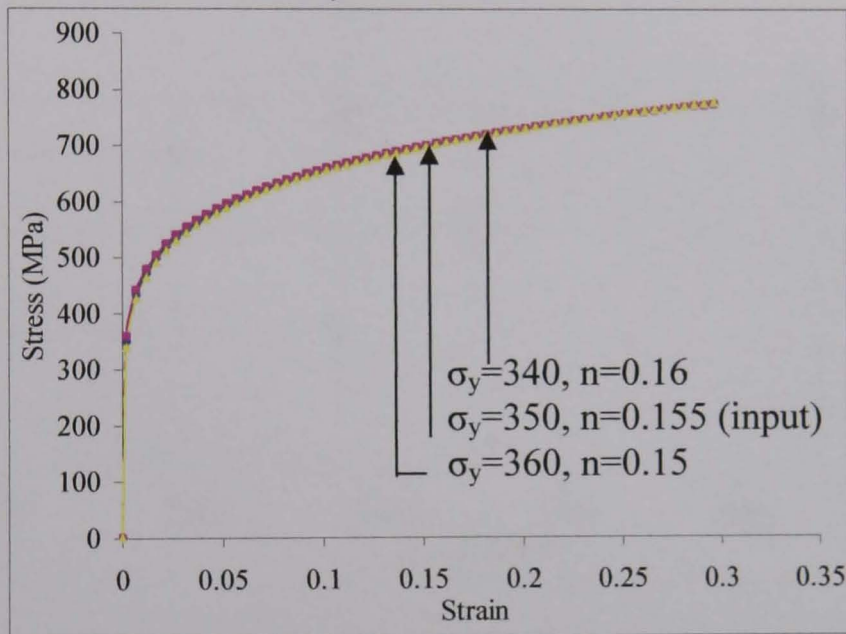
(b) Simulation space at indentation of 0.005 and 0.009 mm.



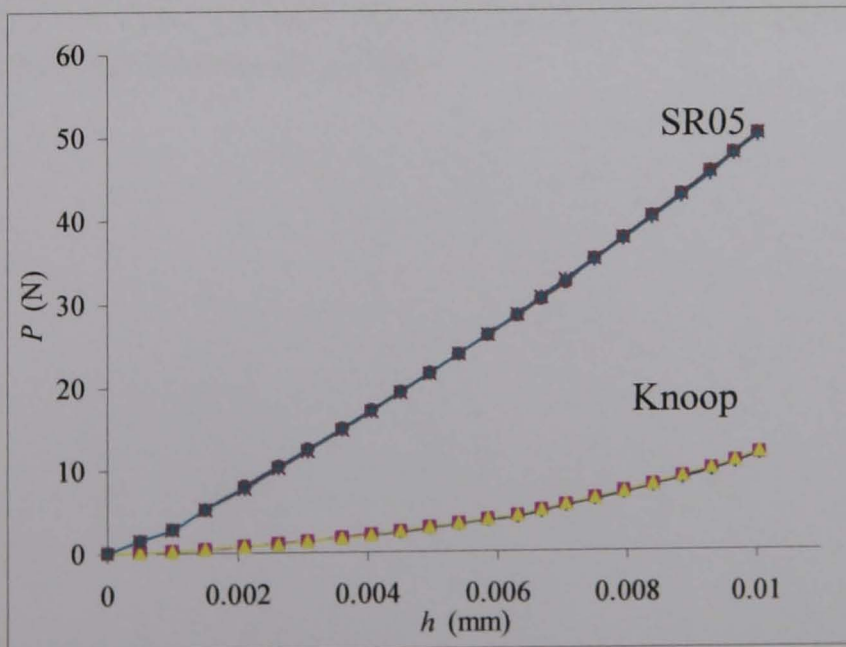
(c) Surface plot of the objective functions over a range of material properties with dual indenters (Knoop indenter and spherical indenter ($R=0.5$ mm)).



(d) Plot of material properties (σ_y and n) with lower objective function values.



(e) True stress-strain curves using the data with $G \leq 0.02$ in (d).



(f) Comparison between the predicted indentation curves using the material sets in (e) and the original input data.

Figure 4.31 Typical data searching process and results based on dual indenters method (Knoop+Spherical).

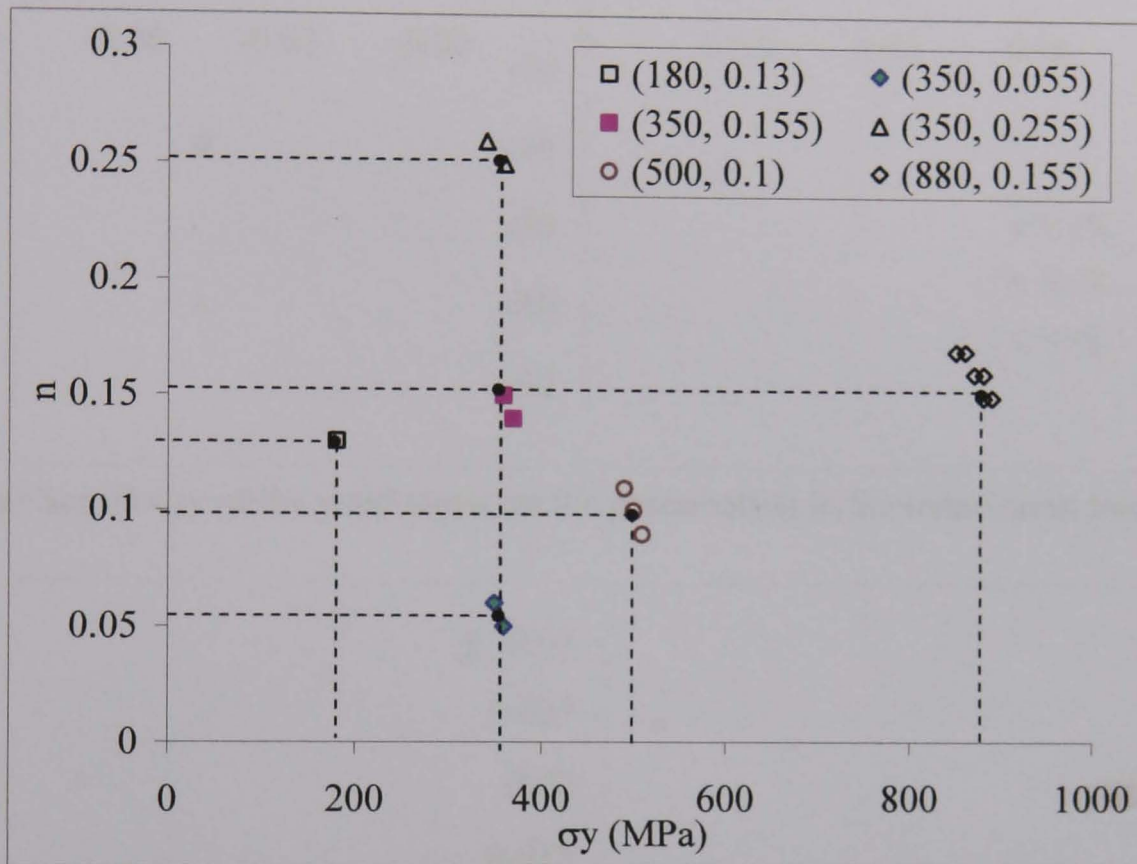
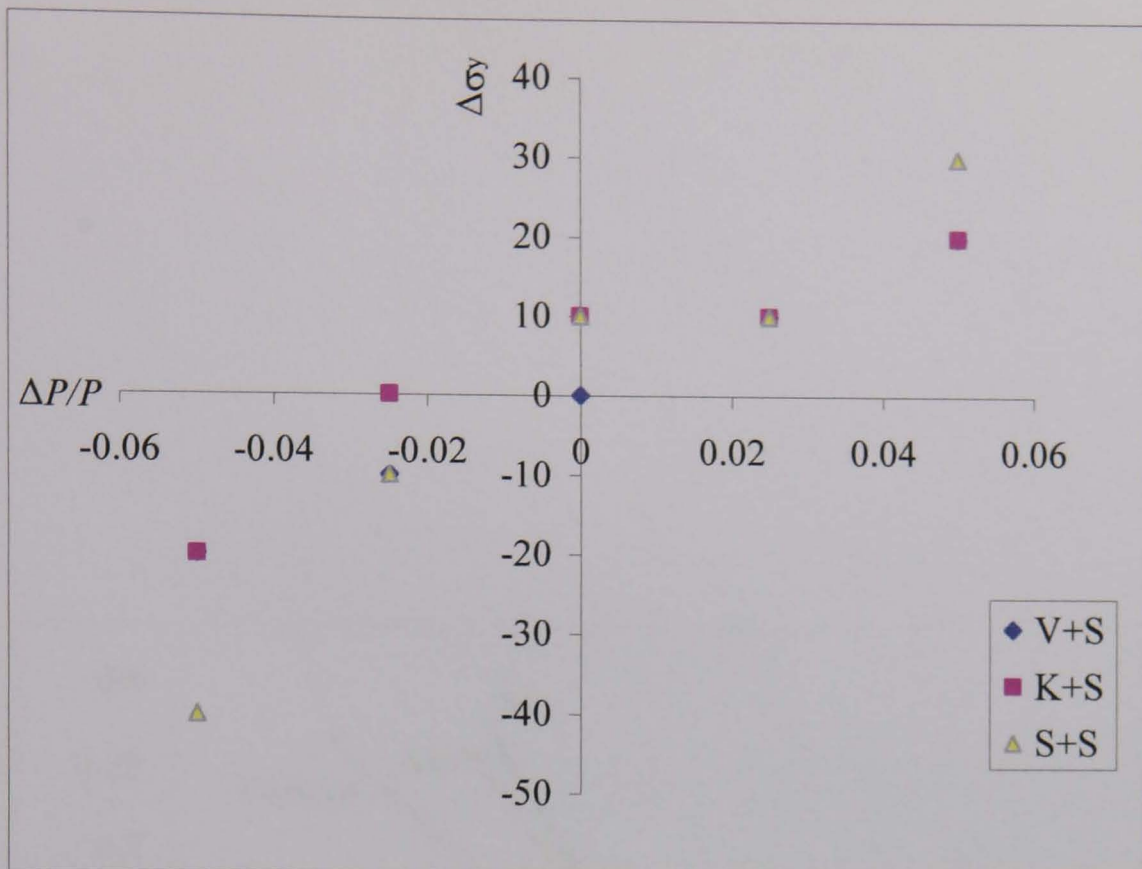
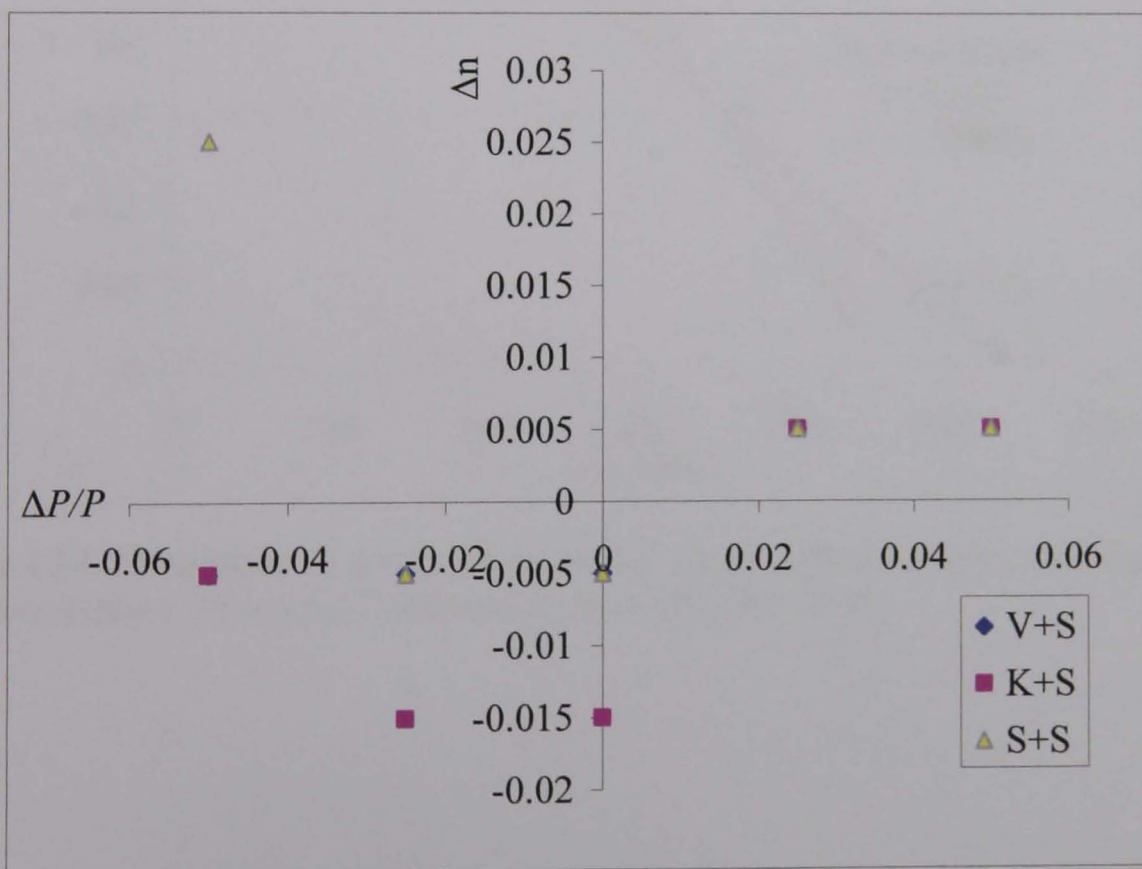


Figure 4.32 Typical predicted properties with comparable objective functions for a range of materials from dual indenters (Knoop+SR05). The point highlighted by the dotted line represents the true material data.



(a) Sensitivity of the yield stress on the perturbation in the indentation force.



(b) Sensitivity of the work hardening coefficient on the perturbation in the indentation force.

Figure 4.33 Typical sensitivity study results for the three dual indenters methods with an input material property of $\sigma_y=350$ and $n= 0.055$. V+S: Vickers and spherical; K+S: Knoop and spherical; S+S: spherical (R1mm) and spherical (R0.5mm).

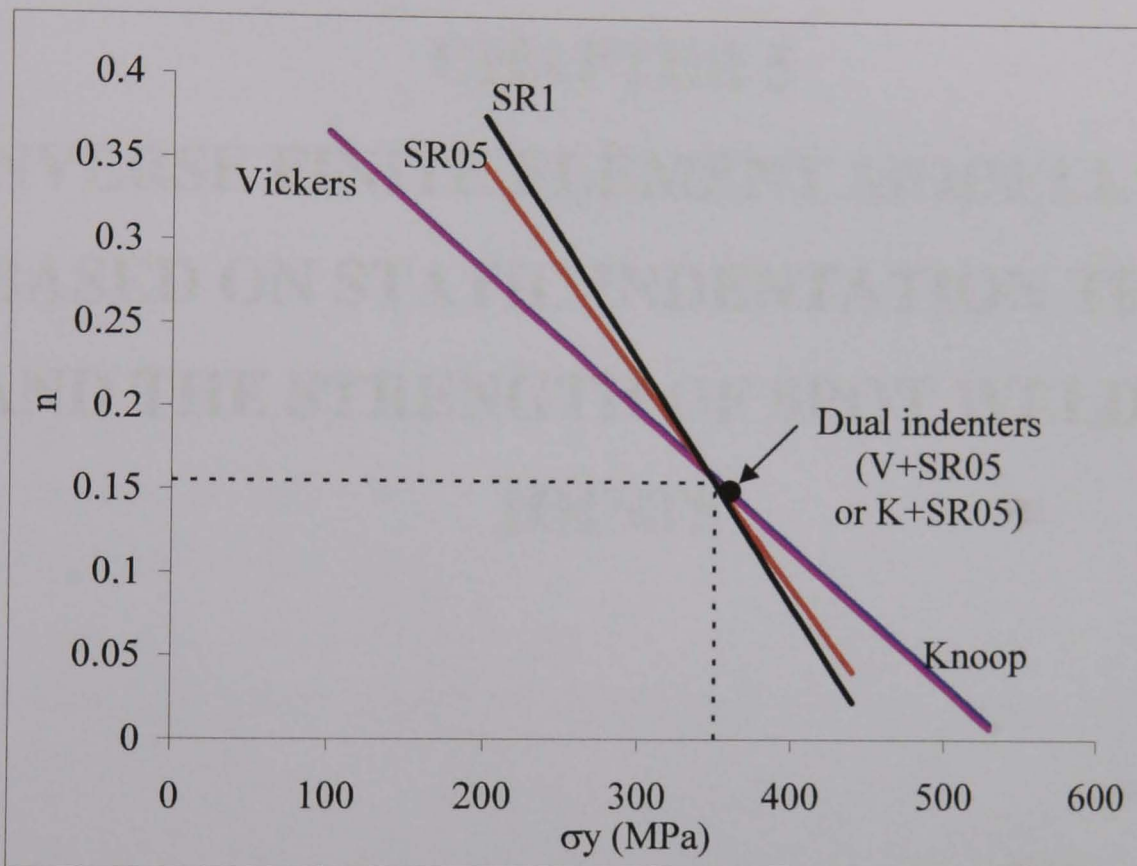


Figure 4.34 Comparison of predicted results by single indenter method and dual indenters method for a typical material set ($\sigma_y=350$, $n=0.155$).

CHAPTER 5

**INVERSE FINITE ELEMENT MODELLING
BASED ON STATIC INDENTATION TEST
AND THE STRENGTH OF SPOT WELDED
JOINTS**

5.1 Introduction

The results presented in chapter 4 have established that the combination of different size/type indenters could give more accurate and robust results. However, approaches using the full force-indentation depth curves ($P-h$) rely on the use of an instrumented indentation machine and sometimes it is not practical/convenient for material systems such as spot welded joints. In this chapter, the dual indenters method has been extended to a more practical approach based on the force-indentation size ($P-d$) data instead of full $P-h$ curves, which can be easily measured on a conventional hardness tester and the position of the test is easy to control using optical microscopy in hardness testing facilities.

The comprehensive study of inverse analysis based on indentation $P-h$ curves, in the previous chapter, showed that the best method to extract the plastic properties is to combine sharp indenter (Vickers or Knoop) and spherical indenters. Preliminary works showed that Knoop indenter is not suitable for spot welded joints due to the effect of gradient material properties over the longitudinal axis direction. Therefore, the combination of Vickers and spherical indentation (V+S) tests was selected to characterise the detailed plastic material properties of the base material and spot welded joints.

In the first section of this chapter, FE models of Vickers and Spherical indentation was developed simulating the loading and unloading process of an indentation test to determine the size of the residual indentation at different loads for elasto-plastic materials. A modified inverse FE modelling approach based on force-indentation size ($P-d$) data has been developed using parametric studies. In the second section, two typical auto steels were characterised using the approach and the results were compared to standard tensile tests of dog-bone shaped and notched specimens. In the third section, the methodology was then used to characterise the material properties of welding zones in spot welded joints of two typical auto steels. In the final section, the predicted material parameters were used to simulate the deformation of spot welded

joints under tensile shear loading; the validated models were further used to predict the effect of nugget size and sheet thickness on the strength of spot welded joints.

5.2 Inverse FE modelling approach based on force–indentation size (P - d) data from static indentation tests

5.2.1 FE models of the Vickers and spherical indentations

Different from continuous indentation test, in a static indentation test, a single load is applied and then withdrawn after a certain period of dwell time (typically a loading time of 18 seconds) and the size of the indentation is measured under an optical microscope. It is easier to operate and commonly used without the requirement of complicated facilities for force measurement and displacement control. In a Vickers test, the indenter is normally made of diamond, which can be treated as a rigid body in the FE modelling. A tungsten carbide sphere (96% WC) (Precision Ball & Gauge Co.) has been used as the spherical indenter to avoid excessive deformation of the indenter itself.

Figure 5.1 shows the FE indentation models for the Vickers and spherical indenters. The model for the Vickers indentation is similar to the one shown in Figure 4.1, where the indenter was treated as a rigid body. In the model, a predefined load is applied then the load is released and leaves a residual indentation on the surface. During the mesh construction, careful steps were taken to minimise the instability which can occur near the perimeter of the indentation. Different from Vickers indenters, spherical indenter is fully axial symmetric. The specimen size is large enough to avoid potential sample size effect. The bottom line was fixed in all degrees of freedom (DOF) and the central line was symmetrically fixed in z direction. Contact has been defined at the indenter and the sample surface with a friction coefficient of 0.15. This is commonly used for metal indenter contact.

In the FE model of spherical indentation test, the element types used are CAX4R and CAX3, which are 4-node and 3-node bilinear axisymmetric quadrilateral with reduced integration, hourglass control elements. A gradient meshing scheme has been developed for different regions. The mesh size is $5\mu\text{m}$ in the regions underneath and around the indenter and the mesh sizes of other regions from the nearest region to the outer edge are $10\mu\text{m}$, 0.05mm and 0.1mm ; the mesh of the transitional regions is

triangle free mesh. The indenter was also assigned similar mesh scheme (fine mesh density on the surface and coarse mesh inside) and the material was considered as a pure elastic material (tungsten carbide, $E=600\text{GPa}$). In the FE model of Vickers indentation, the element type used is C3D8R (a reduced-integration element used in stress /displacement analyses), the same as shown in chapter 4. The finite element models for the Vickers and spherical indentation contain 7200 elements and 4086 elements. Similar mesh sensitivity tests (Section 4.2.3) have been performed and showed the meshing scheme gives accurate result and optimum computing resources.

In the model, a predefined load corresponding to the load in the tests (1, 2, 3, 5N) was applied onto the indenter and then released; the residual indentation left on the surface is measured and recorded. Figure 5.2 shows a typical loading and unloading curve of Vickers indentation with an applied load of 5 N. The predicted residual indentation is shown in Figure 5.2 (b); its size can be determined by measuring the length of the opposite diagonals designated 'd'. Similar to the Vickers indentation test model, a predefined load corresponding to the load in the spherical tests (18.6, 26.02, 37.04, 52.72N) was applied onto the indenter. Figure 5.3 shows a typical loading and unloading curve of a spherical indentation with an applied load of 37.04 N. The residual indentation is shown in Figure 5.3 (b); its size can be determined by measuring the length of the diameter designated 'd'. This mimicks the operations involved in a micro hardness testing process, in which the operator measures the size of the indentation under an optical microscope. The force indentation size data is used to represent the plastic resistance of the materials, which is associated with the two main plastic parameters, the yield stress, σ_y , and the work hardening coefficient, n . The material properties can be predicted by matching the experimental data with numerical results. The simplicity of the testing and requirement of the facility make this a good alternative to continuous indentation process for practical applications. The accuracy and validity of such approach is assessed in the next two sections.

5.2.2 Inverse FE analysis based on static indentation tests

Figure 5.4 is a flow chart showing the inverse modelling process utilising force-indentation size data. The program consists of three main parts — experimental data,

FE modelling data/simulation space and the inverse program based on an objective function. It is similar to the program using continuous indentation curves (Figure 4.16), but the experimental data is in the form of force-indentation size ($P-d$). This is taken by performing indentation tests, then measuring the indentation size on the surface. With different applied loads, there are a series of $P-d$ data, which was then compared to a pre-developed simulation space to find a material set giving the best fit between the numerical results and the experimental data.

The simulation space includes a group of force indentation size data ($P-d$) curves from numerical models covering a wide range of material properties. In this case, ' σ_y ' was varied between 100-900 MPa while ' n ' varied between 0.01-0.3, which covers the properties for most of steels. In the searching process, the program calculates the difference between the input data and the numerical $P-d$ data of different material properties within the simulation space. In each case, the optimum material parameters were determined by mapping the objective function (Eq. 5.1).

$$G = \sum_{i=1}^n \left(\frac{F_{i,e} - F_{i,n}}{F_{i,e}} \right)^2 \quad (\text{Eq. 5.1})$$

where :

- G is the objective function that needs to be minimized.
- $F_{i,e}$ is the experimental force of the indenter at the observation i and $F_{i,n}$ is the numerical model force of the indenter at the observation i .
- The number of observation is n (number of indentation point).

When two indenters are used to predict the plastic material properties, the input data are compared to the $P-d$ data in the simulation space for both indenters. The objective function was determined as

$$G_s = \sum_{i=1}^n \left(\frac{F_{i,e} - F_{i,n}}{F_{i,e}} \right)^2_{\text{Vickers}} + \sum_{i=1}^n \left(\frac{F_{i,e} - F_{i,n}}{F_{i,e}} \right)^2_{\text{Spherical}} \quad (\text{Eq.5.2})$$

The simulation space was developed using parametric studies (ABAQUS 6.4). Parametric studies allow the user to generate, execute, and gather the results of multiple analyses that differ only in the values of some parameters. As shown in Figure 5.5, in the initial stage, the potential range of the material parameters was

identified. In this case, the parameters included the yield stress (σ_y) and the work hardening coefficient (n). Multiple FE models with different combinations of material parameters were then automatically generated and solved. In this case, the yield stress varied from 100 to 900 MPa with an increment of 10. The work hardening coefficients used were ranged from 0.01-0.3 with an increment of 0.01, which is sufficiently accurate for practical applications. The simulation space was structured in an excel file, which allows easy interpretation of the data. In the searching process, the objective function is calculated at each indentation load using predefined program in Microsoft excel for each set of material properties (σ_y , n). The overall objective function was determined by the sum over all the data points. The material data which give minimum objective function was defined as the optimum solution.

5.2.3 Validation of the inverse analysis program by blind test

Similar to the procedure in chapter 4, blind tests have been performed with numerical experimental data to assess the accuracy of the program. The results for a wide range of initial input data are listed in Table 5.1. It clearly showed that the work can achieve good accuracy and high level of sensitivity of the results. In the next section, this method is used to predict the material properties of two steels (A and B) and their spot welded joints.

Table 5.1 Blind test results of inverse FE modelling based on force indentation size ($P-d$) data.

| Input data | | Predicted material parameters | | Sensitivity with 3% error | |
|------------|-------|-------------------------------|------|---------------------------|--------------|
| σ_y | n | σ_y | n | $\Delta\sigma_y/\sigma_y$ | $\Delta n/n$ |
| 180 | 0.13 | 180 | 0.13 | 5.56% | -3.85% |
| 350 | 0.055 | 360 | 0.05 | 5.56% | 10.00% |
| 350 | 0.155 | 350 | 0.16 | 2.78% | -3.33% |
| 350 | 0.255 | 350 | 0.26 | 5.56% | -2.00% |
| 500 | 0.1 | 500 | 0.1 | 6.00% | -10.00% |
| 880 | 0.155 | 880 | 0.16 | 5.62% | -3.33% |

5.3 Inverse characterisation of auto steels

5.3.1 Indentation tests and inverse analysis results

Two auto steels were tested using the indentation approach described in the previous section, and the predicted material properties were compared to the results of standard tensile tests. The details of the material have been given in chapter 3. For indentation tests, the samples were sectioned then polished using diamond paste of 6 micrometer. The indentation tests (Vickers and spherical) have been conducted using a standard micro hardness tester (Figure 3.7). The Vickers tests were performed with a standard diamond indenter. The spherical indenter was made of tungsten carbide sphere with a diameter of 1 mm (Precision Ball & Gauge Co).

Figure 5.6 shows typical results of the Vickers indentation on steel A and the measured indentation sizes with different applied loads. Both diagonal lengths were measured and the average value was used for each load. The data represents the average of at least six tests and the error bar represents the 3% standard error. Figure 5.7 shows typical results with the spherical indenter and the measured indentation sizes with different applied loads. The diameters of the indentation at horizontal and perpendicular directions were measured and the average value was used to represent the indentation size. For each load at least six tests have been measured. These average values were used for inversely prediction of the material properties.

Figure 5.8 and Figure 5.9 show the objective functions for steel A with data from a single Vickers or Spherical indenter. The objective function values G (Eq. 5.1) for each material set (σ_y, n) within a range of material properties ($100 \leq \sigma_y \leq 900$ MPa, $0.01 \leq n \leq 0.3$) was calculated. Figure 5.8 (a) and 5.9 (a) show the surface plots of the objective function vs. the power-law material parameters. The material set with the lowest objective function was marked on the surface plots. Figure 5.8 (b) and 5.9 (b) plot typical material property sets with objective function values close to the minimum value point. For the Vickers indentation, the σ_y and n corresponds to the bottom line of the valley (Figure 5.8 (a)), but for the spherical indentation, material property sets with lower objective functions are scattered around the minimum G

point (Figure 5.9 (b)). In both cases, the result suggests that the material properties can not be predicted based on the single indenter method. Figure 5.10 (a) shows the surface plots of objective functions for the dual indenters approach and the material sets with lower objective functions near the valley. The final result ($\sigma_y=330$, $n=0.1$) with minimum G value is located in the vortex of the σ_y and n plot. Figure 5.10 (b) plots typical material sets with lower objective functions and it clearly shows that the minimum G point is located at the central vortex of all material property sets with lower objective functions.

Figure 5.11 (a) and (b) shows the applied $P-d$ data for Vickers test and spherical indentation on steel B. Steel B is much softer than steel A so the indentation size is much larger under same loads. For each load at least six points have been tested and the standard error (3%) was calculated as shown by the error bar. The error range is comparable to the results for steel A. Figure 5.12 (a) and 5.13 (a) show the surface plots of the objective function vs. the power-law material parameters for the Vickers and spherical indenters. The material sets with the lowest objective function were marked on the surface plots in both cases. There are several sets of material properties over a large range were found to have very close objective function values. Figure 5.12 (b) and 5.13 (b) plot typical material property sets with objective function values close to the minimum value point. In both cases, the result suggests that the material properties can not be predicted based on the single indenter method. Figure 5.14 (a) shows the surface plots of objective function for dual indenters and the material sets with lower objective functions near the valley. The final result ($\sigma_y=160$, $n=0.18$) with minimum G value is located in the central vortex of the σ_y and n plot (Figure 5.14(b)).

5.3.2 Verification of inverse FE modelling results with standard tensile tests

The two steels were characterised in tensile tests and the results were compared to the predicted stress-strain curve from the indentation tests. The use of straight dog-bone shaped specimen allows the direct calculation of the stress-strain curves. Figure 15(a) and (b) compare the true stress-strain curves of the two steels based on the inversely predicted data and the tensile test results. The curve showed reasonable agreement up

to the ultimate point. This suggests that the inversely predicted material data is accurate.

The use of different notch sizes allows further assessment of the accuracy of the predicted data and the estimation of the parameters in the fracture models (details of the GTN model can be found in Chapter 2). Figure 5.16 shows typical FE models for flat specimen (a) and notched steel bar of different radius (b). The thickness of steel A is 1.44 mm and that of steel B bars is 0.8mm. For both FE models, the y-direction displacement at the mid-section (bottom surface) was set to zero due to symmetry. The left end of the specimen was fixed ($U_{x,y,z}=0$) and a displacement (U_x) was applied on the movable end. An element type of C3D8R (a reduced-integration element used in stress/displacement analyses) was used. The material parameters used were based upon the inverse FE modelling result of indentation tests. The fracture behaviour was assumed to follow GTN model (Wang, 2003). Details can be found in Wang (2003) and ABAQUS (6.4). The dog-bone shaped specimen model consists of 5310 elements, while the notched bar models consist of 2100 elements. The suitable element size for the fracture model is about 0.25mm (Wang, 2003), which is applied around the notch. The sensitivities of the mesh density and modelling parameters have been systematically assessed.

The micromechanical parameters introduced in the GTN model were subdivided into the following groups: parameters of the matrix material, i.e. Young's modulus, E , Poisson's ratio, ν , and the initial true stress-strain curves, initial parameters of the rigid inclusion, i.e. the initial void volume fraction f_0 and the volume fraction of void nucleating particles f_n . Parameters affecting the nucleation, growth and coalescence of voids during the loading process includes q_1 , q_2 , q_3 , ϵ_N , s_N , f_c , f_F . The values for material parameters, q_1 , q_2 , q_3 were chosen to be $q_1=1.5$, $q_2=1$, $q_3=2.25$ following Tvergaard (1981) and ABAQUS manual, and they were fixed throughout the analysis. The nucleation strain ϵ_N and standard deviation s_N were assumed to be equal to 0.25 and 0.1 in the first instance. These factors were fitted by manually tuning the parameters using parametric study, which is well established procedure in fitting fracture parameters (Wang, 2003).

Figure 5.17 and Figure 5.18 show the numerical results and the experimental results of the flat and three notched specimens of steel A and B. As shown in the figures, the loading curves, from the original to the ultimate point, showed good agreement, which further validated the inverse FE modelling approach with the experimental data. The simulated fracture process also showed reasonable agreement. Further tuning the fracture data will require a more complex specimen, which is not attainable with the form of the material in this work. A detailed study of the process is to be investigated in another study. All material properties (parameters) obtained for these two base steels are listed in Table 5.2 and used in modelling of spot welded joints under tensile-shear loading.

Table 5.2 The predicted material parameters (yield stress, work hardening coefficient, GTN model's parameters)

| | σ_y | n | ϵ_N | S_N | f_N |
|---------|------------|------|--------------|-------|-------|
| Steel A | 330 | 0.1 | 0.1 | 0.1 | 0.04 |
| Steel B | 160 | 0.18 | 0.3 | 0.1 | 0.04 |

5.4 Characterisation of material properties within spot welded joints of steels

In this section, the method developed was applied to the spot welded joints to extract the detailed material properties of different welding zones. The spot-welded joint was cut through and the surface with the nugget in the centre was polished to make specimens for indentation test with a Leitz miniload hardness tester. The tests were performed in a horizontal orientation across the base, HAZ and the nugget along the line in Figure 5.19 (a). Typical indentations for the Vickers and spherical indentation are shown in Figure 5.19 (b). The dimensions of the indentations were measured and used in mapping the hardness distribution, and some data was then used to predict the plastic properties of the three zones – nugget, HAZ and base.

Figure 5.20 shows a typical Vickers hardness distribution through different weld zones. As displayed, the material in the nugget region is much harder due to the quenching effect. The hardness in the HAZ exhibited a gradient distribution decreasing from the nugget to the base zone. This hardness distribution also clearly shows the diameter of the fusion zone. Figure 5.21 (a) & (b) show the force-indentation size ($P-d$) data of the three welding zones (Base, HAZ and Nugget) using Vickers and spherical ($R=0.5\text{mm}$) indenters. The force-indentation sizes ($P-d$) data are significantly different between these three zones, in which the indentation size of nugget is the smallest and that of the base zone is the largest under identical loads.

Similar procedure has been followed as detailed in section 5.2 and 5.4 to determine the material parameters for these three zones. Figure 5.22 (a-c) plots the objective function value G for the three zones. The yield stress for the three welding zones of steel A are 330, 430 and 620 MPa for the base, HAZ and nugget; the work hardening coefficients n values are 0.1, 0.12 and 0.11. Figure 5.22 (d) shows the true stress-strain curves for the different zones of steel A from the inverse FE modelling.

Figure 5.23 (a) shows a typical hardness distribution for steel B. The distribution is similar to that of steel A but the hardness value is much lower. The hardness in the

HAZ exhibited a gradient distribution decreasing from the nugget to the base zone. The hardness distribution also clearly shows the diameter of the fusion zone. Figure 5.23 (b) &(c) show the force-indentation size points of the three welding zones using Vickers and spherical (R=0.5mm) indenter.

Figure 5.24 plots the objective function value G using Eq. 5.2. The yield stresses for the three welding zones of steel B are 160, 230 and 400 MPa respectively for base, HAZ and nugget; the n values are 0.18, 0.16 and 0.09. The true stress-strain curve is shown in Figure 5.24. Table 5.3 listed the material parameters for the welding zones of steel A and B. The yield stress dropped from the nugget to the base, but the change of the working hardening coefficient is not very significant. These data are used to model the tensile shear test in next section.

Table 5.3 Plastic material properties of the welded zones (σ_y and n).

| | Base | | HAZ | | Nugget | |
|----------------|------------|------|------------|------|------------|------|
| | σ_y | n | σ_y | n | σ_y | n |
| Weld (Steel A) | 330 | 0.1 | 430 | 0.12 | 620 | 0.11 |
| Weld (Steel B) | 160 | 0.18 | 230 | 0.16 | 440 | 0.09 |

5.5 FE modelling of tensile-shear test of spot welded joints

In this section, FE models have been developed to simulate the tensile-shear testing of spot welded joints of the two steels using the predicted material properties. The modelling results were compared to experimental results. The validated FE models were then used to investigate the effects of weld dimensions on the tensile-shear strength of spot welded joints.

5.5.1 FE models of spot welded joints

A plane symmetric FE model of the specimen has been established (Figure 5.25(a)). The material properties used in this model was the material parameters predicted by the inverse FE modelling. An element type of C3D8R (a reduced-integration element used in stress/displacement analyses) was used and the meshing scheme is shown in Figure 5.25(b). Due to symmetry, the y-direction displacement at the mid-section (bottom surface) was set to zero. The left end of the specimen was fixed ($U_{x,y,z}=0$) and a displacement ($U_x=L$) was applied on the movable end. The z displacement at the mid-section was set to zero.

The dimensions of the welding zones were based on the micro-hardness experimental data and optical observation. All these zones were assumed to have elasto-plastic behaviour with isotropic work-hardening. To model the full deformation curve of the spot-welded joint, the fracture behaviour was simulated by incorporating a standard GTN model (ABAQUS 6.4) with the fracture parameters determined in Section 5.3.2 (Table 5.2). The simulation requires significant computing resource and was performed on a high performance cluster of 32 CPU. Mesh size sensitivity testing has been performed and the final models consist of 4609 and 5107 C3D8R elements for steel A and steel B, with finer meshes applied to the nugget and HAZ to increase the modelling accuracy.

Figure 5.26 shows the predicted deformation of the spot welded joint at different stages in comparison to experimental test results. The deformation involved elastic tension and bending of the specimen in the early stage, and then yielding and

eventually fractures within the HAZ. As shown in Figure 5.26 (a) & (b), the predicted deformation pattern agrees well with the experimental observation. The numerical force displacement data of the tensile-shear test also showed good agreement with the testing results. Similar agreement was found with steel B and the result is shown in Figure 5.27.

As shown in Figure 5.26 & 5.27, the modelling results showed a good agreement with the experimental data. This suggests that the material laws predicted by inverse FE modelling of indentation tests for different zones is accurate. The slight differences between numerical and experimental results on the fracture behaviour suggest that detailed fracture for each material zone has to be obtained rather than using parameters from the base material, which requires further investigation.

5.5.2 Effects of nugget size and sheet thickness to the mechanical behaviour of spot welded joint under tensile-shear loading

Two most important structural factors affecting the strength of welded joints are the nugget size and sheet thickness, but this has not been quantitatively investigated with detailed material properties. To investigate this problem, a series of models with different nugget diameters have been developed. Figure 5.28 (a) compares the force-displacement data of four models with a nugget size of 4mm, 5mm, 6mm and 6.5mm. As shown in the figure, the stiffness of spot weld joints was not affected by the nugget diameters; however, it clearly shows that the nugget size had significant effect on the strength, including the yield point, the ultimate force and the fracture point. Three models with same nugget diameter (6mm) but different sheet thickness were also performed to investigate the effect of sheet thickness to tensile-shear test strength; the results are shown in the Figure 5.28 (b). The curves show that the stiffness and strength increased significantly with the increase of base sheet thickness. When the sheet thickness increases 0.5mm (about 30%), the forces at yield and the ultimate tensile strength (UTS) increase about 20%, and the maximum elongation increases about 15%.

As same as for steel A, a series of tensile-shear test models for steel B were created to investigate the effects of nugget diameters on the tensile-shear strength of welded

joints. Figure 5.29 (a) compares the force-displacement data of four models with a nugget size of 3mm, 4mm, 4.5mm, 5mm and 5.5mm. As shown in the figure, the stiffness of spot weld joints was not affected by the nugget diameters, but it clearly shows that the nugget size had significant effect on the strength, including the yield point, the ultimate strength and the fracture strength. Three models with same nugget diameter (4.5mm) but different sheet thickness (0.6mm, 0.8mm, and 1.0mm) were also performed to investigate the effect of sheet thickness; the results are shown in Figure 5.29 (b). The curves show that the stiffness and strength increase significantly with the increase of base sheet thickness. When the sheet thickness increases 0.2mm (about 25%), the forces at yield and the ultimate tensile strength (UTS) increase about 25%, and the increase of the maximum elongation is about 10%.

Figure 5.30 plots the effect of nugget size and the sheet thickness on the yield strength and the UTS of spot weld joints. Both cases show the yield strength and peak strength increase with the nugget diameter. For steel A, it follows a linear relation when the nugget size is lower than 5 mm and eventually reaches a plateau when the nuggets size is over 6 mm. For steel B, yield strength and UTS follow a linear relation when the nugget size is lower than 4.5 mm and then they rise slowly reaching a plateau. These results agree with published experimental work (Aslanlar, 2006). As shown in Figure 5.30 (b), for steel A, the yield strength and the UTS increase with the sheet thickness but the relationship is not entirely linear; for steel B, the yield strength and the UTS displayed a good linear relationship with the sheet thickness. It should be noted that the nugget sizes concerned in this work all fall into the welding lobe of the material and can be defined as a good weld in industrial practice. In many cases, a simplified linear relation has been used to describe the relation between the nugget size and the strength of the joint (Zuniga and Sheppard, 1995; Zhou *et al*, 1999; Zhou *et al*, 2003). This work clearly shows that this may not be sufficient for some materials that have significantly different material properties between each welding zones.

5.6 Summary

A new inverse modelling approach based on static indentation has been developed and validated using blind tests. The evaluation based on numerical experimental data showed similar accuracy to the continuous indentation curve approach. Experimental work on two steels showed that the stress-strain curves predicted are comparable to standard tensile tests and notched specimens, which suggests that the approach is a feasible way to characterise plastic properties. The new method represents a simpler and more practical approach which is suitable for applications where an instrumented indentation tester is not available.

The method developed was successfully used to characterise the plastic properties of different zones in spot welded joints. Results showed the yield stress increased from the base, the HAZ and nugget while the change of work hardening is limited among these three zones in both steels. These plastic material parameters were used in modelling the tensile shear deformation of the spot welded joint and showed good agreement with experimental results. The validated FE models were further used to predict the effect of nugget size and the thickness of the metal sheet on the strength of welded joints.

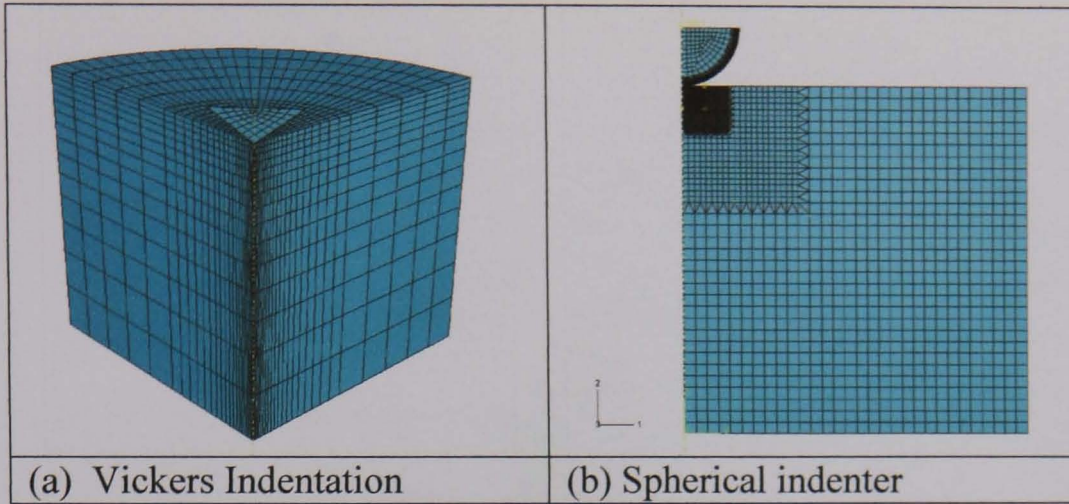


Figure 5.1 FE models of the Vickers and spherical indentation test.

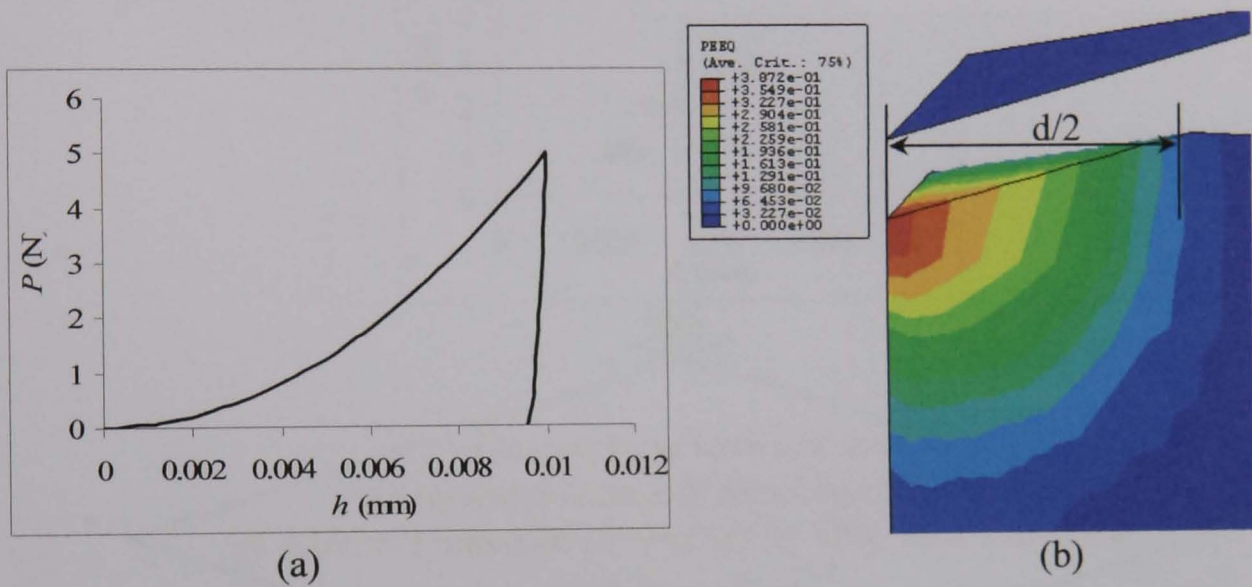


Figure 5.2 Typical loading and unloading curve of Vickers indentation (a) and residual indentation (b).

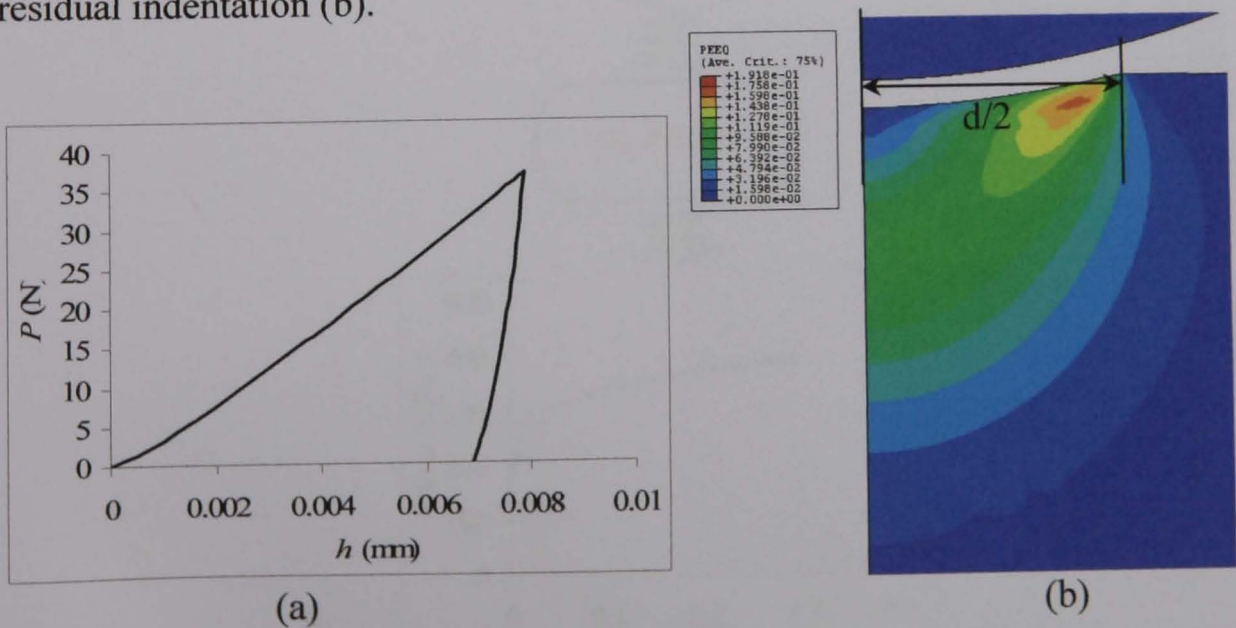
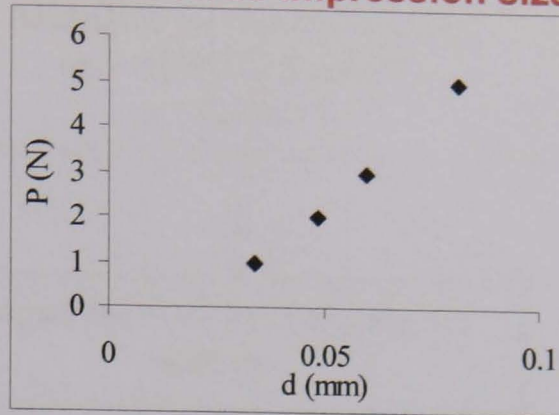
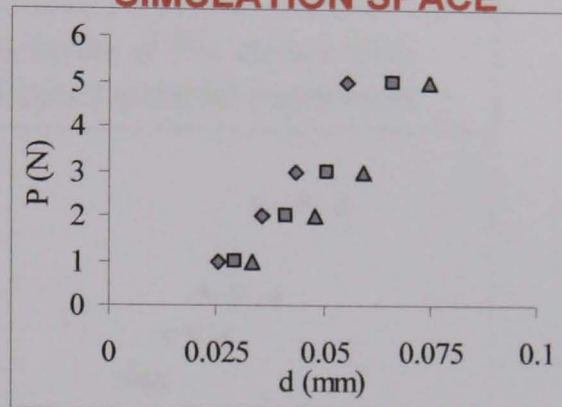


Figure 5.3 Typical loading and unloading curve for the spherical indenter ($R=0.5\text{mm}$) (a) and residual indentation (b).

INPUT (experimental force-impression size (P - d) data)



SIMULATION SPACE



Comparison between the experimental data and numerical P - d data of different material properties by Objective Function

$$G = \sum_{i=1}^n \left(\frac{F_{i,e} - F_{i,n}}{F_{i,e}} \right)^2$$

σ_y and n

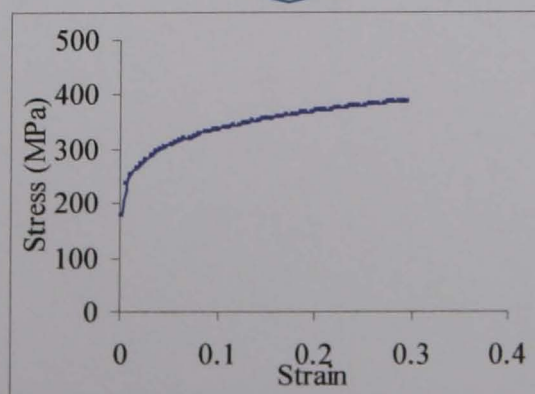


Figure 5.4 Flow chart showing the inverse FE modelling approach based on P - d data.

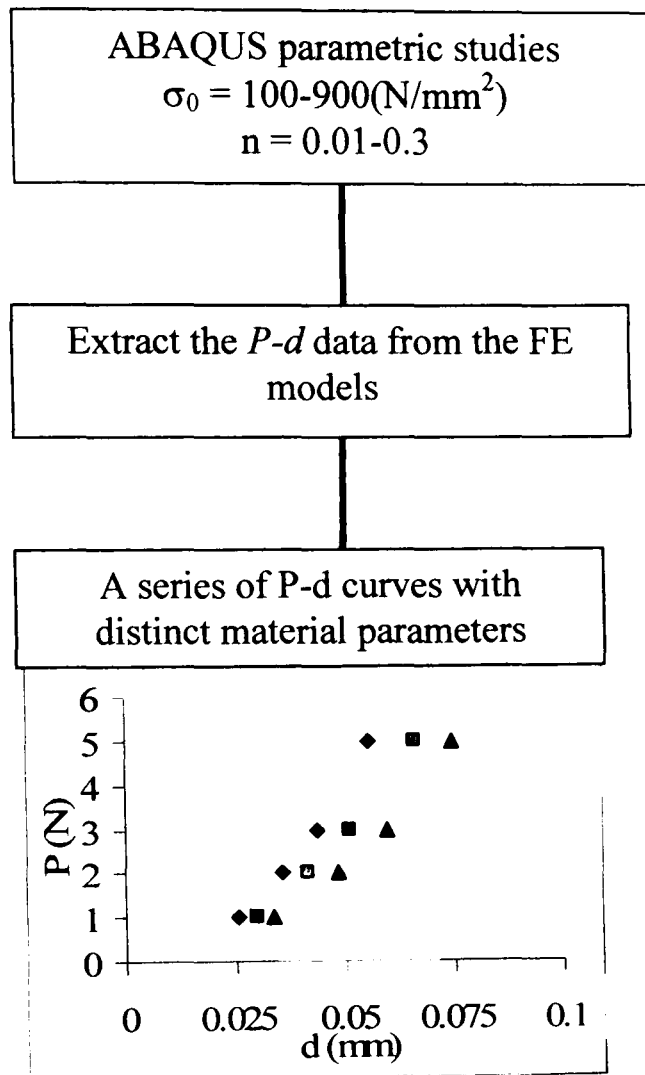


Figure 5.5 Flow chart showing the procedure to construct the simulation space for the inverse FE modelling programme.

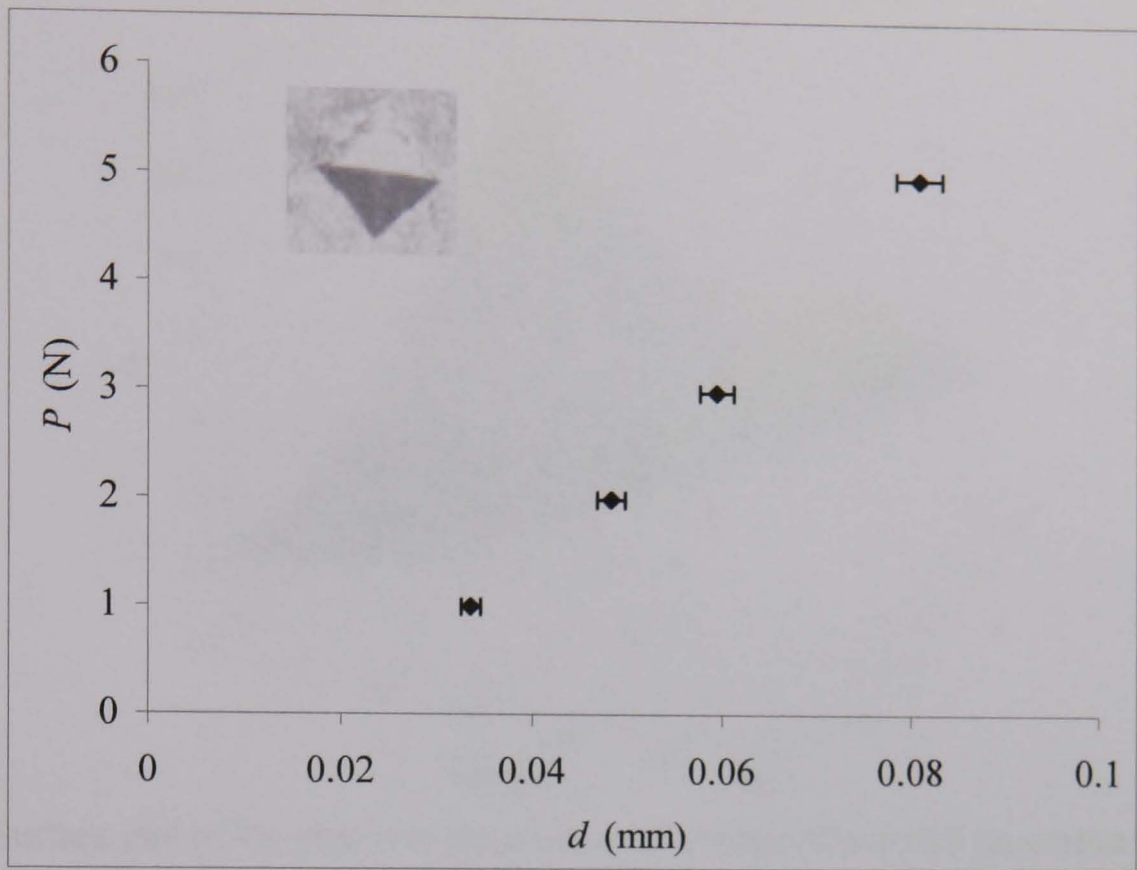


Figure 5.6 Force-indentation size (P - d) data of Vickers indentation tests on base steel A.

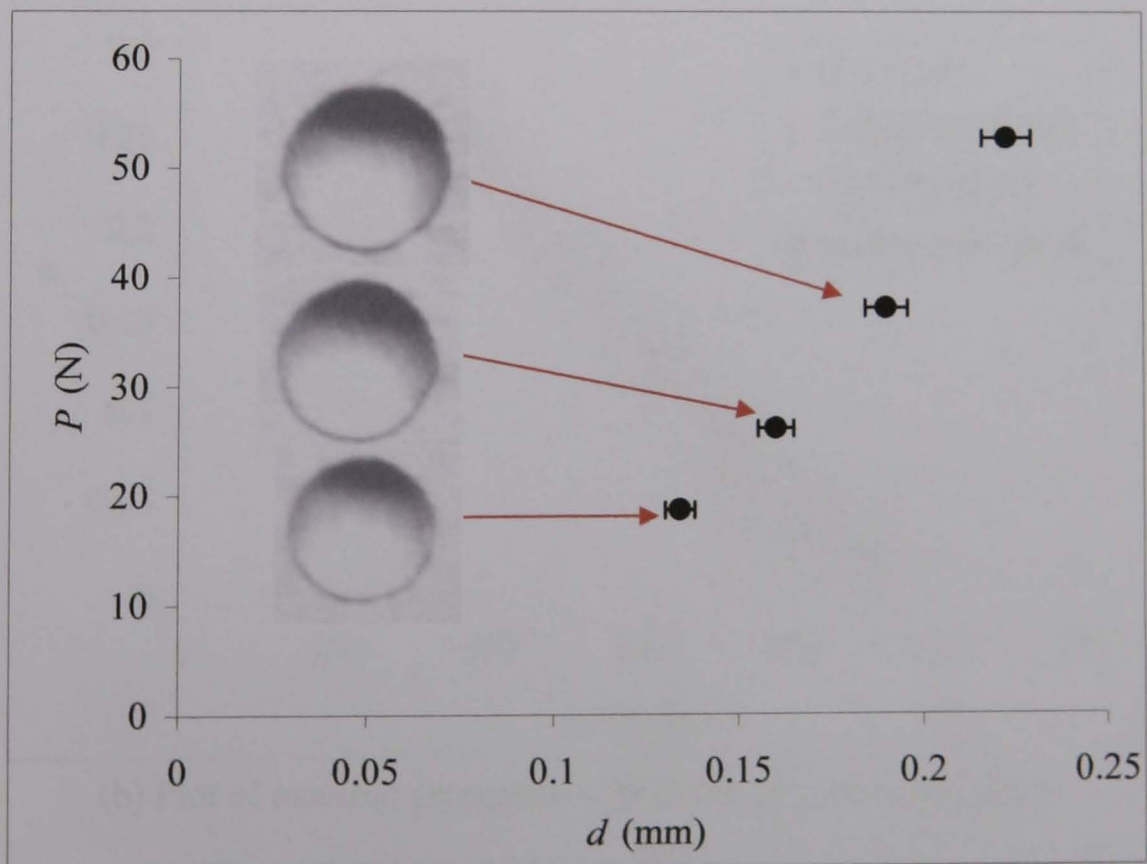
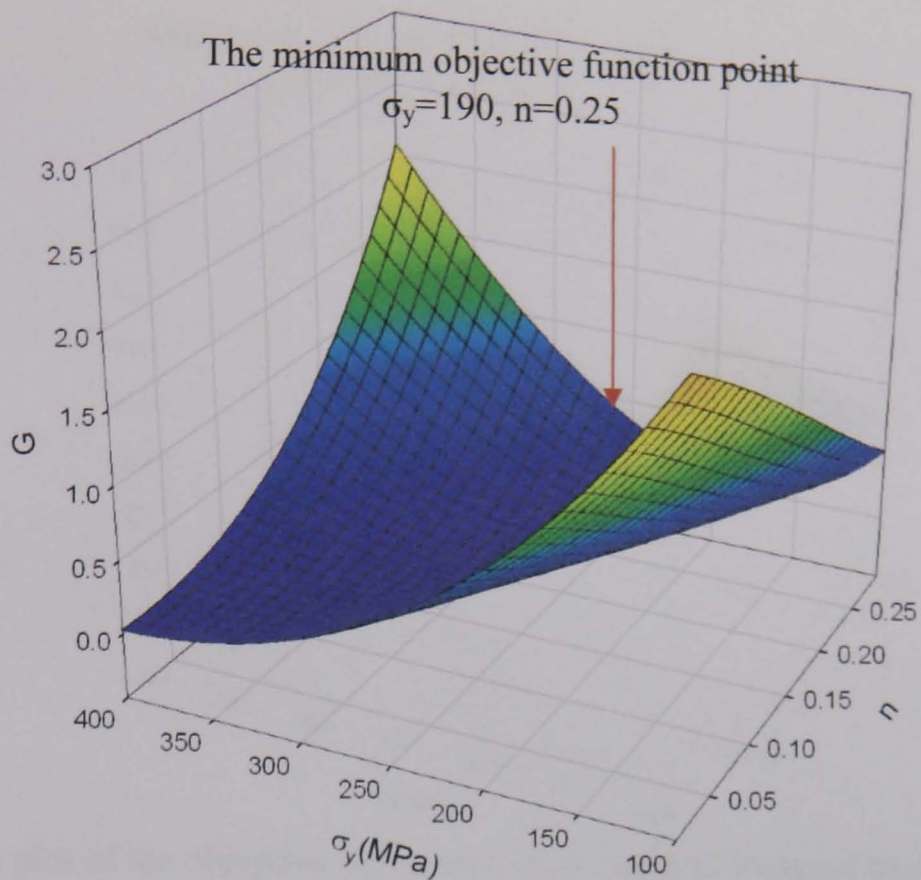
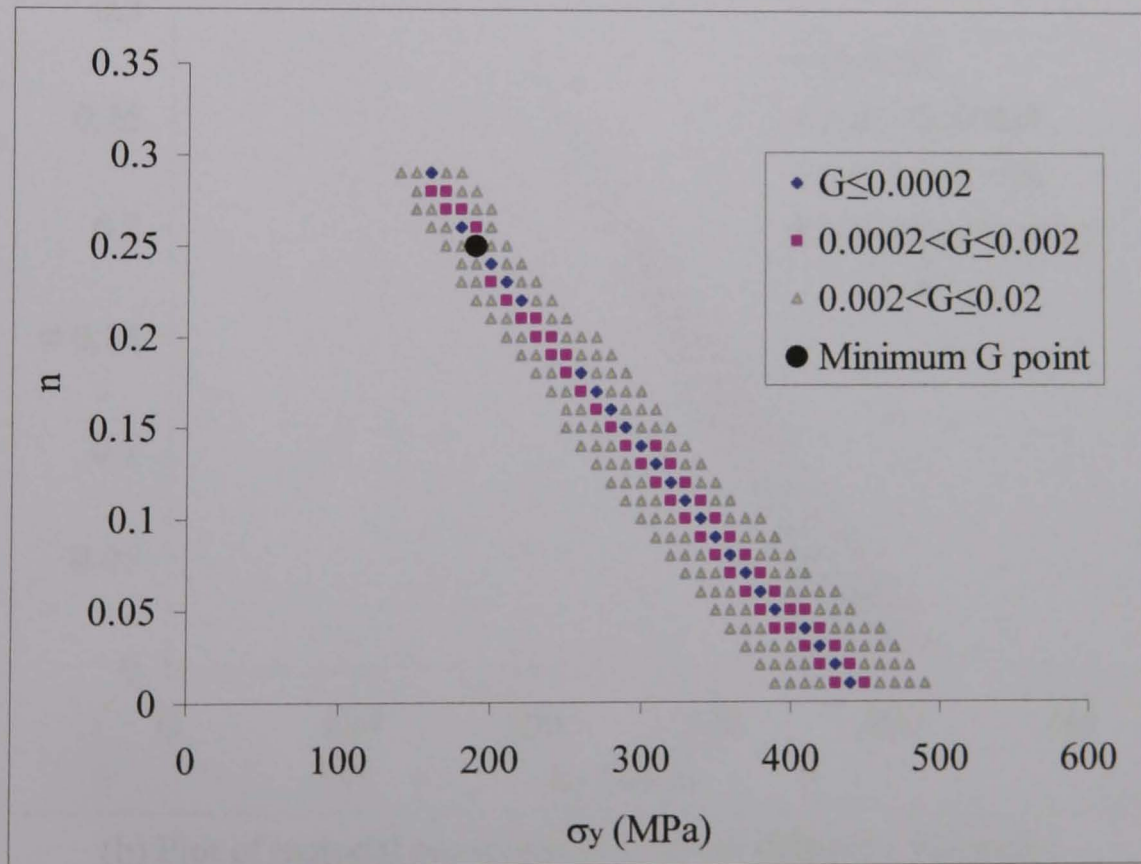


Figure 5.7 Force-indentation size (P - d) data of spherical indentation tests on base steel A.

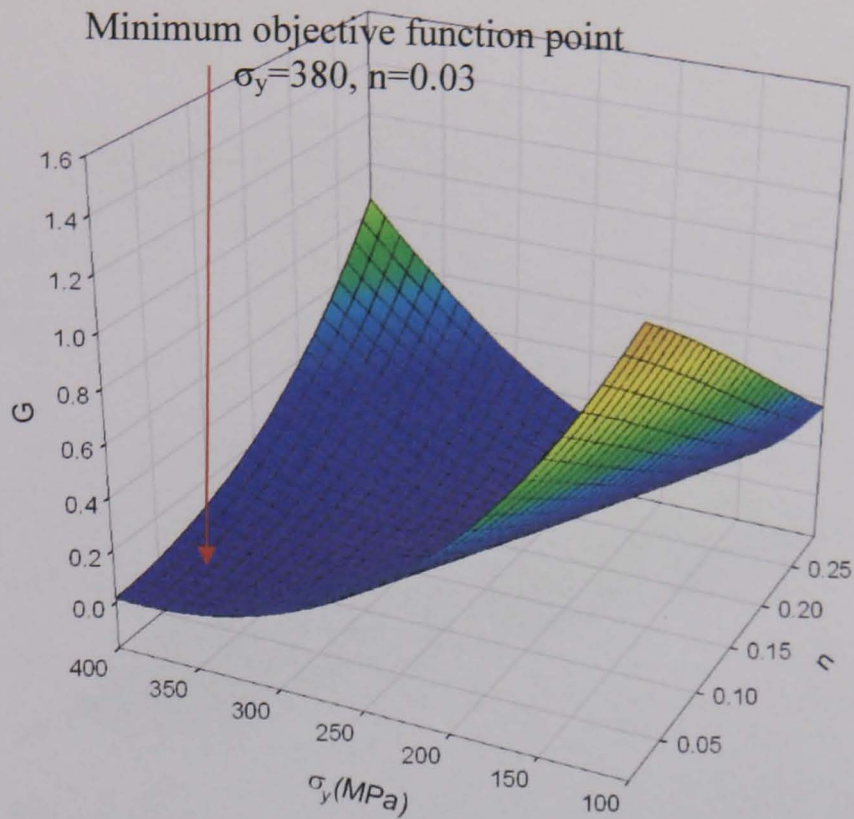


(a) Surface plot of the objective functions over a range of material properties with Vickers indentation.

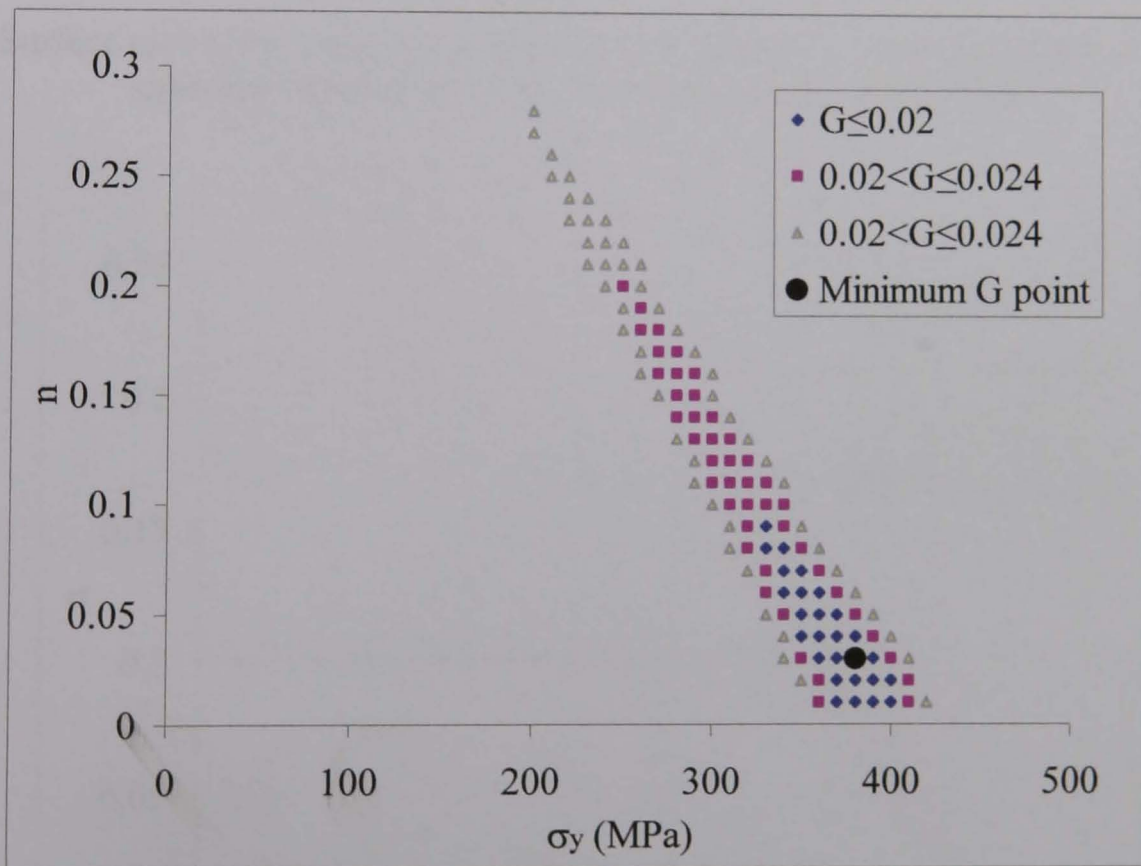


(b) Plot of material properties with lower objective functions.

Figure 5.8 Inverse modelling results based on Vickers indentation test results (Figure 5.6) for steel A.

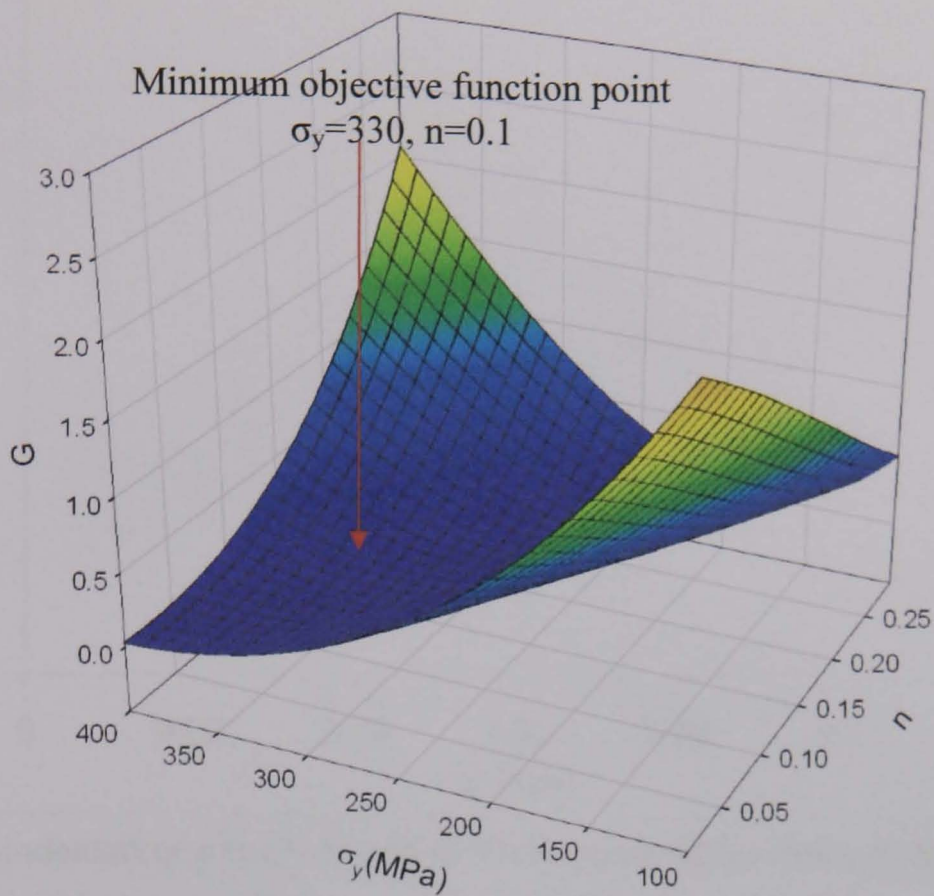


(a) Surface plot of the objective functions over a range of material properties with spherical indentation ($R=0.5\text{mm}$).

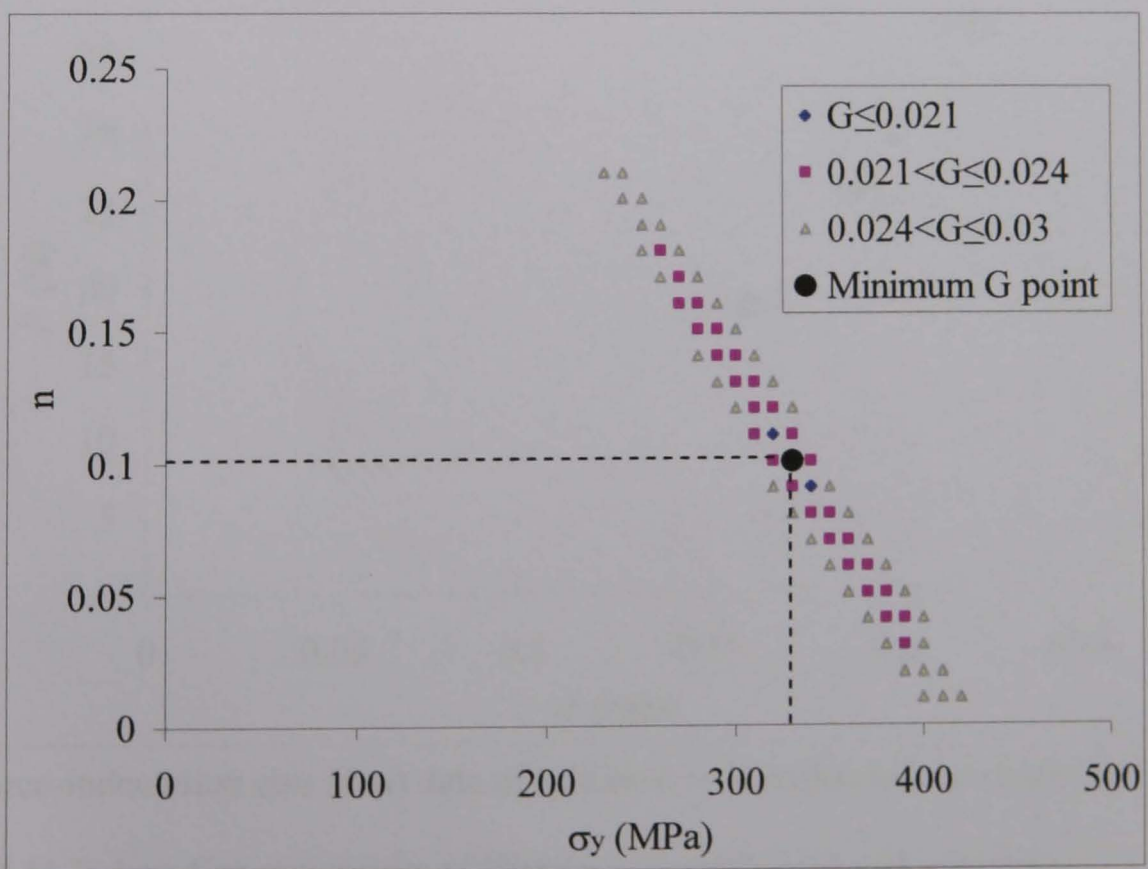


(b) Plot of material properties with lower objective functions.

Figure 5.9 Inverse modelling results based on spherical indentation test results (Figure 5.7) for steel A.

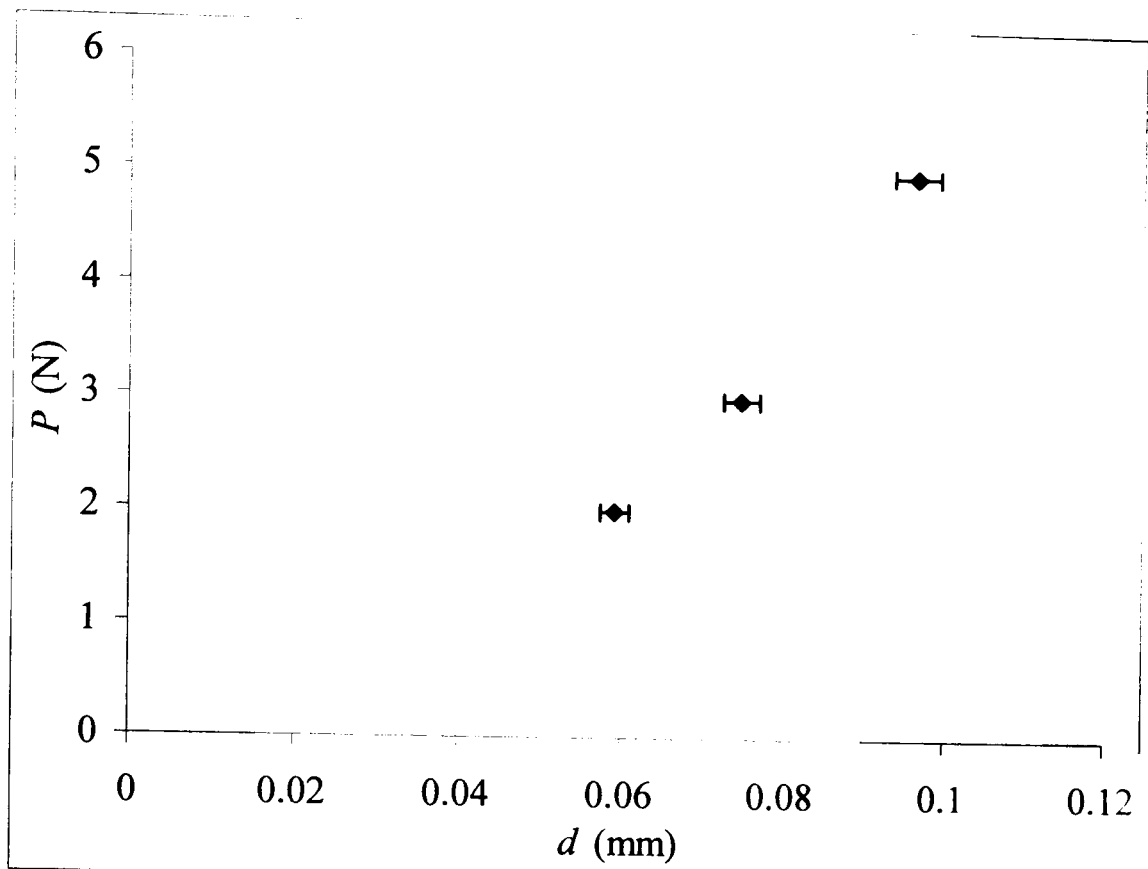


(a) Surface plot of the objective functions over a range of material properties with spherical indentation ($R=0.5\text{mm}$) and Vickers indentation.

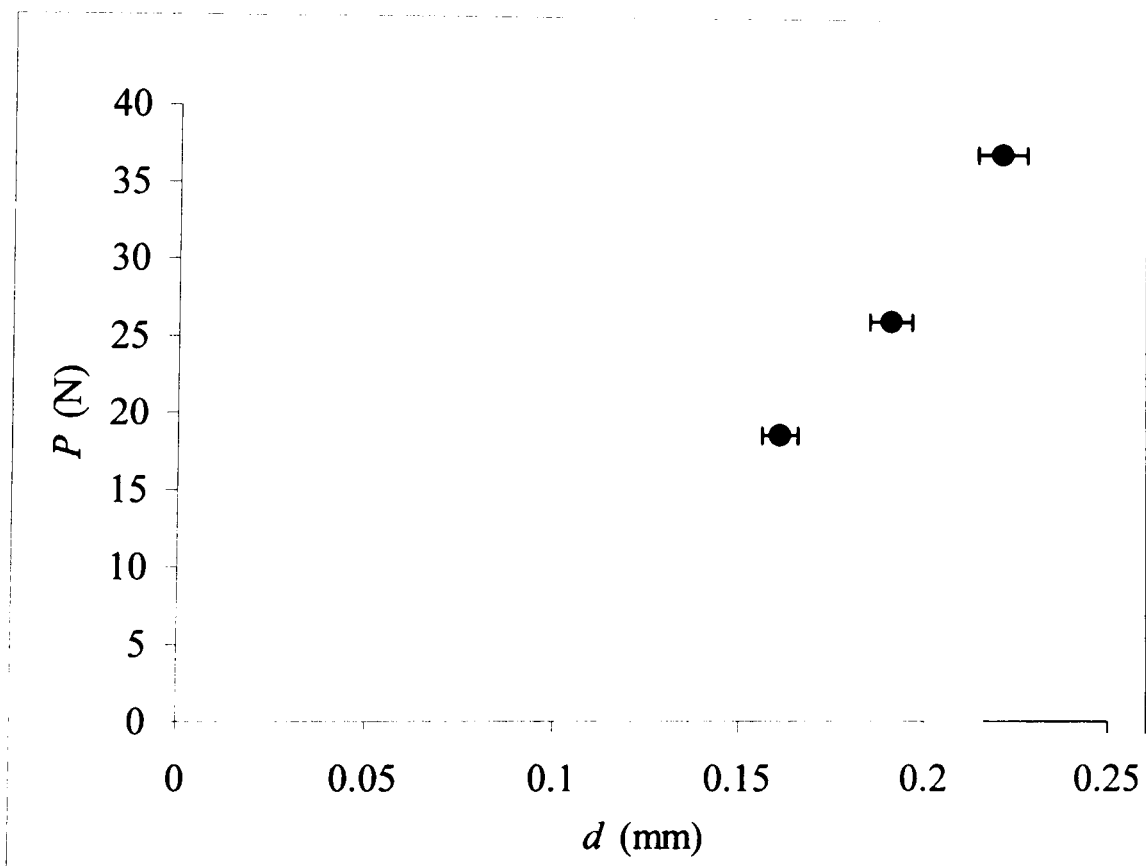


(b) Plot of material properties with objective function close to the minimum point.

Figure 5.10 Inverse modelling results based on spherical and Vickers indentation tests results (Figure 5.6 and Figure 5.7) for steel A.

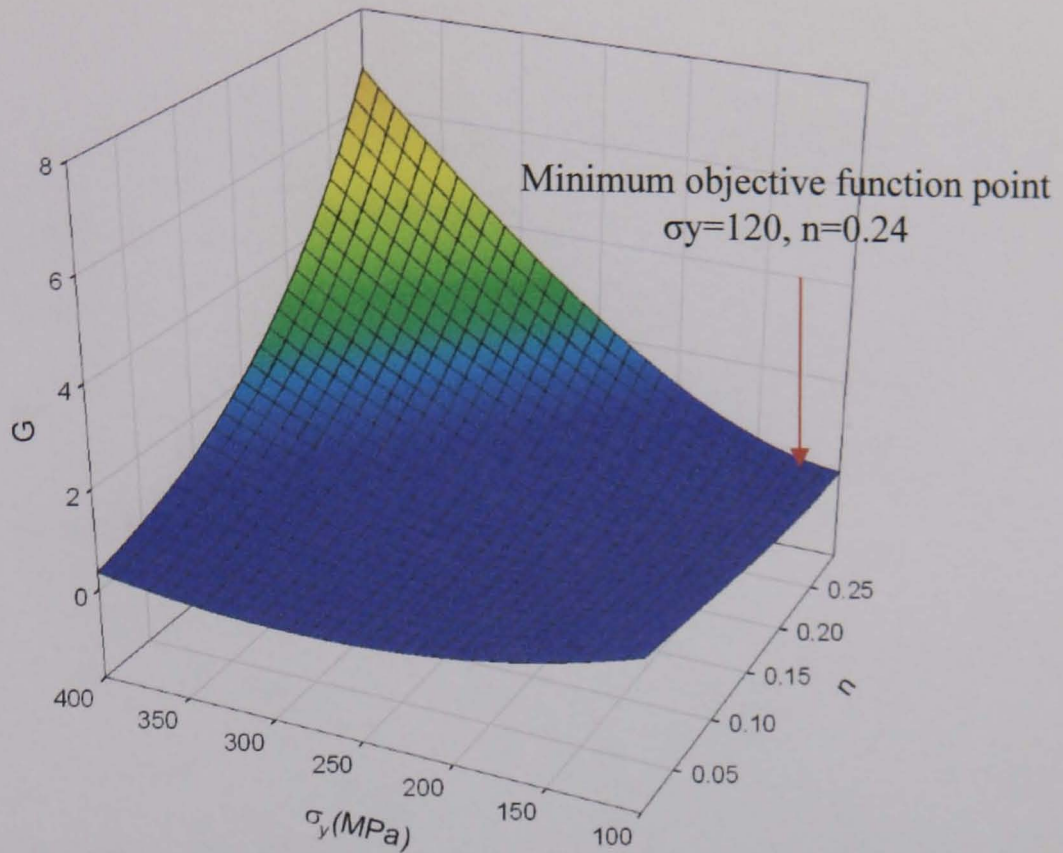


(a) Force-indentation size (P - d) data of Vickers indentation tests on base steel B.

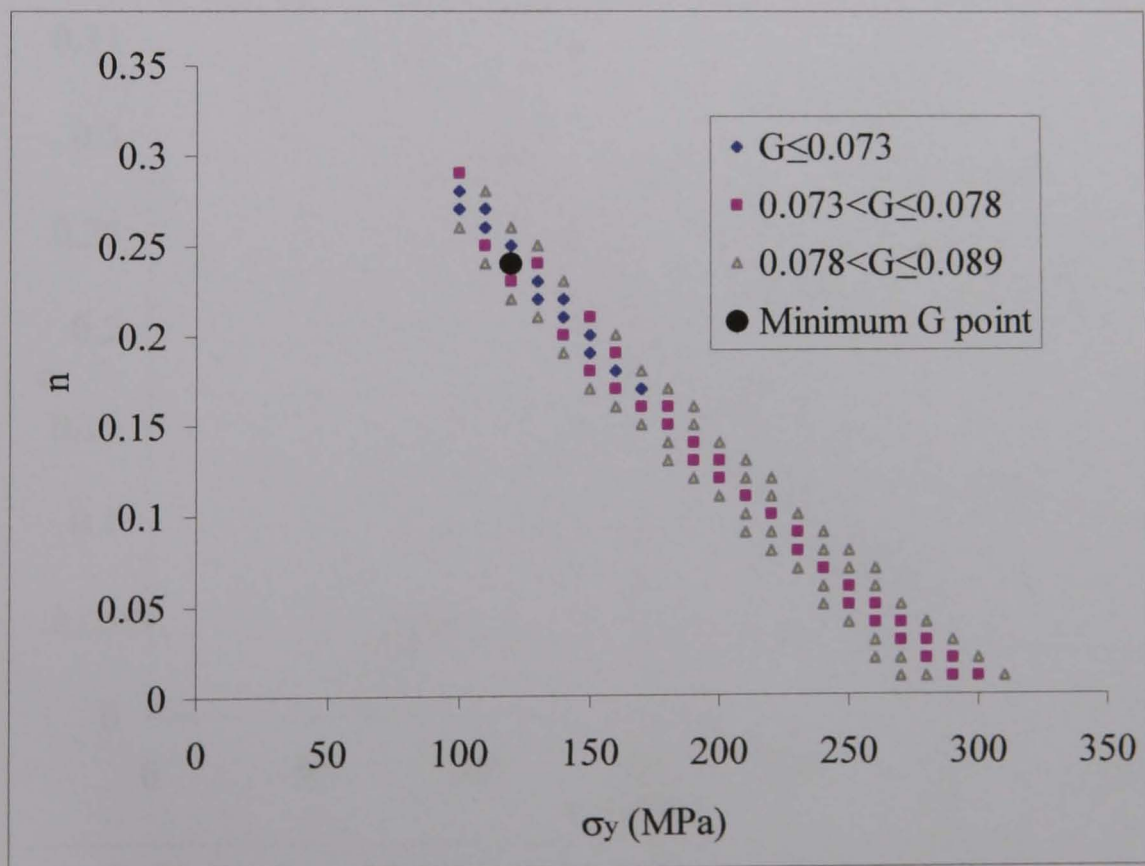


(b) Force-indentation size (P - d) data of spherical indentation tests on base steel B.

Figure 5.11 Indentation test results of Vickers indentation (a) and spherical indentation (b) tests on steel B.

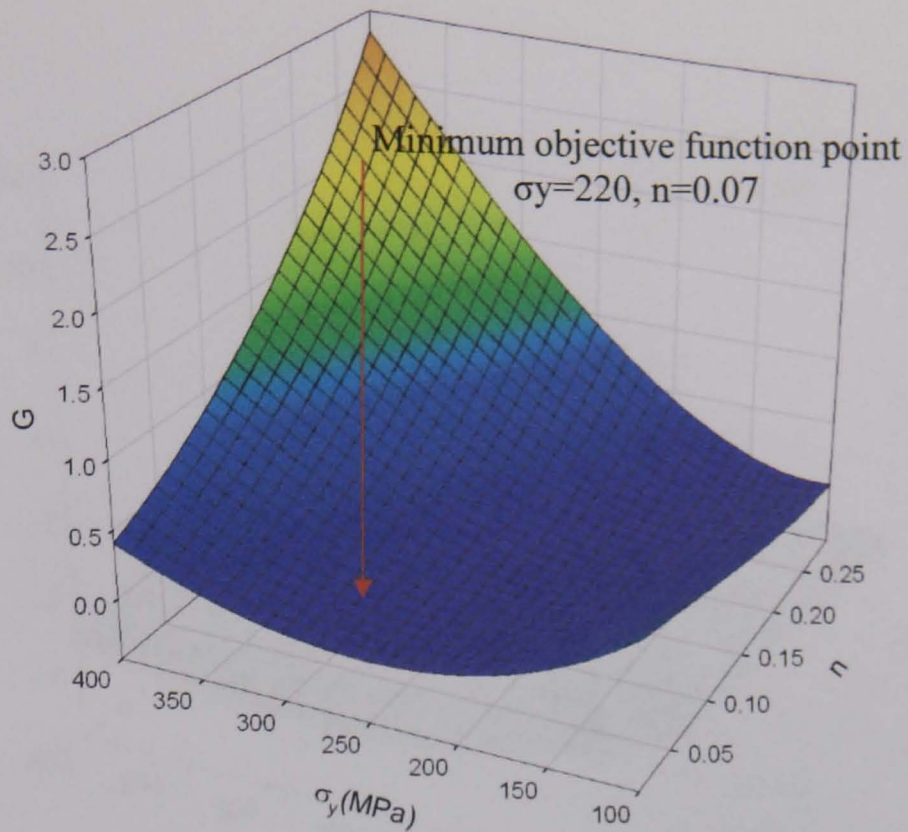


(a) Surface plot of the objective functions over a range of material properties with Vickers indentation.

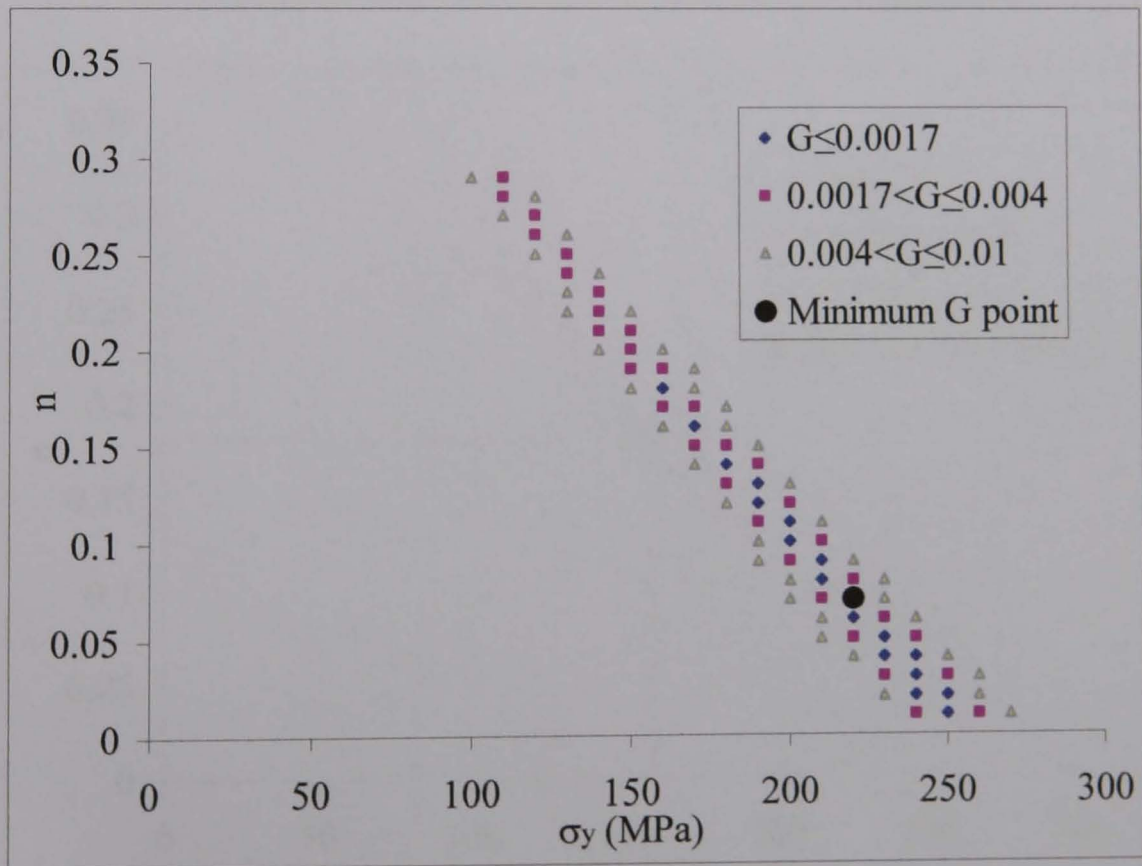


(b) Plot of material properties with lower objective functions.

Figure 5.12 Inverse modelling results based on Vickers indentation test results (Figure 5.11(a)) for steel B.

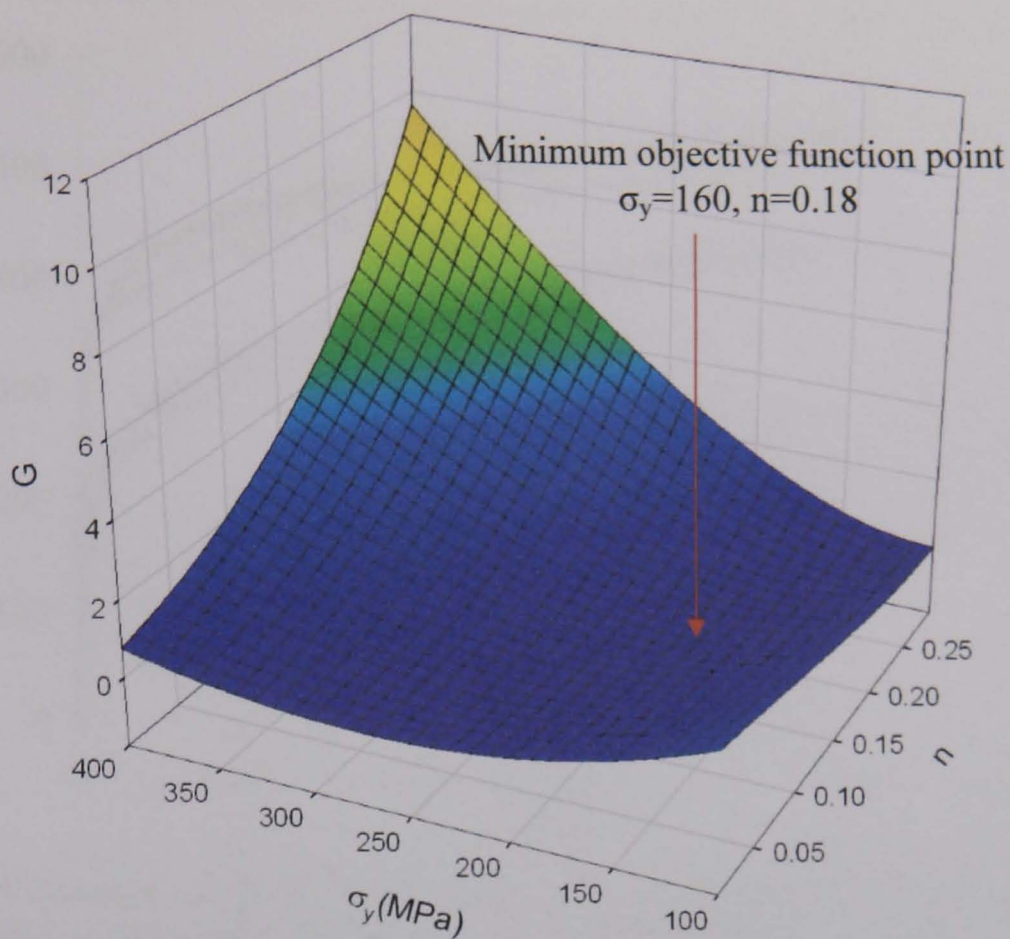


(a) Surface plot of the objective functions over a range of material properties with spherical indentation ($R=0.5\text{mm}$).

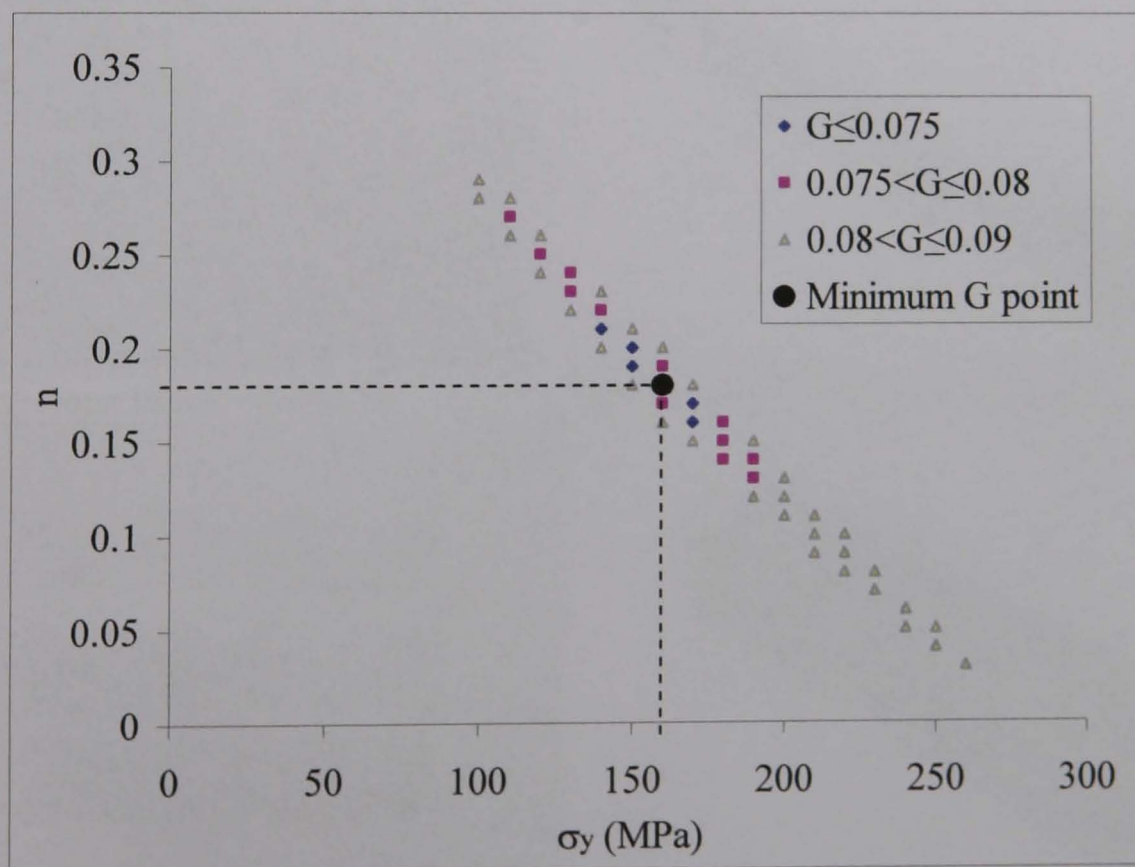


(b) Plot of material properties with lower objective functions.

Figure 5.13 Inverse modelling results based on spherical indentation test results (Figure 5.11(b)) for steel B.



(a) Surface plot of the objective functions over a range of material properties with spherical indentation ($R=0.5\text{mm}$) and Vickers indentation.



(b) Plot of material properties with objective functions close to the minimum point.

Figure 5.14 Inverse modelling results based on Vickers and spherical indentation tests results for steel B.

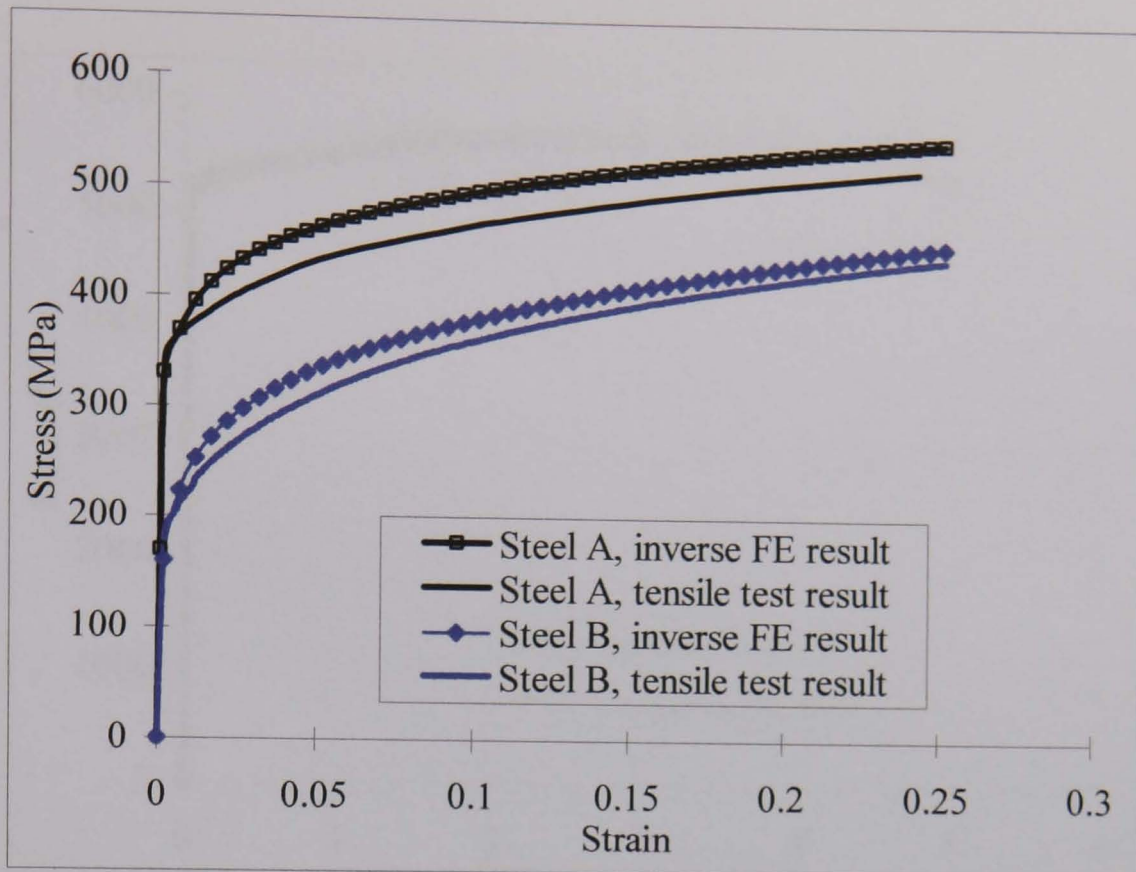


Figure 5.15 Comparison of the stress-strain curves predicted based on the dual indenters method and tensile test data of steel A and steel B.

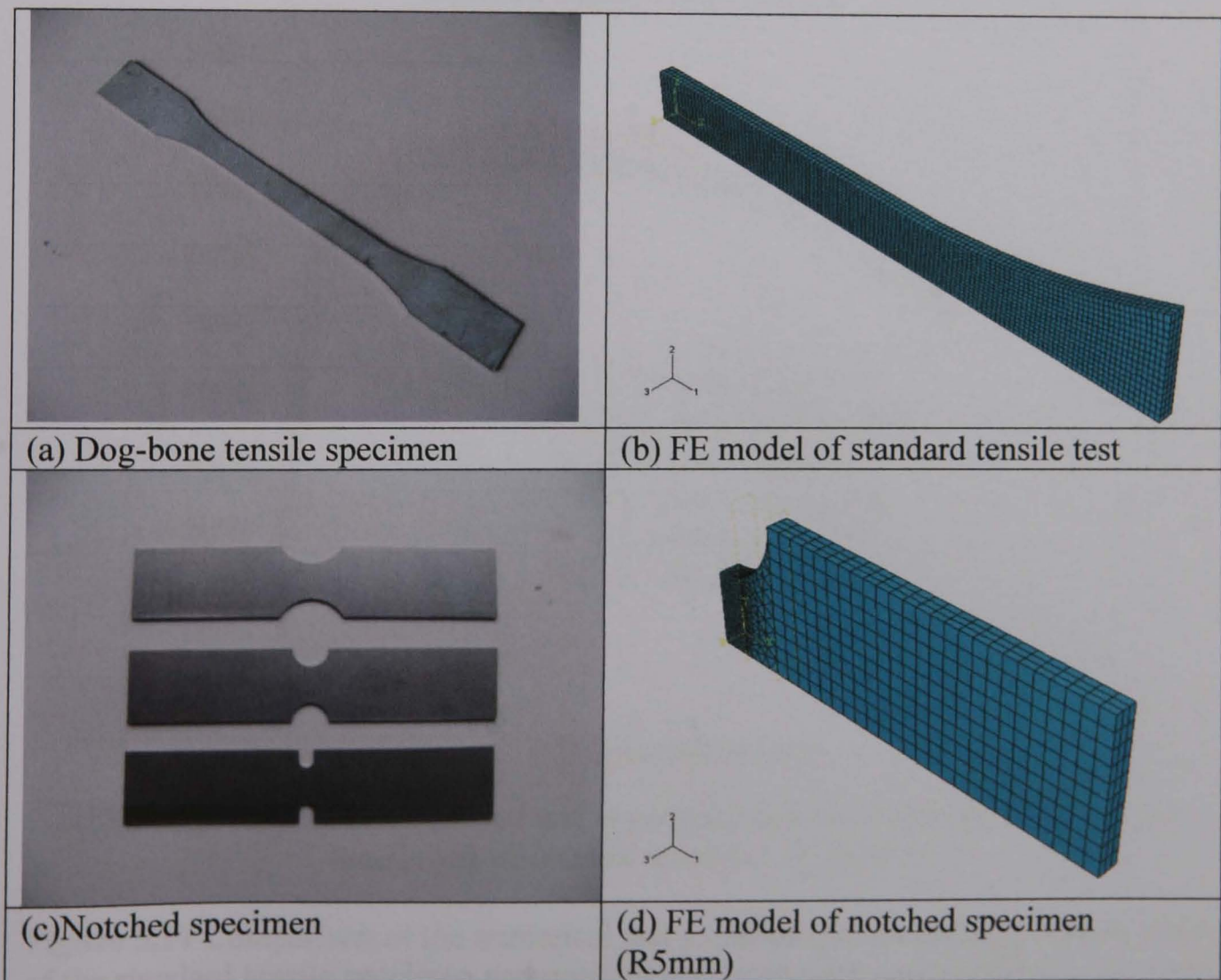
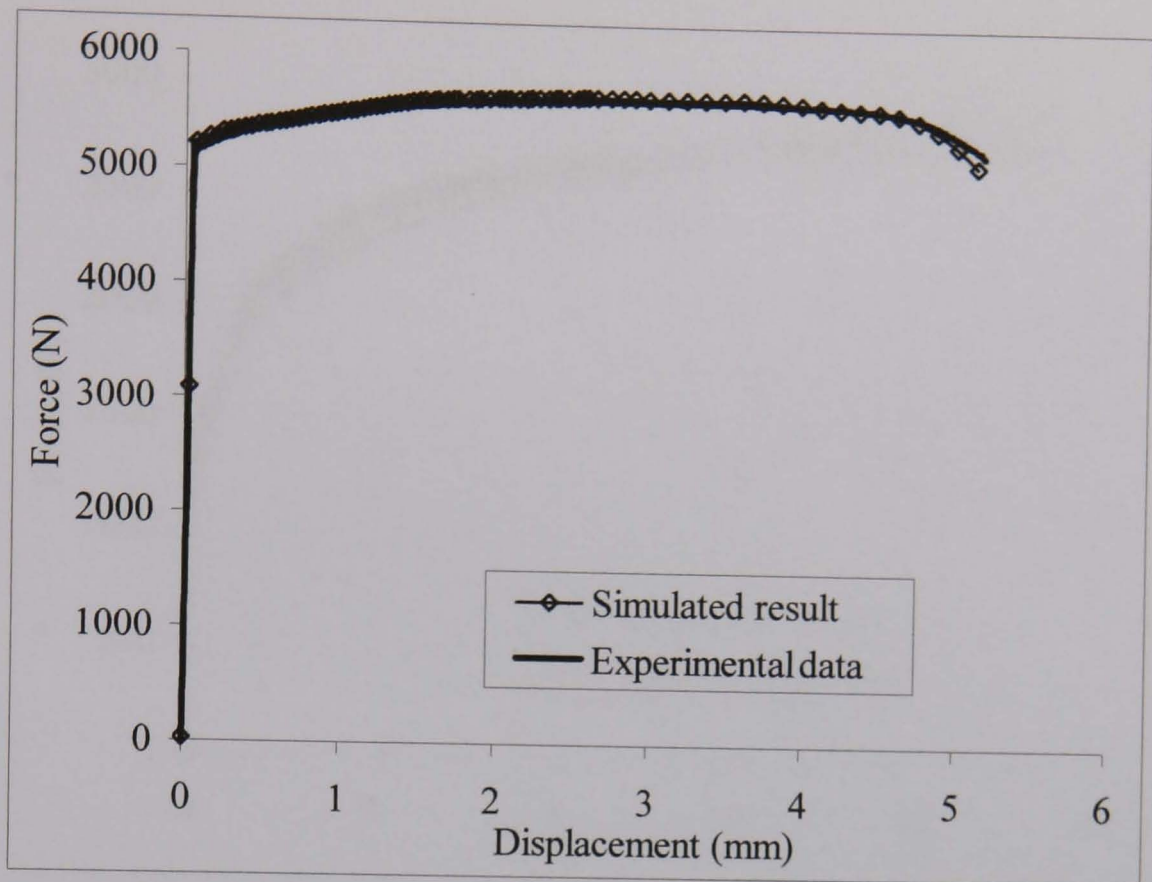
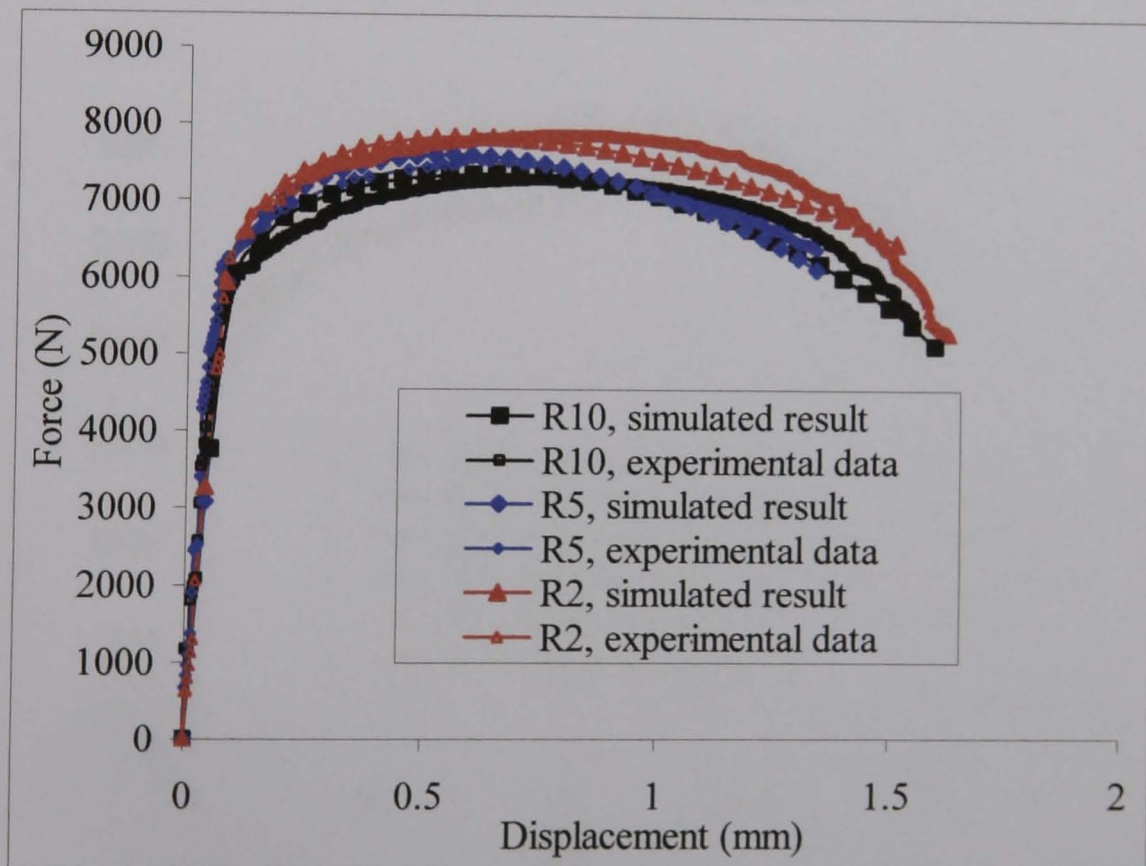


Figure 5.16 Tensile test specimen and FE models of tensile tests. (a) Standard tensile test specimen, (b) FE model of standard tensile specimen; (c) Notched specimen; (d) FE model of a notched specimen.

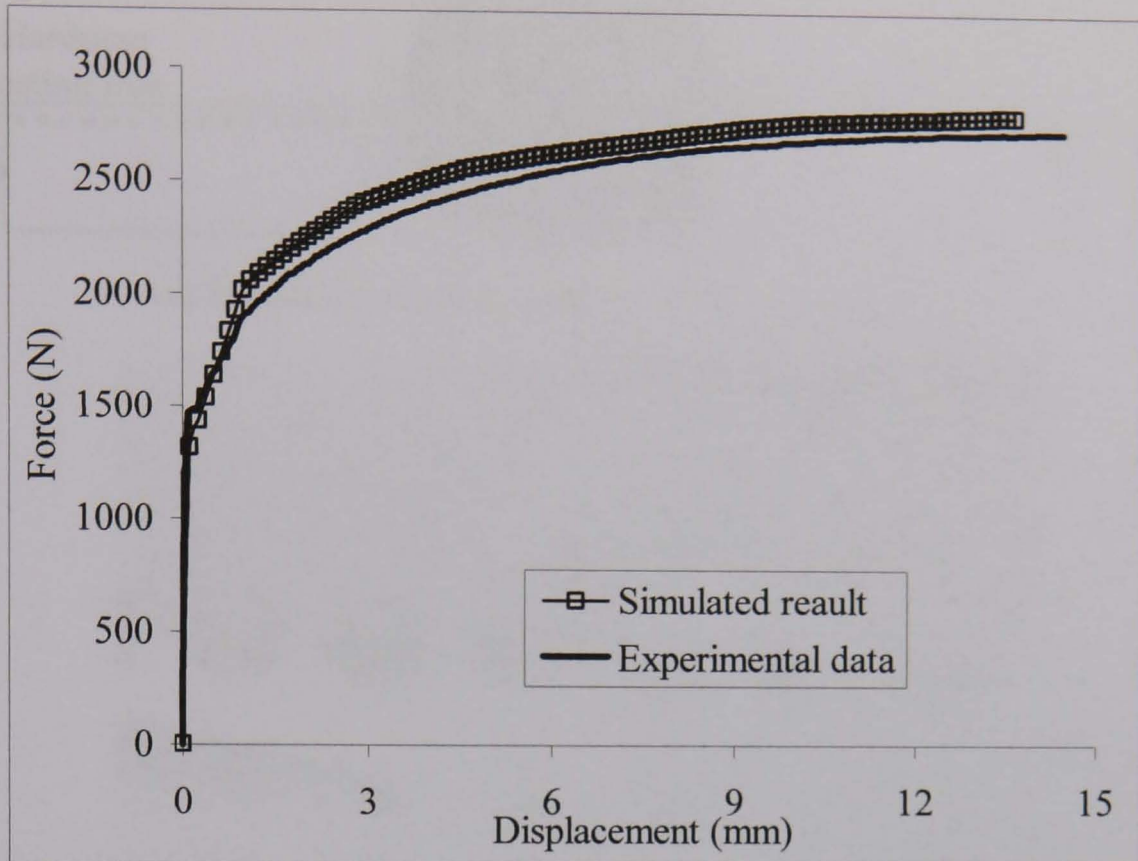


(a) Comparison of the predicted and experimental force displacement curves of standard tensile test of steel A.

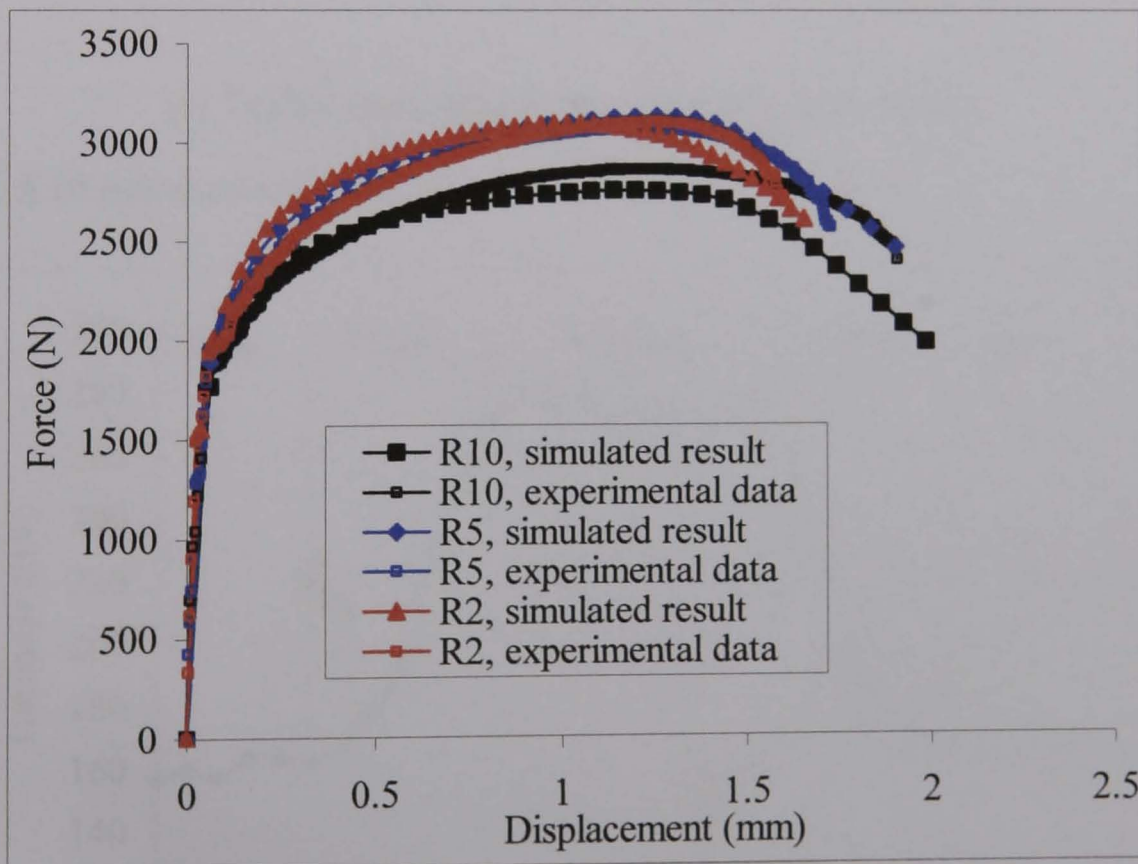


(b) Comparison of the predicted and experimental force displacement curves of tensile test of notched specimen of steel A.

Figure 5.17 Comparison of the numerical and experimental force displacement curve of the standard tensile specimen and notched specimen with notch size of 2mm, 5mm and 10 m for steel A.

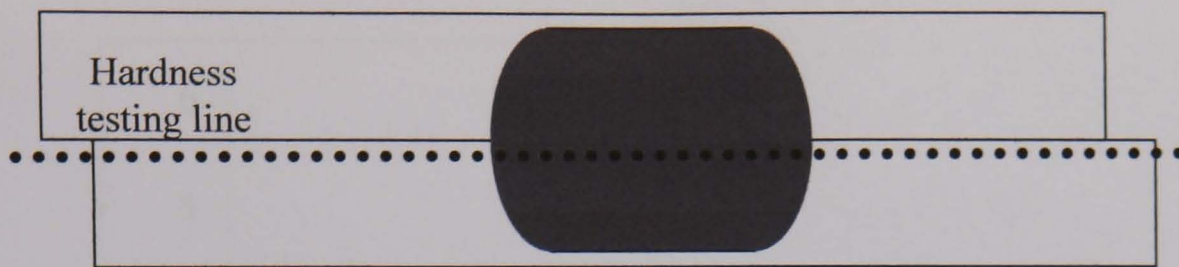


(a) Comparison of the predicted and experimental force displacement curves of standard tensile test of steel B.

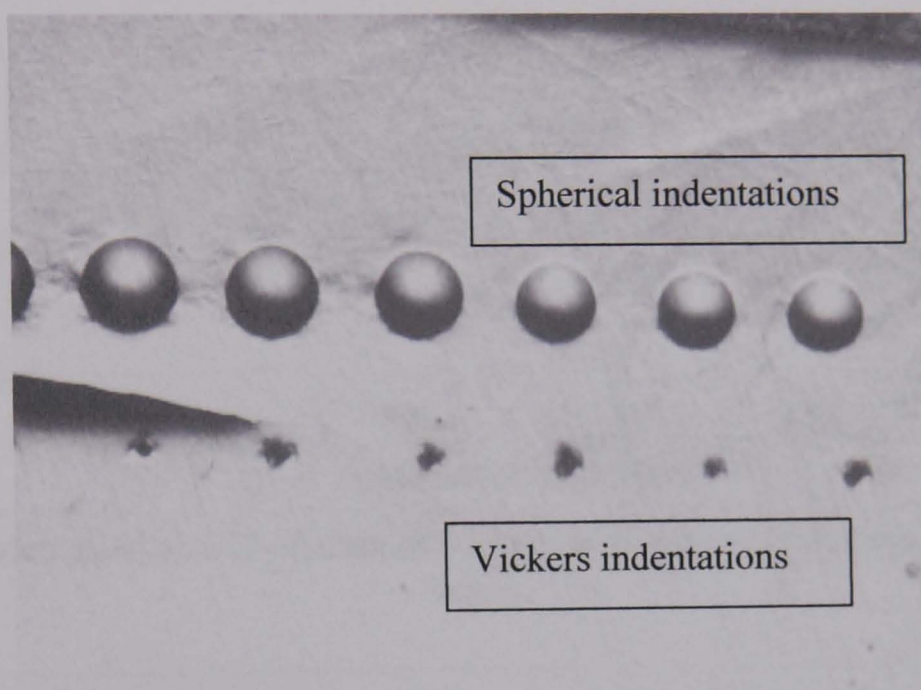


(b) Comparison of the predicted and experimental force displacement curves of tensile test of notched specimen of steel B.

Figure 5.18 Comparison of the numerical and experimental force displacement curve of the standard tensile specimen and notched specimen with notch size of 2mm, 5mm and 10 m for steel B.



(a) Schematic showing scheme of the indentation tests.



(b) Typical indentations across the spot welded joint.

Figure 5.19 Indentation tests of spot welded joint.

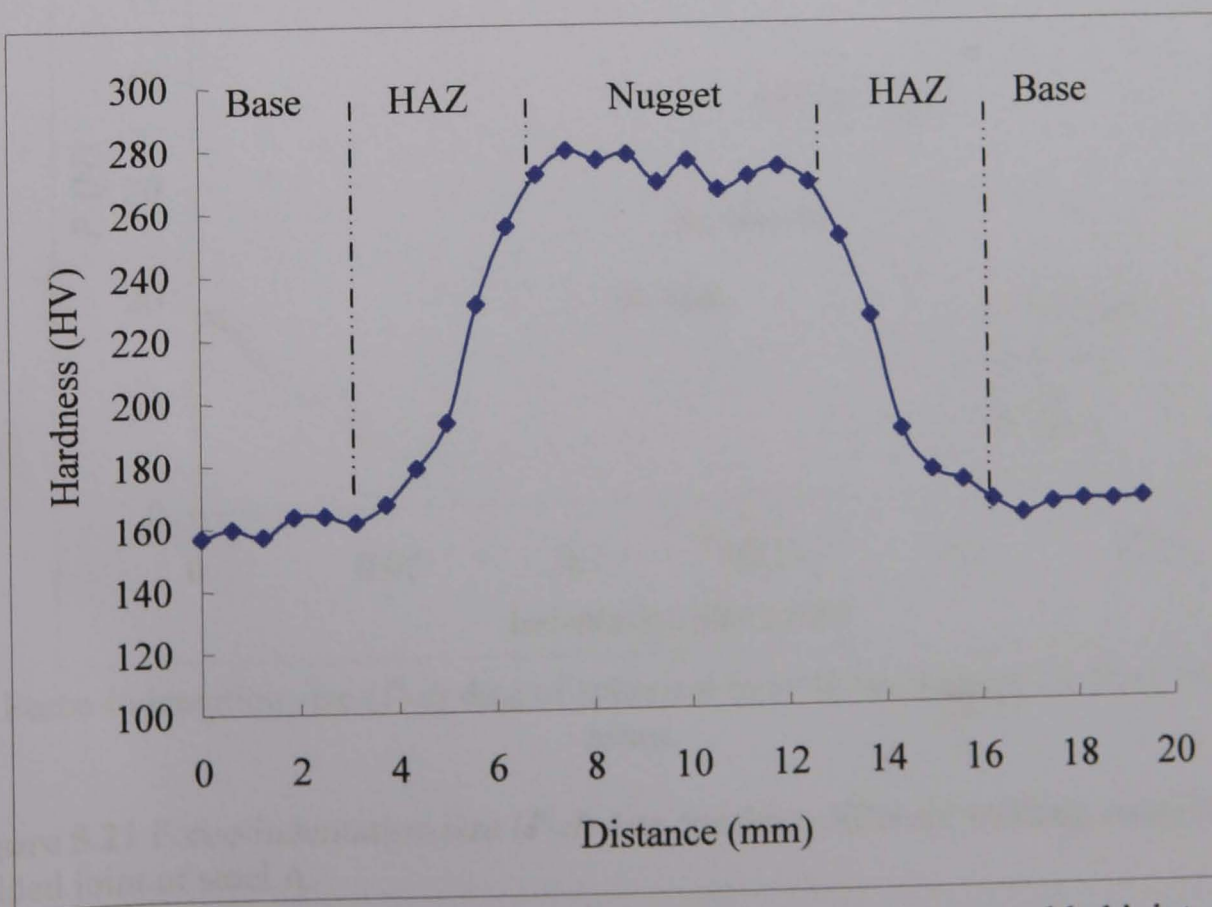
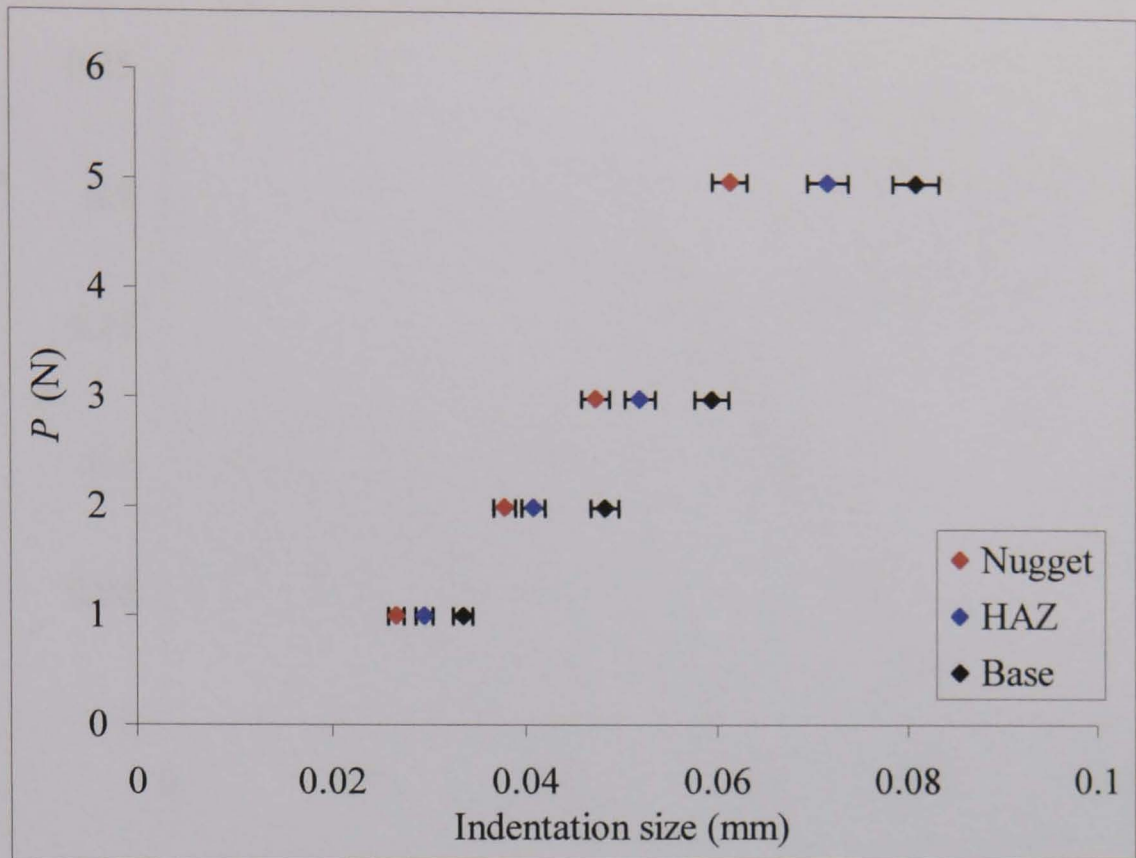
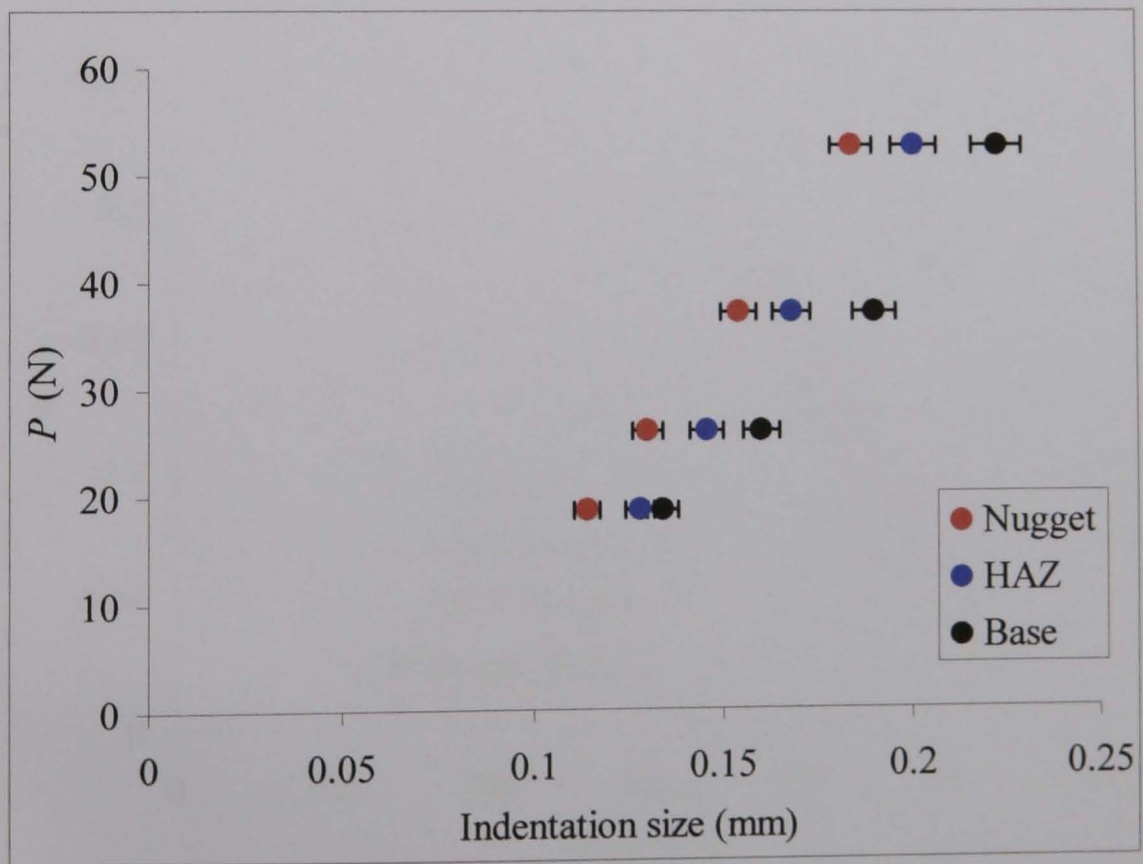


Figure 5.20 Typical Vickers hardness distributions across the spot welded joint of steel A.

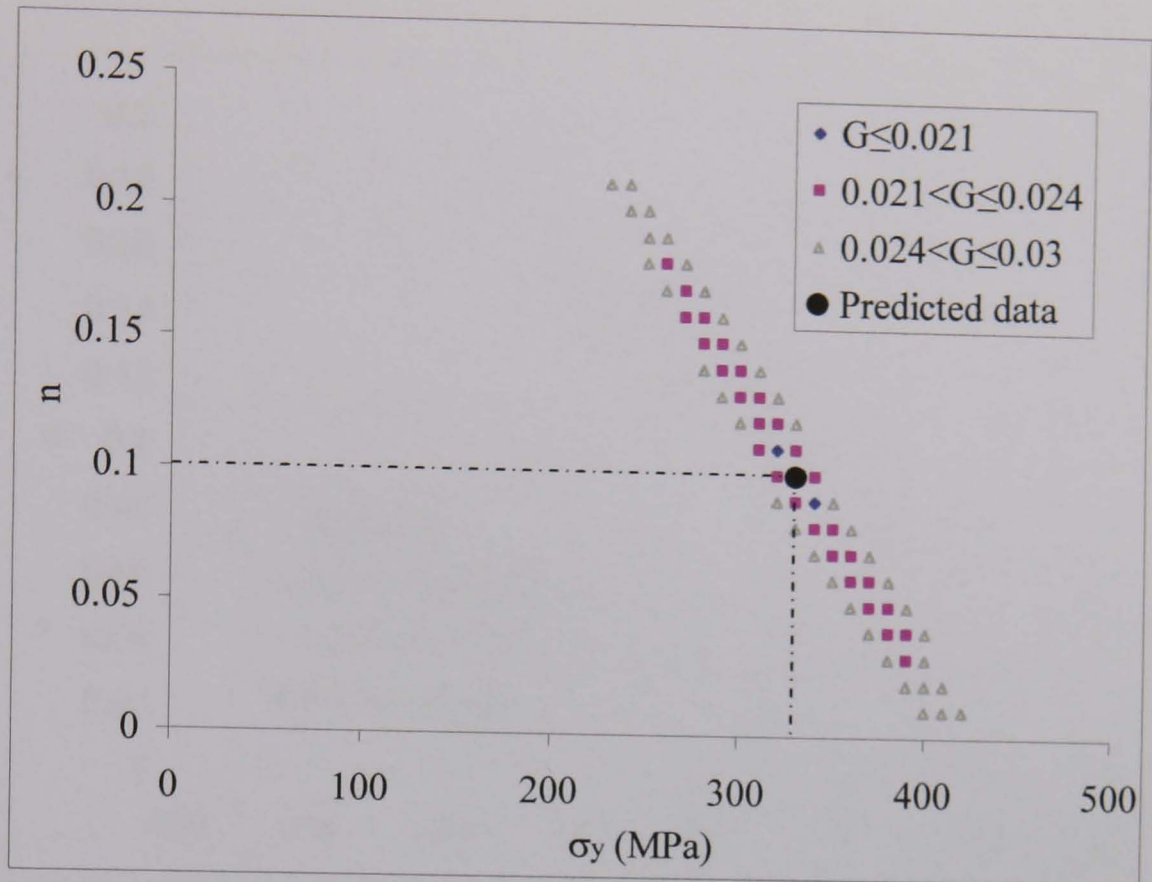


(a) Force-indentation size (P - d) data of Vickers indentation tests of the three welding zones.

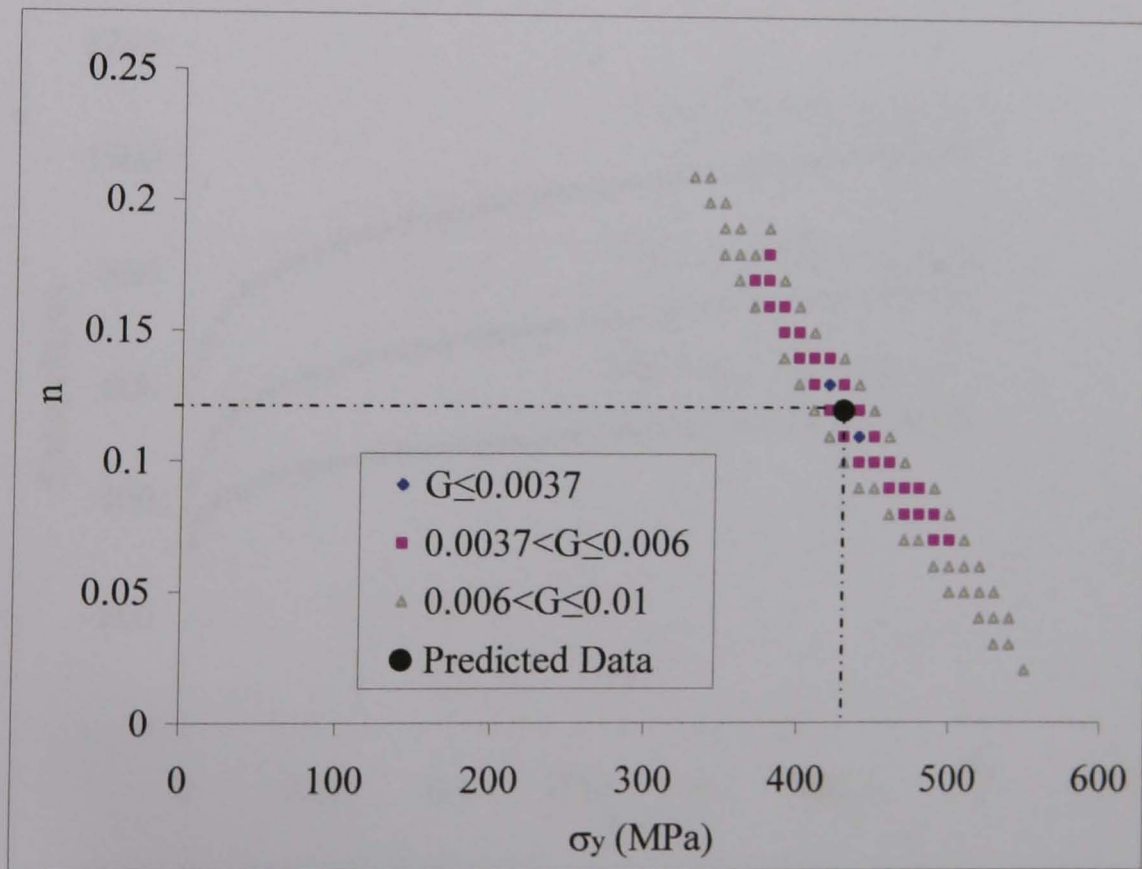


(b) Force-indentation size (P - d) data of spherical indentation tests of the three welding zones.

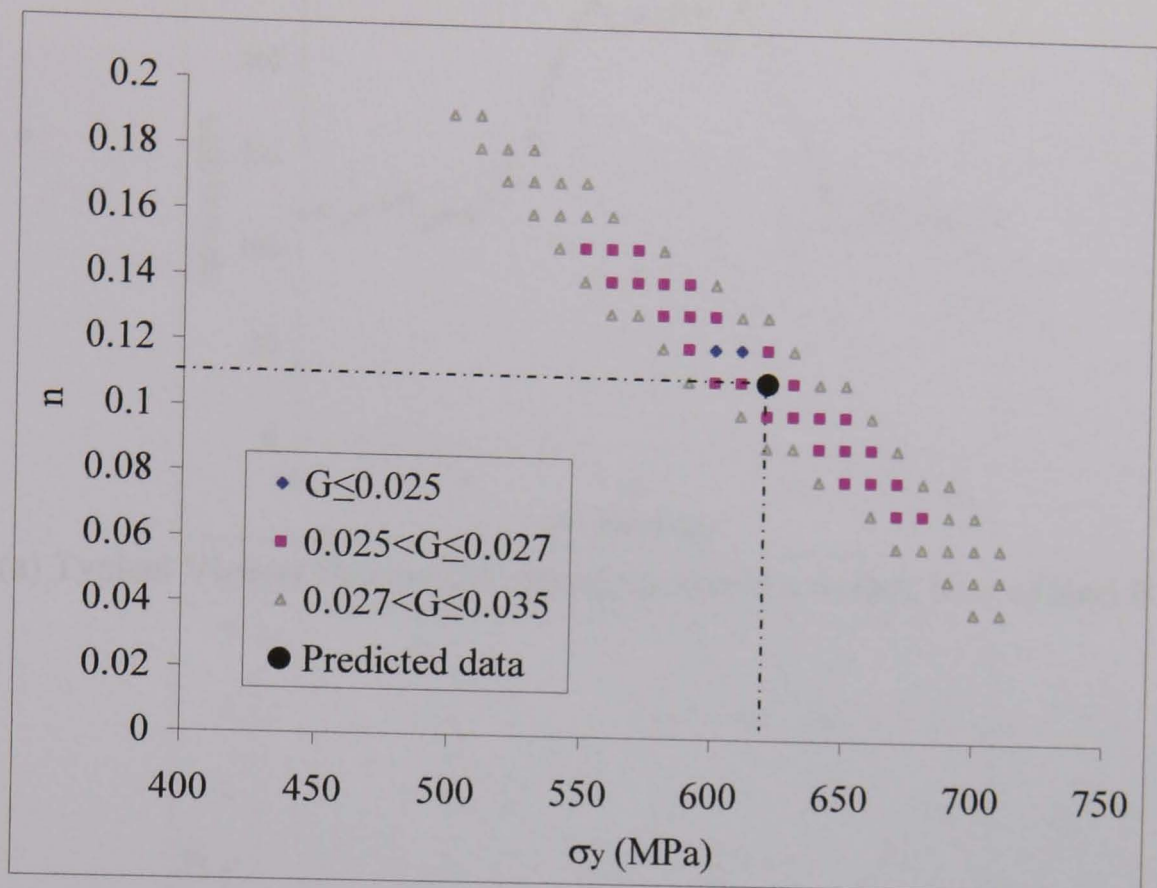
Figure 5.21 Force-indentation size (P - d) data for three different welding zones in the welded joint of steel A.



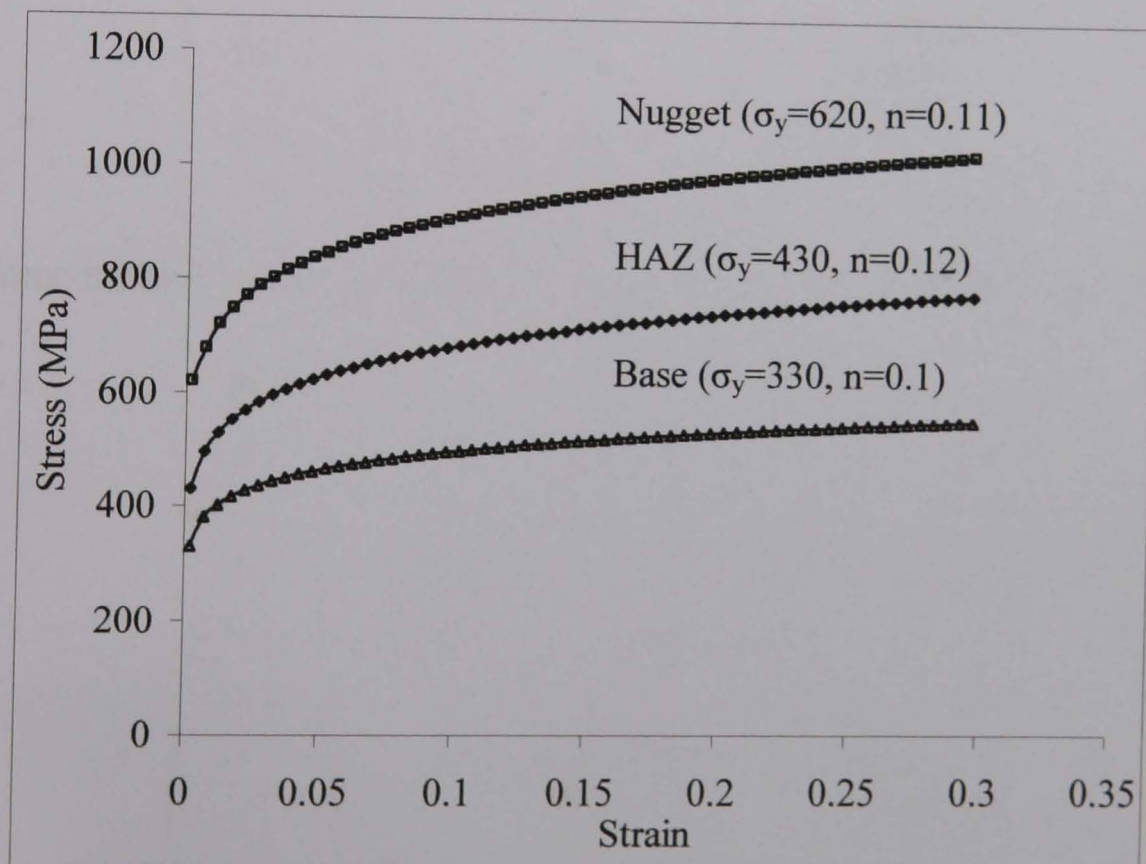
(a) Typical properties with lower objective functions for the base zone.



(b) Typical properties with lower objective functions for the HAZ.

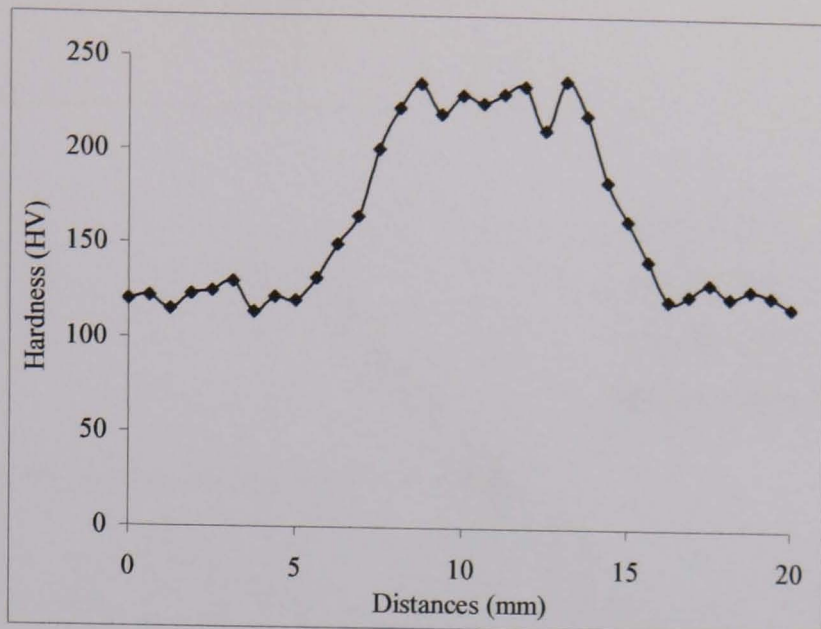


(c) Typical properties with lower objective functions for the nugget zone.

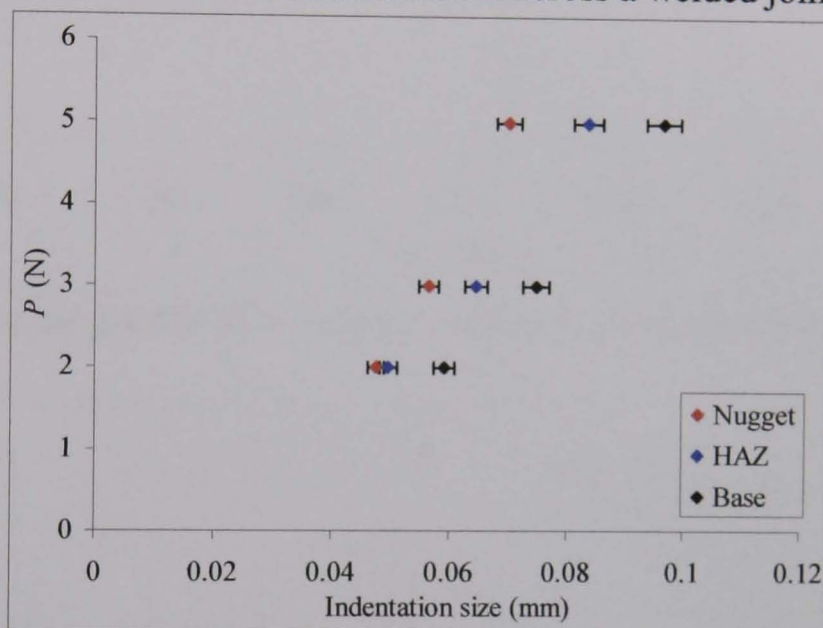


(d) Predicted plastic stress-strain curves for the three welding zones.

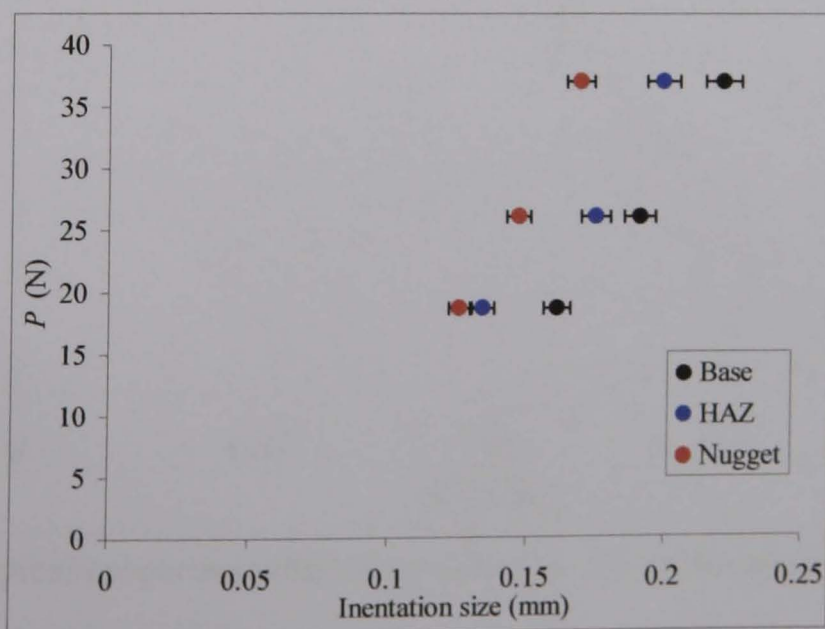
Figure 5.22 Inverse modelling results for the three welding zones of steel A.



(a) Typical Vickers Hardness distributions across a welded joint of steel B.

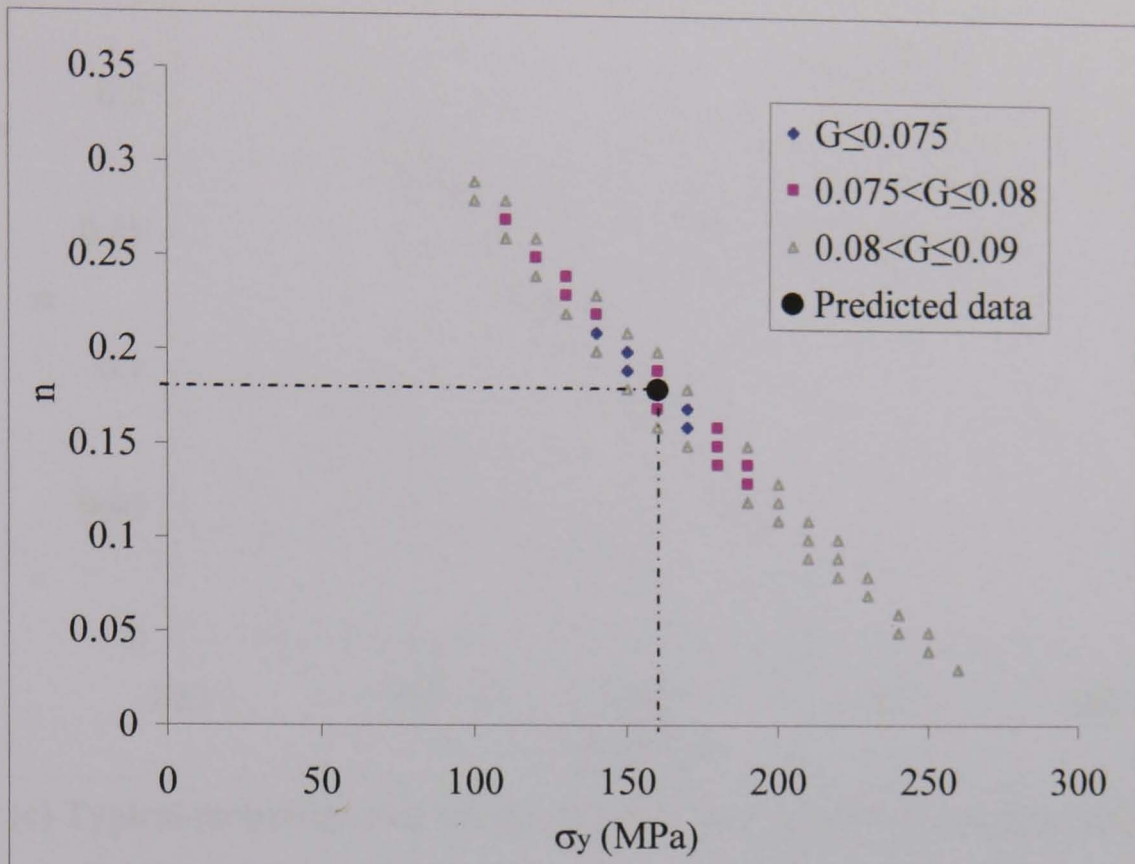


(b) Force-indentation size ($P-d$) data of Vickers indentation tests of the three welding zones.

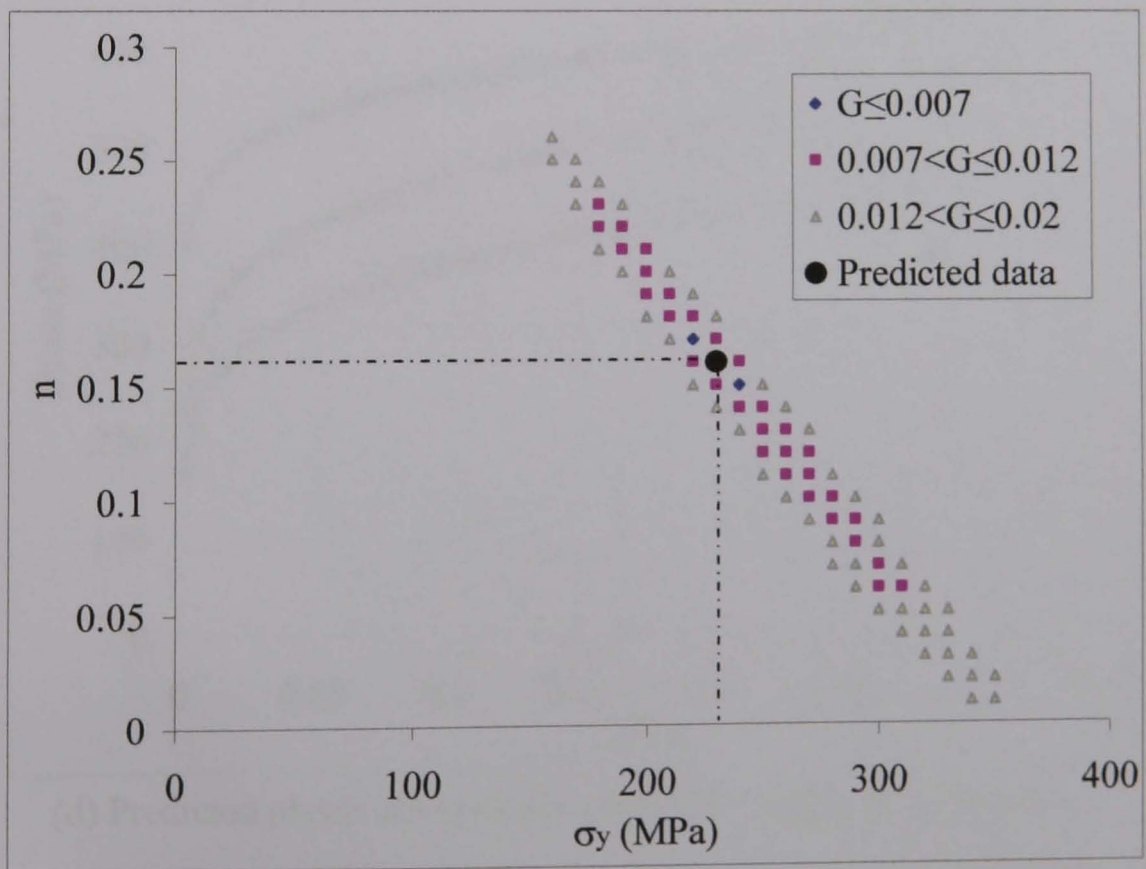


(c) Force-indentation size ($P-d$) data of spherical indentation tests of the three welding zones.

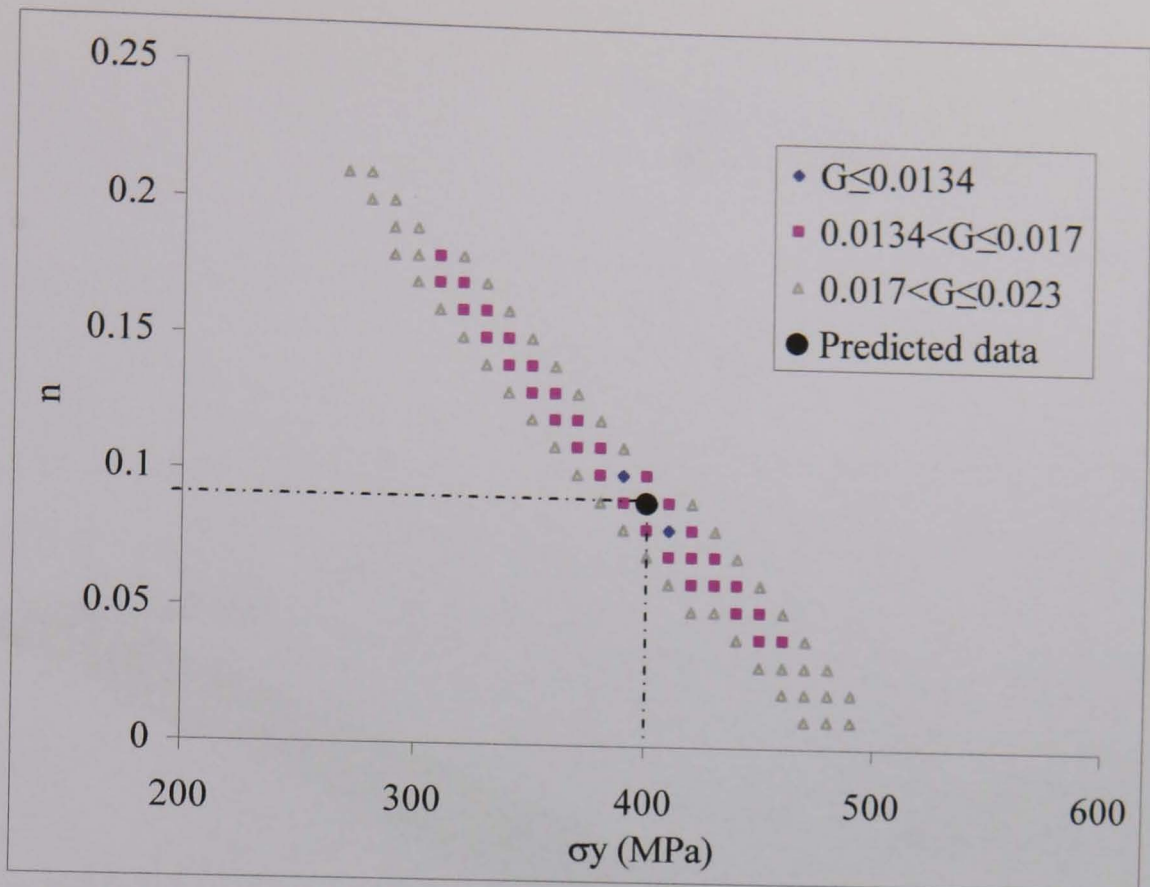
Figure 5.23 Hardness data and force-indentation size ($P-d$) data for the three welding zones in the welded joint of steel B.



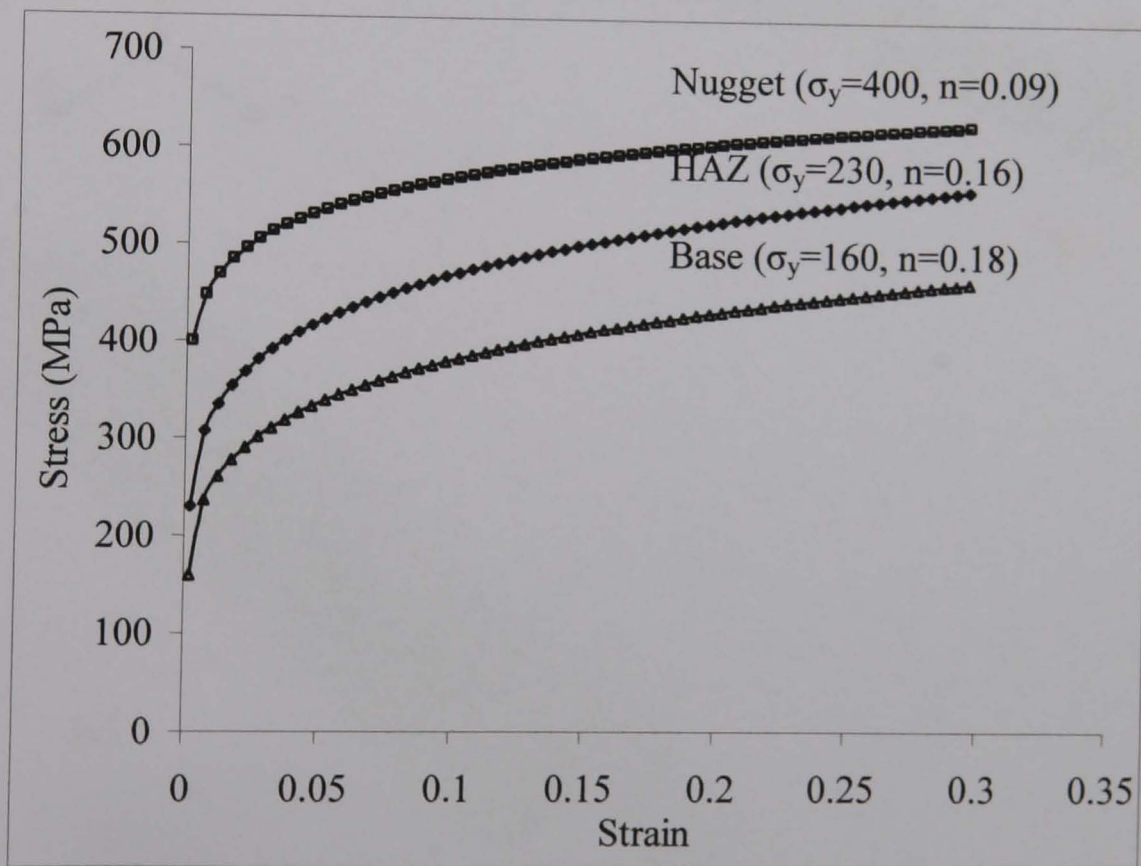
(a) Typical properties with lower objective functions for the base.



(b) Typical properties with lower objective functions for the HAZ.



(c) Typical properties with lower objective functions for the nugget zone.



(d) Predicted plastic stress-strain curves for nugget, HAZ and base.

Figure 5.24 Inverse modelling results for the three welding zones of steel B.

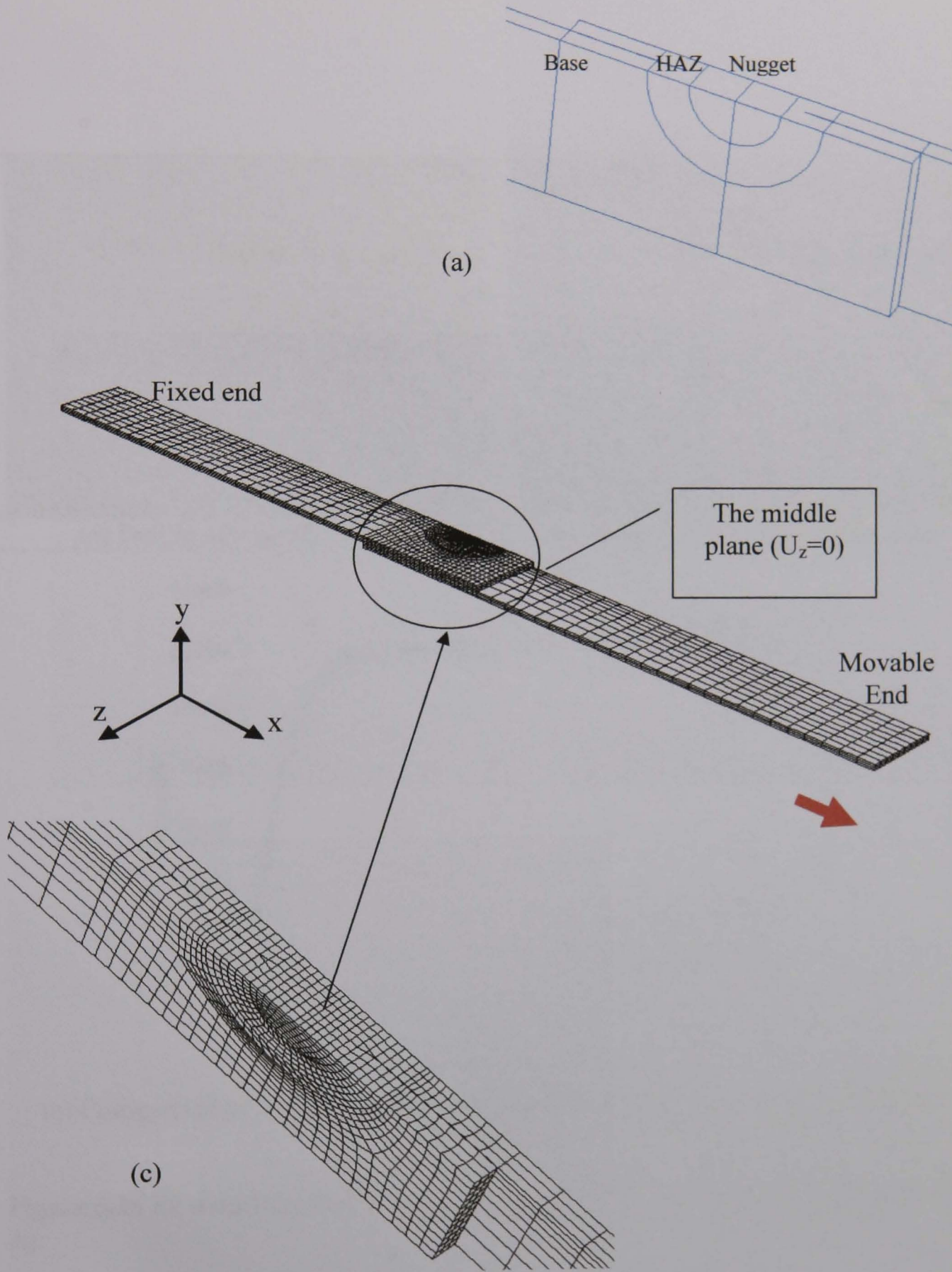
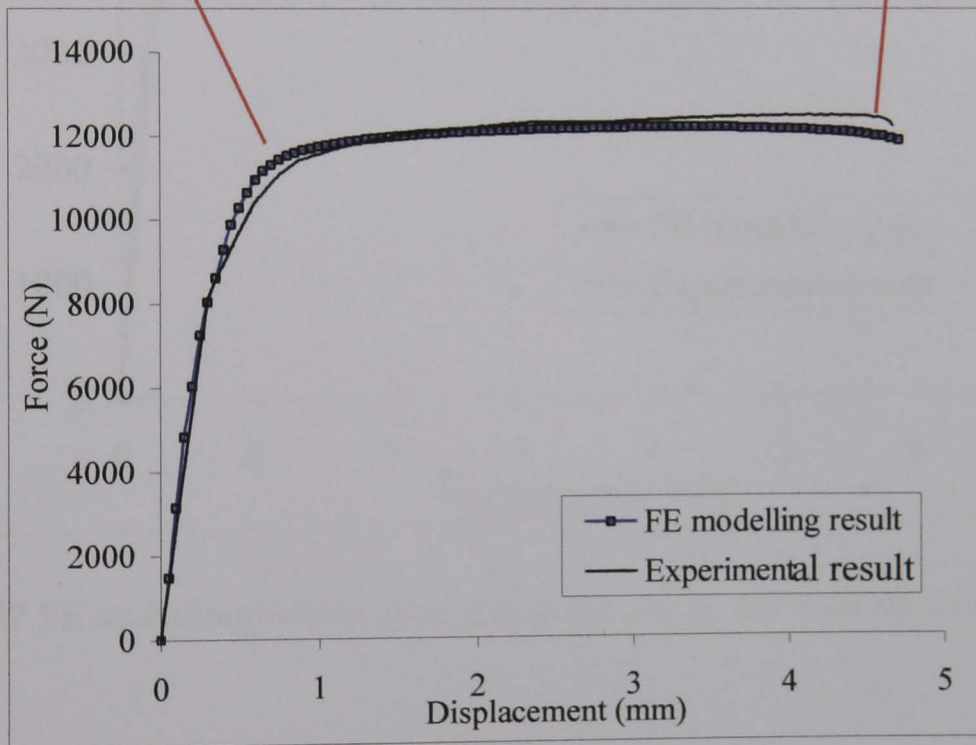
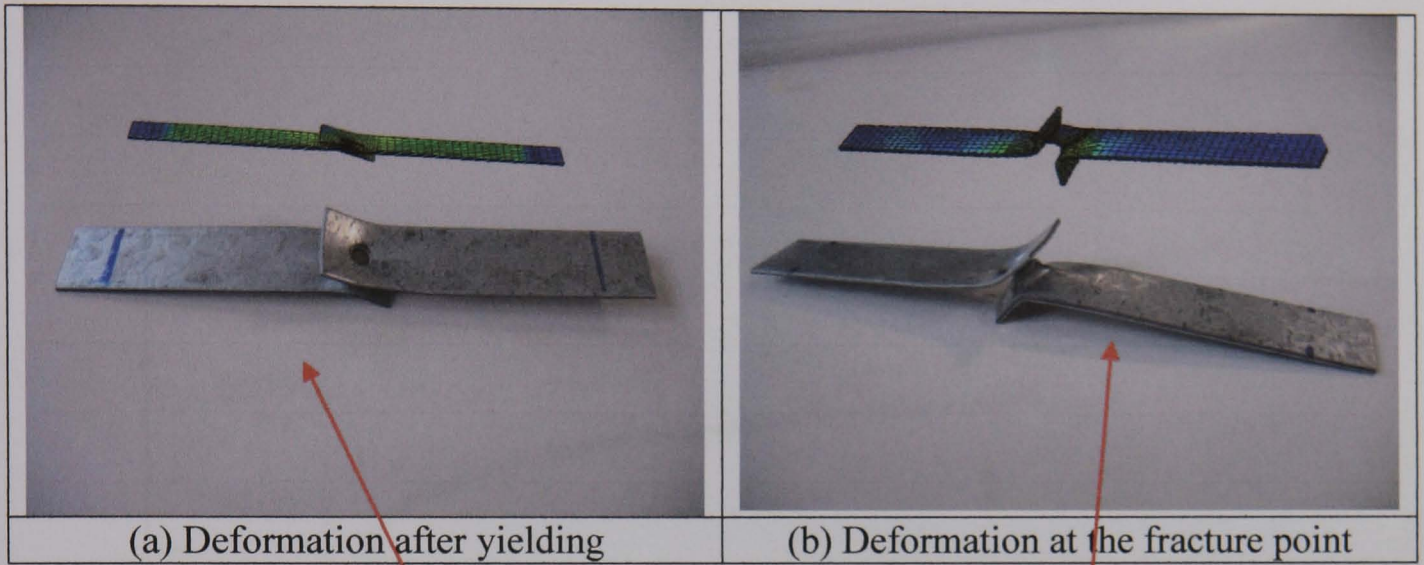


Figure 5.25 Typical FE model of tensile-shear test of spot welded joint.



(c) Comparison of predicted and experimental load-displacement curve of a spot welded joint.

Figure 5.26 FE modelling results of tensile-shear test vs. the experimental data (steel A).

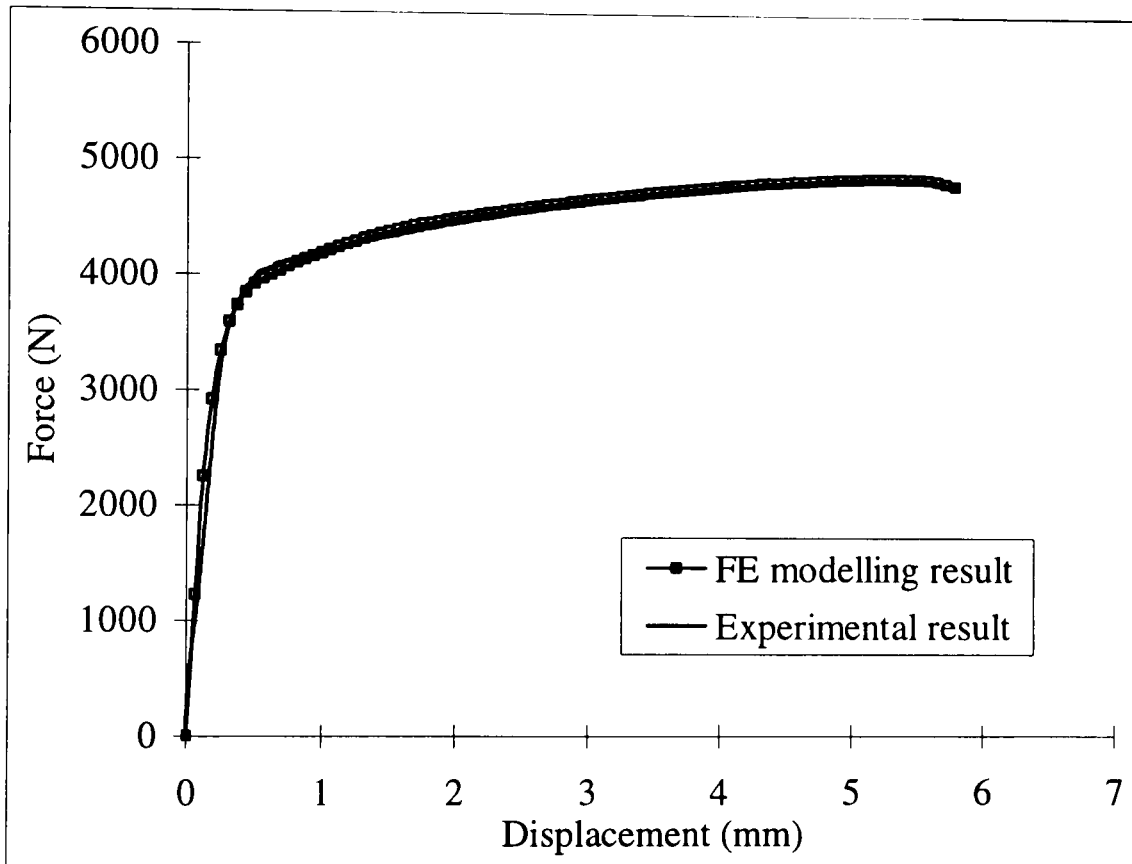
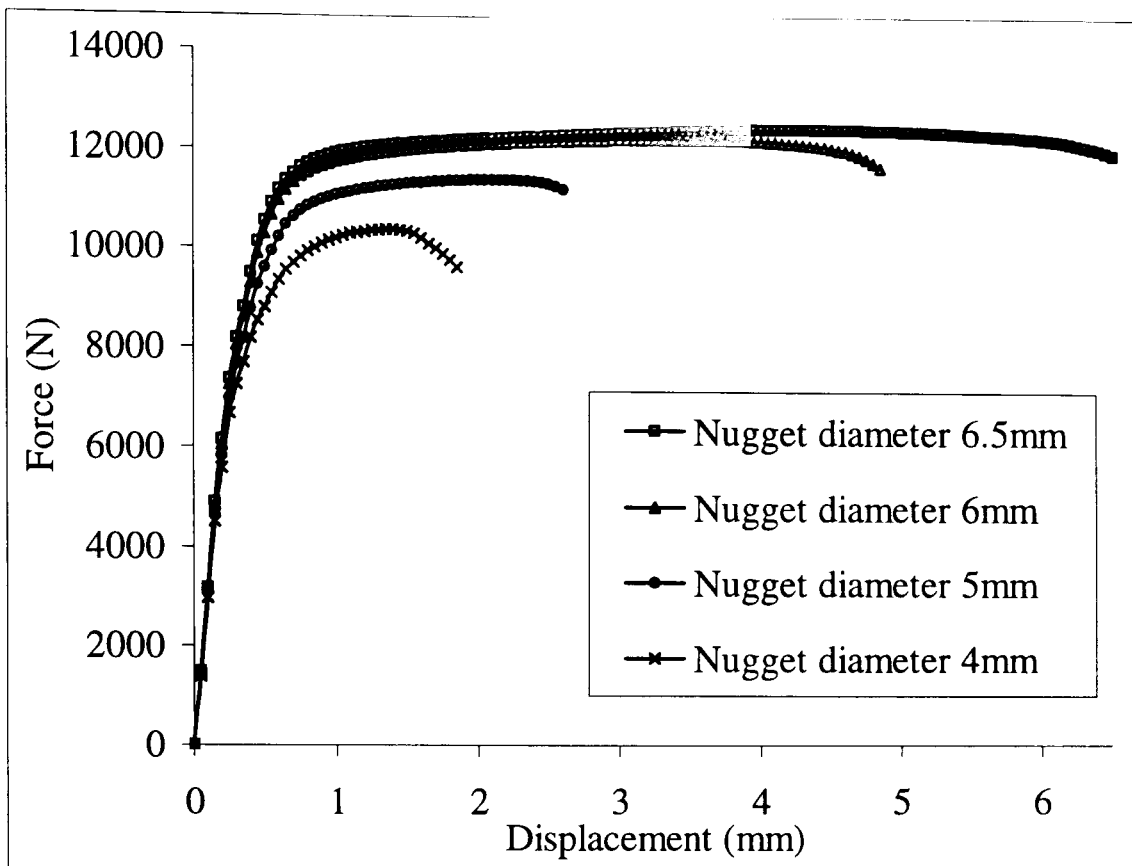
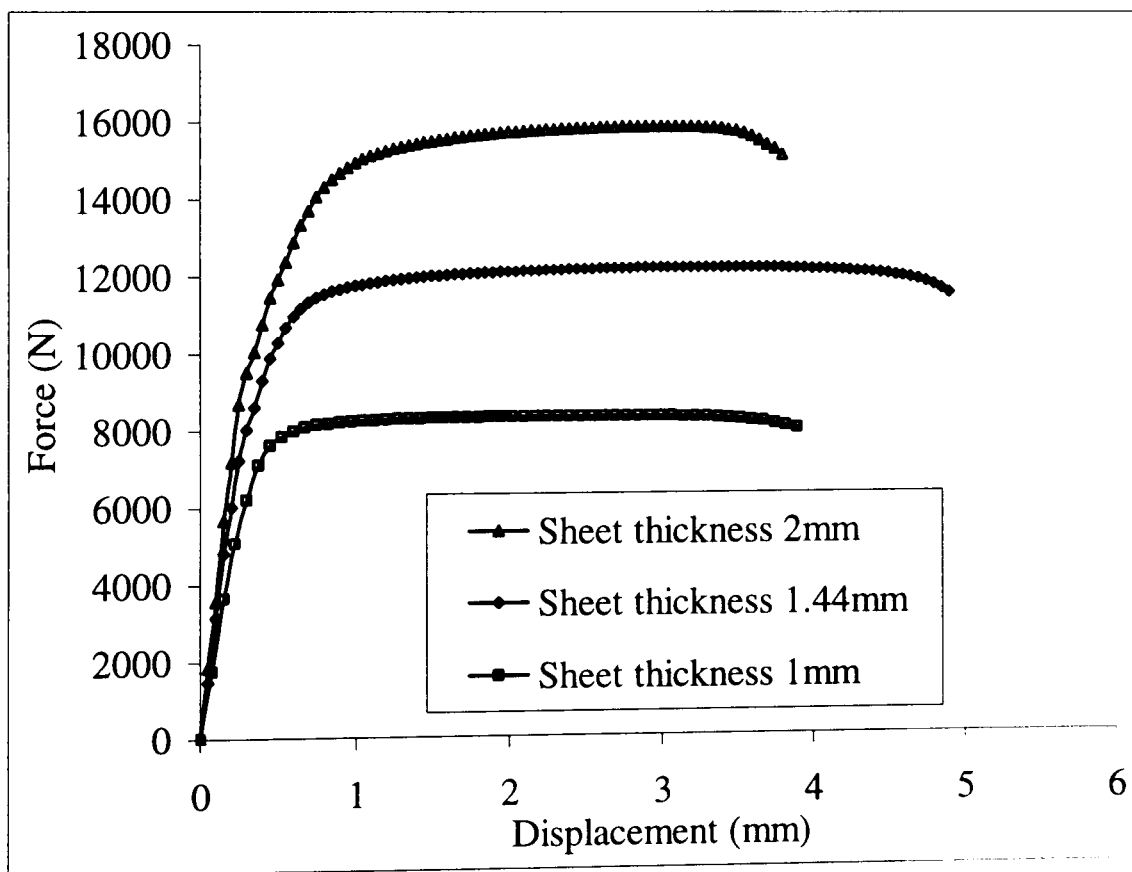


Figure 5.27 FE modelling results of tensile-shear test vs. the experimental data (steel B).

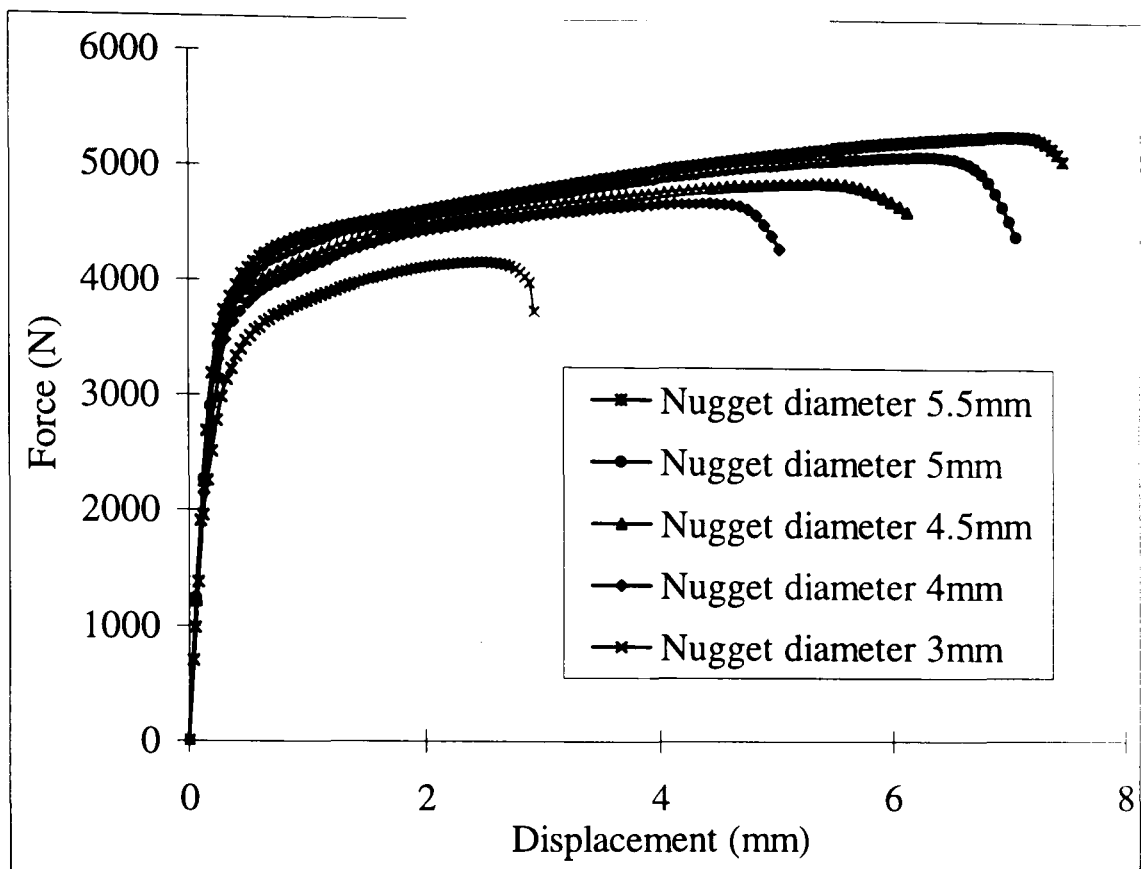


(a) Force-displacement data of welded joints with different nugget diameters (sheet thickness=1.44mm).

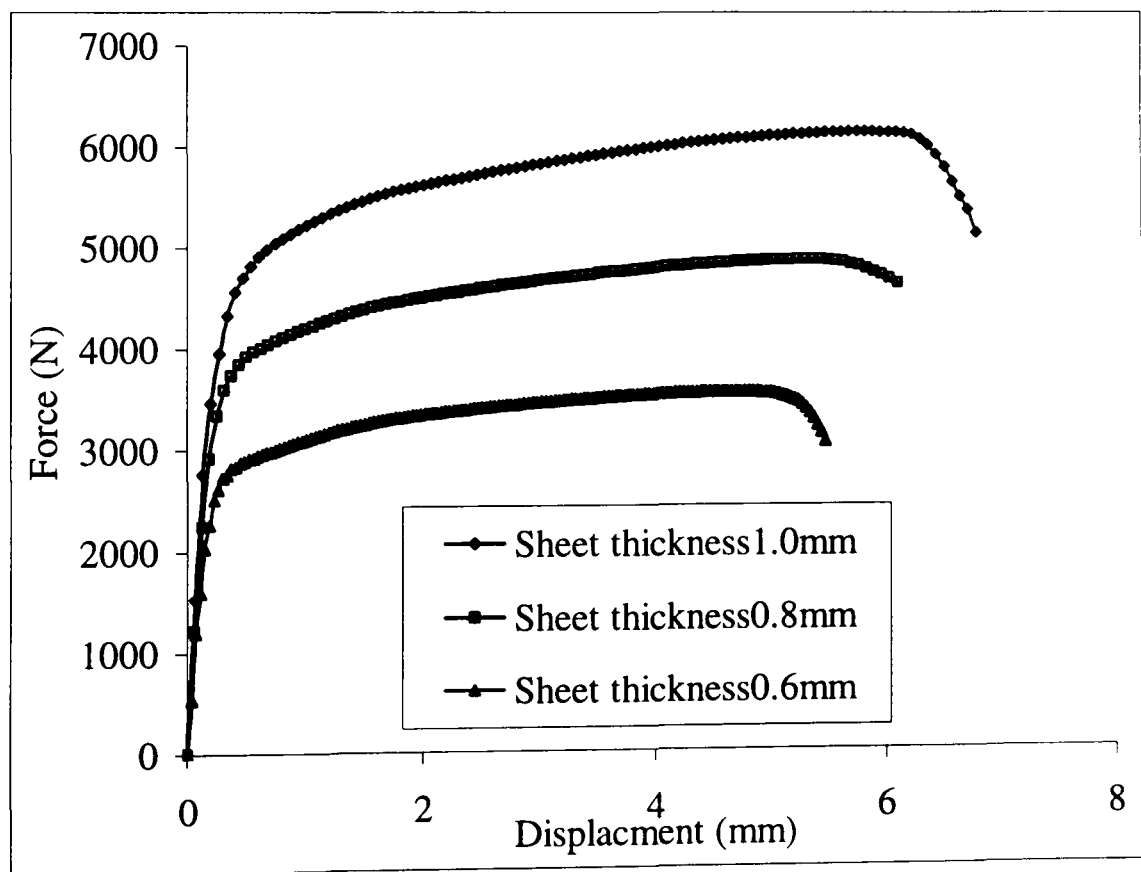


(b) Force-displacement data of welded joints with different sheet thickness (nugget diameter=6mm).

Figure 5.28 Effect of the nugget size and sheet thickness on the tensile shear strength of welded joint of steel A.

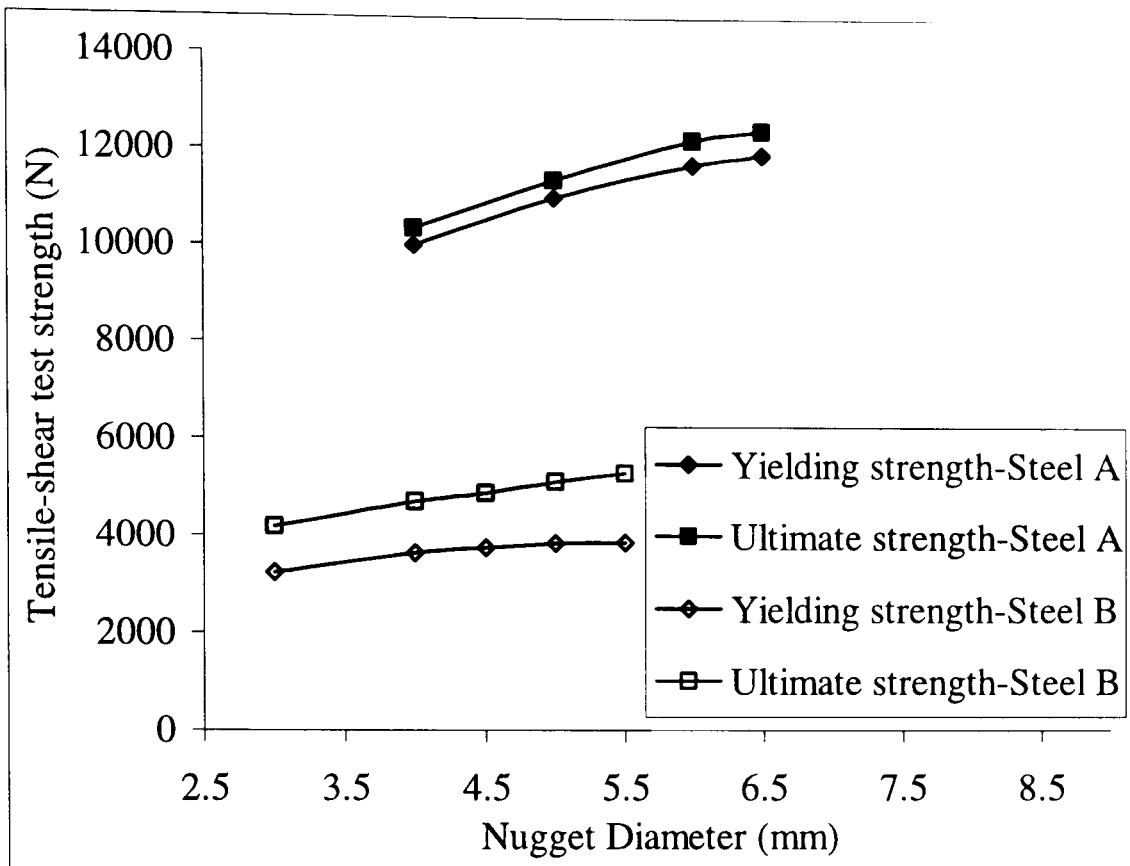


(a) Force-displacement data of welded joints with different nugget diameters (sheet thickness = 0.8 mm).

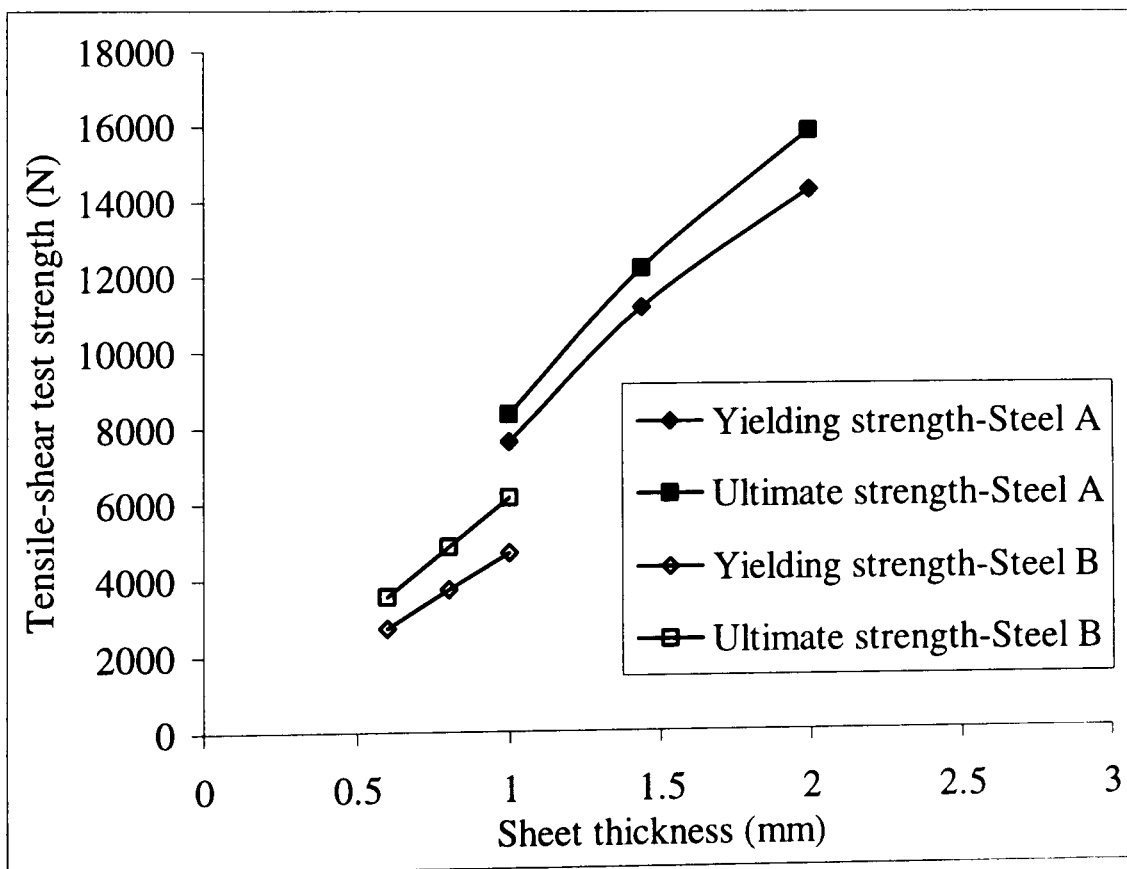


(b) Force-displacement data of welded joints with different sheet thickness (nugget diameter = 4.5 mm).

Figure 5.29 Effect of the nugget size and sheet thickness on the tensile shear strength of welded joint of steel B.



(a) Effect of the nugget diameter on the strength of welded joints under tensile shear loading for steel A and B



(b) Effects of the sheet thickness on the strength of welded joints under tensile shear loading for steel A and B

Figure 5.30 Effects of the nugget diameter (a) and sheet thickness (b) on the strength of the welded joints under tensile shear loading for steel A and B.

CHAPTER 6
DISCUSSIONS

6.1 Use of indentation and inverse FE modelling in characterising material properties

Indentation testing is an important materials testing method in which a sharp or blunt indenter, is pressed into the surface of a material. It can be used to test different types of materials such as brittle (e.g. ceramics), elasto-plastic (e.g. metals) and soft materials (e.g. foams, rubbers, etc.) (Ren *et al*, 2003). One significant advantage of indentation is that it only requires small amounts of material; this makes it very attractive for the characterisation of materials with gradient properties, where standard specimen is not readily available such as *in situ* or *in vivo* tests (Ren *et al*, 2004; Ren *et al*, 2006). As shown in Figure 2.3, spot welded joints represent a typical case for such a situation. As demonstrated in chapter 5, the plastic material properties for the different regions in a spot welded joint have been successfully predicted using a simple approach developed based on the frame-work setup in chapter 4. These material properties were then used in a FE model to predict the performance of spot welded structure under tensile shear loading.

Spot welded joints are widely used in many load bearing situations and their mechanical strengths have a strong influence on the integrity of the whole structure. A large amount of research work have been conducted to study the deformation of spot welded joints, experimentally or numerically, under different loading, such as tensile, bending, impact, etc. (Cavalli *et al*, 2003; Darwish, 2003; Yang *et al*, 2003; Zhou *et al*, 2003). Two important aspects governing the strength of the weld are its elasto-plastic law and fracture behaviour, which have been studied in this work. The elastic properties (e.g. Young's modulus E) of the metal are available from standard test of the base metal, and it is known that the Young's modulus does not vary significantly with structure change associated with thermal history of the material such as heat treatment or welding (ASM, 1966). This made it reasonable to focus on the plastic behaviour of the metal and welding zones.

The plastic behaviour is normally described by the constitutive material equations. The plastic behaviour can be described by two forms of constitutive laws. One form

uses three parameters (Eq. 2.1) while the other form uses two parameters (Eq. 4.1). In many cases, the three parameter power-hardening rule (Eq. 2.1) is used for steels. These material parameters influence both the yielding strength and work hardening behaviour of the spot welded joint. However, most works on inverse modelling used the two parameter power law form (Eq. 4.1) for the true stress-strain curves rather than the three parameter form since the parameter K and n are interlinked. This is confirmed by preliminary work using three parameter equations, which could not predict a unique set of material properties. Most metallic materials can be accurately described by two parameter methods. This made it a lot easier for the inverse prediction of properties, so it has been adopted by several approaches using either the full loading/unloading curves or the loading curve from instrumented indentation tests (Tabor, 1951; Giannakopoulos and Suresh, 1999; Dao *et al*, 2001; Herbert *et al.*, 2001; Nakamura *et al*, 2001; Bucaille, *et al*, 2003; Cao and Lu, 2004; Tho *et al*, 2004; Lan and Venkatesh, 2007).

As shown in Figure 2.18, an inverse FE modelling process has been developed, which consists of three main parts — experimental data, finite element modelling (FE) data and the inverse program. The validity and accuracy of such an approach may be influenced by factors associated with these processes, such as experimental data, FE modelling, searching mechanism, etc. The most crucial fundamental aspect of an inverse program lies in that the input data must be able to provide sufficient material behaviour over different stress-strain conditions. In other words, there must be (or close to) one to one relationship between the stress-strain relationship and the experimental data. This may effectively be achieved by selecting suitable indentation testing conditions (types of indenter or combination of the indenters). This was evaluated using comparative study approaches based on single indenter and dual indenter methods of three most commonly used indenter types — Vickers, Knoop and spherical.

As shown in chapter 4, numerical experimental data, i.e. numerical result with known material properties, were used as the experimental data for evaluation/identification purposes in the blind tests. This allowed the program to make a direct evaluation of estimated solutions, with respect to actual solutions, over a wide range of materials

and systematically compare the uniqueness and accuracy of the results. It also allowed the results from single and double spherical indenter method to be directly compared and their correlation was established. As shown in Figures 4.19, 4.21 and 4.23, the results from the single indenter method (Vickers, Knoop and Spherical) are not unique; multiple properties over a wide range of materials could match the indentation curves. This agrees with the published work (Dao *et al*, 2001; Bucaille *et al*, 2003; Swaddiwudhipong *et al*, 2005a; Luo and Lin, 2007). As shown in Figure 4.25, the work has also further established that the combination of sharp indenters (Vickers and Knoop) could not accurately predict the results either. As shown in Figures 4.17 and 4.28, the combination of the spherical indenters of different size could significantly reduce the range of materials matching the indentation curves, but the range of the converged parameters is still significantly large with distinctly different stress-strain curves. Evident from Figures 4.29-4.32, the combination of the sharp and spherical indenters produced much better results. The predicted results with lower objective functions were confined in a small region with comparable stress-strain curves. In other words, the stress-strain curve can be predicted uniquely with a reasonable range. The V+S and K+S approaches showed better sensitivity to perturbation of indentation force.

The study based on the continuous indentation curves has established a framework in terms of selection of indenters to predict the plastic properties. The force-indentation size approach based on dual indenters method of sharp and spherical indenters is more convenient to study spot welded joints. Preliminary works showed that the Knoop indenter is not entirely suitable as the gradient properties causing some uncertainty when testing the HAZ zones. The new inverse FE program was validated by blind tests (Table 5.1), and standard tensile test results of the two base steels (Figure 5.15). The accuracy achieved is comparable to that based on the $P-h$ curves. The slight difference between the predicted and experimental results is reasonable and will not cause significant difference in describing the material behaviours as shown in Figure 5.17 and Figure 5.18 in this case. The use of the approach in characterising spot welded joint showed that this approach is valid and potentially can be used as an alternative to the continuous testing to characterising plastic properties of materials. It can be used where continuous indentation facility is not readily available.

6.2 Factors affecting indentation and inverse FE modelling process

For elasto-plastic materials, the indentation process involves elastic and plastic deformation until reaching a full plastic regime at a higher indentation depth (i.e. strain level). The indentation resistance of a metal is commonly represented using the force indentation depth ($P-h$) curves, which can be affected by many factors (such as indenter shape, materials deformation around the indenter and experimental conditions, etc.). These factors have to be carefully considered when using the indentation method and FE modelling process. Frictional effect tested using the numerical models (Figures 4.3, 9 and 13) showed that there is significant effect between frictional and frictionless condition over the indentation depth range for the three indenter types used, while the difference between different friction coefficients is limited. This agrees with other published works (Bucaille *et al*, 2003). However, this could provide a significant advantage for inverse FE modelling as it could reduce the uncertainty of result due to frictional condition, which is normally very difficult to characterise.

The different material response with different indenter shapes may provide an important insight to inverse process of properties prediction. As shown in Figure 6.1, the $P-h$ curves for different types of indenter with the same materials were significantly different. Vickers and Knoop indenter can be simplified into cone indenters, with an angle of 70.3° and 77.64° , respectively. The curvatures of their $P-h$ curves are different but varied with the material properties in a similar trend as shown in Figures 4.5 and 4.10. The spherical indenter is significantly different, it has a varying indenter angle with depth. In addition, the contact area also changes with indenter type with the contact area of spherical indenters being significantly larger than the other two indenters (Table 2.2). As shown in Figure 6.2 (a-c), the strain distribution under the indenter is significantly different; this may potentially cause different material behaviours. The representative strain is independent of the indenter size or indentation load but is weakly influenced by the tip angle of the sharp indenter (Bucaille *et al*, 2003). Invoking the existence of this representative strain is a key step in the determination of mechanical properties using reverse method by sharp

indentations (Giannakopoulos and Suresh, 1999). Figure 6.3 shows the strain distribution for R0.5mm at different depths. Strain distribution is also not significantly different. The difference between sharp and spherical indenter may provide the different stress strain condition therefore better inverse modelling to predict the material properties. This is probably the reason behind the better prediction result for the dual indenters method than the single indenter method.

6.3 Comparisons of the accuracy with different approaches

Two main current research focuses to be tackled are the uniqueness of the predicted parameters and their sensitivities to perturbation in experimental data, which is an intrinsic characteristic of the problem in inverse (or reverse) material parameters identifications (Bucaille *et al*, 2003; Lan and Venkatesh, 2007). This has been successfully investigated by directly comparing different approaches for the same input material set.

As detailed in chapter 4, for each single indenter method, there were multiple sets of material properties matching the input $P-h$ curves and all these data fall roughly on a straight line. This agrees with some recent works (Cao and Lu, 2007; Luo and Lin, 2007). Single spherical indenter has reduced the numbers of material sets, but the result is still not unique over the strain range of this work. Dual sharp indenters using Vickers and Knoop have not significantly reduced the number of potential material, and all these data fall roughly on a straight line similar to the single Vickers or Knoop method. The dual spherical indenter method showed significant improvement but the accuracy is lower than the combinations of sharp and spherical indentation.

Figure 6.4 compared the accuracy of the three dual indenter method (S+S: SR05 and SR1; K+S and V+S) with some published results (Dao *et al*, 2001; Bucallie *et al*, 2003; Swaddiwudhipong *et al*, 2005) for material with $\sigma_y=500$, $n=0.1$. Dao *et al* (2001) used the reverse analysis method by sharp indentation $P-h$ curves to characterise the material properties. Bucallie (2003) utilised the reverse analysis method by dual and four sharp indentation $P-h$ curves to characterize the material properties. Swaddlwudhlpong *et al* (2005) used the reverse modelling method by dual and four sharp indentation $P-h$ curves to characterize the material properties. It is clearly shown that the V+S and K+S method developed in this work has achieved significantly better accuracy than the published works in blind test.

6.4 Sensitivity of the inverse FE modelling to perturbation in the indentation force

Sensitivity of the predicted material properties due to variations of the input parameters is essentially an intrinsic characteristic of inverse processes. In this work, the input data were taken from a numerical model, but, in a real testing situation, there can be potentially both system and random errors. Factors such as indenter angle, roundness of the tip, and accuracy of the recorded indentation force or depth all influence the measurement results (Dao *et al*, 2001). This has been studied by adding a small percentage of perturbation to the indentation force, and then comparing the predicted properties with the original data. As shown in Table 4.4 (sensitivity study), a perturbation of 3%, a typical error in indentation tests as established by Dao *et al* (2001), resulted in a variation of ~10% of the yield stress and within ~10% of the work hardening coefficient. It is also shown that the V+S method is significantly better than the dual spherical method. In both cases, the sensitivity results were considerably better than other reported methods. Figure 6.5 compared the sensitivity of the three approaches and some published works with a material properties set of $\sigma_y=500$, $n=0.1$. The combination of sharp and spherical indenters is less sensitive to the perturbation in experimental data than combination of spherical indenters of different sizes. The sensitivity from these methods is considerably lower than the variation associated with dual sharp indenters on similar materials. Bucaille *et al* (2003) have systematically investigated the perturbation in force on the predicted results using a reverse method based on Dao's approach. A 3% increase of the normal force resulted in a difference of 16-44% (cone indenter angle is from 42.3° to 60.3°) on the value of 'n' for steel. Swaddiwudhipong *et al* (2005a) found that the yield stress exhibits rather strong sensitivity to perturbations in input parameters, especially for regions with large n values. At regions with n values less than 0.4, the variation of yielding strength due to perturbations in input parameters is capped at 30%. The maximum variation of n in the domain is about 0.1 for the large value of n of 0.6. This clearly demonstrates that the dual indenters method could further reduce the uncertainty of predicted material properties compared to the dual sharp indenter method.

This reduced sensitivity of predicted material properties to perturbations in the input data is probably due to the fact that the V+S method has introduced a higher degree of redundancy by incorporating the results of more indenters. This could provide a practical approach, which is not dependent on the initial value and strain level.

6.5 Approach based on static indentation test and characterisation of spot welded joints

The instrumented method is an automatic way to determine continuous $P-h$ curves; however, the work relies on the accuracy of testing facilities. In addition, factors such as the contact area, indenter type and alignment may significantly affect the results (Dao *et al*, 2001; Bucaille *et al*, 2003; Swaddiwudhipong *et al*, 2005a,b). The force indentation size approach developed in this work represents a simpler approach. As shown in the blind test (Table 5.1), the work can provide similar accuracy compared with using the $P-h$ curves as shown in Figure 5.15. The predicted material properties showed a good agreement with standard tensile tests. This demonstrated that this is a feasible approach. As detailed in Chapter 5, the correlation between the experimental results is not as close as the blind tests. However, in all the cases, the G values showed a clear focusing point and reasonable small region of similar G values, which suggest that the approach can produce reasonably unique results. The scatter of the indentation may come from many factors associated with the experimental or material factors, which requires further investigation. However, the prediction is reasonably robust and accurate for this application.

As shown in Figure 5.22 (d) and 5.24 (d), the true stress-strain curves of the base, HAZ and nugget were significantly different. This is probably associated with thermal mechanical process of the welding process. As shown in Figure 2.1-2.3, the welding process is a complex interaction between electrical, thermal, metallurgical and mechanical phenomena, which leads to the plastic material property change in distinct welding zones (Figure 5.20 and 5.23). The weld nugget typically consists of a martensite structure due to the high cooling rate while the heat affected zone (HAZ) is a mixture of tempered structure. This caused the difference in the yield stress, which is mainly associated with the structural difference of the phases. The work hardening coefficient varied slightly between the base, HAZ and nugget. The difference between steel A and B is probably due to the potential effect of the production process of these two steels.

Traditionally, the yield stress is estimated using hardness values of welded joints (Zuniga and Sheppard, 1995; Zhou *et al*, 1999). The commonest approach used a ratio of 3 ($\sigma_y \approx H_v/3$). Figure 6.6 and Figure 6.7 compare the yield stress of welding zones predicted in this work (V+S method) and other methods. Also included in the figure was the data for the base metal at an annealed condition (Quenching at 880°C and furnace cooling), which represents a work hardening relieved condition. It clearly showed that, the yield stresses predicted by V+S method and Zuniga's method (Zuniga and Sheppard, 1995) were close to the tensile test result (as shown by the dotted lines) for steel A. However, Zuniga's method failed to predict the material properties for steel B, while the hardness method has over estimated the yield stress of the material. Zhou's method is not for predicting yield stress but the ratio between the Base, HAZ and Nugget. For steel A, the result from the V+S method is comparable to the prediction based on Zhou's method but the prediction is significantly different for steel B. This suggested that the ratio is material dependent, which may limit the application of Zhou's method.

Figure 6.7 compared the predicted work hardening coefficients for different zones with samples of the base metal under annealed condition. The 'n' value has followed a different trend for these two materials. Steel A has a relatively low work hardening coefficient and it increased after annealing (from 0.1 to 0.15). This is probably associated with the release of the work hardening with the heat treatment. The work hardening coefficient increased slightly in the HAZ and the Nugget. While for steel B, the 'n' value showed ignorable change with annealing condition and slightly decreased in the HAZ and the nugget. The different trend of n within two steel joints is probably associated with their initial production conditions.

As an essential tool to achieve automation and prediction of the material/structure behaviour, finite element (FE) modelling has been used in simulating the thermal process, the development of the microstructures and their effect on the performance of welded structures (Cerjak and Easterling, 1993; Chae *et al*, 2002; Aravinth *et al*, 2003; Bayraktar *et al*, 2004; Santos and Zhang, 2004; Yang *et al*, 2005). However, the majority of the works on the mechanical modelling have been using simplified material models (Zhou *et al*, 1999; Deng *et al*, 2000; Langrand and Combescure, 2004;

Rodrigues *et al*, 2004a, b; Rusinski *et al*, 2004) due to the difficulties in measuring the localised material properties. The work developed in this work represents a more thorough approach incorporating the detailed material properties to be able to accurately predict the performances of the structure. The results show that the FE models with material properties predicted from indentation could match the tensile-shear test results. The models were then used to study the effect of nugget size and sheet thickness. As shown in Figure 5.30, in both cases, the relationship is not entirely linear and the structure-strength relationship is clearly material dependent. It should be noted that the nugget sizes concerned in this work all fall into the welding lobe of the material and can be defined as a good weld in industrial practice. One future direction of the work is to develop the model into a design for strength tool. As shown in Figure 6.8, the indentation method could be effectively fitted into a program consisting of welding simulation, material characterisation and mechanical modelling.

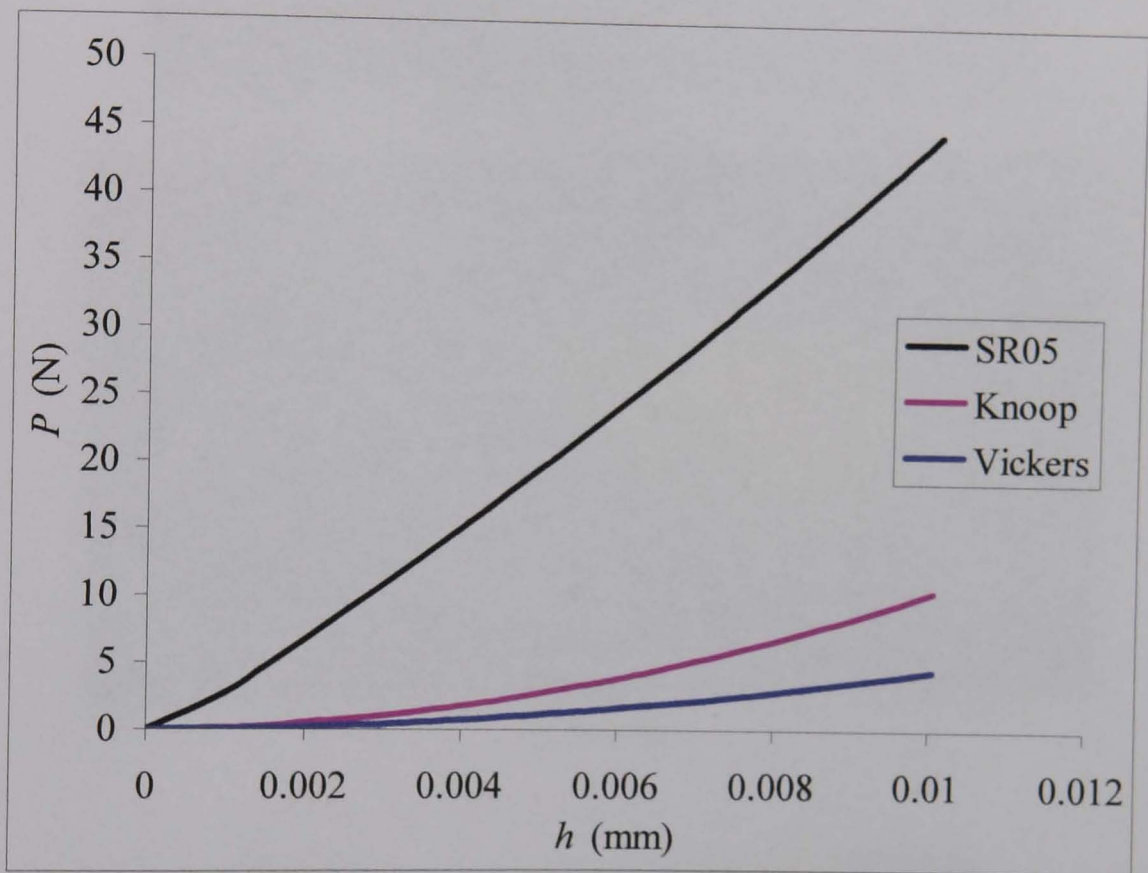
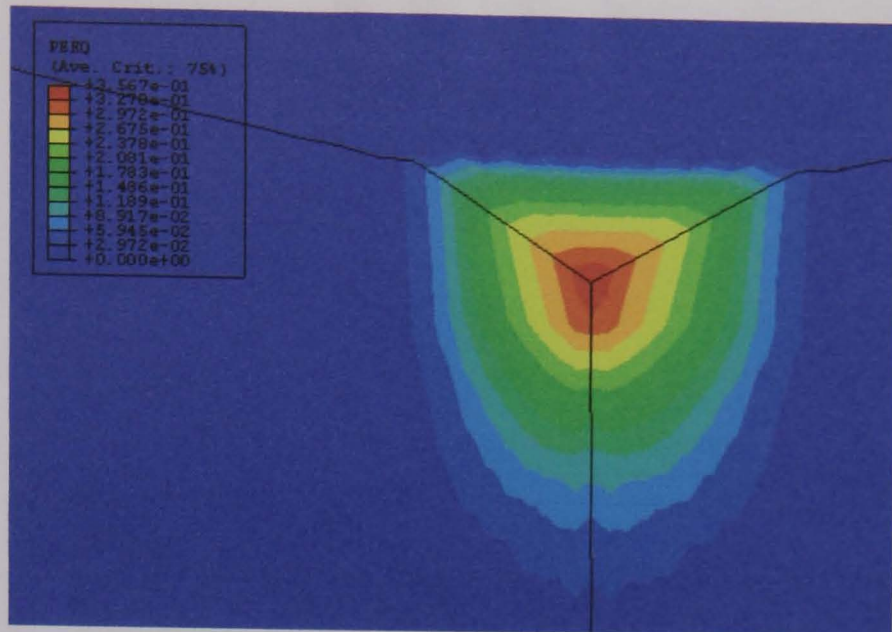
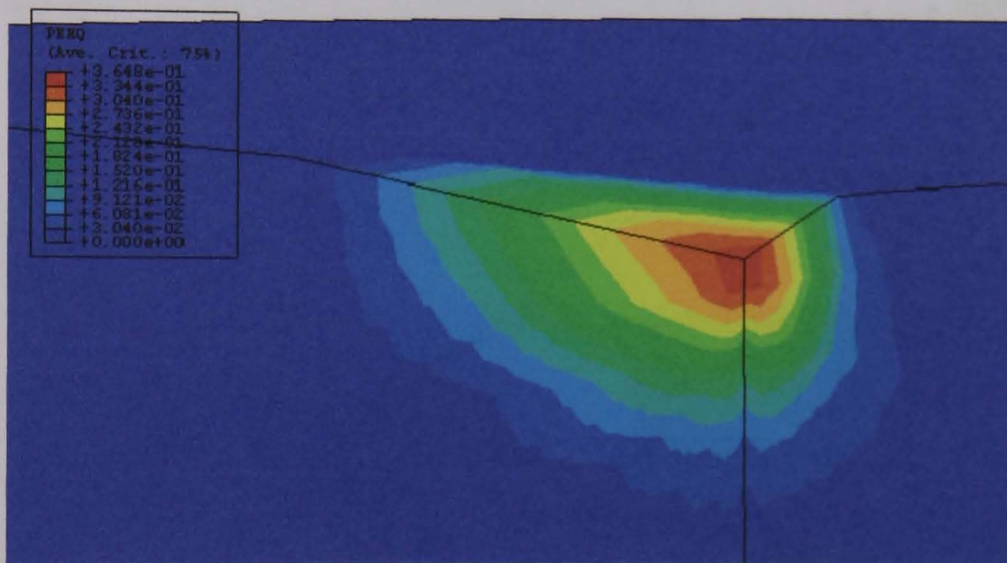


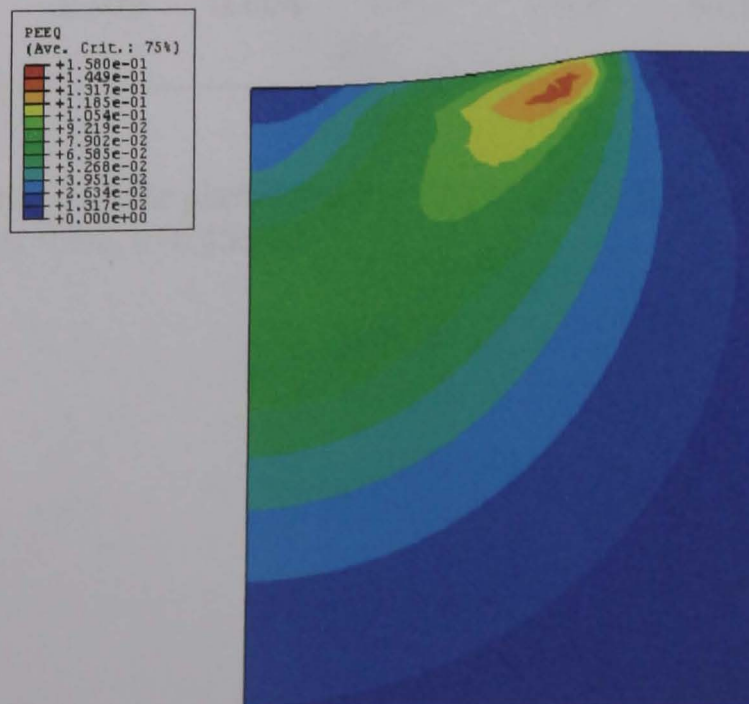
Figure 6.1 P - h curves of different indenter types.



(a) Vickers



(b) Knoop



(c) Spherical indenter (R=0.5mm)

Figure 6.2 Comparison of the equivalent plastic strain field with different type of indenters.

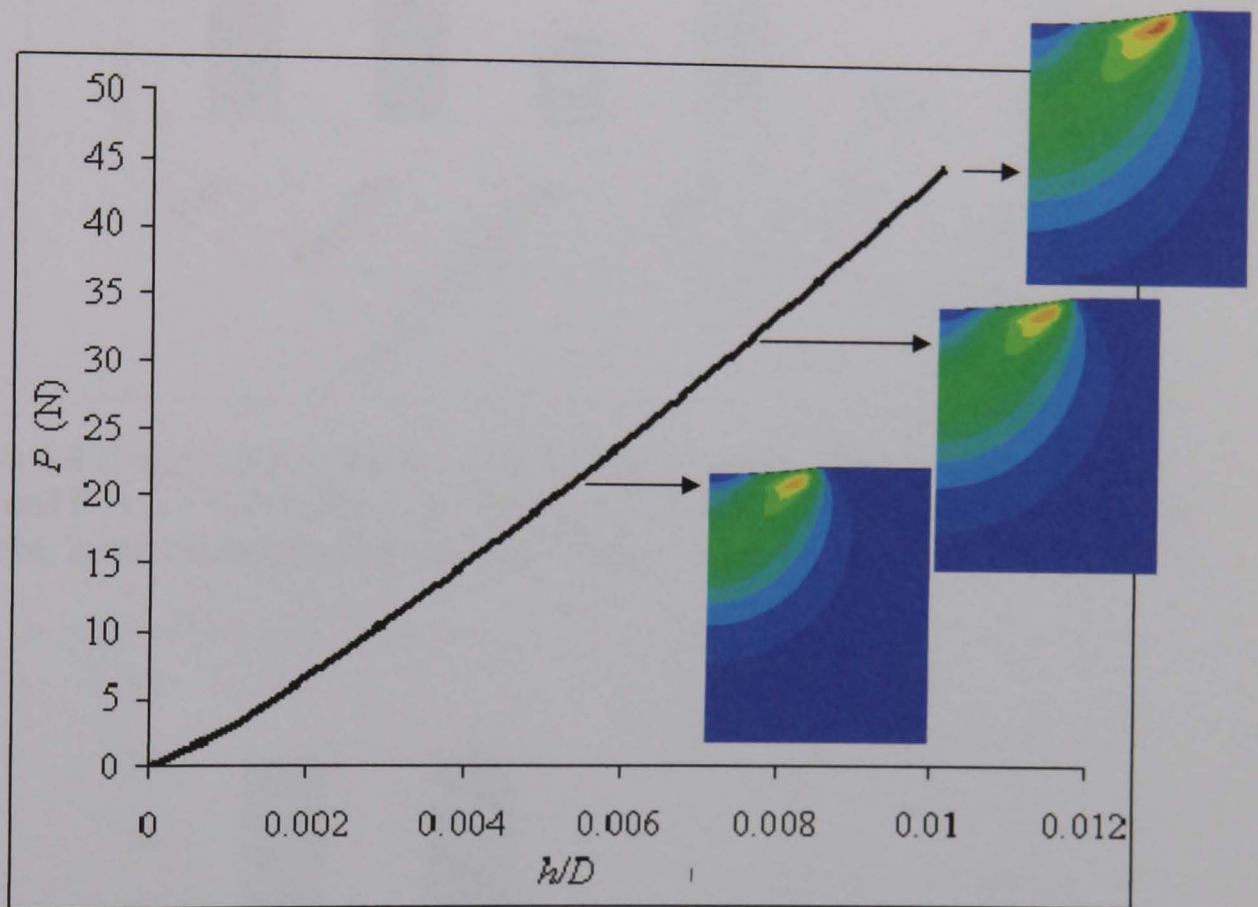


Figure 6.3 Comparison of the plastic strain field for spherical indenter at different indentation depth ($\sigma_y=300$, $n=0.155$).

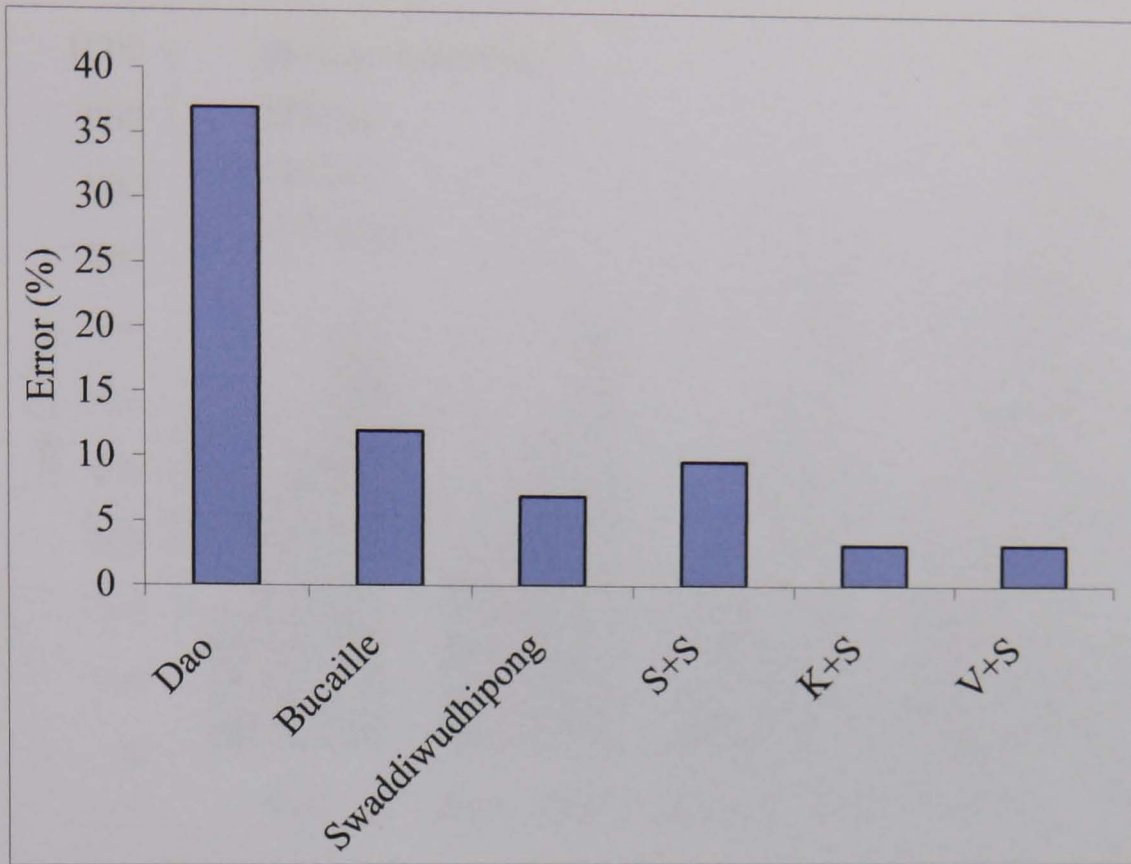


Figure 6.4 Comparison of the accuracy of different dual indenters methods (S+S, (R05 and R1); K+S: (SR05); V+S: (SR05)) with published results (Dao *et al*, 2001; Bucaille, 2003; Swaddiwudhipong *et al*, 2005).

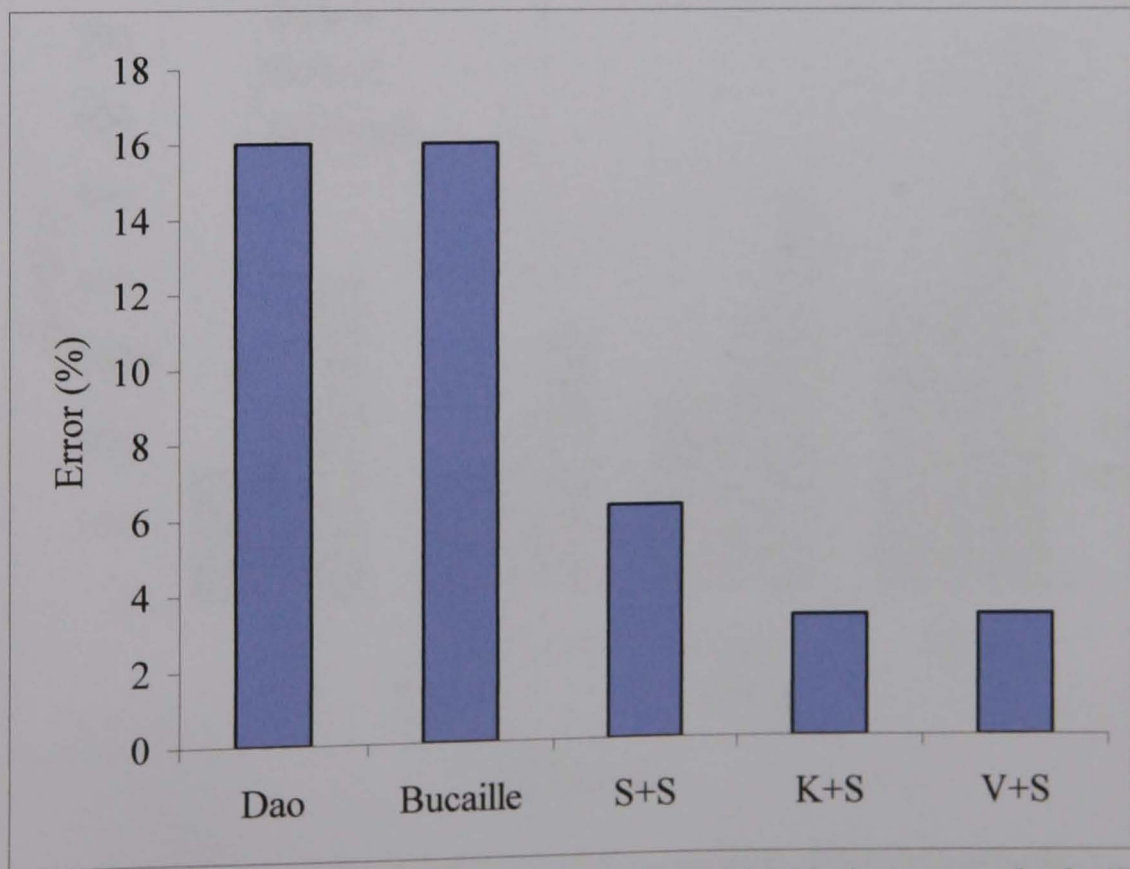
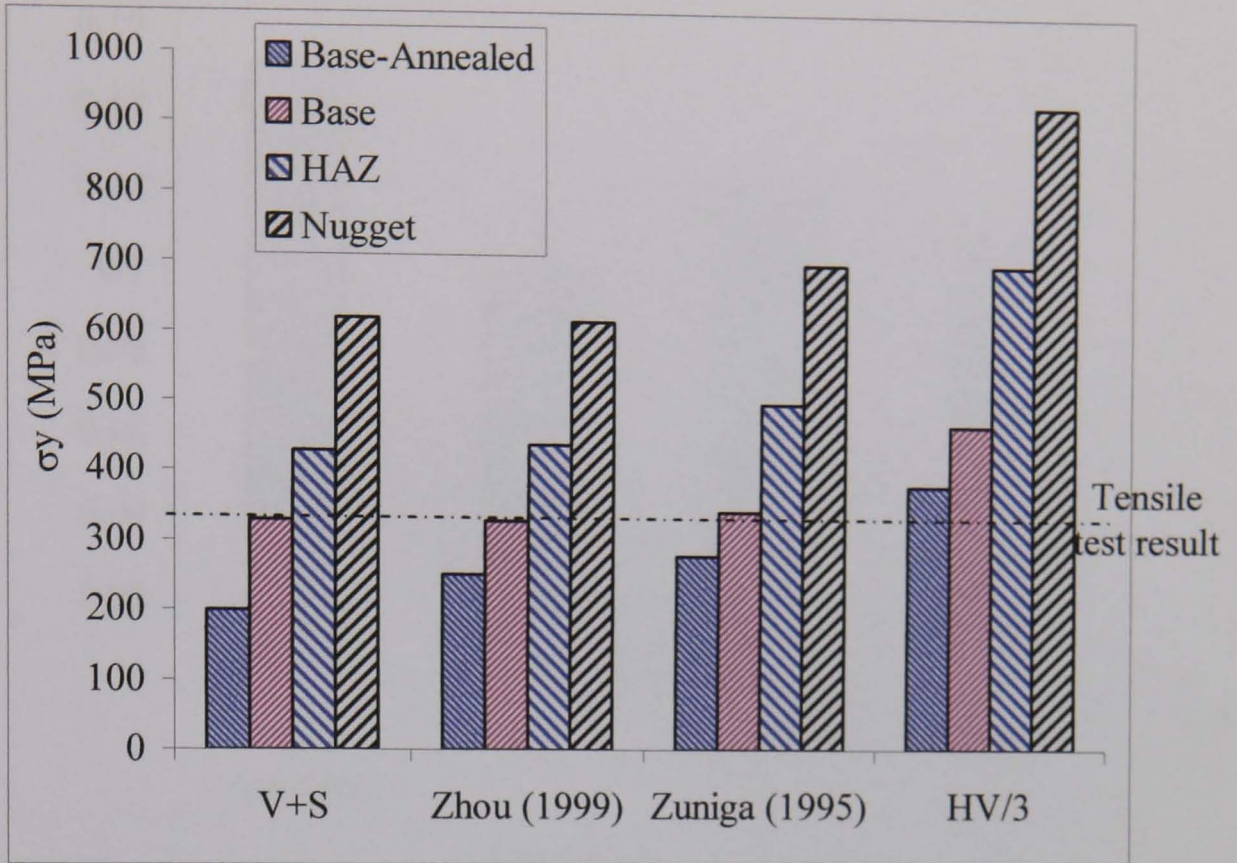
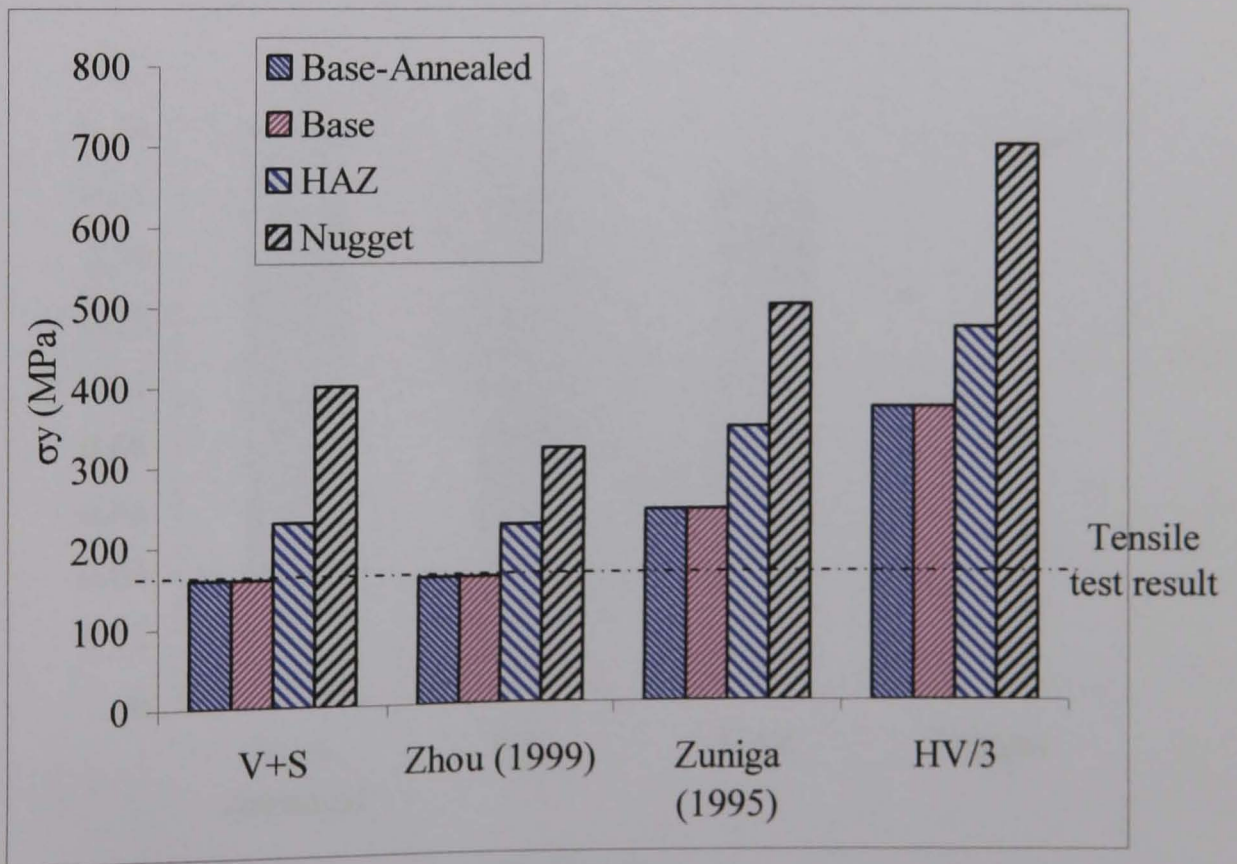


Figure 6.5 Comparison of the sensitivity of different dual indenters methods (S+S, (R05 and R1); K+S: (SR05); V+S: (SR05)) with published results (Dao *et al*, 2001; Bucaille, 2003; Swaddiwudhipong *et al*, 2005).

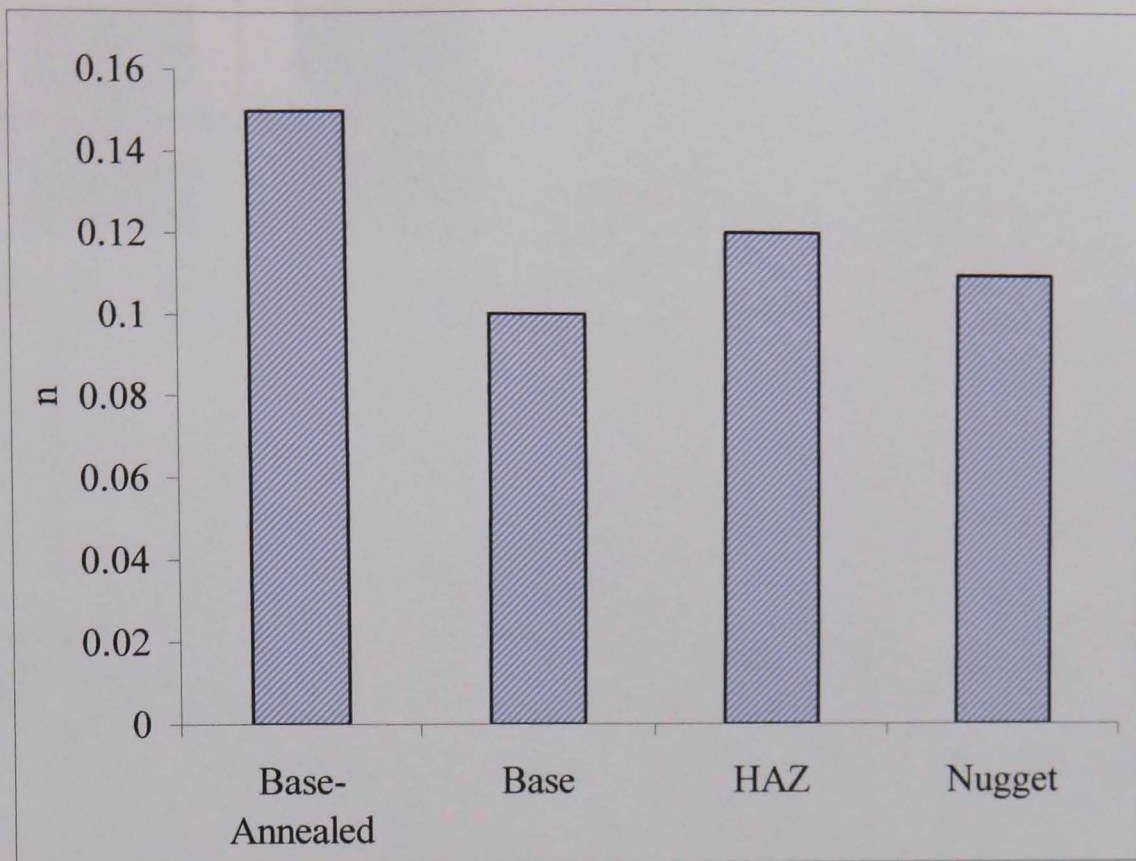


(a) Steel A.

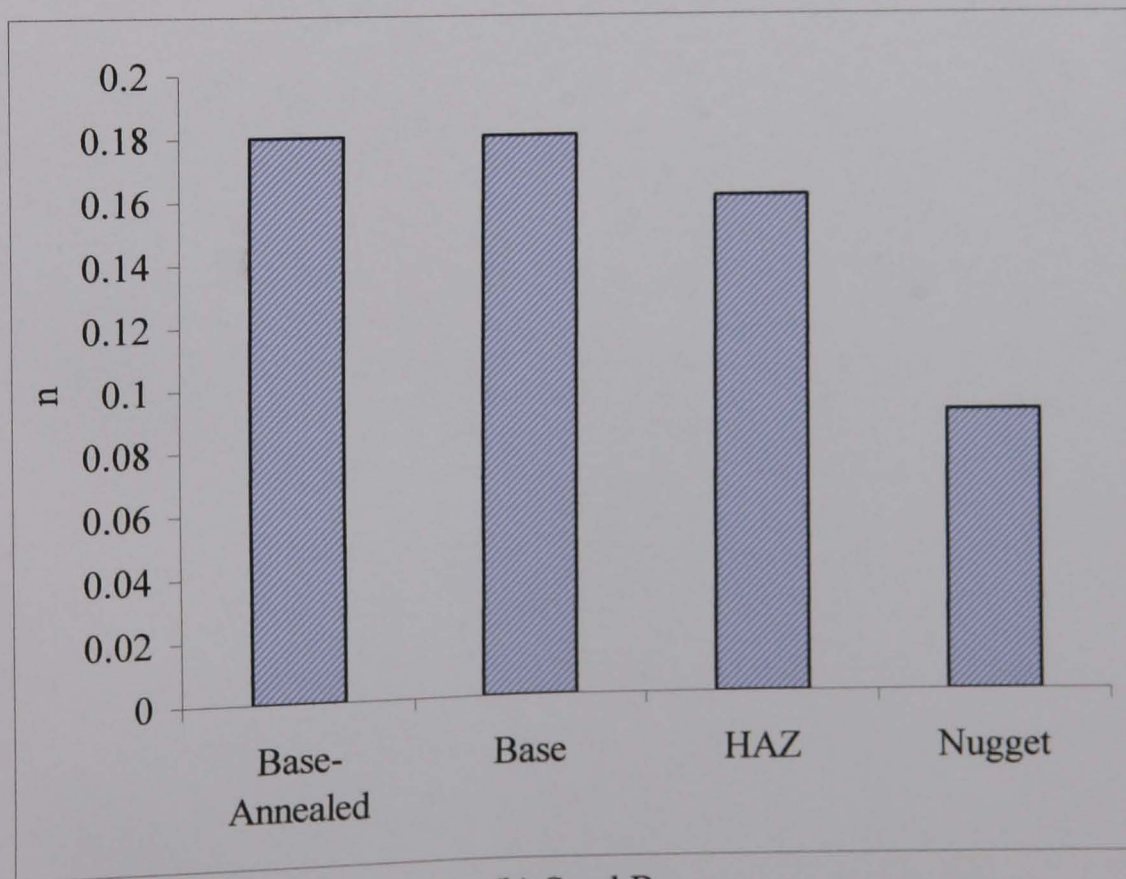


(b) Steel B.

Figure 6.6 Comparison of the predicted yield stress with different methods.



(a) Steel A.



(b) Steel B.

Figure 6.7 Comparison of the predicted work hardening coefficient with different methods.

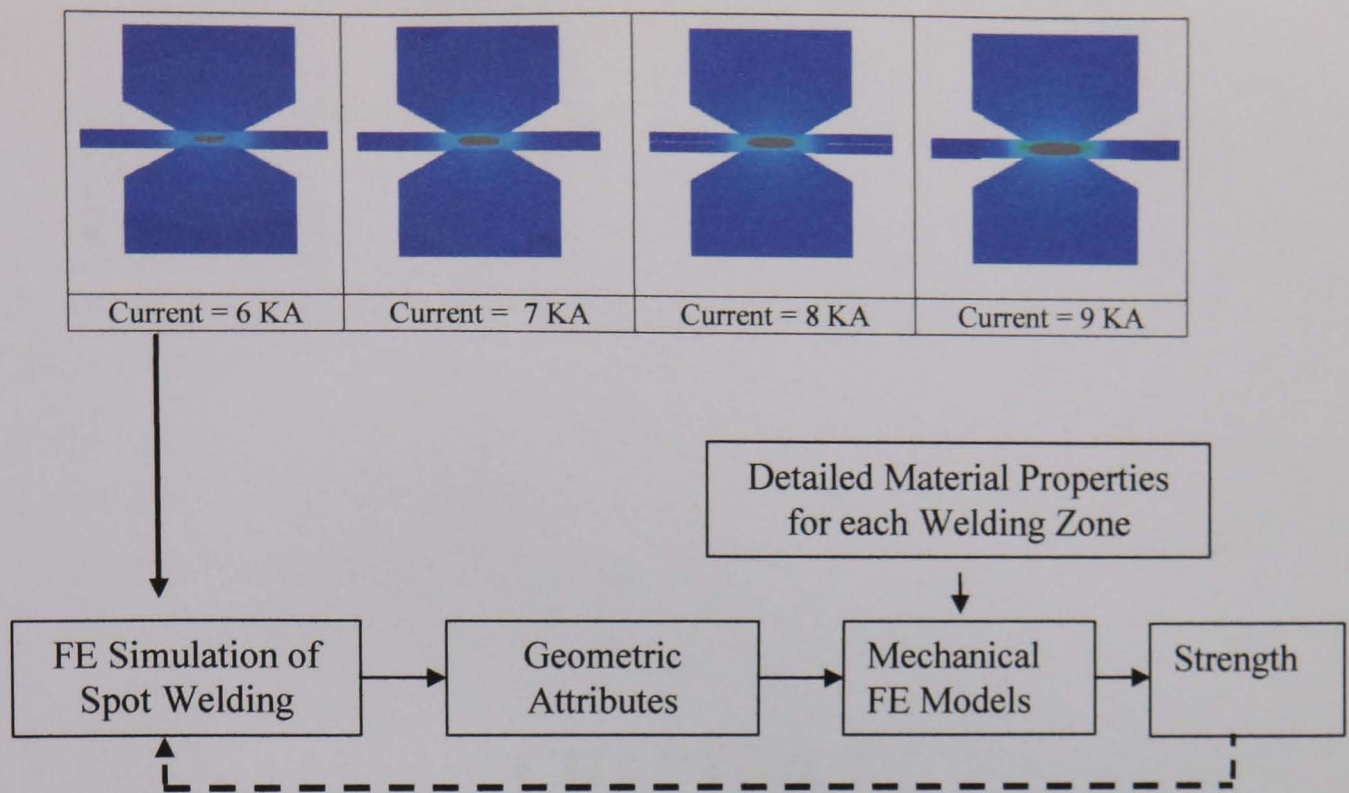


Figure 6.8 The integrated modelling approach to study the effect of welding parameters on the strength of spot-welded joints.

CHAPTER 7
CONCLUSION AND FURTHER WORK

7.1 Summary and conclusions

In this work, the use of an inverse FE modelling indentation method to predict the plastic properties (e.g. yield stress and work hardening coefficient) of elasto-plastic materials has been systematically studied. FE models of three typical indenters have been developed and validated against some published experimental data. An inverse program based on the dual indenters approach and continuous indentation curves has been established and validated, which provides the framework for a new method based on static indentation rather than continuous indentation. The method has been used to study of two typical auto steels and their spot welded joints. These predicted plastic material parameters were then used in numerical modelling of the tensile-shear deformation of spot welded joints. The validated numerical model was successfully used to investigate the effect of nugget size and the thickness of the metal sheets on the strength of welded joints.

An inverse modelling program based on a parametric study technique has been developed to extract material properties based on indentation tests. A range of potential approaches using different indenter types were comparatively studied including their uniqueness, accuracy and sensitivities to perturbation in the input data. A new method based on dual indenters of different shapes (as compared to the single indenter method) has been developed. The results showed that (i) there are multiple materials with different stress-strain relationships but matching indentation curves with Vickers, Knoop or spherical indenters, which suggests that an approach based on single indenter could not predict the material plastic properties unless the range of material properties is pre-known; (ii) The combination of two sharp indenters (e.g. Vickers and Knoop) could not extract the materials properties; (iii) Dual spherical indenters showed great improvement in terms of convergence, but the results are very sensitive to perturbation in the force or other experimental error; (iv) The combination of sharp (Vickers or Knoop) and spherical indenter is proven to be the best approach with accurate and robust results over a wide range of material properties; (v) Comparison of the new approach with other published work using dual sharp indenters showed a clear improvement in terms of both accuracy and sensitivity.

Based on the framework established, a new method using static indentation data rather than continuous indentation data has been developed and integrated with the inverse FE modelling to provide a simpler and more practical approach. The approach is validated using blind tests and the evaluation based on numerical experimental data showed similar accuracy to the continuous indentation curve approach. The method was then used to characterise the properties of two typical auto steels and their spot welded joints. Experimental work on two steels showed the stress-strain curves predicted are comparable to standard tensile tests and notched specimens, which suggests that the approach using static indentation data rather than continuous indentation data is a feasible way to characterise plastic properties. The new method represents a simpler and more practical approach which is suitable for an application where an instrumented indentation tester is not available.

The method developed has been successfully used to characterise the plastic properties of different zones in spot welded joints. Use of the method on spot welded joints showed that the yield stress predicted is considerably more accurate than pure hardness based approach and other empirical methods. Results showed the yield stress increased from the base, HAZ and nugget while the change of work hardening is materials dependent. For both steels studied, the change of work hardening coefficient is not significant. These plastic material parameters were then used in numerical modelling of the tensile shear deformation of the spot welded joint. The validated numerical model was further used to investigate the effect of nugget size and the thickness of the metal sheet on the strength of welded joints. The results showed that the effect of these dimensions is material dependant and it is not a pure linear relationship.

7.2 Recommendations for future works

This work has developed a framework for characterising plastic properties based on indentation tests. The three main outcomes, i.e. optimum combination of indentations for inverse FE modelling, approach based on static indentation method and its application in characterising spot welded joints, have laid a solid platform for future works in the following areas:

1. Use of combination of sharp and spherical combination in other materials systems. The methodology developed represents a general approach which can be used in many other materials systems.
2. Characterisation of different material systems and effect of HAZ on the structure over a wider range of loading conditions.
3. Conversion of the parametric model into a design and process selection tool. The integrated framework developed can be expanded to characterise more complex material systems – welding of low strength and high strength steels. This is an area of significant importance in the design of light structures. Another main area is to develop a programme linking the welding parameter selection and the FE models.

References

- ABAQUS**, User's Manual, version 6.3, Hibbitt, Karlsson & Sorensen, Inc.
- Aidun D. K. and Bennett R. W.**, 1984, 'Effect of resistance welding variables on the strength of spot welded 6061-T6 aluminium alloy', *The Welding Journal*, Vol. 63, p. 15.
- Alcala J., Barone A. C. and Anglada M.**, 2000, 'The influence of plastic hardening on surface deformation modes around Vickers and spherical indents', *Acta Materialia*, Vol. 48, pp. 3451-3464.
- American Society for Metals (ASM)**, 1966, *Lectures of Metals*, materials park, Ohio.
- Aravinthan A.**, 2003, 'An investigation into improve welding strength during spot welding', *Ph.D Thesis*, The Nottingham Trent University.
- Aslanlar S.**, 2006, 'The effect of nucleus size on mechanical properties in electrical resistance spot welding of sheets used in automotive industry', *Materials and Design*, Vol. 27, pp. 125–131.
- Bae D. H., Sohn I. S., and Hong J. K.**, Jan. 2003, 'Assessing the effects of residual stresses on the fatigue strength of spot welds', *The Welding Journal*, pp. 18-23.
- Bao Y., Liu L. and Zhou Y.**, 2005, 'Assessing the elastic parameters and energy-dissipation capacity of solid materials: A residual may tell all', *Acta Materialia*, Vol. 53, pp. 4857-4862.
- Barber J. R. and Billings D. A.**, 1990, 'An approximate solution for contact area and elastic compliance of a smooth punch of arbitrary shape', *International Journal of Mechanical Science*, Vol. 32(12), pp. 991-997.
- Begley M. R. and Hutchinson J. W.**, 1998, 'The mechanics of size dependent indentation', *Journal of the Mechanics and Physics of Solids*, Vol. 35, pp. 1938-1957.
- Bhushan B., Kulkarni B., Bonin A. V. and Wyrobek J. T.**, 1996, 'Nanoindentation and picondentation measurements using capacitive transducer system in atomic force microscopy', *Philosophical Magazine A*, Vol. 74, pp. 1117-1128.
- Bilodeau G. G.**, 1992, 'Regular pyramid punch problem', *Journal of applied mechanics*, Vol. 59, pp. 519-523.
- Bolshakov A. and Pharr G. M.**, 1998, 'Influences of pileup on the measurement of mechanical properties by load and depth sensing indentation techniques', *Journal of Material Research*, Vol. 13, pp. 1049-1058.

- Bolzon G., Maier G. and Panico M.**, 2004, 'Material model calibration by indentation, imprint mapping and inverse analysis', *International Journal of Solids and Structures*, Vol. 41, pp. 2957-2975.
- Bourges P. H., Jubin L. and Bocquet P.**, 1995, 'Prediction of mechanical properties of weld metal based on some metallurgical assumptions', *Mathematical Modelling of Weld Phenomena*, (Cerjack H. and Easterling K. E. Eds), Institute of Materials, London, pp. 201–212.
- Bucaille J. L. and Felder E.**, 2002, 'Finite-element analysis of deformation and scratch tests on elastic-perfectly plastic materials', *Philosophical Magazine A*, Vol. 82(10), pp. 2003–2012.
- Bucaille J. L., Stauss S., Felder E. and Michler J.**, 2003, 'Determination of plastic properties of metals by instrumented indentation using different sharp indenters', *Acta Materialia*, Vol. 51, pp. 1663–1678.
- Cavalli M. N., Thouless M. D. and Yang, Q. D.**, 2003, 'Cohesive-zone modeling of the deformation and fracture of spot-welded joints', Research Report, University of Michigan Ann Arbor, MI.
- Chae S. W., Kwon K. and Lee T.**, 2002, 'An optimal design system for spot welding locations', *Finite Elements in Analysis and Design*, Vol. 38, pp. 277–294.
- Chang B., Shi Y. and Lu L.**, 2001, 'Studies on the stress distribution and fatigue behavior of weld-bonded lap shear joints', *Journal of Materials Processing Technology*, Vol. 108(3), pp. 307-313.
- Chang H. S. and Cho Y. J.**, 1990, 'An iterative learning control system of the resistance spot welding process', *Proceeding of the IEEE International Conference on Intelligent Processing Systems*.
- Cao Y. P. and Lu J.**, 2004, 'A new method to extract the plastic properties of metal materials from an instrumented spherical indentation loading curve', *Acta Materialia*, Vol. 52, pp. 4023-4032.
- Cao Y. P. and Lu J.**, 2007, 'Spherical indentation into elastoplastic materials: indentation response based definition of the representative strain', *Materials Science and Engineering A*, Vol. 454, pp. 1-13.
- Chaudhri M. M.**, 1998, 'Subsurface strain distribution around Vickers hardness indentation in annealed polycrystalline copper', *Acta Materialia*, Vol. 46(9), pp. 3047-3056.

- Chen X., Ogasawara N., Zhao M. and Chiba N.**, 2007, 'On the uniqueness of measuring elastoplastic properties from indentation: The indistinguishable mystical materials', *Journal of the Mechanics and Physics of Solids*, Vol. 55, pp. 1618–1660.
- Cheng Y. T. and Cheng C. M.**, 1999a, 'Can stress–strain relationships be obtained from indentation curves using conical and pyramidal indenters', *Journal of Material Research*, Vol. 14(9), pp. 3493–3496.
- Cheng Y. T. and Cheng C. M.**, 1999b, 'Scaling relationships in conical indentation of elastic-perfectly plastic solids', *International Journal of Solids and Structures*, Vol. 36, pp. 1231–1243.
- Chitkara N. K. and Butt M. A.**, 1993, 'Numerical construction of axisymmetric slip-line fields for indentation of thick blocks by rigid conical indenters and friction at the tool-metal interface', *International Journal of Mechanical Sciences*, Vol. 34(11), pp. 849–62.
- Chollacoop N., Dao M. and Suresh S.**, 2003, 'Depth-sensing instrumented indentation with dual sharp indenters', *Acta Materialia*, Vol. 51(13), pp. 3713-3729.
- Dao M., Chollacoop N., Van Vliet K. J., Venkatesh T. A. and Suresh S.**, 2001, 'Computational modelling of the forward and reverse problems in instrumented sharp indentation', *Acta Materialia*, Vol. 49, pp. 3899–3918.
- Darwish S. M.**, 2003, 'Welding strengthens and balances the stresses in the spot-welded dissimilar thickness joints', *Journal of Materials Processing Technology*, Vol. 134, pp. 352-362.
- Delalleau A., Josse G., Lagarde J., Zahouani H. and Bergheau J. M.**, 2006, 'Characterization of the mechanical properties of skin by inverse analysis combined with the indentation test', *Journal of Biomechanics*, Vol. 36, pp. 1603–1610.
- Deng X., Chen W. and Shi G.**, 2000, 'Three dimensional finite element analysis of the mechanical behaviour of spot welds', *Finite Elements in Analysis and Design*, Vol. 35, pp. 17-39.
- Dickinson D. W., Franklin J. E. and Stanya A.**, 1980, 'Characterisation of the spot welding behaviour by dynamic electrical parameter monitoring', *The Welding Journal*, Vol. 59, pp. 170-176.
- Doerner M. F. and Nix W. D.**, 1986, 'A method for interpreting the data from depth-sensing indentation instruments', *Journal of Material Research*, Vol. 1(4), pp. 601–609.

- Easterling K. E., 1993, *Mathematical Modelling of Weld Phenomena*, (Cerjack H. and Easterling K. E. Eds), Institute of Materials, London, pp.183-200.**
- Feulvarch E., Robin V. and Bergheau J. M., 2004, 'Resistance spot welding simulation: a general finite element formulation of electrothermal contact conditions', *Journal of Materials Processing Technology*, Vol. 153–154, pp. 436–441.**
- Fischer-Cripps A. C., 2004, *Nanoindentation*, Springer-Verlag, New York . USA.**
- Giannakopoulos A. E. and Larsson P. L., 1997, 'Analysis of pyramid indentation of pressure-sensitive hard metals and ceramics', *Mechanics of materials*, Vol. 25, pp. 1-35.**
- Giannakopoulos A. E., Larsson P. L. and Vestergaard R., 1994, 'Analysis of Vickers indentation', *International Journal of Solids and Structures*, Vol. 31, pp. 2679-2708.**
- Giannakopoulos A. E. and Suresh S., 1999, 'Determination of elastoplastic properties by instrumented sharp indentation', *Scripta Materialia*, Vol. 40(10), pp. 1191–1198.**
- Gu Y., Nakamura T., Prchlik L., Sampath S. and Wallace J., 2003, 'Micro-indentation and inverse analysis to characterize elastic-plastic graded materials', *Materials Science and Engineering A*, Vol. 345, pp. 223-233.**
- Han Z. and Indacochea J. E., 1993, 'Effects of expulsion in spot welding of cold rolled sheet steels', *Journal of Materials Engineering and Performance*, Vol. 2, pp. 437-444.**
- Han Z., Indacochea J. E., Chen, C. H. and Bhat S., 1993, 'Weld nugget development and integrity in resistance spot welding of high-strength cold-rolled sheet steels', *The Welding Journal*, Vol. 72, pp. 209-216.**
- Herbert E. G., Oharr G. M., Oliver W. C., Lucas B. N. and Hay J. L., 2001, 'On the measurement of stress-strain curves by spherical indentation', *Thin Solid Film*, Vol. 398-399, pp. 331-335.**
- Hill R., Storakers F. R. S. and Zdunek A. B., 1989, 'A theoretical study of the Brinell hardness test', *Proceedings of the Royal Society of London. Series A, Mathematical and Physical Sciences*, Vol. 423, pp. 301-330.**
- Huh H. and Kang W. J., 1997, 'Electrothermal Analysis of electric resistance spot welding', *Journal of Material & Process Technology*, Vol. 63, pp. 672-677.**

- Ion J. C., Easterling K. E. and Ashby M. F.**, 1984, 'A second report of diagrams of microstructure and hardness for heat-affected zones in welds', *Acta Materialia*, Vol. 32 (11), pp. 1949-1962.
- Jones S. J. and Bhadeshia H. K. D. H.**, 1997, Kinetics of the simultaneous decomposition of austenite into several transformation products, *Acta Materialia*, Vol. 45, pp. 2911-2920.
- Johnson K. L.**, 1970, 'The correlation of indentation experiments', *Journal of the Mechanics and Physics of Solids*, Vol. 18, pp. 115-126.
- Johnson K. L.**, 1985, *Contact Mechanics*, Cambridge: Cambridge University Press, UK.
- Jou M.**, 2003, 'Real time monitoring weld quality of resistance spot welding for the fabrication of sheet metal assemblies', *Journal of Materials Processing Technology*, Vol. 132, pp. 102-113.
- Kimchi M.**, 1984, 'Spot weld properties when welding with expulsion — a comparative study', *The Welding Journal*, Vol. 63, pp. 58-63.
- Kucharski S. and Mroz Z.**, 2001, 'Identification of plastic hardening parameters of metals from spherical indentation tests', *Materials Science and Engineering A*, Vol. 318, pp. 65-76.
- Lan H. and Venkatesh T. A.**, 2007, 'Determination of the elastic and plastic properties of materials through instrumented indentation with reduced sensitivity', *Acta Materialia*, Vol. 55, pp. 2025–2041.
- Lancaster J. F.**, 1986, *Metallurgy of Welding*, Allen & Unwin Ltd.
- Langrand B. and Combescure A.**, 2004, 'Non-linear and failure behaviour of spotwelds: a "global" finite element and experiments in pure and mixed modes I/II', *International Journal of Solids and Structures*, Vol. 41, pp. 6631–6646.
- Larsson P. L., Giannakopoulos A. E., Soderlund E., Rowcliffe D. J. and Vestergaard R.**, 1996, 'Analysis of Berkovich Indentation', *International Journal of Solids and Structures*, Vol. 33(2), pp. 221-248.
- Larsson P. L.**, 2001, 'Investigation of sharp contact at rigid-plastic conditions', *International Journal of Mechanical Sciences*, Vol. 43, pp. 895-920.
- Lesage J., Chicot D., Bartier O., Zampronio M. A. and Miranda P. E. V.**, 2000, 'Influence of hydrogen contamination on the tensile behaviour of a plasma ion nitrided steel', *Materials science and Engineering A*, Vol. 282, pp. 203-212.

- Li W., Feng E., Cerjanec D. and Grzadzinski G. A.**, 2004, 'Energy consumption in AC and MFDC resistance spot welding', *Metal Welding Conference XI*, Sterling Heights, MI, USA.
- Lin C. J., Duh J. G. and Liao M. T.**, 1993, 'Influence of weld parameters on the mechanical properties of spot-welded Fe-Mn-Al-Cr alloy', *Journal of Materials Research*, Vol. 28, pp. 4767-4774.
- Luo J. and Lin J.**, 2007, 'A study on the determination of plastic properties of metals by instrumented indentation using two sharp indenters', *International Journal of Solids and Structures*, Vol. 44, pp. 5803–5817.
- Marx V. and Balke H.**, 1997, 'A critical investigation of the unloading behaviour of sharp indentation', *Acta Materialia*, Vol. 45, pp. 3791.
- Mata M. and Alcala J.**, 2004, 'The role of friction on sharp indentation', *Journal of the Mechanics and Physics of Solids*, Vol. 52, pp. 145 – 165.
- Mirshams R. A. and Parakala P.**, 2004, 'Nanoindentation of nanocrystalline Ni with geometrically different indenters', *Materials Science and Engineering A*, Vol. 372, pp. 252-260.
- Meuwissen M. H. H., Oomens C. W. J., Baaijens F. P. T., Petterson R. and Janssen J. D.**, 1998, 'Determination of the elasto-plastic properties of aluminium using a mixed numerical–experimental method', *Journal of Materials Processing Technology*, Vol. 75, pp.204–211.
- Nakamura T. and Gu Y.**, 2007, 'Identification of elastic–plastic anisotropic parameters using instrumented indentation and inverse analysis', *Mechanics of Materials*, Vol. 39, pp. 340–356.
- Nakamura T., Wang T. and Sampath S.**, 2000, 'Determination of properties of graded materials by inverse analysis and instrumented indentation', *Acta Materialia*, Vol. 48, pp. 4293–4306.
- Oliver W. C., and Pharr G. M.**, 1992, 'An improved technique for determining hardness and elastic modulus using load and displacement sensing indentation experiments', *Journal of Material Research*, Vol. 7(6), pp. 1564–1583.
- Oliver W. C. and Pharr G. M.**, 2004, 'Measurement of hardness and elastic modulus by instrumented indentation: Advances in understanding and refinements to methodology', *Journal of Materials Research*, Vol. 19, pp. 3-20.
- O'Neil H.**, 1967, *Hardness Measurements of Metals and Alloys*, Chapman Hall, New Jersey.

- Palmonella M., Friswell M. I., Mottershead J. E. and Lees A. W.**, 2005. 'Finite element models of spot welds in structural dynamics: review and updating'. *Computers and Structures*, Vol. 83, pp. 648-661.
- Pickett A. K., Pyttelb T., Payenb F., Lauroc F., Petrinicd N., Wernere H. and Christlein J.**, 2004, 'Failure prediction for advanced crashworthiness of transportation vehicles', *International Journal of Impact Engineering*, Vol. 30, pp. 853–872.
- Ren X. J., Hooper R. M., Griffiths C. and Henshall L. J.**, 2001, 'An investigation of the effect of indenter heating on the indentation creep behaviour of single crystal MgO', *Journal of Materials Science Letters*, Vol. 20, pp.1819-1821.
- Ren X. J., Hooper R. M., Griffiths C. and Henshall L. J.**, 2002. 'Indentation size effect (ISE) in single crystal MgO', *Philosophical Magazine A*, Vol. 82(10), pp. 2113-2120.
- Ren X. J., Hooper R. M., Griffiths C. and Henshall L. J.**, 2003, 'Indentation size effect of ceramics –correlation with H/E', *Journal of Materials Science Letters*, Vol. 22, pp. 1105-1106.
- Ren X. J., Smith C. W., Evans K. E., Dooling P. J., Burgess A. and Wiechers J. W.**, 2004, 'The mechanics of human skin', *SEM X International Congress & Exposition on Experimental and Applied Mechanics*, California, USA.
- Ren X. J., Smith C. W., Evans K. E., Dooling P. J., Burgess A. and Wiechers J. W.**, 2005, 'Experimental testing and numerical modelling of mechanical properties of the human skin', *International Foundation of Society of Cosmetic Chemists (IFSCC)*, Vol. 1 , pp. 95-98.
- Ren X. J., Smith C. W., Evans K. E., Dooling P. J., Burgess A., Wiechers J. W. and Zahlan N.**, 2006, 'Deformation of materials under localized tangential loading', *International Journal of Solids and Structure*, Vol. 43, pp. 2364–2377.
- Ren X. J., Li L., English R. and Rothwell G.**, 'Characterisation of Nonlinear Material Parameters of Foams Based on Indentation Tests', *Materials and Design* (under review in a revised form).
- Rodrigues D. M., Menezes L. F. and Loureiro A.**, 2004a, 'Modelling the effect of HAZ undermatching on the crack-tip stress distribution in idealized welds'. *International Journal of Mechanical Sciences*, Vol. 46, pp. 1481–1488.

- Rodrigues D. M., Menezes L. F. and Loureiro A.**, 2004b, 'The influence of the HAZ softening on the mechanical behaviour of welded joints containing cracks in the weld metal', *Engineering Fracture Mechanics*, Vol. 71, pp. 2053–2064.
- Rusinska E., Kopczynskib A. and Czmochowska J.**, 2004, 'Tests of thin-walled beams joined by spot welding', *Journal of Materials Processing Technology*, Vol. 157, pp. 405–409.
- Santella M. L., Babu S. S., Riemer B. W. and Feng Z.**, 2003, 'Influence of microstructure on the properties of resistance spot welds', Research Report, Oak Ridge National Laboratory, Oak Ridge, USA.
- Santos I. O. and Zhang W.**, 2004, 'Weld bonding of stainless steel', *International Journal of Machine Tools and Manufacture*, Vol. 44, pp. 1431-1439.
- Shan Z. and Gokhale A. M.**, 2003, 'Utility of micro-indentation technique for characterization of the constitutive behavior of skin and interior microstructures of die-cast magnesium alloys', *Materials Science and Engineering A*, Vol. 361, pp. 267–274.
- Shriver J., Peng H. and Hu S. J.**, 1999, 'Control of resistance spot welding', *Proceedings of the American Control Conference*, California .
- Stilwell N. A. and Tabor D.**, 1961, 'Elastic recovery of conical indentations', *Proceeding of the Physial Society*, Vol. 78, p. 169.
- Swaddiwudhipong S., Hua J., Tho K. K. and Liu Z. S.**, 2006, 'Equivalency of berkovich and conical load-indentation curves', *Modelling and Simulation in Materials Science and Engineering*, Vol. 14, pp. 71-82.
- Swaddiwudhipong S., Tho K. K. , Liu Z. S. and Zeng K.**, 2005a, 'Material characterisation based on dual indenters', *International Journal of Solids and Structures*, Vol. 42, pp. 69-83.
- Swaddiwudhipong S., Tho K. K., Liu Z. S., Zeng K. Hua J. and Ooi N. S. B.**, 2005b, 'Material characterization via least squares support vector machines', *Modelling and Simulation in Materials Science and Engineering*, Vol. 13, pp. 993–1004.
- Tabor D.**, 1948, 'A Simple Theory of Static and Dynamic Hardness', *Proceedings of the Royal Society of London, Series A, Mathematical and Physical Sciences*, Vol. 192(1029), pp. 247-274.
- Tabor D.**, 1951. 'The hardness and strength of metals', *Journal of the Institute of Metals*, Vol. 79, pp. 1-18.

- Taljat B., Zacharia T. and Kosel F.**, 1998, 'New analytical procedure to determine stress-strain curve from spherical indentation data', *International Journal of Solids and Structures*, Vol. 35(33), pp. 4411-4426.
- Tho K. K., Swaddiwudhipong S., Liu Z. S. and Zeng K.**, 2005, 'Simulation of instrumented indentation and material characterization', *Material Science and Engineering A*, Vol. 390, pp. 202-209.
- Tho K. K., Swaddiwudhipong S., Liu Z. S., Zeng K. and Hua J.**, 2004, 'Uniqueness of reverse analysis from conical indentation tests', *Journal of Material Research*, Vol. 19(8), pp. 2498-2502.
- Tvergaard V.**, 1981, 'Influence of voids on shear band instabilities under plain strain condition', *International Journal of Fracture Mechanics*, Vol. 17, pp. 389-407.
- Venkatesh T. A., Vliet K. J., Giannakopoulos A. E. and Suresh S.**, 2000, 'Determination of elasto-plastic properties by instrumented sharp indentation: Guidelines for property extraction', *Scripta Materialia*, Vol. 42, pp. 833-839.
- Vogler M. and Sharpped S.**, 1992, 'A study of temperature histories in resistance spot welding', *Weld Research International Conference*, Catlingburg, Tennessee.
- Vogler M. and Sharpped S.**, 1993, 'Electrical contact resistance under high loads and elevated temperatures', *The Welding Journal*, Vol. 72, pp. 231-238.
- Wadjaja A.**, 2007, 'Discrete dislocation modelling of nano- and micro-indentation', *Ph.D Thesis*, University of Groningen.
- Wang L.**, 2003, 'Ductile fracture of structure steel using local approach', *Ph.D Thesis*, University of the West of England.
- Yang Q. D., Rugg K. L., Cox B. N. and Shaw M. C.**, 2003, 'Failure in the junction region of T-stiffeners: 3D-braided vs. 2D tape laminate stiffeners', *International Journal of Solids and Structures*, Vol. 40, pp. 1653-1668.
- Yang Q. D., Ren X. J., Li Y. L., Zhao Y. H. and Yao M.**, 2005, 'Effect of welding parameters on residual stress field of 20CrMnTi specimen and its numerical simulation', *Materials Science and Engineering A*, Vol. 392, pp. 240-247.
- Zhou M., Hu S. J. and Zhang H.**, September 1999, 'Critical specimen sizes for tensile-shear testing of steel sheets', *The Welding Journal*, pp. 305-313.
- Zhou M., Zhang H. and Hu S. J.**, April 2003, 'Relationships between quality and attributes of spot welds', *The Welding Journal*, pp. 72-77.

Zuniga S. M. and Sheppard S. D., 1995, 'Determining the constitutive properties of the heat-affected zone in a resistance spot weld', *Modelling and Simulation in Materials Science and Engineering*, Vol. 3, pp. 391-416.

Publication list

Kong X. P., Li B., Yang Q., English R., Rothwell G. and Ren X. J., 'Inverse FE modelling to characterise the gradient properties of HAZ zones of spot welded auto steels', *Materials Science and Engineering A*, in preparation.

Kong X. P., Li B., Yang Q., English R., Rothwell G., Ren X. J., 2008. 'Numerical modelling of the strength of spot welded joints of steels', *Materials and Design*, Vol. 29(8), pp. 1554-1561.

Kong X. P., Li B., Yang Q., English R., Rothwell G. and Ren X. J., 2008, 'Numerical study of the effect of welding parameters on the strength of spot-welded joints', *Applied Mechanics and Materials*, Vol. 10(12), pp. 322-326.

Kong X. P., Ren X. J., English R. and Rothwell G., 2008, 'Determination of plastic properties of materials by dual indenter methods', *9th European Symposium on Nanomechanical Testing*, Germany.

Kong X. P., Li B., Yang Q., English R., Rothwell G. and Ren X. J., 'Numerical study of the effect of welding parameters on the strength of spot-welded joints', *6th Int. Conf. on e-Engineering and Digital Enterprise Technology*, China, 2007.

Kong X. P., Li B., Ren X. J., English R. and Rothwell G., 2007, 'Determination of plastic properties of materials by combined numerical and experimental method', *3rd Int. Indentation Workshop*, Cambridge.